Ab initio LCAO electronic structure calculations of layered transition-metal compounds

Dawson, William G.

Award date:
1988

Awarding institution:
University of Bath

ab initio LCAO ELECTRONIC STRUCTURE CALCULATIONS OF LAYERED TRANSITION-METAL COMPOUNDS

submitted by William G. Dawson

for the degree of PhD of the

University of Bath.

COPYRIGHT

ProQuest LLC
789 East Eisenhower Parkway
P.O. Box 1346
Ann Arbor, MI 48106-1346

SUMMARY

In this work the electronic structure of three systems of layered transition metal compounds are examined using an ab initio tight binding (LCAO) method using the $X\alpha$ exchange/correlation approximation: group VI ditellurides, group IV trichalcogenides and quaternary copper oxide defect-perovskites. A chemical pseudopotential argument is presented in order to justify the use of a small basis set of atomic orbitals. The group VI transition metal compounds $MoTe_2$ and WTe_2 show strong metal-metal interactions and $MoTe_2$ undergoes an unusual phase transition with the lattice parameter perpendicular to the layers decreasing with increasing temperature. The group IV transition metal trichalcogenides provide a useful series for study due to their quasi-1-dimensional character and the occurrence of two closely related structural variants. The atypical compound $ZrTe_3$ is given special attention because of its apparent semimetallic nature. The final group of compounds studied are the high T_c superconducting ceramics Ba-La-Cu-O and Ba-Y-Cu-O. The technological importance of compounds with zero resistance and showing the Meissner effect (expelling magnetic fields) above liquid nitrogen temperatures and the, as yet, undefined nature of the mechanism of superconductivity stresses the need to carefully examine

the electronic structure of these materials. The role of oxygen vacancies, the charge state of the copper ions and the possibility of structural phase transitions are some of the topics considered here. The use of an atomic-orbital basis allows a comparatively straightfoward description of the chemical bonding in a crystal- especially useful when the unit cell contains a large number of atoms.

ACKNOWLEDGEMENTS

Many thanks to many people

especially:-

David Bullett

Eileen Moore

and

Gerry Witchlow.

I am also grateful for a three year grant from the

University of Bath Research Fund.

31. .... g5!!

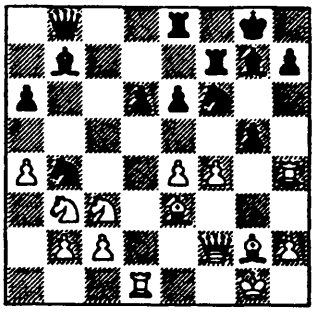

Karpov-Kasparov II

Final game, World Chess Championship.

Moscow, 1985.

CONTENTS

Chapter 1 Introduction

The subject of this thesis is an examination of the chemical bonding via electronic structure of three systems of layered transition metal compounds using an ab intio linear combination of atomic orbitals (LCAO) method within a chemical pseudopotential formalism. These layered crystals are characterised by two distinctly different types of bonding (ie. they are heterodesmic)- covalent interatomic bonds but with van der Waals gaps defining their 2D or occasionally quasi-1D nature. The growth of interest in these low dimensional structures is due to a range of interesting physical and chemical properties which are currently active areas of experimental research. Electronic and optical (eg. Bayliss and Liang, 1982) and electrical transport (eg. Hambourger and Di Salvo,1980) studies have shown the anisotropic nature of these compounds. The occurrence of polymorphism and polytypism, which are common in these compounds (eg. see Wilson and Yoffe, 1969), is discussed later.

The low dimensionality in reciprocal space also allows Fermi surface nesting in some cases, with associated charge-density-wave/ periodic-lattice-distortions (CDW/PLD) (Withers and Wilson, 1986; Wilson et al., 1975). These distortions are currently the subject of

much interest, not least in the field of electron microscopy (where Peierls transitions (Peierls, 1955 and 1933) are observed when passing through the transition temperature (eg. Bird et al., 1984) and for applications in non-linear conduction, due to the Frohlich mode, when incommensurate CDW are depinned from crystal defects (Wilson, 1984). The 'metal rich' group Va transition metal tetrahalides (eg. Bullett, 1985), $ZrTe_3$ (Eaglesham et al., 1985), dichalcogenides (Fung et al., 1981; Eaglesham et al., 1986) are clear examples of the strong metal-metal interactions which can drive these transitions but metal-metal bonding is also found in, for example, the group VIa ditellurides and is explored here.

Intercalation of layered structures provides another reason for interest in these compounds. The layer spacing of these crystals may be comparatively easily increased (eg. by ten fold, Gamble et al., 1971) since the van der Waals gap obviously means that the layers are bound only weakly to each other. This is an advantage over tunnelled structures which can intercalate atoms and molecules only of well-defined sizes. It is now established that an electropositive intercalate has little effect on the band structure of the host (eg. Mc Canny, 1979)- other than the donation of electrons which can change the electrical conduction

of the host material from semiconducting to metallic, and can show superconductivity at low temperatures.

Another family of layered compounds burst with a roar into the physics world and spillled over into the popular media- the high T_c superconducting ceramics. This followed the publication by Bednorz and Muller, 1986 and subsequent award of the Nobel prize for their guided empiricism which led them to the discovery of the high T_c ceramic Ba-La-Cu-O. This work was followed by a plethora of new, related compounds- the most useful of which can carry an electrical current with zero resistance at temperatures above liquid nitrogen. Their electronic properties are obviously in need of detailed examination if, as is the hope, room-temperature superconductivity is to be achieved. The mechanism by which these materials superconduct is still the subject of intense debate- a huge amount of data is now being generated and analysed from these compounds. The difficulty of growing single crystals has hampered workers, but the crystal structures of the superconducting phases are now being established routinely as new high T_c compounds are discovered.

Chapter two of this work is a description of the ab initio LCAO method used to calculate the electronic structure of these layered transition metal compounds.

The usefulness and ease of application of this technique to the computation of electron states and the subsequent analysis in terms of chemical bonding is explained. The intuitive picture of treating a crystal in terms of pairwise interactions (in the two centre approximation) is retained and justified. This method is particularly suited to large unit cells of transition and noble metal compounds since a relatively small basis set of atomic orbitals is used. This method has proved reliable for a range of transition metal compounds (eg. Bullett and Dawson, 1986a and 1986b). The layered compounds are treated here as perfect crystals, therefore they have a well defined reciprocal space which is exploited by this method. The large volumes of empty space (the van der Waals gap) present no obstacle to this method in contrast to the LMTO (linearised muffin tin orbital) or other ASA (atomic sphere approximation) methods where this space is packed with 'empty spheres' (Andersen et al., 1986) which complicate the calculations and introduces extra approximations.

Chapter 3 outlines the reasons for interest in the transition metal dichalcogenides (MX_2's). This is a very large area to cover and the intention is to provide a brief review of past results and models- concentrating on the electronic structure. This chapter gives detail of some of the more important aspects of

low-dimensionality mentioned above. WTe_2 and $MoTe_2$ are found to be anomalous in this series of compounds and electronic structure calculations of these are the subject of chapter 4. In contrast to many of the other MX_2's metal-metal bonding is found in these ditellurides, also they do not crystallise with a trigonal prismatic coordination around the metal atoms as a simple bonding model would predict. Some related crystal structure are also considered in order to help analyse the electronic structure.

Chapter 5 provides background to the group IVa transition metal trichalcogenides (MX_3, M=Ti,Zr,Hf; X=S,Se,Te) and chapter 6 present the results of calculations on them with a discussion. The ab initio method is given a thorough work-out by calculations on these closely related compounds- working down a group of the periodic table and comparing the resulting electronic structures with known trends. Although the group V trichalcogenides have been extensively studied the group IVa crystals have been in need of theoretical electronic structure calculation for some time (Khumalo and Hughes, 1980). Previous experimental studies have been analysed by comparison with the related dichalcogenides. The archetypal $ZrSe_3$ has been examined by theoreticians (Myron et al., 1981; Bullett, 1985). The MX_3's occur as two closely related variants with

some compounds showing both types under similar growth conditions (Furuseth et al., 1975)- all the compounds studied in this work were calculated as both variants and the differences explored. $ZrTe_3$ falls outside the general trend of the MX_3's because it is possibly semimetallic and shows a probable CDW transition. It is therefore given special consideration in both of these chapters.

Chapter 7 starts with a brief review of the high T_c superconducting ceramics. The rate of publication on this topic is phenomenal- it is almost impossible to attempt a thorough and up to date review but the current results and main points of interest are presented. Two of the topics discussed in this chapter are the possible SDW (spin-density-wave) state in La-Cu-O (Guo et al., 1988) and the valence state of the copper ions in the Ba-Y-Cu-O system (Wilson, 1987). The electronic structures of the La-Cu-O and Ba-Y-Cu-O systems are then calculated and discussed. The two systems are usefully compared- indicating some general trends for these materials, especially the nesting of the Fermi surface which is most clearly seen in the La-Cu-O system where there is only one sheet to the Fermi surface.

Chapter 8 concludes the thesis with a short summary of the results, work in progress and proposed future work.

CHAPTER 2. The ab initio LCAO method.

2.1 Introduction to LCAO (The linear combination of atomic orbitals)

The LCAO or tight binding method aims to express the eigenfunctions and/or eigenvalues of an electron system (eg. a molecule or crystal) in a comparatively small basis set of atomic orbitals. That is, the interaction due to neighbouring atoms in the system is considered small enough to treat as a perturbation to the free atomic states- it is therefore apparent that this scheme will be most successful for well-localised atomic orbitals such as the valence 'd' orbitals of the transition metal compounds. This is in contrast to a nearly-free-electron model where a large number of plane waves would be needed to mimic a tightly bound d state. It is not so obvious that the free atom orbitals represent the system wavefunction with s and p orbitals which may have large overlaps. We may hope for the generation of portable matrix elements if this approach is valid- ie. utilising the transferability of the chemical bond.

The translational symmetry of a crystal is exploited by

the use of Bloch's Theorem which reduces the basis set from the total number of atomic orbitals in a crystal down to the number per unit cell, and introducing the $\underline{k}$ dependence of the resulting eigenvalues. Furthermore the basis set is usually restricted to the free atom valence orbitals- therefore incompletely spanning the vector space of the crystal eigenfunction. This incompleteness may cause considerable inaccuracy above the Fermi level but this must be weighed against the computational simplicity of a reduced basis set. The application of the variational method should lead to reasonable eigenvalues near and below the Fermi level. The atomic core orbitals are usually considered non-participating (the frozen-core approximation) since they are so tightly bound (localised) to the nucleus and of large negative energy. Thus is the dimension of the resulting Hamiltonian matrix reduced from the total number of atomic orbitals in the whole crystal down to the comparatively small number of valence orbitals per unit cell.

The LCAO method is presented in most standard solid state physics and chemistry texts, but a brief description is provided here for convenience.

The crystal wavefunctions (Ψ_i) are built from Bloch states of atomic orbitals (ϕ_n) thus:-

$$\psi_k(\underline{r}) = \sum_{n,d,\underline{R}} b_{n,d}\, \phi_{n,d}(\underline{r}-\underline{r}_d-\underline{R})\, e^{i\underline{k}\cdot\underline{R}} \qquad 2.1$$

where n,d and $\underline{R}$ are atomic orbital label, site label and integral units of lattice parameters respectively. The expansion parameter b is therefore a function of site and orbital, with $e^{i\underline{k}\cdot\underline{R}}$ the Bloch phase factor. In order to simplify notation we will consider the case of just one atom in a unit cell. Therefore eqn. 2.1 is rewritten:-

$$\psi_k(\underline{r}) = \sum_{n,\underline{R}} b_n\, \phi_n(\underline{r}-\underline{R})\, e^{i\underline{k}\cdot\underline{R}} \qquad 2.2$$

which satisfies the Schroedinger eqn.:-

$$H|\psi(\underline{r})\rangle = (H_{at} + U(\underline{r}))|\psi(\underline{r})\rangle = \varepsilon_k|\psi(\underline{r})\rangle \qquad 2.3$$

with H and H_{at} the crystal and free atom Hamiltonians respectively. $U(\underline{r})$ the perturbing potential on the atom at $\underline{r}$ due to the other atoms in the system is defined as:-

$$U(\underline{r}) = \sum_{R\neq 0} V(\underline{r}-\underline{R}) \qquad 2.4$$

Thus

$$\langle\phi_m(\underline{r})|H_{at}|\psi(\underline{r})\rangle = \varepsilon_m\langle\phi_m(\underline{r})|\psi(\underline{r})\rangle \qquad 2.5a$$

$$(\varepsilon_k-\varepsilon_m)\langle\phi_m(\underline{r})|\psi(\underline{r})\rangle = \langle\phi_m(\underline{r})|U(\underline{r})|\psi(\underline{r})\rangle \qquad 2.5b$$

where E_m is the free atom eigenvalue.

Since $\langle\phi_n(\underline{r})|\phi_m(\underline{r})\rangle = \delta_{nm}$ then

$$\begin{aligned}(\varepsilon_k-\varepsilon_m)b_m = &-(\varepsilon_k-\varepsilon_m)\sum_n\Big(\sum_{R\neq 0}\langle\phi_m(\underline{r})|\phi_n(\underline{r}-\underline{R})\rangle e^{i\underline{k}\cdot\underline{R}}\Big)b_n \\ &+\sum_n b_n\langle\phi_m(\underline{r})|U(\underline{r})|\phi_n(\underline{r})\rangle \\ &+\sum_n\Big(\sum_{R\neq 0}\langle\phi_m(\underline{r})|U(\underline{r})|\phi_n(\underline{r}-\underline{R})\rangle e^{i\underline{k}\cdot\underline{R}}\Big)b_n .\end{aligned} \qquad 2.6$$

The integrals on the right are of three types:-

1) $\langle \phi_n(\underline{r}) | \phi_m(\underline{r}) \rangle$ which is the simple overlap integral (S or occasionally O). This is set to zero in some approximations (CNDO- Complete Neglect of Differential Overlap). Overlaps can be quite large terms, and thus neglecting these terms appears to be an oversimplification- however the pseudopotential formalism given below shows that this approximation is not as drastic as it may seem.

2) $\langle \phi_m(\underline{r}) | U(\underline{r}) | \phi_n(\underline{r}) \rangle$ The crystal field term. This is the effect of the perturbing potential of the environment on the atom at $\underline{r}$. This term shows the lifting of the energy degeneracy of orbitals of the same angular momentum number (s,p,d etc.) when the spherical symmetry of the free atom is broken. Applications from group theory are usefully applied here- especially for commonly encountered atomic environments such as octahedral (transforming under the group O_h into e_g and t_{2g}) which lifts the 5-fold degeneracy of transition metal d orbitals. The crystal field term contains no $\underline{k}$ dependence and, therefore, provides a rigid shift to the diagonal term in the Hamiltonian matrix- constant for all $\underline{k}$ points.

3) $\langle \phi_n(\underline{r}) | U(\underline{r}) | \phi_m(\underline{r}-\underline{R}) \rangle$ The hopping integral. Matrix elements of this form describe the interaction of 2 different orbitals under the influence of the

perturbing potential. The Bloch phase factor attached to the hopping integral in eqn. 2.6 gives the dispersion of the resultant energy bands space even when the overlap term is set to zero.

A two-centre approximation is commonly made to eqn. 2.6- that is three centre and higher terms are considered negligible. Only sites with the orbitals and potentials on two atoms simultaneously contribute to the matrix elements. This allows an enormous simplification of the integrals which may then be considered in terms of a diatomic molecule with cylindrical symmetry along the bond axis.

2.2 Pseudopotentials.

Given that the atomic orbitals used in the tight binding approximation must form an incomplete subspace of the true crystal wavefunction, it would appear that the application of the variational principle will give the best energies based on this sub-set. In fact we can show formally that the free atomic orbitals can be used in a Hamiltonian which will make them a good expansion set (at least up the the Fermi level). The technique is a pseudopotential method which localises the one electron orbitals by projecting out valence-valence orbital interactions. Historically pseudopotentials were

developed to justify a plane-wave basis in the OPW (orthogonalised plane-waves) formalism- the basis of plane-waves is orthogonalised to the atomic core states, effectively projecting out the deep core potential and resembling a nearly free electron approximation of the crystal wavefunction. The effect of the pseudopotential is shown schematically in fig. 2.1.

2.3 OPW and pseudopotentials.

In the OPW formalism (eg. Harrison, 1966) a solution of the one-electron time-independent Schroedinger equation

$$H|\psi_i\rangle = (T + V(r))|\psi_i\rangle = \epsilon_i|\psi_i\rangle \qquad 2.7$$

with T=K.E.= $-\hbar^2/2m\,\nabla^2$ and V($\underline{r}$) the self consistent potential on each electron is solved in terms of plane waves $e^{i\underline{k}\cdot\underline{r}}$.

However a large basis would be needed in order to localise some states onto the atomic sites. One method of reducing the size of the Hamiltonian matrix and solve eqn. 2.7 with a basis of plane-waves (ϕ_k) is to orthogonalise them to the atomic core states ($\psi_\alpha(r)$) (Herring,1940).

$$|\phi_k\rangle = |e^{i\underline{k}\cdot\underline{r}}\rangle - \sum_\alpha |\psi_\alpha(r)\rangle\langle\psi_\alpha(r)|e^{i\underline{k}\cdot\underline{r}}\rangle \qquad 2.8$$

with ϕ_k consisting of a plane wave Schmidt orthogonalised to the core states (ψ_α). Note that

Fig. 2.1 Schematic pseudopotential.

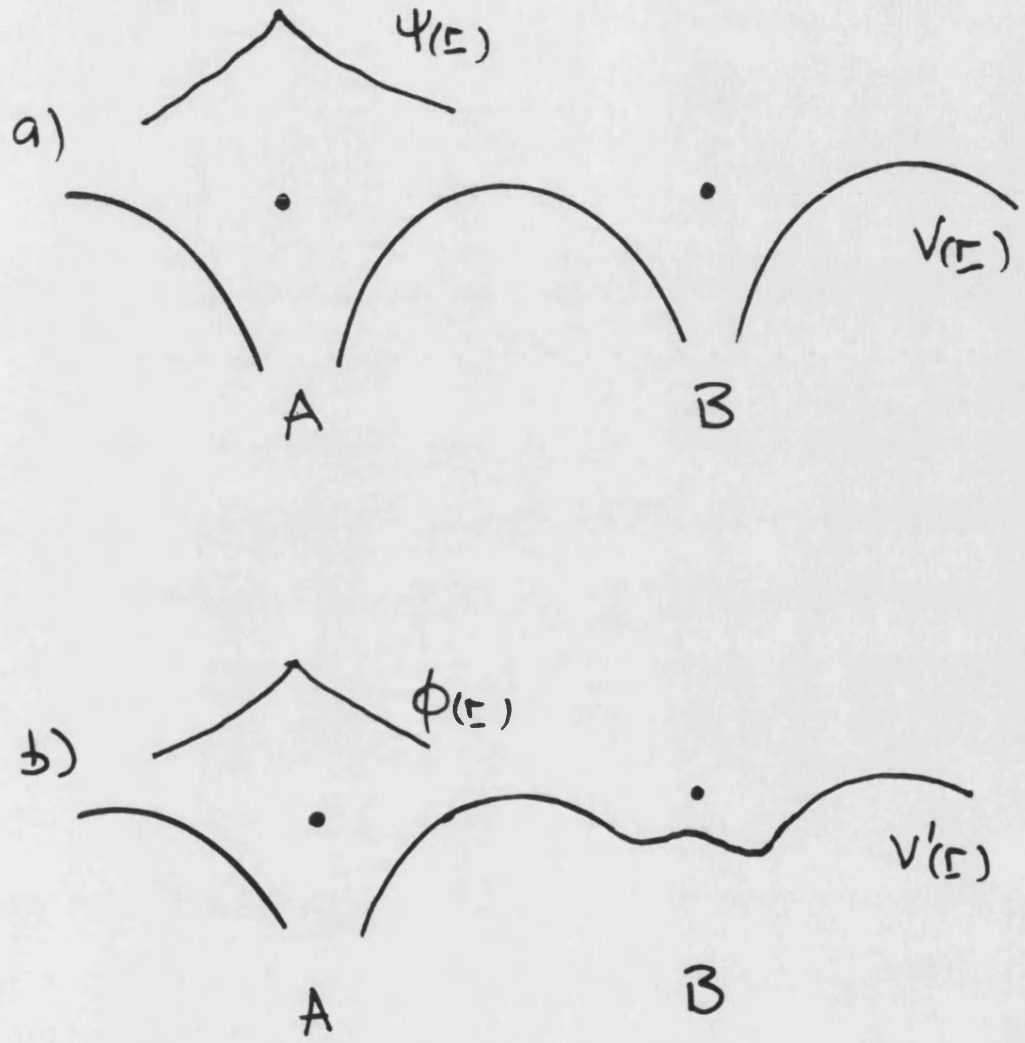

a) Wavefunction Ψ centred on atom at A sees large crystal potential ($V(\underline{r})$) due to atom at B.

b) Pseudofunction ϕ sees reduced potential at B due to projecting out core potential on atom B and leaving only pseudopotential $V'(\underline{r})$.

$\langle \psi_\alpha | \phi_k \rangle$ =0 since core states are orthogonal.

Normalising the plane waves to the volume Ω :-

$$|k\rangle = \frac{1}{\sqrt{\Omega}} e^{i\underline{k}\cdot\underline{r}} \qquad 2.9$$

We can write eqn. 2.8 as

$$OPW_k = |k\rangle - |\alpha\rangle\langle\alpha|k\rangle \quad \text{implied sum over } \alpha .$$

The orthogonaliser can be written as the projection operator

$$P = |\alpha\rangle\langle\alpha| \text{ (Pick and Sarma, 1964)} \qquad 2.10$$

thus:-

$$OPW_k = (1-P)|k\rangle \qquad 2.11$$

$$\text{therefore } \psi_k = \sum_q a_q(k)(1-P)|k+q\rangle . \qquad 2.12$$

Substituting eqn. 2.12 back in the Schroedinger eqn. gives

$$\sum_q a_q(k) H(1-P)|k+q\rangle = E_k \sum_q a_q(k)(1-P)|k+q\rangle \qquad 2.13$$

Closing through with $\langle k+q'|$ leads to the secular equation which is approximated in the OPW method by a basis of 20-30 plane-wave terms. Justifying the, initially surprising, resemblance of the resulting band structure (for many materials- especially metals) to a nearly free electron (NFE) model Phillips and Kleinman (1959) rewrote eqn. 2.7 as

$$T\phi_k + W\phi_k = E_k\phi_k \qquad 2.14$$

with W, the pseudopotential, defined as

$$W = V(r) + V'(r) = V(r) + \sum_\alpha (E_k - E_\alpha)|\alpha\rangle\langle\alpha| = V(r) - (E_k - H)P . \qquad 2.15$$

Therefore, if W can be shown to be small, the OPW's (pseudofunctions) can be seen to be a good expansion set for the crystal. It can be seen that the non-local

operator $V'(r) = \sum_{\alpha}(E_k - E_\alpha)|\alpha\rangle\langle\alpha|$ (which can be approximated to a local function, eg. see Phillips and Kleinman (1959)) is expressed in terms of states which are orthogonal to the crystal valence states for which the Schroedinger eqn. is solved. Thus any $V'(\underline{r})$ of the form $V'(r) = \langle r(\alpha)|\phi\rangle|\alpha\rangle$ can be used to satisfy eqn. 2.15. Austin et al., 1962 showed a range of pseudopotentials which lead to the same crystal eigenvalues.

Summarising the pseudopotential $W=V(\underline{r})+V'(\underline{r})$:- whereas the potential $V(\underline{r})$ is attractive the core projection term in $V'(\underline{r})$ is repulsive- thus reducing the effect of the potential on the pseudofunctions. Choosing the most appropriate form of $V'(\underline{r})$ can minimise the pseudopotential. The pseudofunctions and pseudopotentials are not uniquely defined- the same eigenvalues can be obtained from an arbitrary $F(\alpha)$ in eqn. 2.15.

The pseudopotential theory given so far relates to a basis set of plane waves but we are interested in expanding the crystal wavefunction in terms of well localised (ideally free atomic) orbitals.

2.4 Localised orbitals and pseudopotentials.

We can use the pseudopotential method to allow a good expansion of the one-electron crystal eigenfunctions in terms of well localised orbitals (eg. see Bullett, 1980). The localisation is brought about by the use of a projection operator (P) which is composed of the valence and core orbitals of the electronic system (eg. molecule or crystal) rather than just the core orbitals as before. We assume that the system eigenfunction may be expanded in a basis of non-orthogonal, localised orbitals ϕ_α . The use of a non-orthogonal set allows these functions to be more localised than, for example, Wannier functions which, in addition to the difficulty of calculating them, are less localised by virtue of the 'wiggly tails' introduced by the orthogonality constraint. We are aiming to exploit the portability of the resulting matrix elements when using well localised orbitals. If the localised orbitals $|\phi_\alpha\rangle$'s span the space of the system wavefunctions $|\psi_i\rangle$'s then

$$|\phi_\alpha\rangle = P|\phi_\alpha\rangle \qquad \text{is exact} \qquad 2.16$$

with $P = |\psi_i\rangle\langle\psi_i|$ (summation convention applying)

and P, the projection operator, satisfies

$$P^2 = P \text{ and } [P,H] = 0 \,. \qquad 2.17$$

Thus eqn. 2.16 can be written in the Hermitian form

$$H|\phi_\alpha\rangle = PHP\,|\phi^\circ_\alpha\rangle \qquad 2.18$$

The free atom Hamiltonian (H_a) obviously satisfies

$$H_a |\phi_\alpha^\circ\rangle = \epsilon_\alpha^\circ |\phi_\alpha^\circ\rangle \qquad 2.19$$

with the free atom orbitals ϕ_α°.

The basis functions ϕ_α may be defined as localised in the form suggested by Adams (1971)

$$P H_a P |\phi_{\alpha i}\rangle = \epsilon_{\alpha i} |\phi_{\alpha i}\rangle \qquad 2.20$$

with the lowest energy solution ϵ_i° corresponding to the atomic-like orbital.

Adding eqns. 2.18 and 2.20 gives

$$H|\phi_\alpha\rangle - P(H-H_a)P|\phi_\alpha\rangle = \epsilon_\alpha |\phi_\alpha\rangle \qquad 2.21$$

or equivalently

$$H_a|\phi_\alpha\rangle + (U_a - PU_aP)|\phi_\alpha\rangle = \epsilon_\alpha |\phi_\alpha\rangle \qquad 2.22$$

with $U_a \equiv H - H_a$ ie. the perturbation to $|\phi_\alpha\rangle$ from the rest of the system.

Eqn. 2.22 shows the reduced perturbation (U_a-PU_aP) as a residual screened interaction- which explains why the localised orbitals $|\phi_\alpha\rangle$ could form a small expansion set for the $|\psi_i\rangle$'s . Note the resemblance between eqn. 2.22 and the standard pseudopotential eqn. developed previously. In eqn. 2.22 we wish to project on to the unknown valence orbitals of the system and this equation must therefore be solved self-consistently unless some approximations are introduced.

The projection operator may be expressed in terms of the non-orthogonal localised orbitals $|\phi_\alpha\rangle$ preserving normalisation (see Lowdin, 1968)

$$P = \sum_{\alpha,\beta} |\phi_\alpha\rangle (S^{-1})_{\alpha\beta} \langle\phi_\beta| \qquad 2.23$$

where $S_{\alpha\beta} = \langle \phi_\alpha | \phi_\beta \rangle$

which can be seen to satisfy the projection operator properties $P^2=P$ and $[P,H]=0$.

Writing eqn. 2.22 as

$$H_a|\phi_\alpha\rangle + \sum_{b\neq a} V_b - PV_bP|\phi_\alpha\rangle = \epsilon_\alpha|\phi_\alpha\rangle . \qquad 2.24$$

Anderson (see Weeks et al., 1973) suggested replacing the ugly projection operator of eqn. 2.23 with the approximate form

$$PV_b \simeq P_bV_b \quad \text{where } P_b = |\phi_\beta\rangle\langle\phi_\beta| . \qquad 2.25$$

Since $P|\phi_\alpha\rangle = |\phi_\alpha\rangle$ the resulting non-hermitian eqn. is

$$[H_a + \sum_{b\neq a}(V_b - P_bV_b)]|\phi_\alpha\rangle = \epsilon_\alpha|\phi_\alpha\rangle \qquad 2.26$$

or equivalently

$$H|\phi_\alpha\rangle = \epsilon_\alpha|\phi_\alpha\rangle + \sum_{\beta\neq a}|\phi_\beta\rangle\langle\phi_\beta|V_b|\phi_\alpha\rangle . \qquad 2.27$$

We will retain this reduced projection operator in order to simplify the notation, substituting the full form back as required.

Anderson (1968), studying the π system of a benzene ring demonstrated that the self-consistent $|\phi_\alpha\rangle$'s closely resembled the free atomic orbitals- thus suggesting that it may be a reasonable approximation to replace the $|\phi_\alpha\rangle$'s with free atom $|\phi_\alpha^\circ\rangle$.

We can futher simplify eqn. 2.27 by writing the action of the Hamiltonian on a basis member as

$$H|\phi_\alpha\rangle = \sum_\beta |\phi_\beta\rangle D_{\beta\alpha} \qquad 2.28$$

since the $|\phi_\alpha\rangle$ span the space of the eigenfunctions $|\psi_i\rangle$'s of H. Taking matrix elements we can see that $\underline{D} = \underline{S}^{-1}\underline{H}$, and that that $\underline{D}$ is hermitian only when $\underline{H}$ and $\underline{S}$ commute. The usefulness of the matrix $\underline{D}$ is apparent when written in the form

$$H|\phi_\alpha\rangle = \epsilon_\alpha|\phi_\alpha\rangle + \sum_{\beta\neq\alpha}|\phi_\beta\rangle D_{\beta\alpha} \qquad 2.29$$

with the definition $D_{\alpha\alpha} = \epsilon_\alpha$

Therefore if we expand the vector space $|\psi_i\rangle$ in terms of $|\phi_\alpha\rangle$ ie.

$$|\psi_i\rangle = \sum_\alpha c_{\alpha i}|\phi_\alpha\rangle \qquad 2.30$$

then

$$H|\psi_i\rangle = \sum_\alpha c_{\alpha i} H|\phi_\alpha\rangle = \sum_{\alpha,\beta} c_{\alpha i}|\phi_\beta\rangle D_{\beta\alpha} = E_i\sum_\alpha c_{\alpha i}|\phi_\alpha\rangle. \qquad 2.31$$

Swopping labels α and β and assuming linear independence of the orbitals on different sites eqn. 2.31 leads to the secular equation

$$\det|D_{\alpha\beta} - E_i\delta_{\alpha\beta}| = 0 . \qquad 2.32$$

The matrix elements of $\underline{D}$ are given by comparing eqns. 2.27 and 2.29

$$D_{\alpha\alpha} = \epsilon_\alpha = \langle\phi_\alpha|H_{at} + \sum_{\beta\neq\alpha}(1 - |\phi_\beta\rangle\langle\phi_\beta|)V_\beta|\phi_\alpha\rangle$$

$$\text{and } D_{\beta\alpha} = \langle\phi_\beta|V_\beta|\phi_\alpha\rangle . \qquad 2.33$$

For a periodic structure the $|\phi_\alpha\rangle$'s are written in the Bloch form $e^{i\underline{k}\cdot\underline{R}}|\phi_\alpha\rangle$ and equation 2.32 is solved for the $\underline{k}$ dependent energy eigenvalue on a computer using a standard library (NAG) routine for non-hermitian matrices. The non-hermicity of $\underline{D}$ may result in complex energies, but in practice the

imaginary parts of E are negligible. Weeks et al. (1973) (and references therein) discuss the advantages of using the non-Hermitian form of $\underline{D}$. The right and left eigenvectors of $\underline{D}$, although not simply adjoint, have common eigenvalues and are orthogonal for differing, non-degenerate eigenvalues. The left eigenvector can be shown to be more localised than the right, thus reducing the error in eigenvalues for the localised atomic-like orbital basis (eg. see Boys, 1969).

The reduced projection operator P given above can be seen to be exactly pairwise (ie. involving only two centre terms), using the full form of P

$$P = \sum_{\alpha,\beta} |\phi_\alpha\rangle (S^{-1})_{\alpha\beta} \langle\beta| \qquad 2.34$$

we can retain the picture of transferable diatomic parameters by using only the orbitals centred on the two atomic sites in question, ie. of the leftmost bra and rightmost ket of eqn. 2.33.

We apply the two centre approximation to the evaluation of the matrix elements of $\underline{D}$. Thus we can tabulate the matrix elements of the secular equation for pairs of atoms as a function of the distance between the atoms over a suitable range and interpolate for the specific case using the Slater-Koster scheme given below.

2.5 The Slater-Koster interpolation scheme.

Slater and Koster (1954) showed how the two centre terms of an LCAO matrix may be calculated for an arbitrary bond vector by rotating the spherical harmonics of the atomic orbitals. They give a table of the 14 basic possible inter-orbital interactions for s, p and d orbitals in terms of the familiar σ, π and δ type orbital overlaps defined by the direction cosines of the 'molecular' bond vector. For example the combination of a p_x orbital on one site and a d_{xy} on another may be expressed relative to a cartesian frame as

$$p_x, d_{xy} \rightarrow \sqrt{3}l^2m(pd\sigma) + m(1-2l^2)(pd\pi) \qquad 2.35$$

with l,m and n the direction cosines on the x,y and z axes repectively. This is shown pictorially in fig. 2.2.

Sharma (1979) developed an equivalent but general procedure using a rotation matrix to generate two centre matrix elements quantised along the bond axis using group theory techniques. That is the atomic orbital ϕ_α can be rewritten thus

$$\phi_\alpha(n,l,m) = \sum_{m'} [A^l(d)]_{mm'} \phi'_\alpha(n,l,m') \qquad 2.36$$

with A' the (unitary) rotation matrix (for a bond vector $\underline{d}$) of dimension 2l+1 (the allowed values of m_l) leaving ϕ_α quantised w.r.t. $\underline{d}$.

The Slater-Koster scheme obviously cannot be applied for

Fig 2.2 The combination of p_x and d_{xy} orbitals in terms of σ and π interactions within the Slater-Koster scheme.

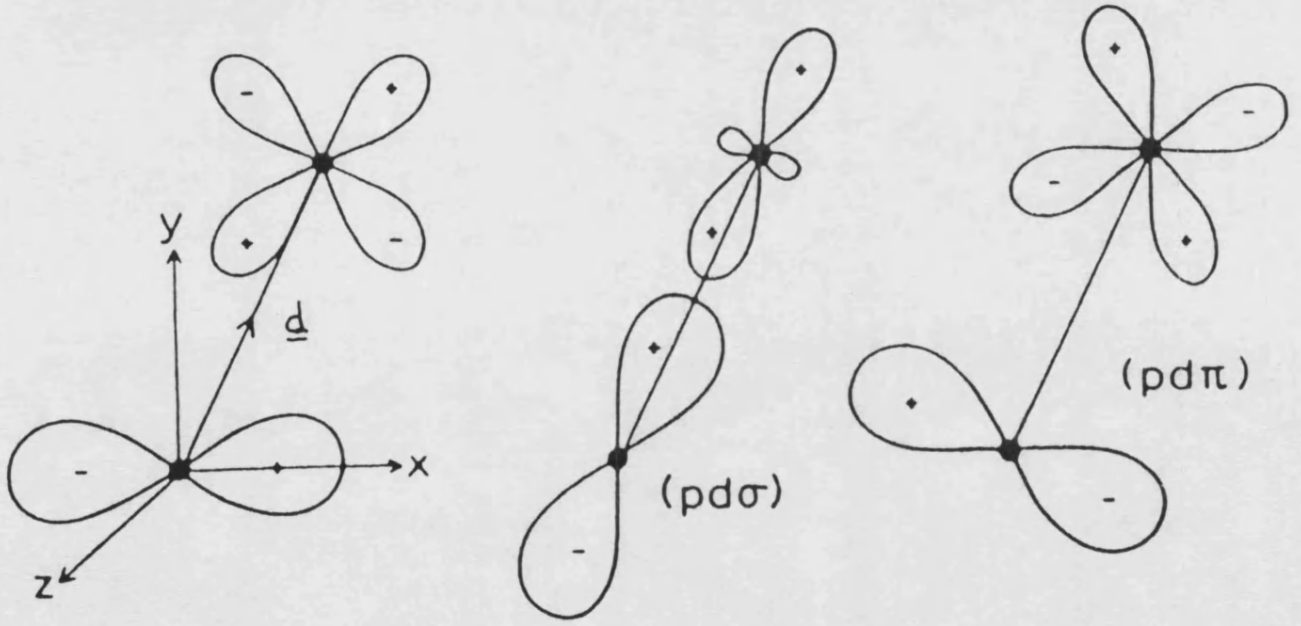

three and higher centre terms and the loss of portability and added difficulty of calculation of these terms accounts for the common useage of the two centre approximation.

This interpolation scheme may then be used to evaluate matrix elements containing operators with cylindrical symmetry such as the potential terms used in the D matrix above.

2.6 Calculation of the atomic orbitals

A standard library routine by Herman and Skillman (1963), using a self-consistent Hartree-Fock-Slater one-electron equation, is used to generate the free atomic orbitals which are used as the basis to set-up the $\underline{D}$ matrix. To obtain the Hartree-Fock equation the total atomic wavefunction is expressed as a Slater determinant of the one-electron orbitals- this then satisfies the anti-symmetry requirement for fermions. The appplication of the variation principle (eg. Bransden and Joachian, 1983) leads to the solutions of the orthonormal single electron wavefunction O_i (eg. Ashcroft and Mermin, 1981)

$$-\hbar^2/2m\nabla^2\phi_i(\underline{r}) - Ze^2\sum_R \frac{1}{|\underline{r}-\underline{R}|}\phi_i(\underline{r}) + e^2\sum_j \int d\underline{r}' |\psi_j(\underline{r}')|^2 \frac{1}{|\underline{r}-\underline{r}'|}\phi_i(\underline{r}) - \sum_j \int dr' \frac{e^2}{|r-r'|}\phi_j^*(\underline{r}')\phi_i(r')\phi_j(\underline{r})\delta_{s_i s_j} = \epsilon_i\phi_i(\underline{r}) \qquad 2.37$$

with the terms on the left being (respectively) the K.E., the electron-nucleus Coulomb term, the electron-electron term and the exchange-correlation term. The exchange term is not only non-linear in ϕ but also non-local- it is an integral operator and presents a severe obstacle to the solution of eqn. 2.36 in the solid state. For this reason approximations are sought for the exchange-correlation term. In a constant potential (ie. when the solutions are plane waves) it is possible to evaluate the exchange term exactly (eg. Ashcroft and Mermin, 1981)

$$\langle \epsilon_{exchange} \rangle = -0.916/(r_s/a_o) \text{ Ryd.} \qquad 2.38$$

where r_s is the radius of a sphere per conduction electron and with r_s/a_o 2-6 for metals. The Bohr radius $a_o = \hbar/me^2 = 0.529A$.

Slater (1951) suggested for a non-homogenous distribution in a periodic potential, that eqn. 2.38 could be used to approximate the exchange as a local density function

$$V_{ex}^{Slater}(r) = -3e^2 \left(\frac{3\rho(r)}{8\pi} \right)^{1/3} \qquad 2.39$$

with an electron density $\rho(r)$. Kohn and Sham (1965) and Gaspar (1954) have suggested evaluation V_{ex} at $k=k_F$, because of the physical interest at the Fermi level. This led to the introduction of the adjustable parameter α, where

$V_{ex} = \alpha V_{ex}^{Slater}$ $\quad 2/3 < \alpha < 1$. 2.40

This is known as the Xα approximation. Slater (1974) has self-consistently solved the Hartree-Fock equation for a number of elements to find the best α . Following these results a value of 0.7 is used in the Hartree-Fock-Slater calculations for all the atoms used in this work. The Herman and Skillman program, for a given atomic charge configuration, outputs the following (as a function of the radial distance from the nucleus):-

1) the atomic coulomb potential
2) the exchange potential
3) the valence orbitals
4) the core (filled shell) orbitals.

2.7 Building and solving the D matrix.

The first stage to solving the secular equation in $\underline{D}$ is to use a computer program to calculate a table of matrix elements as a function of distance for interactions between the constituent atom types of a particular compound in order to utilise the Slater-Koster scheme outlined above. Thus terms like $ss\sigma$, $sp\sigma$, $pp\pi$ etc. are calculated for distances of 2 to 9 au.. in steps of 1 au. and for infinity. The integrals are performed numerically by dividing space into cubes, which are smaller near the atom cores where the wavefunctions are

more rapidly varying. The full projection operator (P) of eqn. 2.34 is used with the constraint that the orbitals are used in a strictly pairwise fashion- thus retaining the model of a transferable diatomic molecule. The core orbitals are retained in the projection operator in order to orthogonalise the valence orbitals of an atom to the neighbouring atom's core thus partially screening the core potential, in accordance with the pseudopotential scheme. The matrix elements at this stage are not k-dependent and not structure dependent terms; they are functions of distance only. They are then stored for the setting up of the $\underline{D}$ matrix for a given crystal.
The next program takes as input:-

1) the initial form of the matrix elements as calculated above

2) the crystal structure of the compound to be analysed

3) the free atomic energies for each atomic orbital for a given angular momentum number (l).

The free atomic energies (self-energy) are fed in along the diagonal of $\underline{D}$. Then, taking each atom in an origin unit cell in turn, the program loops through real space finding

i) the distance to neighbouring atoms

ii) their direction cosines

iii) and Bloch phase factor.

By interpolating from the initial matrix elements the $\underline{D}$ matrix elements are calculated at the correct distances using the Slater-Koster expressions. An interatomic cut-off distance (eg. 8 au.) is employed beyond which the magnitude of the matrix elements becomes negligible.

2.8 Self consistency of the D matrix.

The tightly bound nature of the d electrons of atoms in the transition series means that the energy of these orbitals is very sensitive to the electron occupation. The more spatially dispersed s and p orbitals present less of a problem since their energy varies only slowly with occupation- and therefore the assignment of these electrons to a particular atom in the crystal is of reduced importance. The diagonal energy of the d orbital however is crucial to the form of a band structure since it often defines a fermi or (non-metal) p-d (metal) gap in transition metal compounds. Therefore these calculations are made self-consistent in the d orbital

energy/occupation.

A number of atomic orbital energies from the Herman and Skillman program are plotted as output energy vs. input electron orbital configuration. This graph is then used to iterate through solutions of the $\underline{D}$ matrix until the input energy and output d occupations converge. Thus we need a method of assigning weights to the calculated eigenvectors in order to compute the projected densities of states onto the d orbitals- the Mulliken 'gross atomic population' technique is used here. That is where the weight of the overlap term is divided equally between two orbitals ϕ_α and ϕ_β . The charge division is given, in terms of the crystal eigenvectors thus :- Using $\underline{D}=\underline{S}^{-1}\underline{H}$, and since $\underline{H}$ and $\underline{S}^{-1}$ are Hermitian the right and left eigenvectors of $\underline{D}$ can be seen to satisfy :-

$$|\psi_i^L\rangle = S\,|\psi_i^R\rangle \qquad 2.41$$

or, in term of the basis vectors

$$|\psi_i^L\rangle = \sum_\alpha b_{i\alpha}\,|\phi_\alpha\rangle$$

$$|\psi_i^R\rangle = \sum_\alpha a_{i\alpha}\,|\phi_\alpha\rangle = \sum_\beta b_{i\beta}\,|\phi_\beta\rangle\,(S^{-1})_{\alpha\beta} \qquad 2.42$$

with coefficients a and b for the bra and ket of D respectively. Thus the normalised vector is written

$$\langle\psi_i^R|\psi_i^R\rangle = \sum_{\gamma,\alpha,\beta} a_{i\gamma}^*\,\langle\phi_\gamma|\phi_\beta\rangle\,(S^{-1})_{\alpha\beta}\,b_{i\beta} \qquad 2.43$$

$$\therefore 1 = \sum_{\gamma,\alpha,\beta} a^*_{i\gamma} b_{i\beta} \delta_{\gamma\beta} = \sum_{\gamma} a^*_{i\gamma} b_{i\gamma} \quad . \qquad 2.44$$

And thus the weight on the basis orbital ϕ_γ for the eigenvector ψ_i is given by $a^*_{i\gamma} b_{i\gamma}$. The occupation of the d orbitals is therefore calculated by summ ing the normalised eigenvector weights through the occupied eigenstates.

2.9 The densities of states and E(k).

The band structure (E($\underline{k}$)) graphs are now a simple matter of diagonalizing the D matrix for $\underline{k}$ points along the high symmetry lines of the irreducible portion of the Brillouin zone for a given crystal structure. A variable number of points can be chosen in order to increase the resolution of a region of interest.

For the densities of states and projected densities of states the irreducible part of the zone is sampled using a net of weighted points- for the layer compounds calculated here fewer points are used along the axis of reduced dispersion. The use of a small basis set in LCAO permits the fast computation of a large number of $\underline{k}$ points, although a special points method (Chadi and Cohen, 1973) may be used with small loss of accuracy for large unit cells. The resulting eigenstates are stored in the form of a histogram and smoothed by convolution

with a gaussian function of convenient width before being plotted.

2.10 Conclusion

The method outlined above has shown how to calculate the electronic structure of a large unit cell containing transition metal atoms in a computationally fast and straightforward manner with no adjustable parameters other than the well documented values of α for use in the Xα approximation. The use of the atomic orbitals as the basis set allows a direct analysis of the results in terms of a chemical bonding picture. The use of the chemical pseudopotential method gave a non-hermitian matrix which can be shown to localise the left eigenfunctions of the matrix D, and justify the use of the tight binding set. The idea of a simple diatomic molecule (but with the crystal Bloch phase factor) is preserved throughout- thus an intuitive physical picture can be employed.

CHAPTER 3. The layered transition metal dichalcogenides.

3.1 Introduction

Attention was originally drawn to the transition metal dichalcogenides (TMDC) in 1969 following the publication of the seminal review article of Wilson and Yoffe (1969). A vast amount of research has now been devoted to these compounds, for example they feature strongly in the series "Physics and Chemistry of Materials with low-dimensional structures" (Levy, 1977). This chapter is an attempt to provide a brief outline of the reasons why these materials are a source of such fascination and to review some of the more important results of these investigations to date. Rather than attempt a thorough update of Wilson and Yoffe's (1969) review the major features of interest of the MX_2 compounds are highlighted.

As a stepping stone to appreciation of the transition metal dichalcogenides MX_2 (M= transition metal; X= S,Se,Te) it is useful to put them into context by recognising that they belong to a larger family of 1-D and 2-D layer compounds. These show common features such as anisotropic transport properties, intercalation of

electron donating atoms and molecules and some occurrence of CDW-PLD (charge-density-wave, periodic lattice distortion) states- which are discussed below. Other important and related members of the family include the group MX_x (M=transition metal, X= chalcogen or halogen; with x=3,4,5).

The 1-D and quasi-1-dimensional crystals are structurally related by all being composed of infinite chains running through the crystal, but with different types of chain which are displaced or varying in number per unit cell for different compounds. For the 2-D crystals of this family the chained character (quasi-1 dimensionality) is lost giving layered compounds with the layers being defined by a van der Waals gap. The layered nature of these materials means that thin platelets of crystals can be cleaved; this is very useful for optical and electron transmission studies.

An introductory example of 1-D behaviour is shown by the metal rich group V halides TaI_4 and NbI_4 where, in a simple bonding picture, one electron remains after completing the halide octets- so-called metal rich compounds. This enables a pairing of the metal atoms along the chain- reducing the Fermi energy and stabilising the structure (Simon, 1981). The resulting structure shown in fig. 3.1, has alternate metal-metal

Fig. 3.1 The NbI_4 structure

a) Paired metal atoms are displaced from the centre of the coordination octahedra

b) The hexagonal close packed iodine lattice with pairs of metal atoms in interstitial sites of alternate layers.

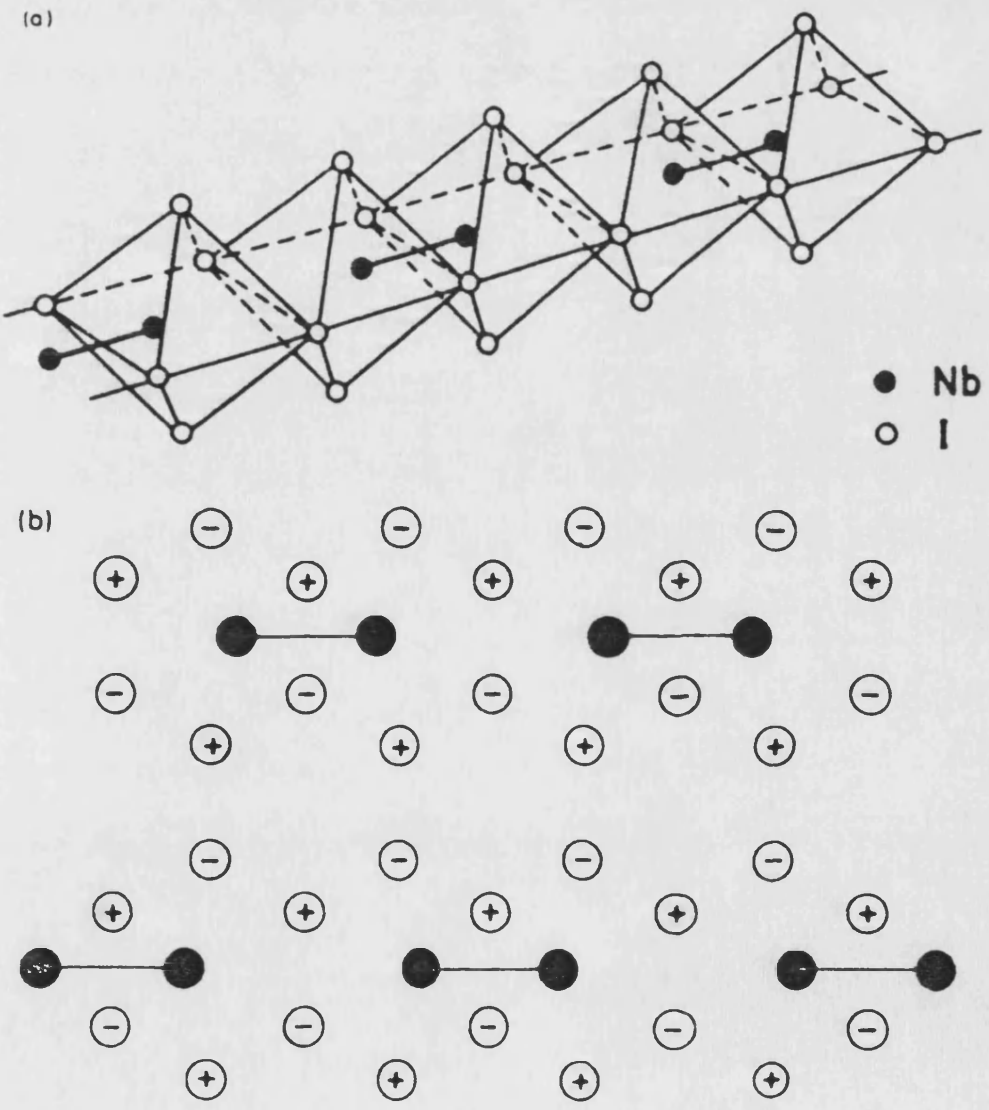

distances of 3.3A and 4.3A along a chain, each metal atom being displaced by 0.26A from the centre of an octahedron of iodine atoms. Bullett (1985) gives ab initio LCAO calculations, by the same method as this thesis, showing how this commensurate Peierls distortion acts to reduce the Fermi level. The mechanism of this effect is that the σ bonding band due to the metal d_{z^2} orbital (directed along the chain axis) is pushed down by the reduced metal-metal distance. The semiconducting gap is also opened further when the anion radius is reduced (ie. by moving up the periodic table), thus allowing a closer approach of the paired metal atoms.

In this chapter the layered TMDC of groups IV to VIb are reviewed- leading into the following chapter where the calculated electronic structures of the tellurides of group VI elements Mo and W are presented and discussed.

3.2 Crystal and electronic structure

The MX_2 compounds with their structures and electrical properties are shown in table 3.1 (from Wilson and Yoffe 1969, and Levy, 1976). This table shows the high incidence of layer structures for the MX_2's (about 40 from a total of 60). It can be seen that the layer compounds of groups IV to VIb fall into 3 groups, but that these basic structures cover a wide range of

Table 3.1

Structural types found in the MX_2s.(after Wilson,1969).

M/	X_2	$-S_2$	$-Se_2$	$-Te_2$	Electrical character
IV	Ti	L oct	L oct	L oct	Diamagnetic semiconductors,
d^2	Zr	L oct	L oct	L oct	ρ>1 ohm cm,E_g~0.2-2.0 eV.
	Hf	L oct	L oct	(L oct)	Ti(1^{st} series metal,yields
					non-stoichiometric products.)
V	V	(L oct)	L oct	L dis. oct	Undistorted compounds are narrow
					band metals,ρ~10^{-4} ohm cm Pauli
d^3	Nb	L tr. pr	L tr. pr	L tr. pr	paramagnetic,band antiferromagnetic
	Ta	L tr. pr	L tr.pr	L dis. oct	Superconducting Free carrier
		dis oct	dis oct		absorbtion in I.R. Others diamagnetic
					semi-metals.Oct TaS_2/Se_2 perhaps
					semi-conducting.
VI	Cr	-	-	-	(i)The undistorted compounds
d^4	Mo	L tr. pr	L tr. pr	L tr. pr	are diamagnetic semiconductors,
				dis. oct	ρ>1 ohm cm.E_g^{opt}>1.5 eV,
					E_g^{th}~0.15 eV.
	W	L tr. pr	L tr. pr	L dis.oct	(ii)The distorted octahedral
					structures are semi-metals
					ρ~10^{-3} ohm cm. Diamagnetic,
					low Seebeck coefficients.
VII	Mn		Pyrites		(i) Mn compounds quasi-ionic
					antiferromagnetic semiconductors.
d^5	Tc	L dis. oct	L dis.oct	L dis.	(ii) TcS_2 possibly also a pyrite
					form.
	Re	L dis. oct	L dis. oct	L dis.	(iii) ReS_2 and $ReSe_2$ are small
					gap semiconductors, dia magnetic,
					and with no free carrier absorbtion.
VIIIa	Fe	Pyrite	Marcasite		'Non-magnetic' semiconductors.
d^6	Ru				
	Os		Pyrites		
VIIIb	Co	Pyrites	Pyrites	Marcasite	Pyrite,marcasite and layer types
			Marcasite	L oct	metallic. CoS_2ferromagnetic.
d^7	Rh	(Pyrite)	$IrSe_2$	Pyrite	β-$RhSe_2$ and $RhTe_2$ super-
			Pyrite	L oct	conductors.
	Ir	$IrSe_2$	$IrSe_2$	L oct	$IrSe_2$types semiconducting.
VIIIc	Ni		Pyrites	L oct	(i) Tellurides, metallic Pauli
					paramagnetic ρ~10^{-5} ohm cm.
					$PdTe_2$ superconducting.
d^8	Pd	Layer type showing X-X links		L oct	(ii)Pd & Pt/S_2 & Se_2 semiconducting
	Pt	L oct	L oct	L oct	E_g~ 0.4 eV,ρ~1 ohm cm Diamagnetic,
					large Seebeck coefficients.

Key: L Layered;tr. pr trigonal prismatic;oct octahedral;dis. distorted.

physical properties, including the extremes from electrical insulators to metallic conductors.

A useful approach to analysing this spread of behaviour is to employ a simple band model examining the filling of the 'd' band/s moving across the periodic table and recalling that the crystal field splitting, and resultant degeneracy of the 'd' bands, is dependent on the coordination number and symmetry around the metal atoms for each of the 3 basic structure types of the layered compounds. These are outlined below:-

1) The cadmium iodide structure. (space group P-3m1). Hexagonal packed layers of anions with cations at (0,0,0) and anions at $\pm$(1/3,2/3,u), u about 1/4. This gives a slightly distorted h.c.p. structure, with the metal atoms in a near octahedral coordination and the resulting layered structure of strong covalent intralayer bonding with much weaker (about 100X) interlayer forces.

2) The cadmium chloride structure (space group R-3m). A rhombohedral unit cell with cations at (0,0,0) and anions at $\pm$(u,u,u), again the metal atoms are octahedrally coordinated but the anions are cubically packed, and with the cation coordination polyhedra staggered in 2 possible alignments- leading to the

possibility of many stacking arrangements.

3) The molybdenum disulphide structure which occurs in two variants:-

a) 2 formula units per unit cell- (space group P63/mmc), with metal atoms at $\pm(1/3,2/3,1/4)$ and anions at $\pm(1/3,2/3,u)$ and $\pm(2/3,1/3,1/2+u)$

b) 1 formula unit per unit cell- (space group R3m), with metal atoms at (0,0,0) and anions at (0,0,u) and (0,0,1/2-u). An example of this structure is NbS_2. Both the MoS_2 types have trigonal prismatic coordination around the metal atoms.

For all three structure types the close packed anions and metal atoms form sandwich layers with van der Waals gaps between each sandwich of anion/cation/anion and with the metal atoms in either octahedral or trigonal prismatic coordination.

From table 3.1 it can be seen that the unlayered compounds feature only in groups VII to VIIIb with group VIIIc going back to layer type, this phenomenon is examined by Wilson and Yoffe (1969) and is attributed to the filling of the van der Waals gap by transition metal atoms- resulting in a non-layered nickel arsenide structure from the (layered) cadmium iodide structure. These 'extra' atoms, which destroy the 2-D anisotropy of

the crystals, can give rise to a range of compositions; eg. for titanium sulphide- from TiS_2 (NiS_2) to TiS (NiAs) with stable non-stoichiometric intermediate phases plus a Ti_2S_3 phase (Blitz et al., 1956; and Hahn and Harder, 1956).

Thus the crystals of groups IV,V and VI form layer compounds- with group IV metals in octahedral coordination, group VI preferring a trigonal prismatic arrangement and group V mixed (with some compounds showing both types of coordination) as detailed below. The group IV's are semiconducting with the 'd' bands above the Fermi level and octahedral coordination preferred to reduce the coulombic repulsion (Madelung term) between anions (which would sit above each other in the alternative trigonal prismatic system). The IV materials semiconducting gap values are up to about 2 eV (see Wilson and Yoffe, 1969) with the large anion/cation ratios of $TiSe_2$, $TiTe_2$ and $ZrTe_2$ showing small values. Some doubt about these values is attributed to the non-stoichiometry of the crystals, especially for Ti- the first member of the series in the periodic table. Theoretical band gaps have shown wide variation; eg. for TiS_2 two self consistent calculations give 0.2 eV (LCAO-Zunger and Freeman, 1977) and 1.5 eV (OPW- Krusius et al., 1975). The highest occupied band is always from the anion 'p' band , while the metal 'd' is the lowest

unoccupied band. The 'd' bands are split by the crystal field into e_g (d_{xz},d_{yz}) and t_{2g}(d_{z^2},d_{xy} and $d_{x^2-y^2}$). There is a large charge transfer to the much more electronegative chalcogen atoms (eg. Δe_{neg} Ti-S = 1.38).

For the group VI materials, with two electrons remaining after a simple octet filling of the chalcogens, a semiconducting gap is induced by a trigonal prismatic coordination (crystal field) which splits the 5 metal 'd' derived bands into 1,2 and 2 with the lowest and non-degenerate band normally labelled d_{z^2} (when z is perpendicular to the layers), which is filled in this case. For the group V crystals this simple band model is confounded since the remaining 'd' electron would be expected to result in a metallic material with a half filled 'd' band, but this is not always found to be the case due to the spin-orbit coupling found in some materials (Jellinek et al., 1971) and the possibility of a Peierls distortion- which introduces a semiconducting gap from the unit cell doubling.

3.3 Polymorphism

N.B. Here the usual convention is followed - ie. polytypism is defined as a type of polymorphism, then the distinction is disregarded. Polymorphism, the

occurence of different crystal structures for the same chemical compound, is common in the MX_2 materials- especially in the group V (Nb and Ta) materials.

Inspection of these crystal structures, with their weak bonding across the van der Waals gap, leads to the expectation of polytypism which does in fact occur, but with a surprising rarity when compared with, for example, isostructural CdI_2 in which up to 120 layers can form a repeat unit. Polytypism is a special form of polymorphism in which only one lattice parameter is affected- it may occur by shifting successive layers in these compounds, thus stacking them in different ways leading to an integral multiple of the lattice parameter perpendicular to the layers (Verma and Krishna, 1966). Polytypes are further defined since they show short-range order (ie. first and second nearest neighbours) with differences found only for longer ranges. This leads to the formations of polytypes under identical growth conditions or even regions of the same crystal showing different polytypes, termed "syntactic coalescence".

In contrast to polytypes, polymorphs exhibit temperature and pressure transition regions since the Gibbs free energy is minimised (Balachin, 1976). However the distinction between these two forms is blurred by the

fact that higher order polytypes can be reduced at high temperatures.

The contortions performed by the group V compounds together with the resulting CDW states are the subject of much experimental and theoretical interest (eg. Smith et al., 1985; Zunger and Freeman, 1979; Eaglesham et al., 1986). As pointed out by Wilson et al. (1974) the CDW-PLD state found in these compounds is possible due to the 2D Fermi surface of these layered compounds.

3.4 Phase transitions

As may be expected these layered compounds show sensitivity to temperature and pressure changes reflected in electrical, mechanical, optical and magnetic properties- phase transitions may also be induced. For instance Nb, Ta, Mo, and W diselenides and disulphides exhibit polymorphism with a temperature driven transition (Grams 1961, Bongers et al. 1968, Engelsman et al., 1972). The room temperature phase is with the metal atoms in a trigonal prismatic coordination (2H) which on heating (about 850°C) become near octahedral with mixed intermediate structures. For the group V crystals, TaS_2 and $TaSe_2$, the lower

temperature phase is metallic (from the half-filled d_{z^2} orbital derived band) while the higher temperature phase can be quenched to give a (very!) narrow gap semiconductor at low temperatures. The semiconducting gap of the 1S phase (Jellinek, 1972) is induced by spin-orbit coupling of the lower bands (t_{2g}) from the octahedral crystal field, with a value of about 0.02 eV (Thompson et al., 1971) Interestingly isostructural VSe_2, with much reduced S-O coupling, is still metallic in this phase after quenching.

The effect of pressure on these materials is most noticeable in the increase of crystal dimensionality as the width of the van der Waals gap is reduced. The mapping of exciton peaks of the members of the dichalcogenides (S,Se) from groups IV,V and VI (Grant et al., 1972) has shown the trends for energy shifts against small pressure changes. The group IV compounds contrast with the group VI in that the semiconducting gap closes as the 'p' bands broaden, in the group VI the gap is due to the splitting off of the lowest 'd' band and it would appear that the 'd' bands are broadened at increased pressures thus increasing the semiconducting gap for these materials. In can be seen that the 'p' bands broaden less quickly than the 'd' bands, as a function of pressure.

At higher pressure quite dramatic differences can be found. For example, NbI_4 and TaI_4 lose their 1-D character as the inter-chain distance is reduced; this broadens the 'p' derived bands thus pushing up the metal's occupied 'd' bands. This results in a transformation from a semiconducting to metallic state.

3.5 Intercalation

In these remarkable solid state systems the van der Waals gap is invaded by electron donating (Lewis bases) atoms or molecules, which form stable compounds of the type A_xMX_2 (x between 0 and 1); the most widely studied systems being with A=Li,Na,K,Cs or an organic molecule such as pyridine (C_5H_5N). Another case is with the intercalate being a transition or post-transition metal. This intercalation is accompanied by an increase in the 'c' lattice parameter (perpendicular to the layers) and, to a much lesser extent the 'a' parameter. In an extreme case (Rimmington, 1973) crystals shattered after taking up pyridine, with a maximum increase in the 'c' parameter for the group IV dichalcogenides of between 3 and 9%. Even larger lattice expansion can be found for these systems, for example NbS_2 with 'c' > 30A (DiSalvo et al., 1971, and Gamble et al., 1971) and a massive increase of about 57A was found for TaS_2 intercalated with stearamide (Gamble et al., 1971). Some typical

lattice expansions are given in table 3.2, taken from Rimmington, 1973).

The intercalation process has been found to be highly reversible- leading to the proposal of using intercalated transition metal dichalcogenides as high energy density, ambient temperature batteries (Whittingham, 1976 and refs. therein). TiS_2 with Li, for example, was found to be still perfectly reversible after more than 1100 (shallow) charge/discharge cycles.

The reversibility of this process indicates that no strong chemical bonds are being made or broken during the cycles- suggesting a strongly ionic component of the intercalate structure. This idea was proposed by Wilson and Yoffe (1969) in their rigid band model- where the intercalate simply donates an electron to the system and has little effect on the band structure other than raising the Fermi level into the lower 'd' band/s. Indeed this model seems to have stood the test of time being only slightly dented by later studies such as McCanny 1979, who used a parameterised LCAO method to calculate the electronic structure for TiS_2/Li intercalated system. Even Li_xTiS_2 with x=1 small differences were found from the TiS_2 alone.

It is interesting to note the effects of intercalation

Table 3.2

Maximum lattice expansion for pyridine intercalated layered MX_2s (after Rimmington, 1973).

Compound	Normal length of c axis (A)	c-axis after maximum intercalation (A)	Maximum lattice expansion (%)
CdI_2	5.8744	7.2038	23
SnS_2	5.8853	6.5915	12
SnS Se	6.0483	6.5225	8
$SnSe_2$	6.1255	6.8536	12
TiS_2	5.6883	6.1404	8
$TiSe_2$	6.0036	6.5376	9
$TiTe_2$	6.5935	6.9296	5
ZrS_2	5.8193	6.1175	5
$ZrSe_2$	6.1324	6.6186	8
HfS_2	5.8456	6.0086	3
$HfSe_2$	6.1487	6.4507	5

even though they are not large. The crystal structure used is the original 1T with Li atoms in the octahedral interstices between layers. Examination of the relevant eigenvectors confirms the electronic charge transfer from the Li atom which enters the lowest 'd' band. The Li 2s orbital and Ti s orbitals which are of the same symmetry and comparable energies mix and result in a bond-antibond pair which pushes down the Ti 's' band into the metal 'd' bands. A similar effect, of greatly reduced magnitude, increases the binding energy of the chalcogen 'p' band. The calculated band structures of McCanny (1979) show the upper valence band (chalcogen 'p' type) as having a reduced dispersion and a narrow band width- attributable to the increased lattice parameter which reduces interlayer interaction- rather than the direct influence of the Li itself. Thus it appears that even in the extreme case (where x=1) the rigid band model is a reasonable approximation (especially around the Fermi level)- this is futher confirmed by experimental data (Acrivos et al. 1971, Beal et al. 1976, Friend et al. 1977).

Further interest was generated in these systems with the discovery of superconducting intercalated compounds- for example the variation of the superconducting transition temperature against intercalate for MoS_2 is tabulated by Somano et al. (1973). All these intercalates were found

to be superconducting- fuelling the electron donor picture outlined above- showing an increased electron density at the Fermi level. Gamble et al. (1970), from their electrical resistivity measurements on group V dichalcogenides (S and Se) intercalated with pyridine conclude that the superconductivity is 2-D and parallel to the layers.

3.6 Structure Models.

In addition to, but not always in competition with, the minimization of the electronic energy (predicted by the rigid band model) entropy and the lattice configurational energy (eg. coulombmic effects) must be considered in any explanation of the crystal structures of the various MX_2 compounds (see Wilson and Yoffe, 1969). This follows from the compounds which do not follow the simple crystal field induced band splitting rule or, as in the case of the group V compounds, no structure preference can be easily deduced and the crystals appear in either or both forms. A good example of 'anomalous' behaviour is WTe_2 (distorted octahedral) where the large Te ions do not sit above each other in the trigonal prismatic coordination as expected. But $MoTe_2$, from the same periodic group and with a similar metal ion radius (W has a lanthanide contraction) exists

both as the 2H- trigonal prismatic form and also a high temperature distorted octahedral structure (which is meta-stable when quenched to room temperature). TaS_2 and $TaSe_2$ also exist in both forms, and the high temperature 1T structures are stable at room temperature. The tellurides in particular show the importance of atomic/ionic radii. Ionicity also is likely to play an important role since the coulombic repulsion between anions is reduced for the octahedral case.

Various authors have explored the effects of ionicity and ionic radii in the MX_2 crystal structures. Two of these are summarised below.

1. White and Lucovsky (1972), Lucovsky et al. (1973).

This model is used to complement I.R. reflectance data for the octahedral group IV and trigonal prismatic group VI MX_2's. A simple band model is invoked here to account for the apparent d^4sp hybridization of the metal ions in the group VI (trigonal prismatic) materials but the ionic radius ratio is considered an important factor which is used to account for the metallic behaviour of the group IV tellurides and Ti dichalcogenides (the Ti ion is very small)- metallic behaviour is considered possible when the radius ratio approaches 0.33. Their ionic radii are taken from Azaroff and Brophy (1963),

and the coordination of the metal ions from the structures given in Wyckoff (1963). Some confusion seems to have arisen here since the authors find, for the group IV compounds, ($Zr,Hf;S_2,Se_2$), effective charges on the metals of about 4^{+}- which they then appear to consider almost completely ionised, but these are effective charges only. Very ionic materials cannot form the directional bonds neccesary for the layer structures found here. Also introduced are chalcogen-chalcogen bonds of a 'd' character- possibly between layers. Whilst the idea of chalcogen 'd' bonds is supported (at least at the reciprocal zone centre) by the band calculations of Murray et al. (1972), the proposed interlayer bonds seem a little unreal.

This model excludes the rigid band model by emphasising the very different nature of the chemical bonding in the group IV and group VI compounds, since the effective metal charges calculated from I.R. data show the group IV materials to be much more ionic.

For the interesting group V materials the authors do not apply the radii ratio test but revert to the isolated atomic valence orbitals relative energies to explain the metallic conduction found here. Since these compounds would only half-fill the d_{z^2} based band split off by trigonal prismatic coordination, it is important to

incorporate them into any structure model.

It would appear that, unless the anomalies suggested by this model are accepted, the ionic radius ratios alone are insufficient to explain the preferred crystal structures for the layered MX_2 compounds.

2. Gamble F.R. (1974).

In this model the atoms are considered partially ionised and a coordination correction to the ionic radius is used as before, but now the next improvement to the approximate ionic radius is considered- ie. the covalency of the chemical bond expressed as the fractional ionic character (f.i.c.). This allows the rigid sphere model to be slightly relaxed when the atoms can distort a little as a function of the structural force. Undeterred by Megaw (1973), who said of ionic radii- "It is dangerous to assume that meaningful calculations can be done with very high precision", this model searches for, and finds, a definition of ionic radii which separates the MX_2's into trigonal prismatic and octahedral coordination. The two coordination regions are shown for the 24 MX_2's considered in fig. 3.2 which is a plot of radius ratios (metal in 4^+ state from Shannon and Prewitt (1969), corrected for 6-fold coordination; and anion radii (2^- from Pauling , 1960)

Fig. 3.2 (after Gamble, 1973)

Radius ratios versus fractional ionic character.

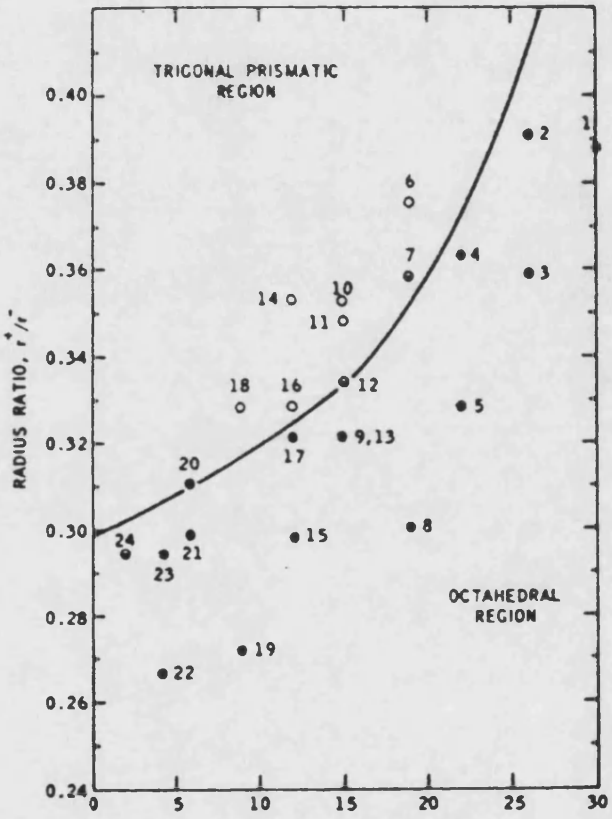

1. HfS_2
2. ZrS_2
3. $HfSe_2$
4. TiS_2
5. $ZrSe_2$
6. 2H-NbS_2
7. 2H-TaS_2
   1T-TaS_2
8. $TiSe_2$
9. VS_2
10. 2H-WS_2
11. 2H-$NbSe_2$
12. 2H-$TaSe_2$
    1T-$TaSe_2$
13. $HfTe_2$
14. 2H-MoS_2
15. VSe_2
16. 2H-WSe_2
17. $ZrTe_2$
18. 2H-$MoSe_2$
19. $TiTe_2$
20. $NbTe_2$
21. $TaTe_2$
22. VTe_2
23. WTe_2
24. 2H-$MoTe_2$

Filled circles- octahedral coordination

Empty circles- trigonal prismatic coordination

Half filled circle show both types of coordination.

versus f.i.c. (Pauling, 1960). The ionic radii used here are shown in table 3.3.
2H-$MoTe_2$ appears anomalous here, but it is interesting that $MoTe_2$ has a high temperature phase with distorted octahedral coordination. The effective charges found by Lucovsky et al. (1973) are matched here in an interesting fashion- by taking the anion radius as half the 'a' lattice parameter and, using this to calculate the metal radius (employing a touching rigid sphere model), and comparing the metal radius with those given by Shannon and Prewitt (1969) extrapolating the effective charges.
This method gives very good agreement with the I.R. deduced charges.

This model has two main points of disagreement with the previous model:-

1) the charge distribution is primarily dependent on differences in electronegativity <u>not</u> structure

2) the reduced chalcogen-chalcogen bond lengths found in the group IV compounds are due to strong covalent chalcogen-metal bonds rather than artificial chalcogen-chalcogen bonds.

However two important aspects are overlooked by this model:-

a) Polarisation effects

Table 3.3 Ionic radii (after Gamble, 1973)

Atom	X*	Shannon and Prewitt radii +6	+5	+4	+3	+2	Pauling radii -2	Slater radii	Effective metal radii R_s	R_{se}	R_{Te}
Hf	1.3			0.71				1.55	0.74	0.79	0.85
Zr	1.4			0.72				1.55	0.73	0.78	0.85
Ti	1.5			0.61	0.67	0.86		1.40	0.72	0.77	0.83
Ta	1.6		0.64	0.66	0.67			1.45	(2H)0.82	0.87	-
									(1T)0.76	0.81	-
V	1.7		0.54	0.59	0.64	0.79		1.35	0.73	0.79	0.87
Nb	1.6		0.64	0.69	0.70	0.71		1.45	0.82	0.87	-
W	1.7	0.60		0.65				1.35	0.83	0.87	-
Mo	1.8	0.60	0.63	0.65	0.67			1.45	0.84	0.85	0.97
Te	2.1						2.21	1.40			
Se	2.4						1.98	1.15			
S	2.5						1.84	1.00			

X* Pauling electronegativity. Radii in angstroms.

b) the metal-metal bonding found in distorted octahedrally coordinated WTe_2.

The following chapter is an examination of the group VI ditellurides which fall outside the scope of these simple structure models.

Chapter 4. The electronic structure of $MoTe_2$ and WTe_2

4.1. Introduction.

The layered transition metal dichalcogenides (LTMD) have proved a fruitful area of study for solid state physicists for about 20 years- especially following the seminal review by Wilson and Yoffe, 1969. A simple band model has been usefully employed to account for the trigonal prismatic coordination around the metal atoms of the group VI dichalcogenides- stabilized by the filled d_{z^2} orbital split off by this crystal field. The ditellurides of Mo and W differ from their diselenides and disulphides in that they can crystallise with a distorted octahedral coordination around the metal atoms- which are displaced from the centre of the octahedra and form chains running through the crystal. The layer structure is preserved in this form although the layers are now buckled- giving possibilities of different keying positions of adjacent layers.

Due to the lanthanide contraction second and third row transition metals in a given column (eg. Mo and W respectively) have remarkably similar properties and, indeed, chemists can often to a good approximation treat them as identical. Therefore it might be expected that

the ditellurides of Mo and W would crystallise in a similar structure. In fact $MoTe_2$, but not WTe_2, has been grown with a trigonal prismatic coordination around the metal (in the 2H polytype). In contrast with the semiconducting trigonal prismatically coordinated group VIb dichalcogenides, including 2H-$MoTe_2$, the compounds with distorted octahedral coordination are semimetallic. We investigate here the differences between (a) the group VIb ditellurides and disulphide/diselenides and (b) the Mo and W ditellurides as reflected in their electronic structures.

Electronic structure calculations have been carried out for the following materials:-

1. Trigonal prismatic coordination

   2H-WSe_2

   2H-$MoTe_2$

   2H-WTe_2 (ideal)

2. Octahedral coordination

   1T-WTe_2 (ideal)

3. Distorted octahedral coordination

   B-$MoTe_2$

   Td-WTe_2

   Td-$MoTe_2$

Although a range of techniques have been employed for both theoretical (eg. Matthiess, 1973 (APW); Bullett, 1978 (LCAO); Zunger and Freeman, 1979 (S-C LCAO); Hind and Lee, 1980 (KKR)) and experimental (eg. Beal and Hughes, 1979; McGovern et al., 1979; Ohno et al., 1983) band structures for the LTMD, little work has been done to date on the metallic group VI ditellurides. Thus, to assist analysis, WSe_2 and the idealized structures 2H-WTe_2 and 1T-$WTe_2$are also included in these calculations. B-$MoTe_2$ (a high temperature polymorph of 2H-$MoTe_2$) is believed to show the metastable state Td-$MoTe_2$ which closely matches the distorted octahedral structure of as-grown Td-WTe_2.

4.2 Method.

The results shown were calculated by the ab initio LCAO method (Bullett, 1980) of chapter two which gave good results for other LTMD from groups IV,V and VIb with 2H and 1T structures. The use of a limited basis set of atomic orbitals is justified by the pseudopotential form of the Schroedinger equation:-

$$H|\phi_i\rangle - |\phi_j\rangle\, S^{-1}_{jk} \langle \phi_k | V | \phi_i \rangle = \varepsilon_i |\phi_i\rangle$$

within a two-centre approximaton (Anderson, 1969; Bullett, 1980). The Hamiltonian H is centred on atom A

then perturbed by atom B (V'), with a similar equation for B perturbed by A. The atomic orbitals (ϕ_i) are constructed using the Herman-Skillman atomic orbital program, with $\alpha=0.7$ in the $X\alpha$ approximation for the exchange/correlation term. The portability of these atomic orbitals in a pseudopotential formalism allows the use of an interpolation scheme for the matrix elements- calculated to map interactions between all relevant atomic species. Interactions are considered for inter-atomic distances of up to 8 au. The matrix elements are calculated using the Slater-Koster (1954) quantisation procedure. For the transition metals 9 atomic orbitals (s, p and d valence) per atom per unit cell contribute to the matrix to be diagonalised, with 4 (s and p) for each chalcogen. A degree of self-consistency is achieved by converging the input and output d orbital occupancy (and thus energy)- the energies of the s and p orbitals being relatively insensitive to occupancy. The d-electrons are relatively tightly bound to individual metal atoms and their energy is highly dependent on the d-orbital occupation, whereas the outer s and p orbitals are much looser and the assignment of this part of the electron cloud to individual metal atoms in each crystal structure would be less significant.

4.3 Crystal structures.

a) 2H trigonal prismatic.

Here there are 2 formula units per unit cell (z=2) in the MoS_2 structure ($P6_3/mmc$, no. 194) as shown in table 4.1a with calculated bond lengths given in table 4.1b. The 2H structure is shown in perspective in fig. 4.1. The structure refinement parameters for 2H-WTe_2 are calculated from the as-grown Td-WTe_2 structure (Brown, 1966)- assuming preservation of the average bond lengths, as found for the 1T and 2H polymorphs of $TaSe_2$ with Ta-Se distances of 2.58 and 2.59 A respectively (Brown and Beerntsen, 1965).
The structure of WSe_2 is defined using the lattice parameter given by Brixner, 1962 and the structure refinement parameters for $MoSe_2$ from James and Lavik, 1963. $MoTe_2$ structure is from Puotinen and Newham, 1961 and Knop and MacDonald, 1961. Since the calculation of these results the structure refinement and lattice parameters of WSe_2 have been published by Schutte et al. (1987). Since WSe_2 is given here for comparison only and the new parameters (a=3.282A, c=12.96A) are so close to the ones used in this work (therefore the electronic structure would only be minimally effected) the structure was not recalculated.

Table 4.1

a) 2H lattice parameters (WSe_2, $MoTe_2$ and WTe_2)

Space group $P6_3/mmc$ Hexagonal.

WSe_2 a=3.286A c=12.98A
WTe_2 a=3.600A c=14.18A
$MoTe_2$ a=3.519A c=13.97A

Atom positions (z=0.621)

M	2(c)	$\pm$(0.333,0.667,0.25)
X	4(f)	$\pm$(0.333,0.667,z) $\pm$(0.333,0.667,z+0.5)

b) 2H bond lengths (WSe_2, $MoTe_2$ and WTe_2)

	Bond lengths (A)		
	WSe_2	$MoTe_2$	WTe_2
Metal-metal	3.29	3.52	3.60
Metal-Te	2.49	2.71	2.77
Across layer Te-Te	3.24	3.60	3.66
Between layers Te-Te	3.76	3.95	4.01

Figure 4.1 Trigonal prismatic (2H) structure.

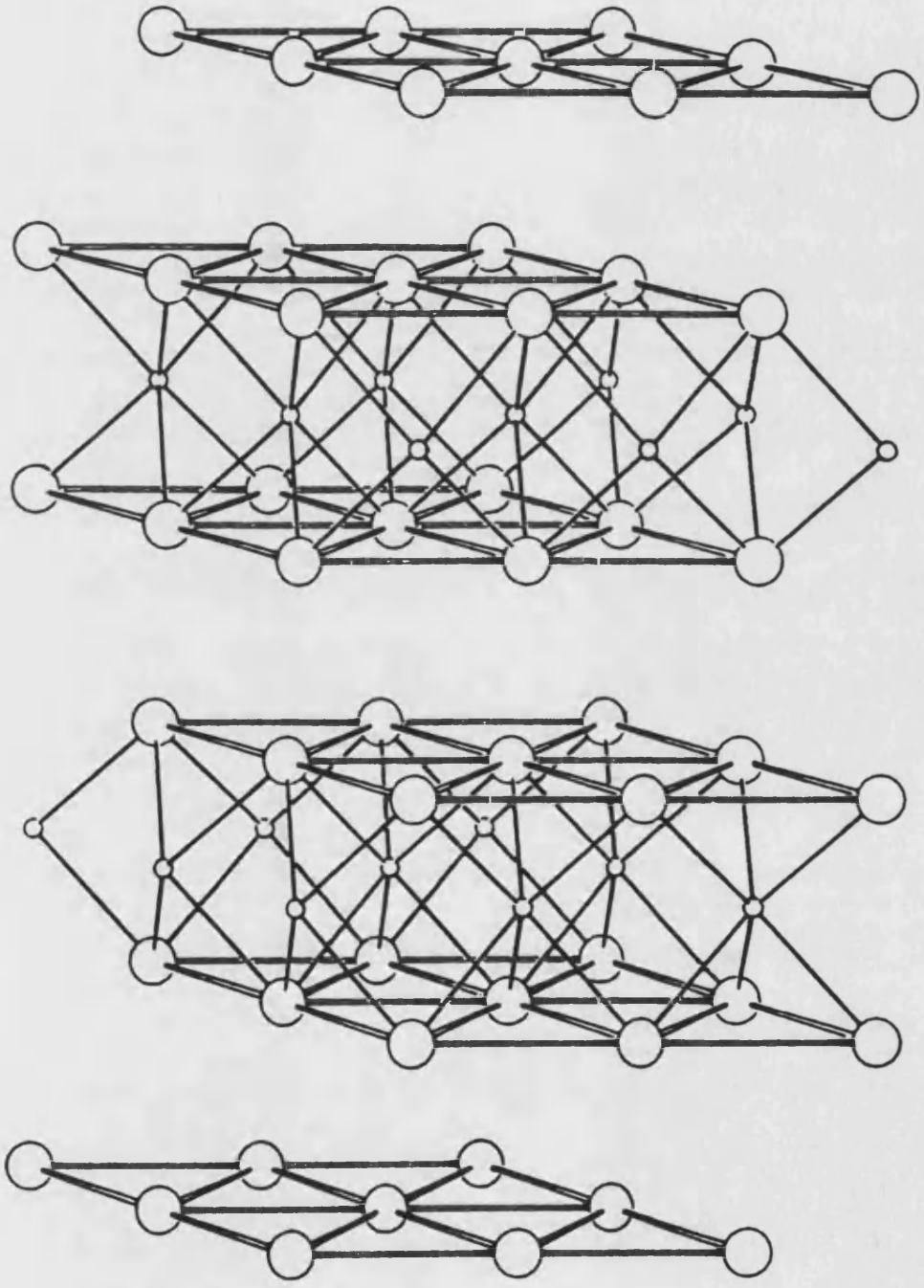

Small circles- metal
Large circles- chalcogen

The 2H structure can be described as sandwiches of 3 planes of 2D hexagonally packed atoms, chalcogen-metal-chalcogen, with strong covalent intralayer bonds and with the sandwiches separated by a van der Waals gap as shown in fig. 4.1. The metal atoms are trigonal prismatically coordinated by 6 chalcogen atoms, with the prism slightly elongated perpendicular to the layers. Metal atoms in successive layers are displaced such that the resulting structure forms the 2H polytype. The Madelung term for this structure is larger than, for example, the 1T octahedral coordination found in the Group IVa LTMDs since the non-metal atoms sit directly above each other in the trigonal prism. It has been shown that octahedral coordination can reduce the Madelung term by about 20%, assuming no change in charge transfer between the two structures (Shen and Liang, 1983).

b) Octahedral

Calculations were made for WTe_2 in an undistorted octahedral coordination (1T-WTe_2), with one layer per unit cell. The bond lengths are calculated using the average bond lengths of Td-WTe_2, giving a hexagonal unit cell (P -3m1) with a=3.60A and c=7.035A; W-Te distance is 2.77A with Te-Te distances of 4.21 across layers and 3.96 between layers. The calculated lattice

parameters and bond lengths used are given in tables 4.2a and 4.2b respectively.

c) Distorted octahedral.

The lattice parameters and structure refinement parameters for these compounds are given in table 4.3. Figures 4.2a, b and c show the two forms of distorted octahedral coordination and the metal environment respectively.

1) B-$MoTe_2$

At temperatures above about 900^{0}C a monoclinic ($P2_1/m$) polymorph of $MoTe_2$ is found to exist (Brown, 1966). The layer structure is preserved but the coordination around the metal atom is of a slightly distorted octahedron of tellurium atoms, with the metal atoms displaced from the central postition and making chains which run through the crystal in the crystallographic 'y' direction. This increases the coordination number for the metal from 6 to 8. The tellurium atom octahedra undulate along the 'x' direction as shown in fig 4.2a. The stacking of layers sitting in the potential of the buckled Te octahedra results in monoclinic symmetry, with four formula units per unit cell. The crystallographic data shown in table 4.3 for B-$MoTe_2$ is taken from Brown 1966, who found the crystals stoichiometric to a high degree

Table 4.2

a) 1T lattice parameters WTe_2

Space group P-3m1 Hexagonal.
WTe_2 a=3.600A c=7.035A

Atom positions

M	(0.0 ,0.0 ,0.0)
X	$\pm$(0.333,0.667,0.26)

b) 1T bond lengths WTe_2

	Bond lengths (A)
Metal-metal	3.60
Metal-Te	2.77
Across layer	
Te-Te	4.21
Between layers	
Te-Te	3.96

Figure 4.2 Distorted octahedral structure.

a) B type- viewed down b axis.

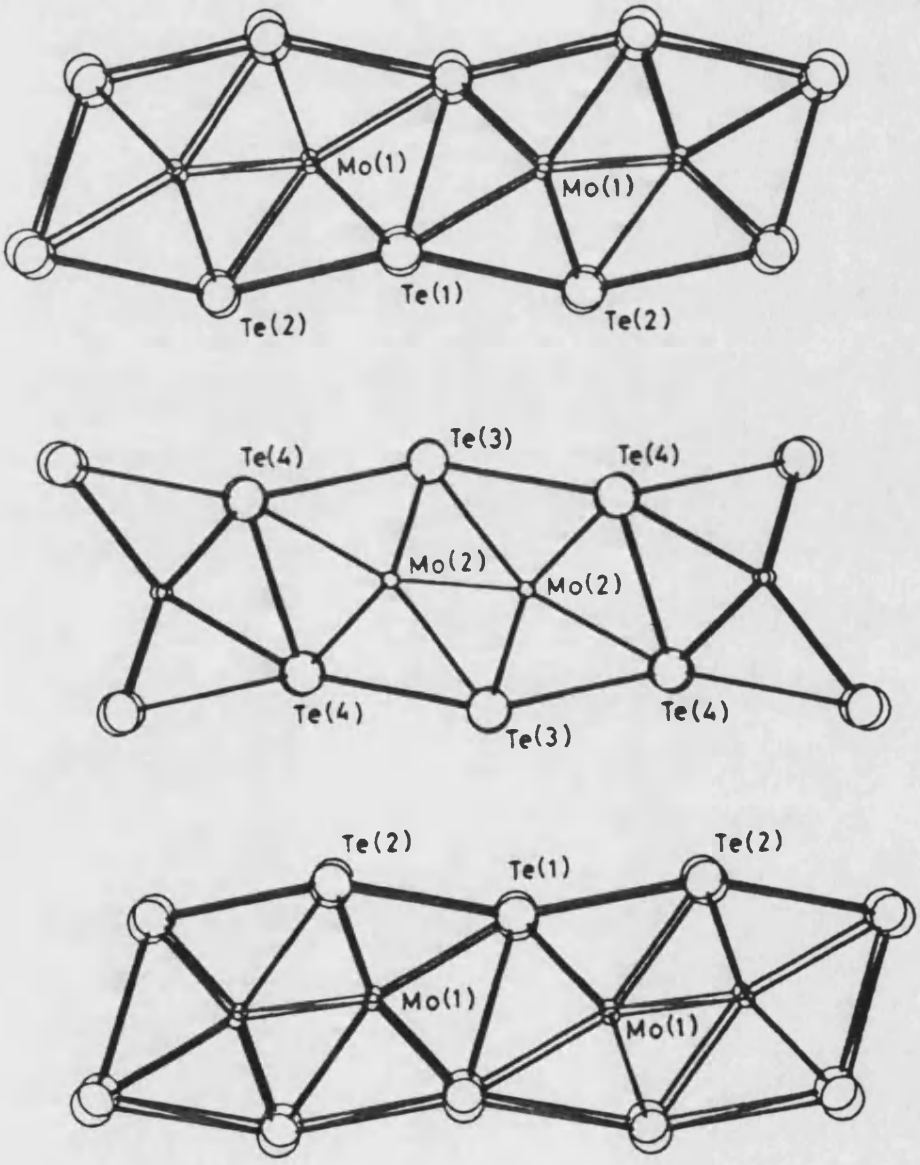

Figure 4.2 Distorted octahedral structure.

b) Td type- viewed down b axis.

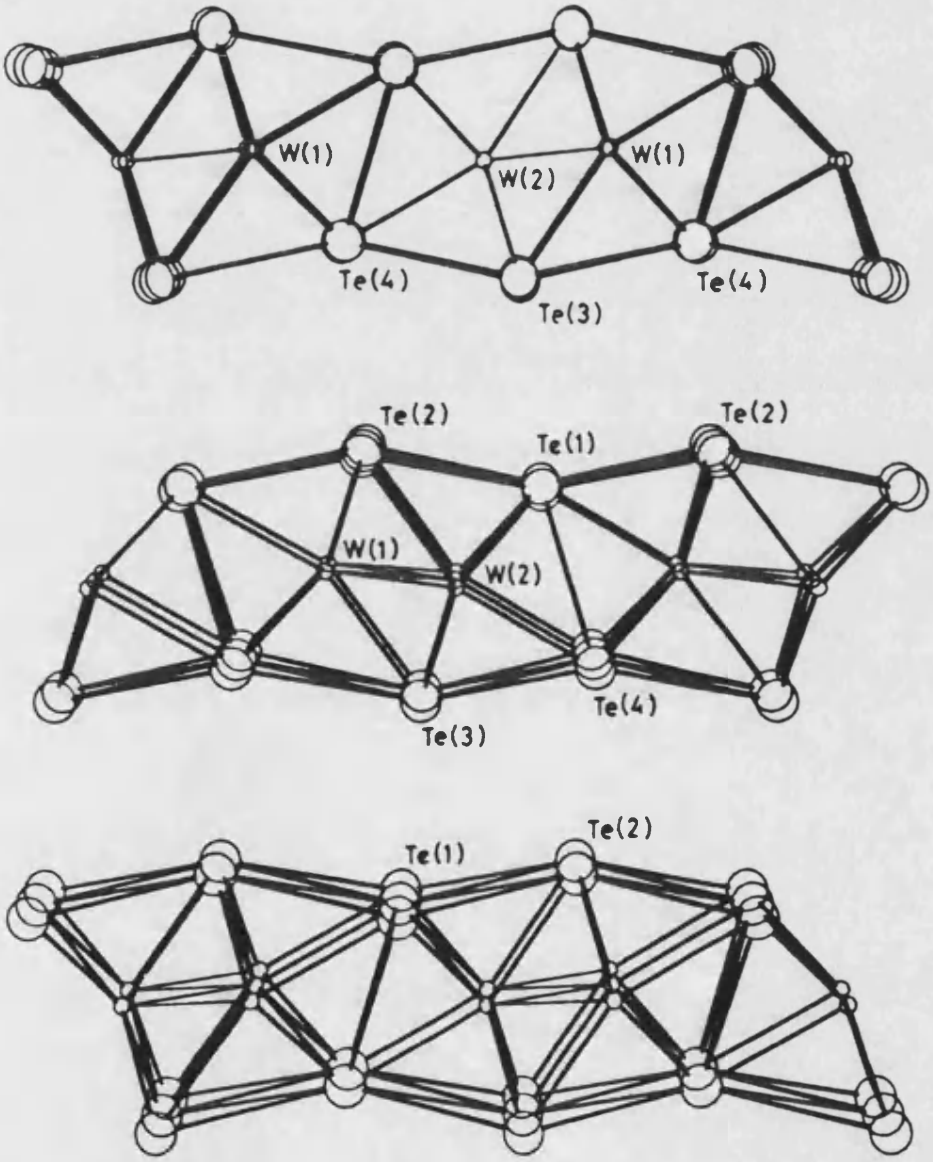

Figure 4.2 Distorted octahedral structure.

c) W enviroment in Td-WTe_2.

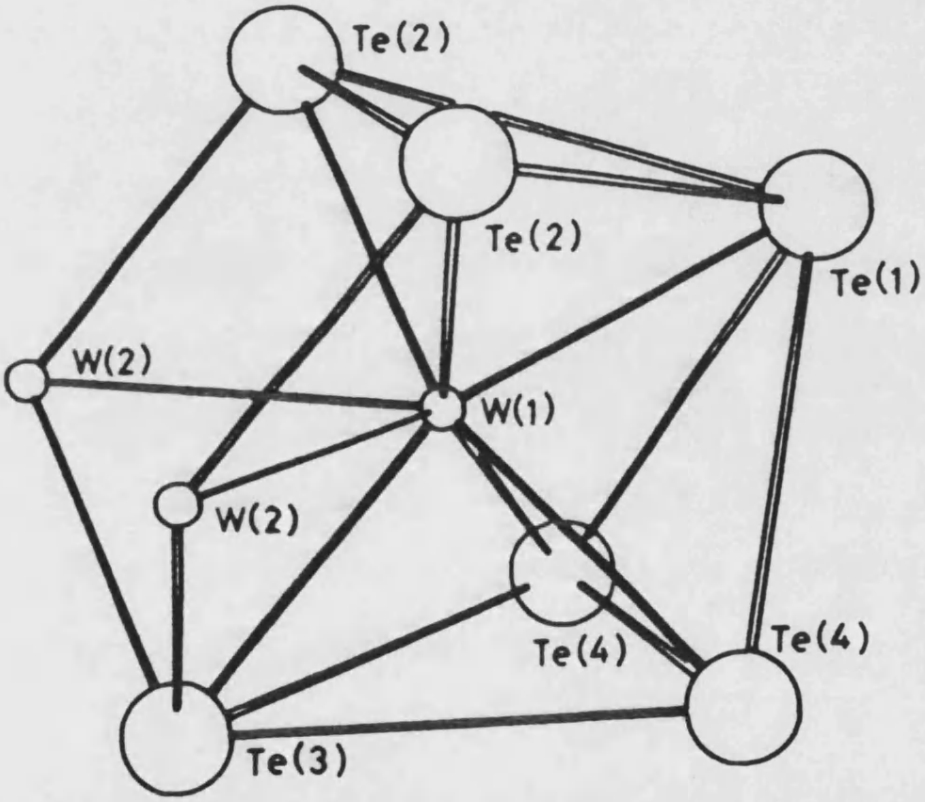

Table 4.3

a) B-$MoTe_2$ lattice parameters.

Space group P $2_1/m$ Monoclinic.

B-$MoTe_2$ a=6.330A b=3.469A c=13.86A B=93° 55'

Atom positions

Mo	2(e)	±(0.183,0.25,0.007)
Mo	2(e)	±(0.318,0.75,0.507)
Te	2(e)	±(0.589,0.25,0.104)
Te	2(e)	±(0.097,0.75,0.149)
Te	2(e)	±(0.557,0.75,0.352)
Te	2(e)	±(0.056,0.25,0.396)

b) Td lattice parameters (Td-$MoTe_2$ and Td-WTe2)

Space group P $nm2_1$ Orthorhombic

Td-$MoTe_2$ a=6.33 A b=3.469 c=13.83A

Td-WTe_2 a=6.282A b=3.496 c=14.07A

Atom positions

((x,0,z),(-x,0.5,0.5+z))

M	2(a)	(0.900,0.500,0.000)
M	2(a)	(0.541,0.000,0.985)
Te	2(a)	(0.294,0.500,0.097)
Te	2(a)	(0.800,0.000,0.140)
Te	2(a)	(0.356,0.000,0.345)
Te	2(a)	(0.852,0.500,0.389)

($Mo_{0.985}Te_2$).

2) WTe_2

Brown, 1966, also reports the structure of WTe_2 and finds this to be almost isostructural with B-$MoTe_2$. However the layer stacking here results in a unit cell again with four formula units but with orthorhombic symmetry (space group $Pnm2_1$). The environment of the metal atoms is little altered compared with B-$MoTe_2$. The short metal-metal distances of 2.86A for WTe_2 is only 0.13A more than the pure metal crystals. For $MoTe_2$ the difference is slightly greater- the elemental Mo-Mo length is 0.19A shorter than the Mo-Mo length in $MoTe_2$.

3) Td-$MoTe_2$

When cooling B-$MoTe_2$ Clarke et al., 1978 report an interesting phase transition in which the layers appear to shift quasi-continuously tending to an orthorhombic crystal, closely resembling Td-WTe_2. This is confirmed by the work on $MoTe_2$ phase transitions by Manolikas et al., 1979. The possibility of this transition was suggested by anomalies in resistivity measurements at around 247K by Hughes and Friend (1978). An unusual mechanism is believed to enable this structural alteration- the c lattice parameter (perpendicular to layers) increases with decreasing temperature as one layer lifts over the potential barrier of the rippled

'surface' of the other and then it decreases as the layers lock in to the new stacking formation. The a and b lattice parameters show the normal decrease with falling temperature. This mechanism appears to cause considerable lattice strain with domain walls showing a variation from the monoclinic angle of 93° down to the orthorhomic 90°- indicative of the large potential barrier crossed in this process. It is satisfying to find that the W and Mo ditellurides can share a common crystal structure considering the similarity of the two metal atoms. Orthorhomic $MoTe_2$ is here termed Td-$MoTe_2$.

The unit cell for Td-$MoTe_2$ is calculated from the structure refinement parameters for Td-WTe_2 with lattice parameters based on B-$MoTe_2$ - converting the unit cell from monoclinic to orthorhombic symmetry. The resulting bond lengths for Td-WTe_2,Td-$MoTe_2$ and B-$MoTe_2$ are given in table 4.4.

The occurence of metal-metal bonds is well known in the transition metal oxides when the metal atoms retain excess valence electrons. Mixed systems of the type $Ti_{1-x}V_xO_2$ and $V_{1-x}Mo_xO_2$ have been used to study the effect of these 'spare' electrons on metal-metal bond formation by moving along the periodic table (Marinder et al., 1957 and Marinder et al., 1962). The high Mo content of octahedrally coordinated Mo_2S_3 also shows

Table 4.4

Bond lengths for $MoTe_2$ and WTe_2 in distorted octahedral coordination

	Bond lengths (A)			
	Td-$MoTe_2$	Td-WTe_2		B-$MoTe_2$
Metal-metal				
M(1)-M(2)	2.87	2.86	M(1)-M(1)	2.89
			M(2)-M(2)	2.90
M-X octahedron 1				
M(1)-Te(1)	2.83	2.82	M(1)-Te(1)	2.82
M(1)-Te(2)(2)	2.68	2.71	M(1)-Te(2)	2.70
M(1)-Te(3)	2.69	2.71	M(1)-Te(1)(2)	2.79
M(1)-Te(4)(2)	2.80	2.81	M(1)-Te(2)(2)	2.70
M-X octahedron 2				
M(2)-Te(1)(2)	2.80	2.81	M(2)-Te(4)	2.81
M(2)-Te(2)	2.70	2.72	M(2)-Te(3)(2)	2.70
M(2)-Te(3)(2)	2.68	2.71	M(2)-Te(3)	2.71
M(2)-Te(4)	2.82	2.81	M(2)-Te(4)(2)	2.79
X-X parallel to layers				
Te(1)-Te(2)	3.69	3.68	Te(1)-Te(2)	3.70
Te(1)-Te(2)	3.62	3.61	Te(1)-Te(2)	3.62
Te(3)-Te(4)	3.64	3.63	Te(3)-Te(4)	3.65
Te(3)-Te(4)	3.68	3.67	Te(3)-Te(4)	3.67
Te-Te (b-axis)	3.47	3.50		3.47
X-X between layers				
Te(1)-Te(3)	3.86	3.93	Te(2)-Te(3)	3.91
Te(2)-Te(4)	3.87	3.93	Te(2)-Te(4)	3.86
X-X across layers				
Te(1)-Te(4)	3.48	3.52	Te(4)-Te(4)	3.49

metal chains running through the crystal with the Mo atoms displaced from the octahedral centre (Jellinek, 1961).

4.4 Calculations.

The general features of the results of these calculations are shown in table 4.5. The Brillouin zones used with labelled high symmetry points are shown in figs. 4.3 a, b and c. The converged metal d orbital occupations are given in table 4.6.

a) Trigonal prismatic coordination.

The band structure E vs. k graphs in eV, are along the high symmetry lines covering all edges of this zone, calculated using 45 points between each pair of symmetry points. The densities of states (dos) and projected dos are calculated using a regular net of 256 k points through the irreducible Brillouin zone shown in fig 4.3a. The dos are smoothed by a gaussian (FWHM=0.1 eV) and cut off at -1.0 eV. The 2H structure band structures and densities of states are shown in figs. 4.4 to 4.9. The converged metal d energies are given in table 4.6, these correspond to Mulliken populations of 4.95, 5.23 and 5.22 electrons for WSe_2, WTe_2 and $MoTe_2$ respectively for the d orbitals (see table 4.5). The similarity of WTe_2 and $MoTe_2$ is already apparent here.

Table 4.5

Collected results of calculations (Data in eV).

	WSe_2 2H	WTe_2 2H	WTe_2 1T	WTe_2 Td	$MoTe_2$ 2H	$MoTe_2$ B	$MoTe_2$ Td
E_g	1.1	0.7	-	-	0.7	-0.3**	-
Band widths							
Lower valence	3.4	3.0	3.8	4.0	3.4	3.5	3.5
Upper valence	8.2	6.5	9.8*	9.8*	6.9	7.2	9.4*
Lower conductn	2.2	1.9			2.1	2.4	
Fermi level	-4.57	-4.66	-4.17	-4.10	-4.33	-4.11	-4.11
d charge (e's)	4.95	5.23	5.22	5.23	5.29	5.25	5.25

Key

* upper valence and lower conduction combined

** indirect band overlap

Fig. 4.3 Irreducible Brillouin zones.

a) Hexagonal

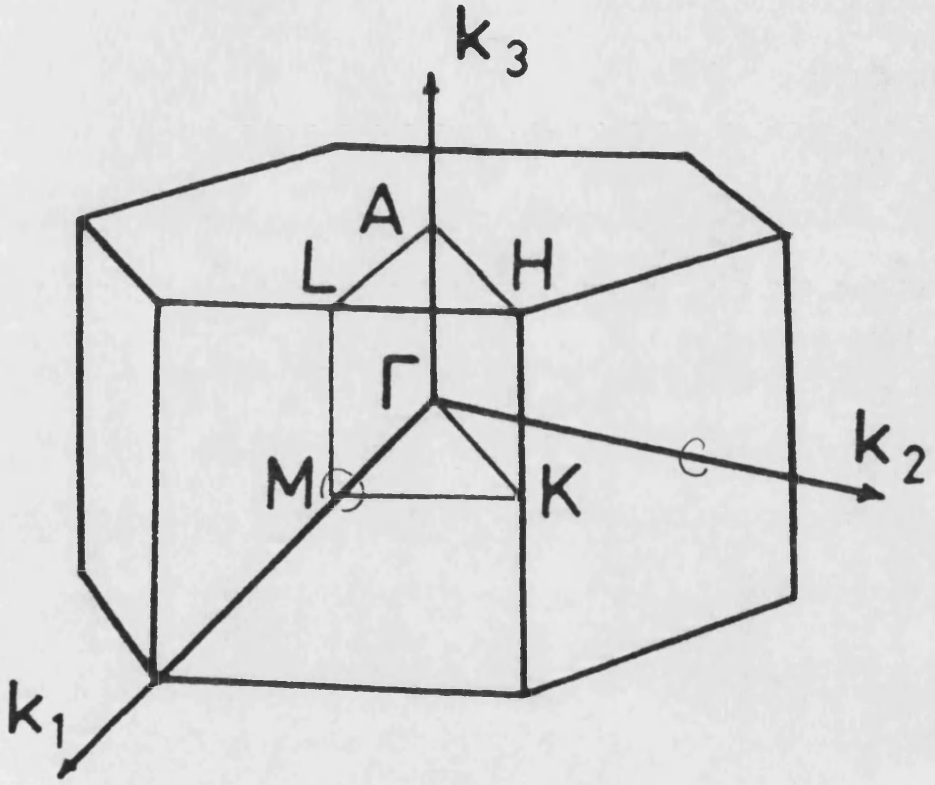

	k_1	k_2	k_3
Γ	0	0	0
M	1/2	0	0
K	1/3	1/3	0
Γ	0	0	0
A	0	0	1/2
L	1/2	0	1/2
H	1/3	1/3	1/2
A	0	0	1/2
M	1/2	0	0
L	1/2	0	1/2
H	1/3	1/3	1/2
K	1/3	1/3	0

Fig. 4.3 Irreducible Brillouin zones.

b) Orthorhombic

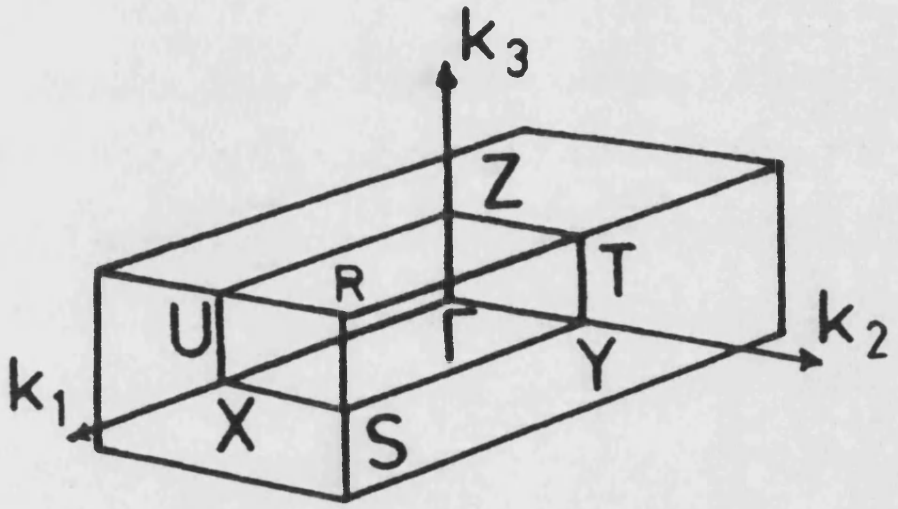

	k_x	k_y	k_z
Γ	0	0	0
X	1/2	0	0
U	1/2	0	1/2
Z	0	0	1/2
Γ	0	0	0
Y	0	1/2	0
T	0	1/2	1/2
Z	0	0	1/2
X	1/2	0	0
S	1/2	1/2	0
R	1/2	1/2	1/2
T	0	1/2	1/2

Fig. 4.3 Irreducible Brillouin zones.

c) Monoclinic

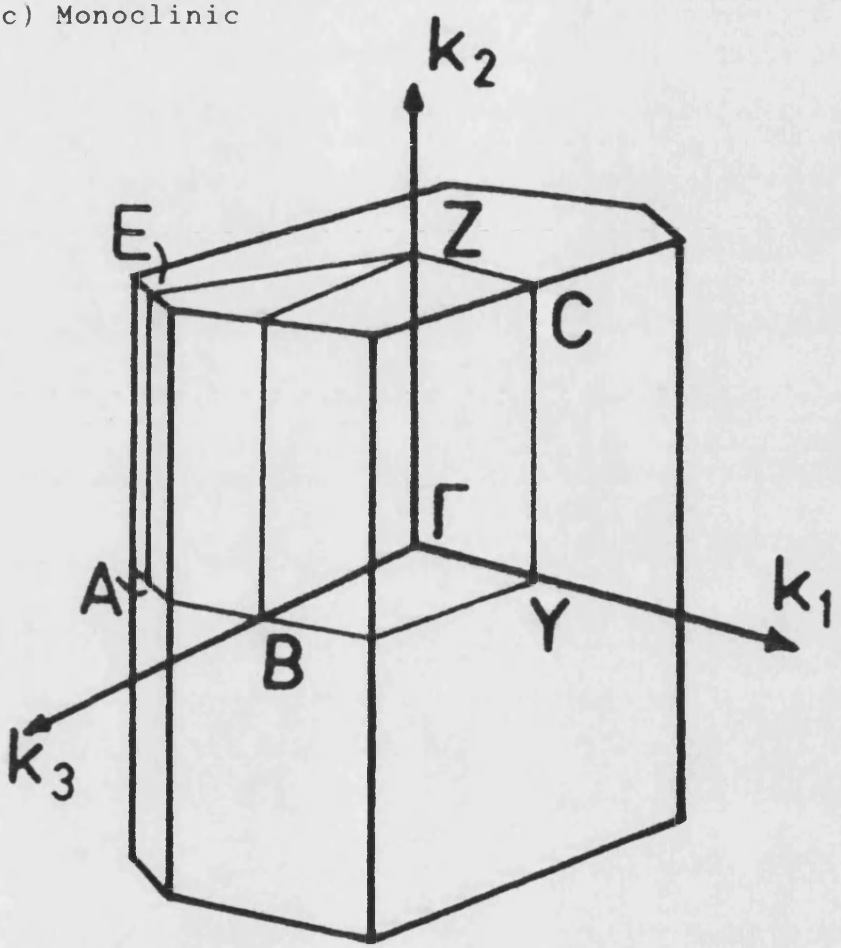

	k_1	k_2	k_3
Γ	0	0	0
Y	1/2	0	0
C	1/2	1/2	0
Z	0	1/2	0
E	-1/2	1/2	1/2
A	-1/2	0	1/2
Γ	0	0	0
B	0	0	1/2
D	0	1/2	1/2
Z	0	1/2	0

Table 4.6

Converged atomic orbital input energies (eV).

1) 2H WSe_2, $MoTe_2$ and WTe_2.

	s	p	d
Tellurides			
Mo	-5.10	-2.91	-4.56
W	-5.10	-2.91	-4.53
Te	-14.55	-6.67	
Selenide			
W	-5.20	-2.90	-4.95
Se	-17.46	-7.41	

2) 1T-WTe_2

	s	p	d
W	-5.20	-2.90	-4.58
Te	-14.55	-6.67	

3) B-$MoTe_2$

	s	p	d
Mo	-5.05	-2.91	-4.49
Te	-14.55	-6.67	

4) Td-$MoTe_2$ and Td-WTe_2.

	s	p	d
Mo	-5.10	-2.91	-4.53
W	-5.20	-2.90	-4.50
Te	-14.55	-6.67	

Fig. 4.4 2H-WSe2

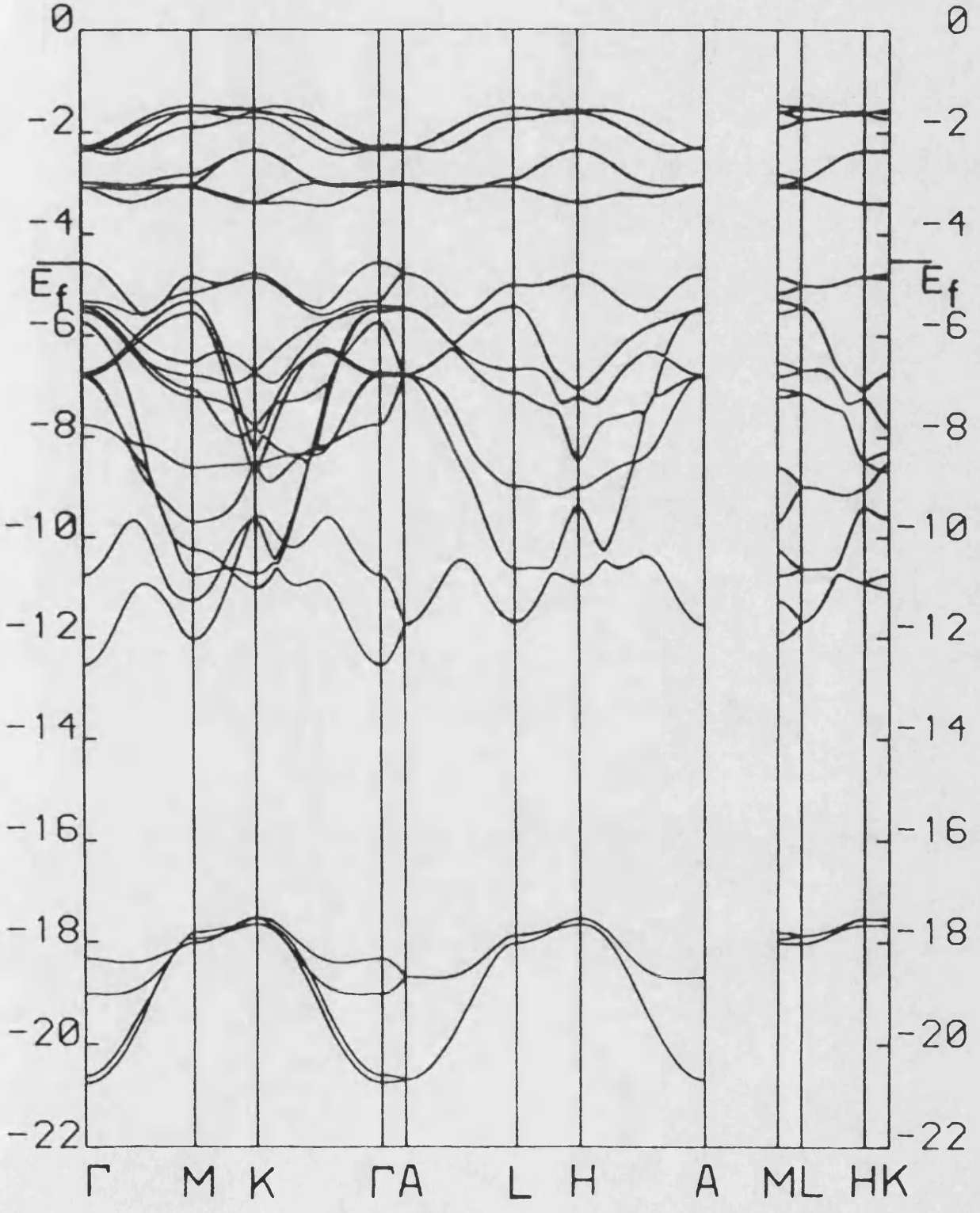

Fig.4.5 2H-WSe2

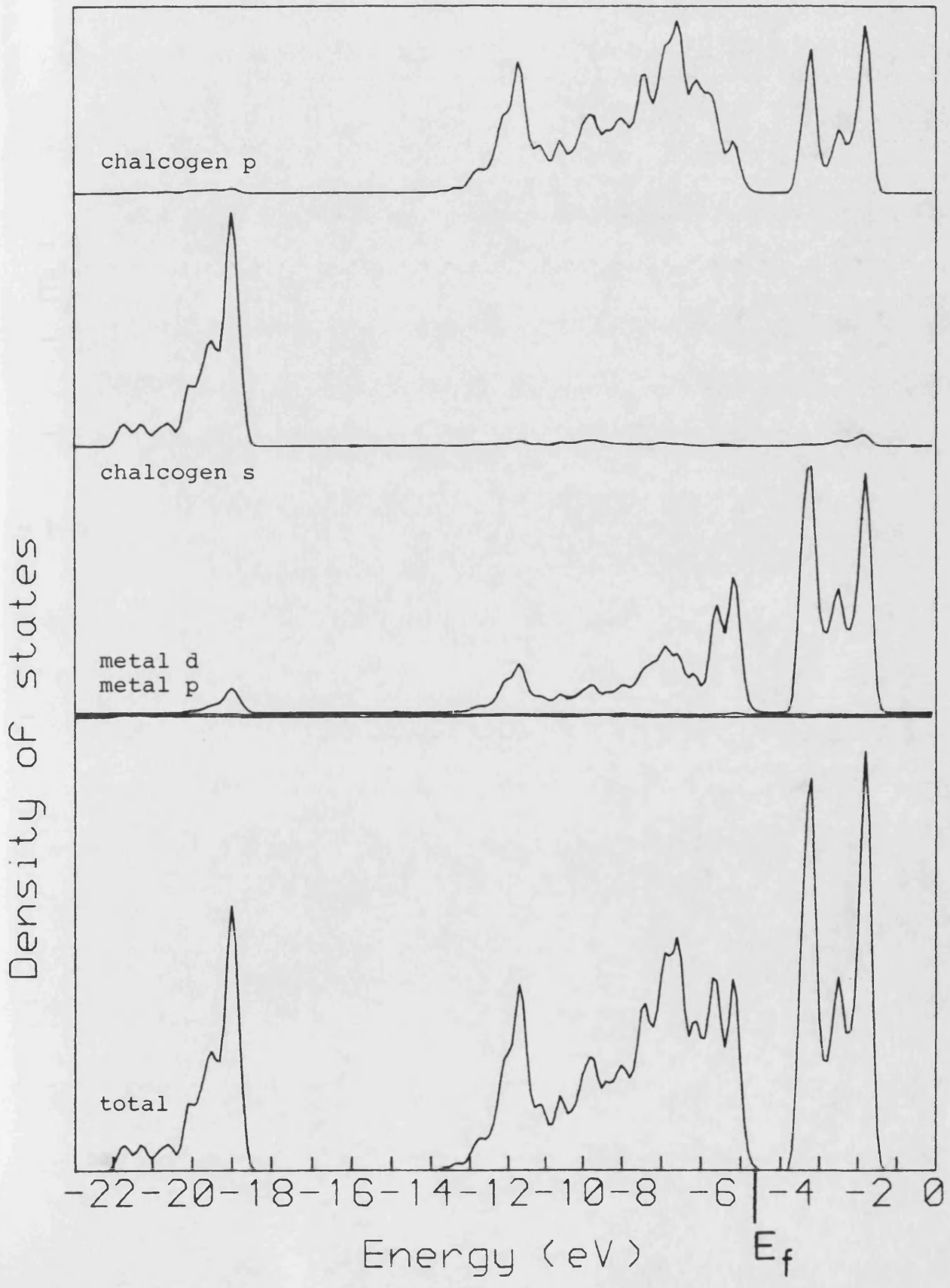

Fig. 4.6 2H-MoTe2

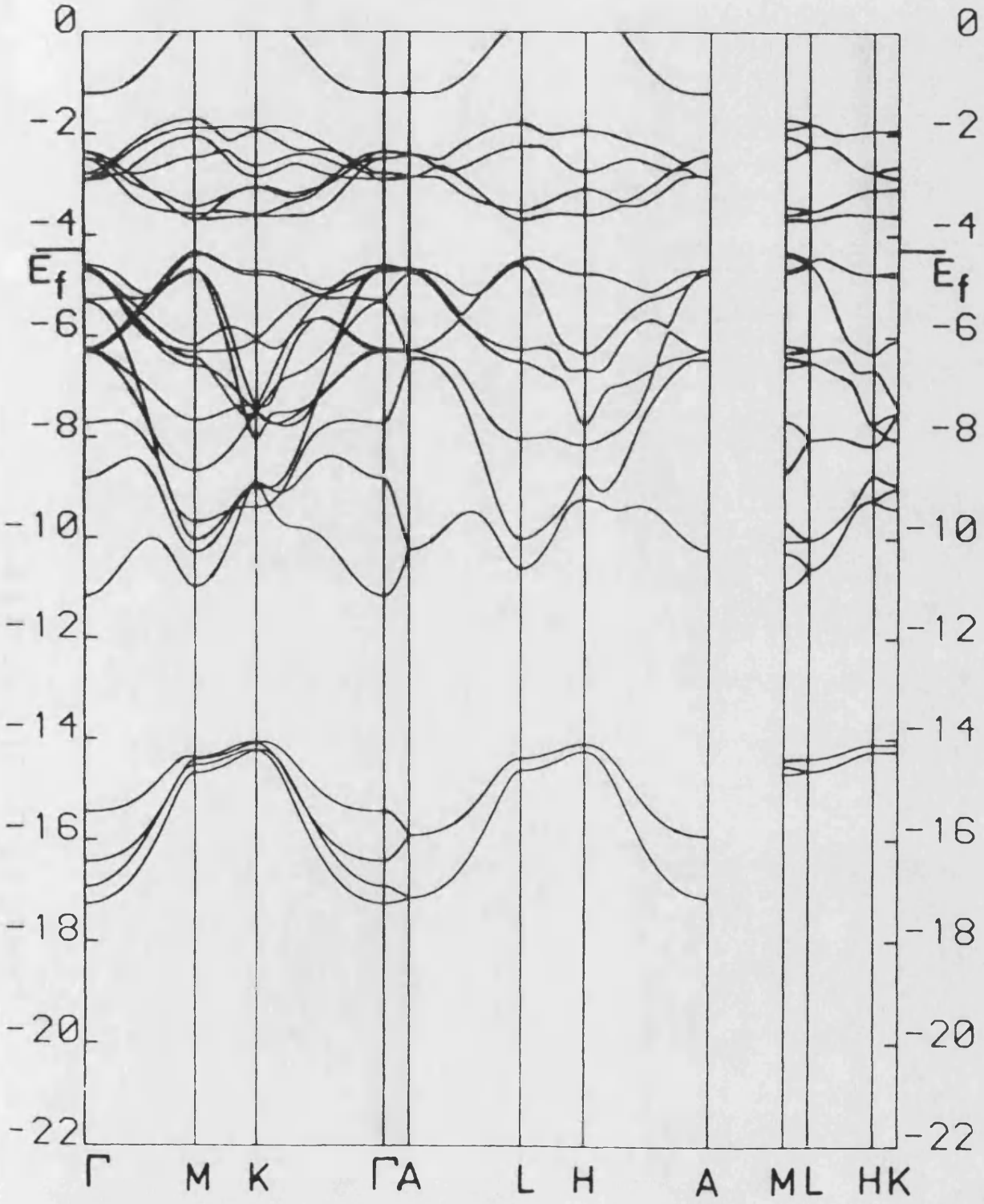

Fig. 4.7 2H-MoTe2

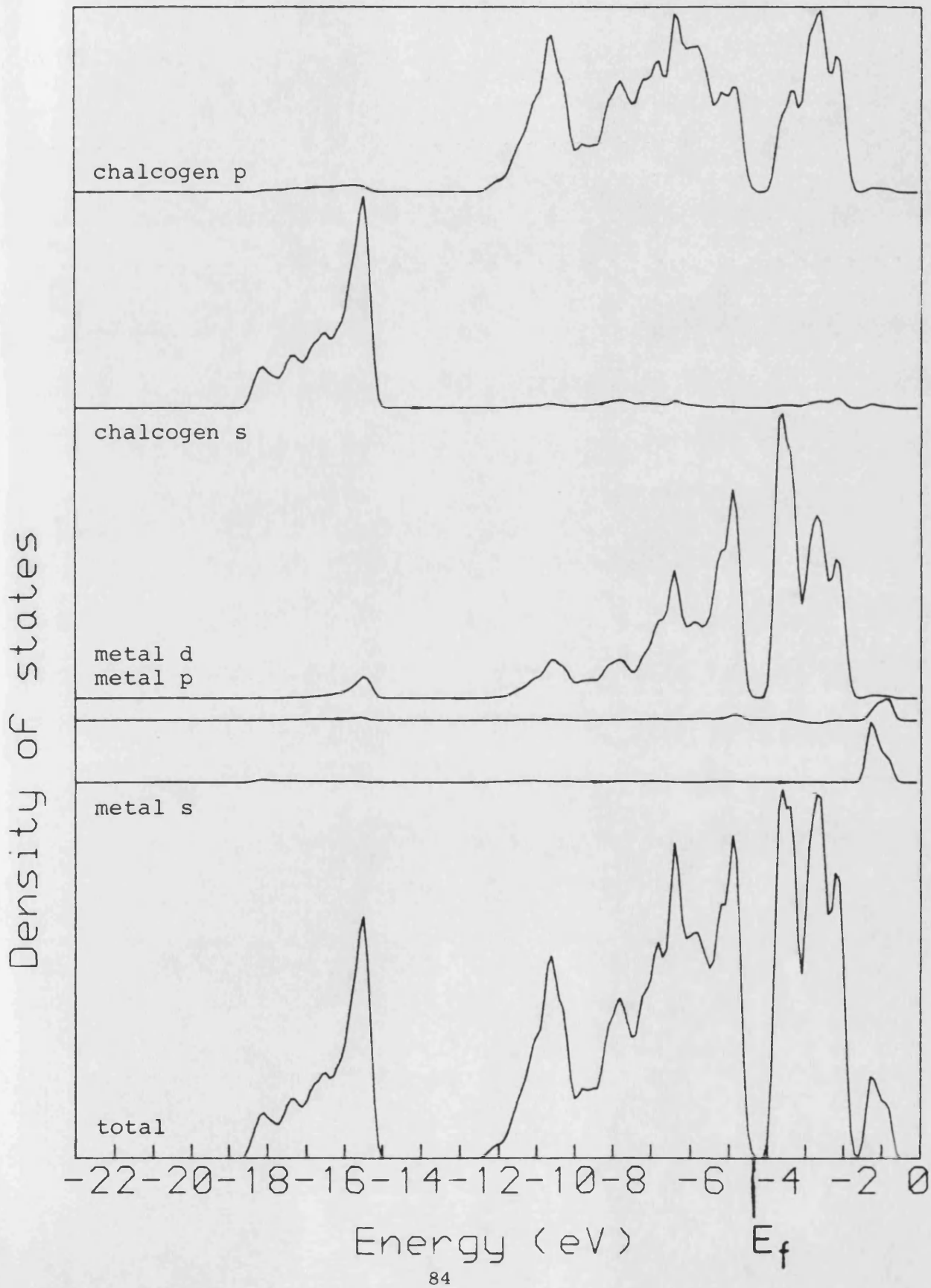

Fig. 4.8 2H-WTe2

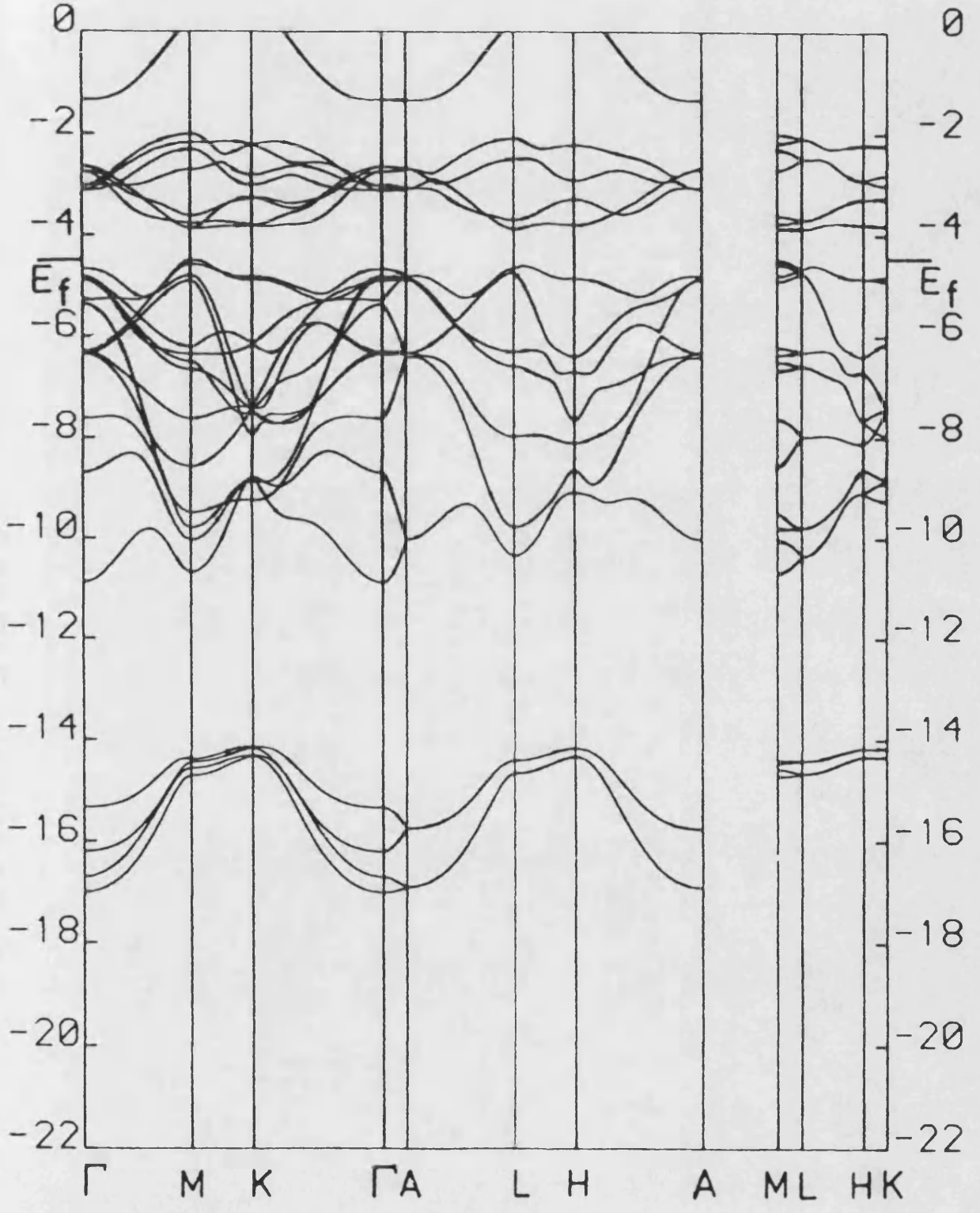

Fig. 4.9 2H-WTe2

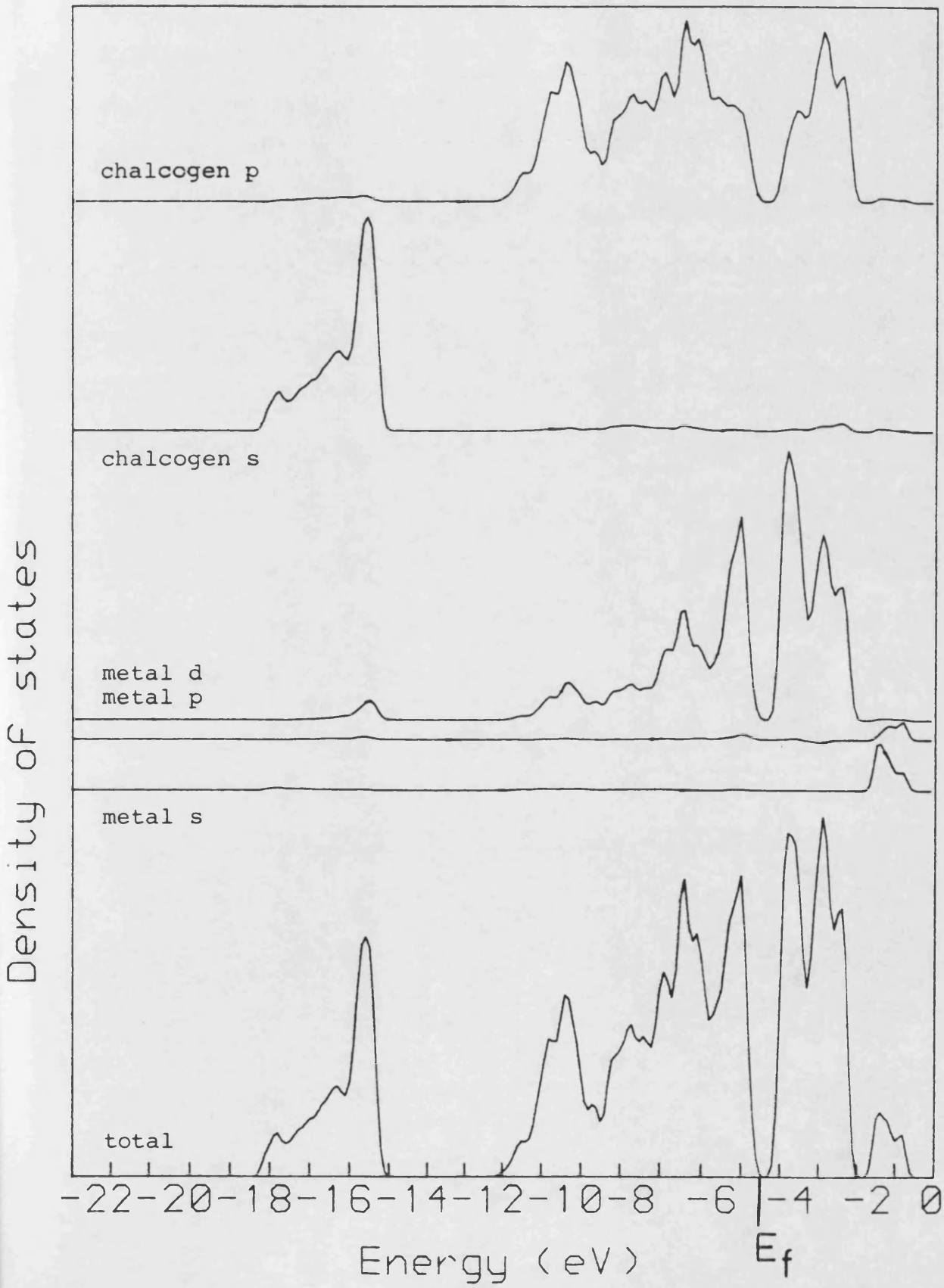

The crystal field

The effect of the trigonal prismatic crystal field is to lift the 5-fold degeneracy of the free atom metal 'd' orbitals giving 3 distinct energy values in the crystal. Two of these are doubly degenerate and one singly degenerate, namely

i) d_{xy} and d_{x2-y2}

ii) d_{yz} and d_{zx}

iii) d_{z2}.

There has been some dispute over the ordering of energies for these orbitals; (eg. Goodenough 1968, and Huisman et al., 1971) but it is now accepted that the d_{z^2} orbital has the lowest energy. Various suggestions have been made for the position of the d_{z2} band for this trigonal prismatic coordination (Wilson and Yoffe, 1969; Huisman et al., 1971 and Williams and Shepard, 1973). It is shown here that this band lies at the top of the non-metal p band, but without overlap for the less covalent cystals.

Bromley et al., 1972 discuss the proposed small energy gaps (about 0.1 eV) found for the group VIa dichalcogenides; their existence is supported to some extent by the experimental evidence of Wilson and Yoffe,

1969; Connell et al., 1969 and Williams and McEvoy, 1971. However there are compelling reasons to believe these small values are due to extrinsic effects, with a larger intrinsic semiconducting gap for these materials. 2H-$MoTe_2$ is assigned a gap of 1.0 eV from resistance measurements by Vellinga et al., 1970, while infrared spectra of 2H-MoS_2 by Weiting and Verble, 1971, and Huisman et al., 1971, find no evidence of small semiconducting gaps. The increased ionicity of the selenide compound causes a larger calculated semiconducting gap of 1.1 eV compared with the tellurides which have calculated gaps of 0.7 eV, as given in table 4.5.

The form of the 3 dos graphs are essentially similar. The deepest energy bands shown are due to chalcogen bonding s based orbitals mixing with metal d in turn hybridized with metal s orbitals- the metal d and s orbital energies are very close, especially for the selenide.The sharp peak at higher energies that can be seen here is due to mixing of chalcogen s with metal d. The broad upper valence band region is composed of mainly chalcogen p heavily mixed with metal d character. The deeper binding energy of the Se p orbital resulting in an increased chalcogen weighting in this region when compared with the tellurides, as shown in the projected dos.

The band structure graphs show the fourteen bands of the upper valence region which, along with the four lower chalcogen s bands, can accomodate the 36 valence electrons found in the unit cell of $(MX_2)_2$ and result in the expected semiconducting behaviour. The double degeneracy of the top face of the Brillouin zone (A-L-H-A) is echoed in the E vs. K graphs. The greater magnitude of the crystal field splitting terms for the more ionic WSe_2 is demonstrated most clearly in the lower conduction band region. In contrast with the tellurides the selenide shows no direct crossing of the two set of bands which are doubly degenerate at gamma. The metal d_{yz} and d_{zx} orbitals are directed approximately towards the ligands and are therefore both well mixed with the chalcogen p orbitals and pushed to higher energies than the d_{xy} and $d_{x^2-y^2}$ orbitals. The more covalent tellurides show greater dispersion in this region with $d_{zx/yz}$ based orbitals crossing the d_{xy/x^2-y^2} based bands when moving away from gamma (along sigma and lambda). At smaller binding energies the metal s and p based bands are pushed above the d bands, much higher for the selenides and slightly more separated for $MoTe_2$ than for WTe_2. The metal p orbitals are of much higher free atom energy and the metal s shows strong overlap with the chalcogen orbitals.

The essentially non-bonding d_{z^2} forms a distinctive peak in the dos at the top of the valence band. For WSe_2 the d_{z^2} band remains above the chalcogen p bands with no direct overlap throughout the Brillouin zone, in contrast to the mixing found in the tellurides. The $MoTe_2$ bands are all slightly wider than the WTe_2 bands due to the smaller unit cell and consequent shorter bond lengths. The increased ionicity of the selenide, in an even smaller unit cell, produces the largest band widths, especially noticeable for the p/d upper valence region.

Eigenvalues at gamma

Tables 4.7-4.9 show the eigenvectors of the basis set at the Brillouin zone centre- split into band regions. The lower band region can be seen to be heavily weighted on the chalcogen s orbitals, showing some metal s and d character. In the lowest distinct band of the upper valence band manifold the metal s/d_{z^2} hybrid mixes with the chalcogen p orbitals. The deeper energy of the selenide is demonstrated by a greater chalcogen character in this region. The 'non-bonding' chalcogen p_z based band does show some interaction in the larger and more covalent telluride compounds. This depresses the p_z energy slightly from the free atom value. Three other

Table 4.7

Eigenvalues at zone centre for 2H-WSe_2.

Eigenvalue	Orbital (Percentage character of bands)												
	Selenium				Tungsten								
	s	p_x	p_y	p_z	s	p_x	p_y	p_z	d_{xy}	d_{yz}	d_{zx}	$d_{x^2-y^2}$	d_{z^2}
-20.75	88				10								
-20.61	84			4	10								
-19.02	96							3					
-18.33	96							3					
-12.55	4			68	8								20
-10.76	4			52	6								36
- 7.76				100				1					
- 6.80			40									60	
- 6.80		40							60				
- 6.74			40									62	
- 6.74		40							60				
- 5.74				100				1					
- 5.52		60									40		
- 5.51			60							40			
- 5.43		56									43		
- 5.43			56							43			
- 5.32				24									78
- 4.57				36									62
- 3.07		60				1			40				
- 3.07			60									40	
- 2.98		64				1			36				
- 2.98			64				1					36	
- 2.34			40							60			
- 2.34		40									60		
- 2.28			44							57			
- 2.28		44									57		

Table 4.8

Eigenvalues at zone centre for 2H-$MoTe_2$.

Eigenvalue	Orbital (Percentage character of bands).												
eV	Tellurium				Molybdenum								
	s	p_x	p_y	p_z	s	p_x	p_y	p_z	d_{xy}	d_{yz}	d_{zx}	$d_{x^2-y^2}$	d_{z^2}
-17.26	93				6								
-16.93	88			4	8								
-16.43	95				4			2					
-15.44	98			2									
-11.18				80	8								10
- 8.86	4			56	8								32
- 7.72	4			96									
- 6.38			32									66	
- 6.38		32							66				
- 6.32			32									68	
- 6.32		32							68				
- 5.38				12	2								86
- 5.31				100				1					
- 4.78		32									68		
- 4.78			32							68			
- 4.72		28									72		
- 4.72			28							72			
- 4.66				32									68
- 2.95			68							32			
- 2.95		68									32		
- 2.81			72							28			
- 2.81		72									28		
- 2.52		68								34			
- 2.52			68								34		
- 2.39		70							30				
- 2.39			70									30	
- 1.21	4			8	86								4
- 1.21	8			4	86								4

Table 4.9

Eigenvalues at zone centre for 2H-WTe_2.

Eigenvalue (eV)	Orbital (Percentage character of bands).												
	Tellurium				Tungsten								
	s	px	py	pz	s	px	py	pz	d_{xy}	d_{yz}	d_{zx}	$d_{x^2-y^2}$	d_{z^2}
-17.00	94				6								
-16.70	88			4	8								
-16.20	95			4				2					
-15.33	98							2					
-10.88				80	8								10
- 8.69	4			60	8								30
- 7.61				100									
- 6.34			36									64	
- 6.34		36							64				
- 6.29			36									66	
- 6.28		36							66				
- 5.36				100				1					
- 5.28				12									86
- 4.89		40									62		
- 4.87			40							62			
- 4.83		36									64		
- 4.81			36							66			
- 4.66				32									68
- 3.11			60							38			
- 3.09		60									38		
- 3.02			54							34			
- 3.00		54									36		
- 2.74		68				1			36				
- 2.74			68				1					36	
- 2.64		68				1			34				
- 2.64			68				1					36	
- 1.33	6			8	85								3
- 1.33	4			6	85								3

i) the antibonding p_z-p_z type band- possibly across layers

ii) the mixing with the 'non-bonding' d_{z2} metal orbital when the crystallographically inequivalent chalcogen layers are (π) out of phase. This anti-bonding p orbital is of higher energy than the metal d energy thus these bands show a large metal d weighting.

iii) for the tellurides, the metal d_{z2} mixes with the bonding (or in phase) p_z orbitals.

The remaining bands of this upper valence region show a 2-fold degeneracy at gamma from the linear combination of the chalcogen p_x and p_y orbitals. These are in phase within a layer, thus resulti ng in 'antibond' type orbitals. Symmetry forbids the mixing of these orbitals with metal d_{z2} at gamma. The antibonding character of these doubly degenerate orbitals pushes their energy above the metal d energy, giving a large metal weighting in the upper valence manifold. For WSe_2 slightly less d character is found because of the initially more tightly bound Se $p_{x/y}$ orbital energies. For $MoTe_2$ the smaller unit cell allows a closer approach of the Te atoms- increasing the antibond effect and thus the metal d character below E_f.

Moving above the fermi level- the increased crystal field effect for the more ionic Se compound reverses the order of the $d_{x2-y2/xy}$ and $d_{yz/zx}$ based bands compared to the Te crystals. Crystal symmetry favours the overlap of metal $d_{zx/yz}$ orbitals with the chalcogen p, which further decreases the binding energy of these metal orbital based bands. At gamma the mixing of the metal $d_{zx/yz}$ with the chalcogen p is reduced by the phase of the chalcogen orbitals within each layer (x-y plane) but the band structure shows increasing interaction moving away from gamma.

The stabilization of a trigonal prismatic coordination is clearly demonstrated here, with the semiconducting gap induced by the crystal field splitting of the transition metal d orbitals. The non-degenerate d_{z2} orbital is filled (below Ef) in the group VI compounds with the remaining d orbitals at the bottom the the conduction band and therefore forming the energy gap. The near equivalence of the Mo and W compounds is confirmed by a comparison of almost all the relevant parameters, such as energy gap and Mulliken population. The consequence of replacing Te with the more ionic Se is shown. The calculated 1.1 eV semiconducting gap for WSe_2 is slightly smaller than experimental values of about 1.5 eV (Goldberg et al., 1975; Upadhyayula et al., 1968; Gobrecht et al., 1978) to 1.7 ev (Anedda et al,

1978 and Beal and Liang, 1976). However the inability of the local-density approximation of the exchange-correlation potential to make precise predictions of band gaps must be borne in mind here. In contrast to the band structure calculated here, those of Bromley et al., 1972, using an empirical T.B. method, show crossing of the higher energy d bands through the Brillouin zone. However their appproach utilises only one formula unit in a 1H cell of a 2-D lattice and without metal p orbitals.

b) WTe_2 in octahedral coordination

Here one formula unit in a hexagonal unit cell is taken with the z axis perpendicular to the layers, in the CdI_2 (1T) structure. The unit cell parameters are calculated from the as-grown Td-WTe_2 structure, using half the c lattice parameter and the average Te-Te bond lengths within a layer and preserving the W-Te distance. This unit cell, therefore, has the large Te atoms not directly atop each other as in the 2H structure; increasing the Te-Te cross layer distance to 4.21A (cf. 2H distance of 3.66A) while the metal remaining 6-fold coordinated by Te atoms.

The band structure E vs. k graphs in eV, (figs. 4.10 and 4.11) are along the high symmetry lines covering all

Fig. 4.10

1T-WTe2

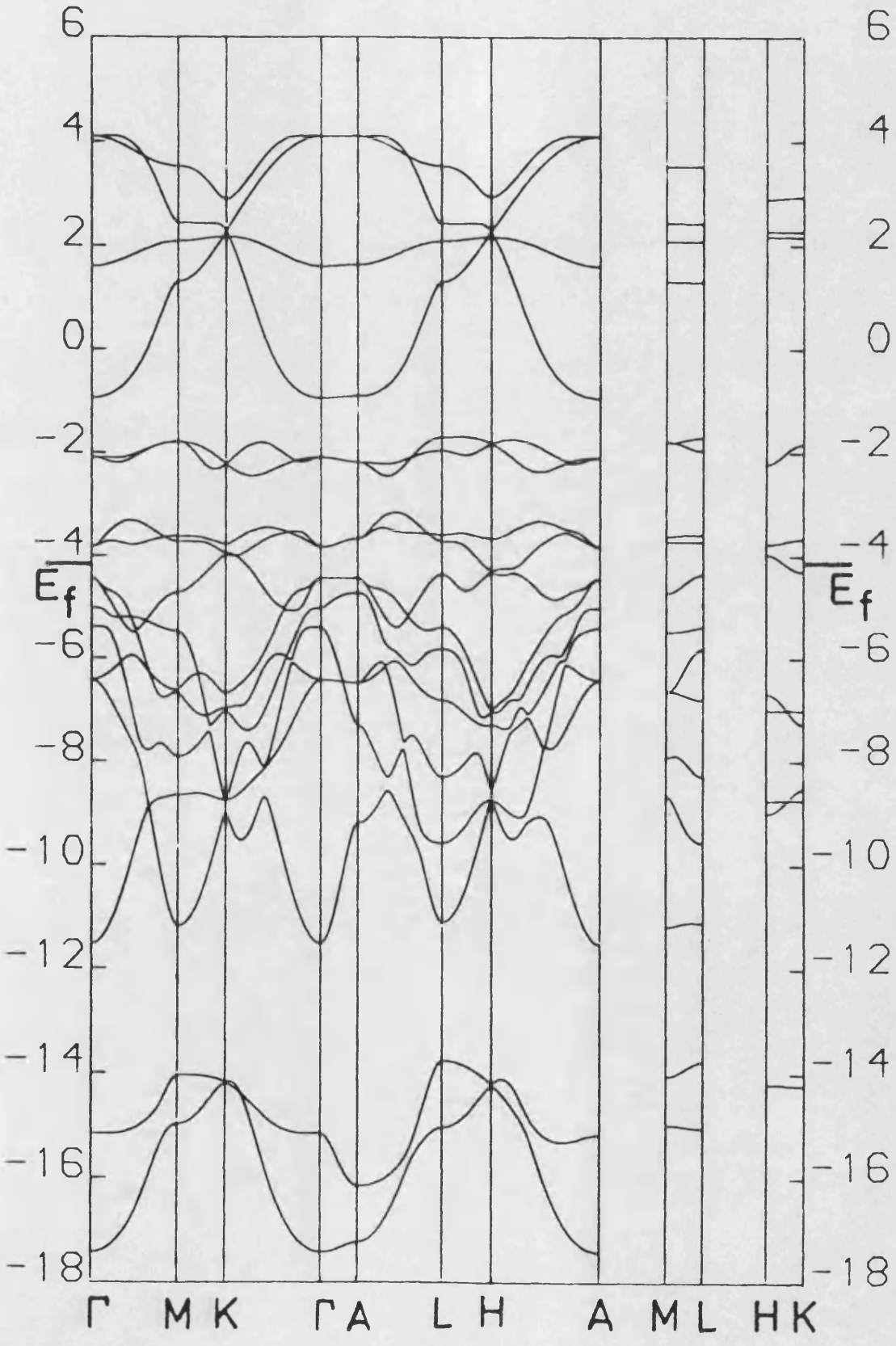

Fig. 4.11 1T-WTe2

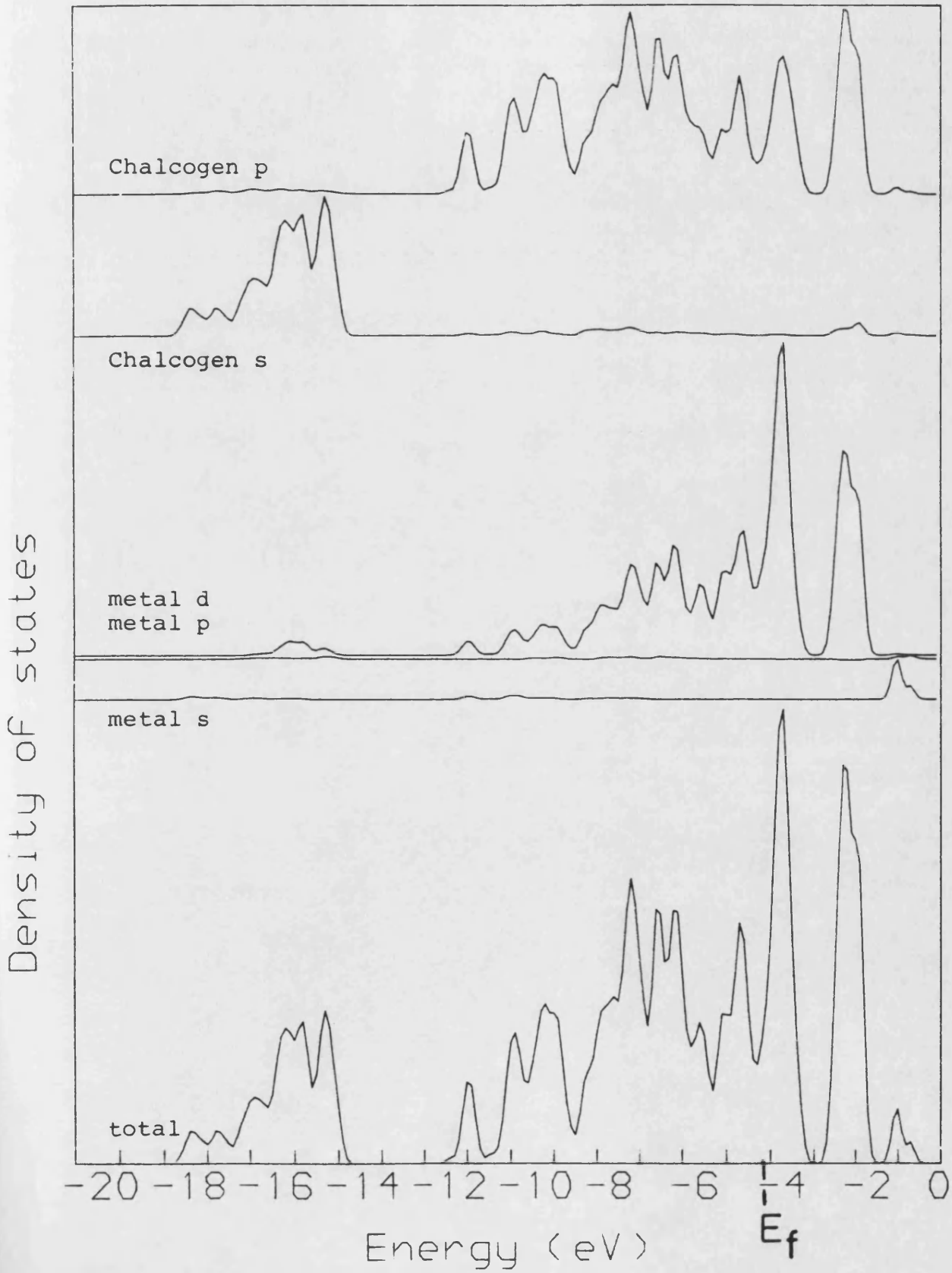

edges of this zone, calculated using 60 points between each pair of symmetry points. The E vs. $\underline{k}$ graph is shown for the irreducible zone corresponding to the zone used for the 2H polytypes (fig. 4.3a)- ignoring the negative k_z volume. The densities of states (dos) and projected dos were calculated using a regular net of 100 $\underline{k}$ points through the whole irreducible Brillouin zone. The dos are smoothed by a gaussian (FWHM=0.1 eV) and cut off at -1.0 eV. The converged metal d energies are given in table 4.5; these correspond to a Mulliken population of 5.23 electrons for the metal d orbitals.

The 1T form of WTe_2 has not been grown- it is analysed here to explore the effect of the reduced Madelung term for the increased Te-Te bond length. A reduction in Coulomb energy of about 20% has been shown for the octahedral coordination over the trigonal prismatic case (Shen and Liang, 1983). This calculation assumes no charge transfer in going from one coordination to the other- this approximation is valid in this case- the Mulliken populations calculated here show little difference in the converged metal d orbital populations for the two structures.

The crystal field splitting for a transition metal in an octahedral ligand coordination (point group O_h) is well known (eg. Barrow, 1979). With the ligands directed

along cartesian axes the d degeneracy is lifted giving two distinct energy values:-

i) two fold degenerate d_{z^2} and d_{xy} of e_g symmetry which are directed towards the ligands- showing large overlaps and raising the d energy for electronegative non-metals

ii) three fold degenerate $d_{x^2-y^2}$, d_{yz} and d_{zx} (t_{2g}) which are restricted by symmetry from interactions with the ligands and are thus little perturbed from the free energy state except by the atomic potential of the ligand atoms.

For materials with bands of appreciable ionic character the 5 metal d orbitals may form a discrete manifold well separated from the chalcogen p generated bands, with the decrease in ionicity reflected in increasing metal character of the chalcogen p based bands. Semiempirical band structure calculation on the group IV dichalcogenides ZrS_2, $ZrSe_2$, HfS_2 and $HfSe_2$ (Murray et al., 1972) demonstrate this clearly. These compounds all crystallise in the 1T form- with the d bands above the fermi level and with a semiconducting gap separating them from the chalcogen p bands. The electronegativity differences inducing a range of gaps from 1.3 to 2.1 eV.

In the group VIIIc dichalcogenides octahedral coordination is also favoured since here the triply degenerate lower energy t_{2g} d bands are completely filled. Thus the group VIIIc compounds can be semiconducting even with increased covalency causing the lower d bands to overlapping the non-metal p band manifold.

For the 1T-WTe_2 bands shown in fig. 4.10 it can be seen that the t_{2g} bands overlap with the Te p bands but there are insuffient electrons to fill this manifold- thus resulting in a metallic compound.

The small electronegativity difference (covalency) between W and Te is again revealed in the heavy mixing of the Te p and metal d orbitals especially clearly shown in the upper valence band region of the projected densities of states (fig. 4.11). The large isolated d e_g type and the Te p projected dos show mixing very clearly. The metal d is also shown mixed with the chalcogen s orbitals while the metal s and p bands are pushed well above the d band manifolds as bond-antibond pair interaction with the Te orbitals. The metal s free atom energy is similar to the metal d but large overlaps and symmetry considerations result in this increased energy movement. The dip in the dos near Ef is clearly insufficient to prevent 1T-WTe_2 from behaving in the

semi-metallic manner expected for this coordination.

Eigenvectors at gamma

Table 4.10 shows the eigenvectors for each eigenvalue at the Brillouin zone centre- examined here to expand the analysis of the dos,projected dos and E vs. k graphs. (The lower valence band region is due to the bonding of in-plane with some mixing with metal s and Te p_z). Here, with the z direction defined as perpendicular to the layers, the Te atoms are not therefore along the cartesian axes. The t_{2g} bands are thus formed of hybrid d orbitals rather than from the pure basis set. Nevertheless the crystal symmetry is revealed clearly in the eigenvectors with mainly d_{zx} and d_{yz} little perturbed from the free atom energy at gamma, and the Te p_x and p_y orbitals forming doubly degenerate anti-bonds (thus of higher energy than free atom values) within each layer. The metal d_{z2}, with some metal s mixes with Te p_z out of phase in each layer. Large overlaps are seen by the metal orbitals in the x-y plane at gamma, with the Te $p_{x/y}$ energy above the metal d and therefore large metal d character appears below Ef. The effect of the increased Te-Te bond length between the layers is seen in the non-bonding Te p_z eigenvalue at the free atom energy.

Table 4.10

Eigenvalues at zone centre for 1T-WTe_2.

Percentage character of bands at gamma.

Eigenvalue	Orbital												
	Tellurium				Tungsten								
	s	p_x	p_y	p_z	s	p_x	p_y	p_z	d_{xy}	d_{yz}	d_{zx}	$d_{x^2-y^2}$	d_{z^2}
-17.42	90				10								
-15.16	98							3					
-11.52	2			76	10								11
- 6.42			34							4		63	
- 6.42		34							63		3		
- 5.38				14									86
- 5.01				100				1					
- 4.42			6						14		81		
- 4.42		6								81		14	
Fermi level													
- 3.82			100				1						
- 3.82		100				1							
- 2.09		62							23		16		
- 2.09			62							16		23	
- 0.94	0.08			10	80								3

c) Distorted Octahedral coordination

The total density of states (dos), projected dos and E(k) graphs are shown in figures 4.12 to 4.17. All 3 crystals with this distorted octahedral coordination have 4 formula units per unit cell giving a 68x68 matrix. The E vs. k graphs along high symmetry lines for the monoclinic and orthorhombic irreducible zones use 36 points between each pair of symmetry points. It is convenient to split the E(k) graphs into four regions- consisting of the deep chalcogen s based bands (region A), the chalcogen p with some d manifold (B), the upper d bands (C), and the higher metal s and p bands (D). 64 points of a regular net through the irreducible Brillouin zone were used for the dos and projected dos. These are smoothed by a gaussian (FWHM=0.1eV) and cut off at -1.0 eV.

B-$MoTe_2$

B-$MoTe_2$ has a dip in the dos close to the Fermi level but matches the semi-metallic conduction found experimentally- this shows a 10^6 increase in conductivity when compared with 2H-$MoTe_2$ (Revolinsky and Beerntsen, 1966). The E vs. k calculations show an indirect overlap of about 0.3 ev between the upper d and lower d/p bands. The highest energy point of the

Fig.4.12 β-MoTe2

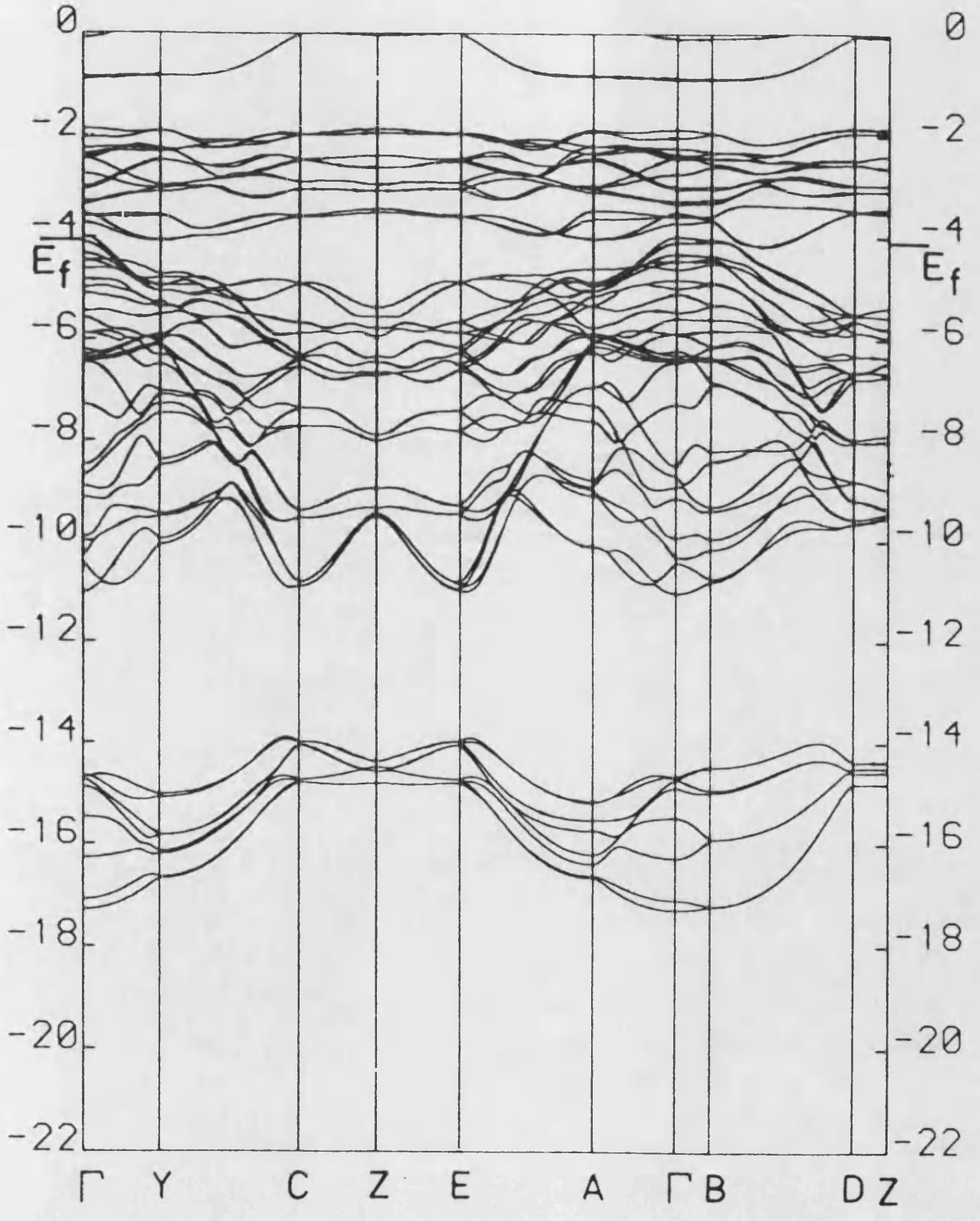

Fig. 4.13 β-MoTe2

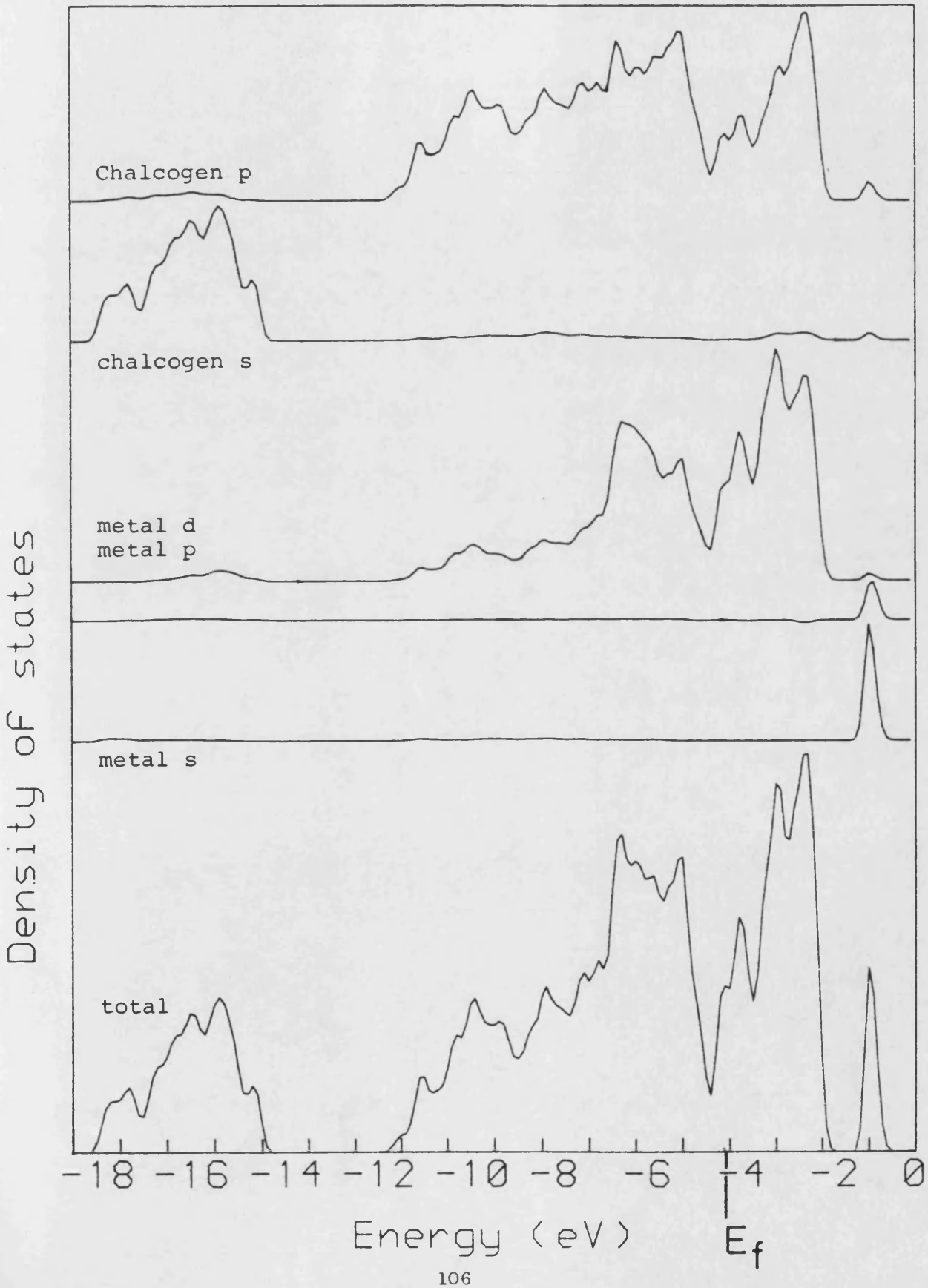

Fig. 4.14 Td-MoTe2

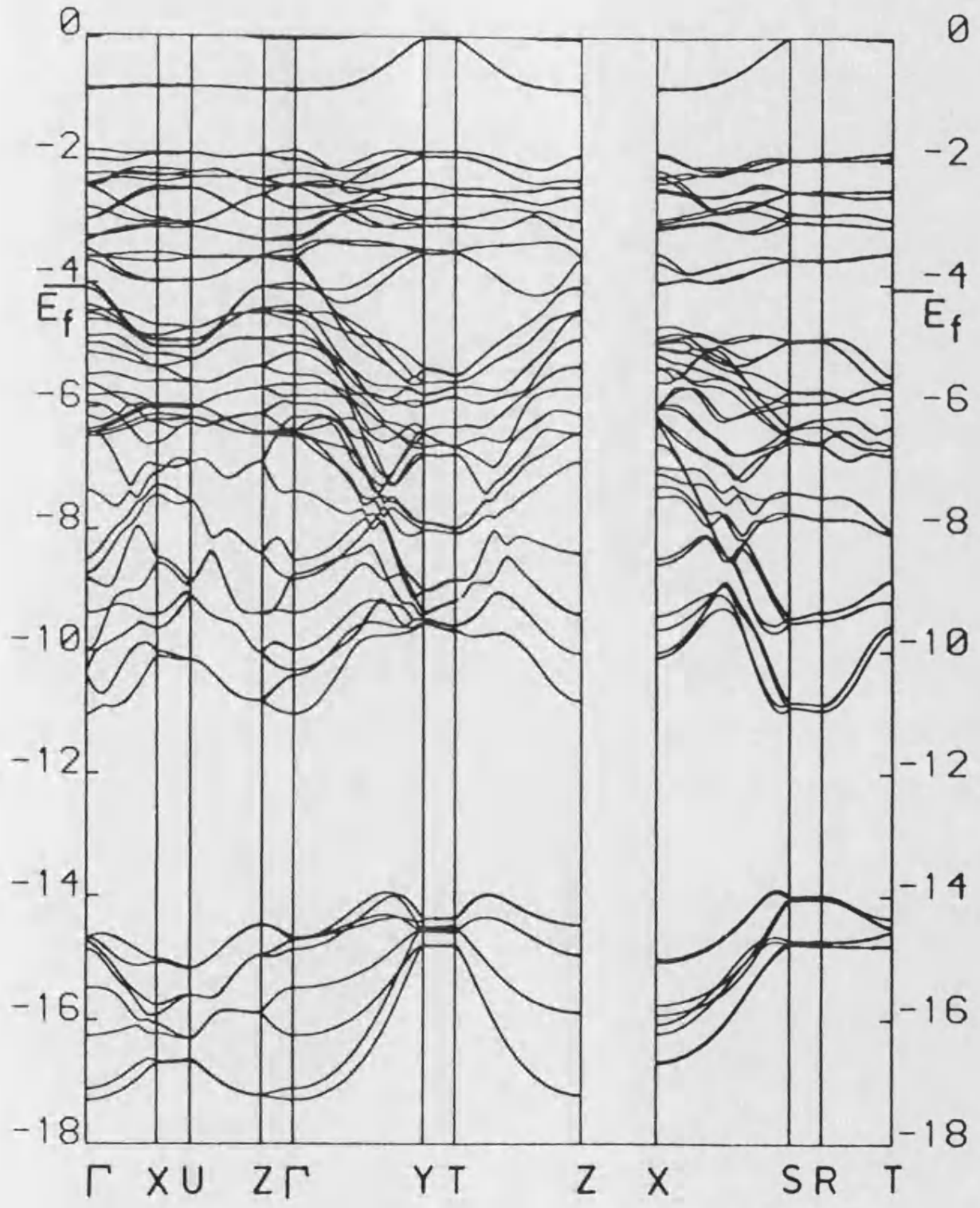

Fig. 4.15 Td-MoTe2

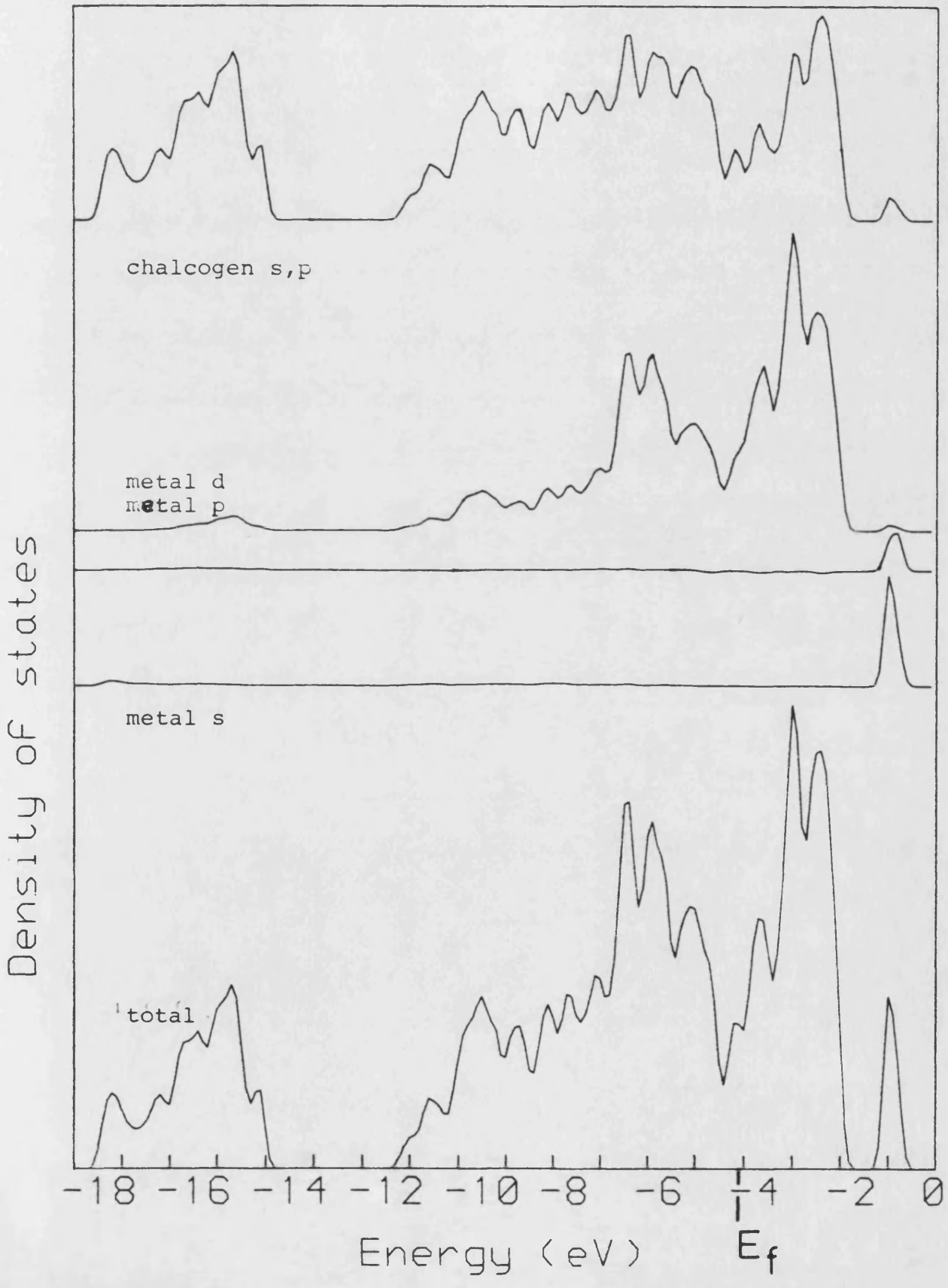

Fig.4.16 Td-WTe2

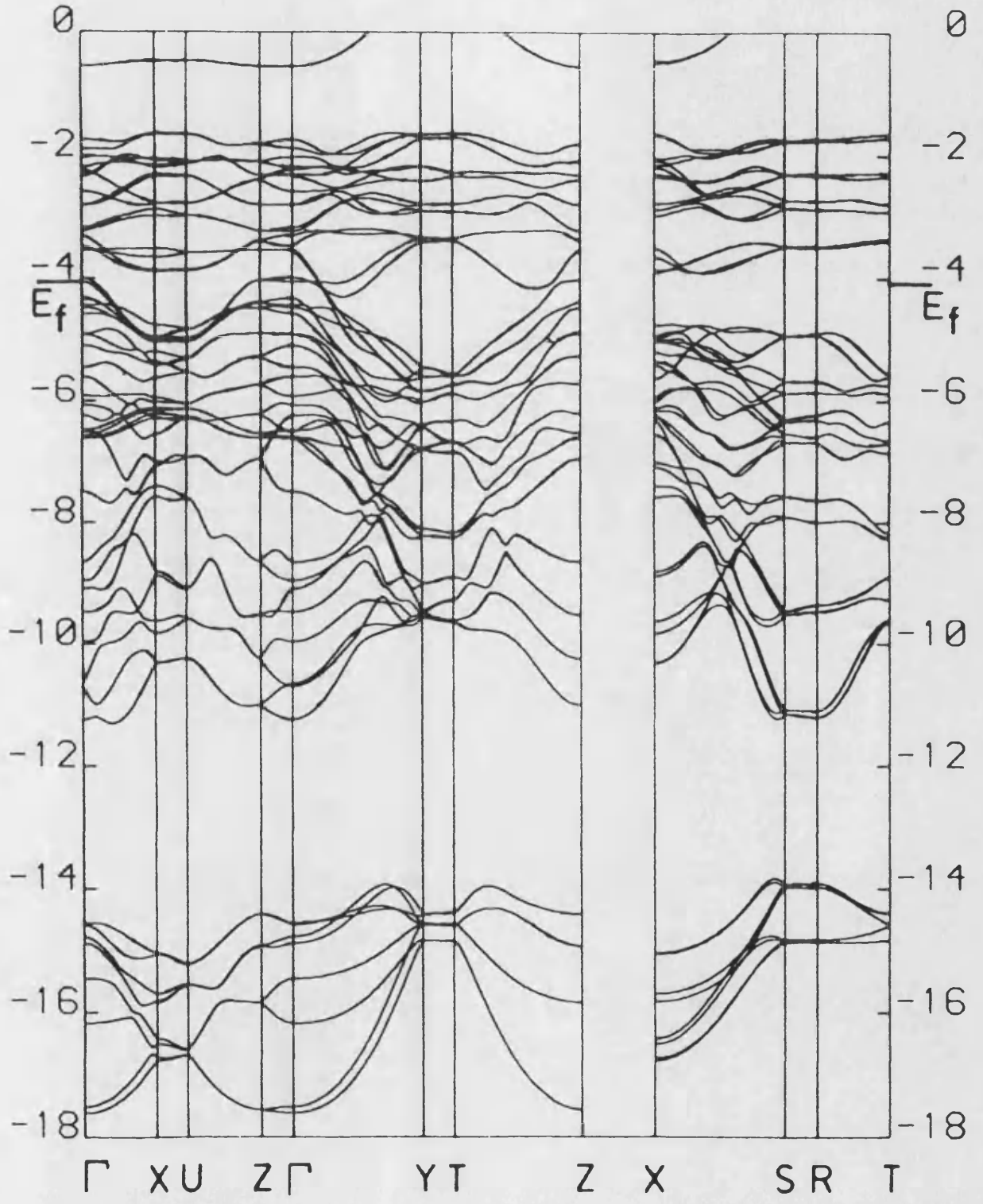

Fig. 4.17 Td-WTe2

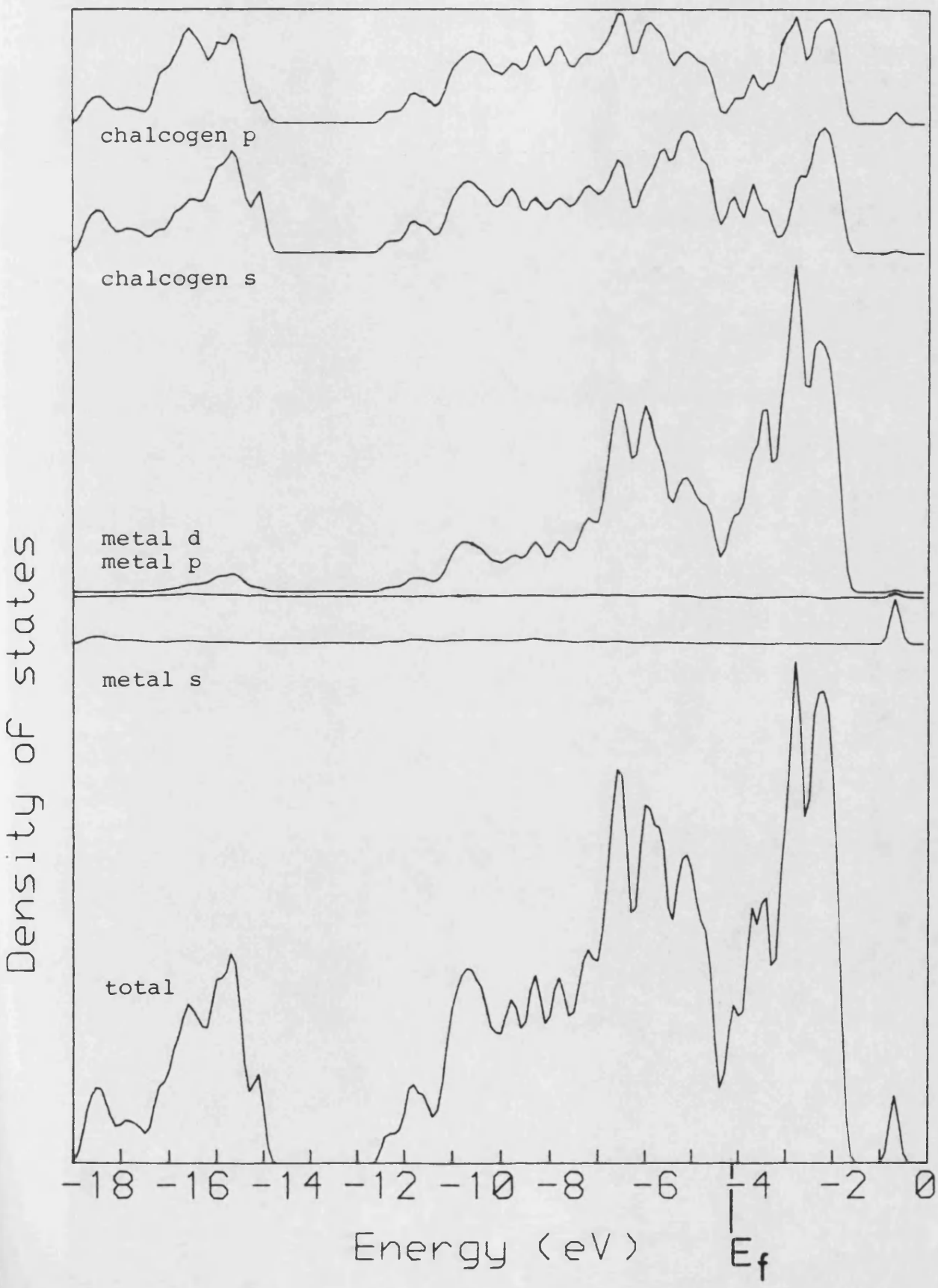

chalcogen p/lower metal d is at gamma, while the upper d band manifold minimum is calculated to be between B and D. The monoclinic crystal symmetry is reflected in the double degeneracy along the top face of the Brillouin zone C-Z-E and D-Z. The calculated eigenvalues at the zone centre are shown in table 4.11.

The upper d band manifold contains 16 bands, showing one d orbital split off for each of the 4 metal atoms in the unit cell. This crystal field effect is not obvious from the distorted octahedral metal coordination. The effect is reminiscent of the trigonal prism splitting but here the energy difference is insuffient to create the semiconducting gap found in the 2H compounds. The upper d band manifold is wider by 0.5 eV (table 4.5) than for 2H-$MoTe_2$ since the reduced metal-metal separation increases d orbital overlap. The smallest Te-Te distance of 3.48A (compared with 3.52A for 2H-$MoTe_2$) also contributes to increased band widths. The higher conduction bands (D) of metal s and p character are well separated from the d bands (C).

The covalent nature of this compound is again emphasised by the heavy mixing of the metal d and chalcogen p orbitals in region B as can be seen in the projected dos (fig. 4.13). The small difference between the two types of metal environment appear to affect their projected

Table 4.11

Eigenvalues at zone centre for Td-$MoTe_2$.

Eigenvalue	Orbital												
	Tellurium				Molybdenum								
	s	px	py	pz	s	px	py	pz	dxy	dyz	dzx	$d_{x^2-y^2}$	d_{z^2}
-17.29	94				6								
-17.11	84			8	8								
-16.25	92			4				4					
-15.48	91							4			4	2	
-14.87	94										4	2	
-14.71	84			3							8	5	
-14.69	88			8									4
-14.67	98												2
-11.03		79		4	2						5	6	4
-10.40		76		2	2						10	6	2
-10.31	10	2		73	6								8
- 9.98	2	75		12							6		2
- 9.37	2	48		29							9	9	4
- 8.81	2	39		30							8	16	3
- 8.74	6	5		61	2							4	19
- 8.50	8	8		54	2						2	17	7
- 7.38		4		60	4	2					4	10	4
- 6.47			43							56			
- 6.42			24						76				
- 6.41			24						76				
- 6.40	2	6		48								30	14
- 6.36			41							60			
- 6.16	2	22		45								27	2
- 5.94		10		14							21	35	16
- 5.81		14		16							10	21	38
- 5.63		37		14							16	26	2
- 5.47		38		15							21	19	2
- 5.12		25		20							23	2	29
- 4.97		18		55							1	1	21
- 4.85		5		26							10		55
- 4.59	2	28		15							20		34
- 4.49			59							39			
- 4.45		26		46							2		27
- 4.36			33						4	3			
- 4.09			52						4	41			
- 4.00			78						4	18			
- 3.64		4		8							45	33	9
- 3.58			78						24				
- 3.57			76						25				
- 3.46		7		18							34	30	9
- 3.30		48		4								11	37
- 3.24		51		6							2	11	29

Table 4.11 continued

Eigenvalues at zone centre for Td-$MoTe_2$.

Eigenvalue	Orbital												
	Tellurium				Molybdenum								
	s	p_x	p_y	p_z	s	p_x	p_y	p_z	d_{xy}	d_{yz}	d_{zx}	d_{x^2}	d
- 2.97			26						75				
- 2.96			27						73				
- 2.78	4	10		27							46	8	6
- 2.44			63						17	19			
- 2.42			47								25	27	
- 2.40			63						17	19			
- 2.40	4	8		44							33	8	4
- 2.23		51									21	26	
- 2.00			55							44			
- 1.85			56							42			
- 0.88	2	2		8	68	13		2					2
- 0.85	3	2		8	70	11		2					2
- 0.04		4		2	65	31		1					
- 0.03		2		2	67	32							

dos little.

Td-WTe_2 and Td-$MoTe_2$.

The band structure and dos for Td-WTe_2 and Td-$MoTe_2$ (figs. 4.14 to 4.17) show again the similarity of the two metal atoms. The environment of the metal atom is similar to that in B-$MoTe_2$ with Mo-Te bond lengths differing by up to only 0.03A, as shown in table 4.4. This table also shows similar Te-Te separations- both across and within layers. These small diferences, plus the keying position of the layers, result in the band crossing between the symmetry points gamma and Y shown in figure 4.14. This feature apart, the electronic structure in going from the monoclinic to orthorhombic form of $MoTe_2$ is essentially unchanged- the band widths (table 4.5) are of similar values as is the lowest energy point (at about -17.7 eV) and the position of the metal s/p band centre (about -1.0 eV). Table 4.6 lists the converged metal d orbital energies showing negligible differences.

4.5 Discussion

The band widths shown for the 3 compounds studied here show that wider bands are found for the distorted octahedral coordination crystal- this is expected from

the increased metal-metal interaction of the metal chains running through the layers. The band width increase is especially noticeable for Td-WTe_2 compared to 2H-WTe_2 with the upper d and lower d/Te p bands combined width of 9.8 eV including overlap while 2h-WTe_2 total is 8.4 eV plus the semiconducting gap of 0.7 eV. For Td-WTe_2 the metal-metal distance is relatively shorter than for Mo-Mo compared with their respective elemental crystal separations. This must act to stabilize the Td-WTe_2 structure and gives a clue as to why WTe_2 does not (yet?) appear as the 2H polymorph.

The reason why WTe_2 is not found in the trigonal prismatic coordination in contrast with $MoTe_2$ is not immediately apparent from these electronic structure calculations. However spin-orbit coupling may play an important role here, with the heavier W atoms causing a decreased semiconducting gap for a 2H structure and thus a reduction in the energy saving which stabilizes the trigonal prismatic crystal field. For the 2H polytypes estimates of spin-orbit splitting at the valence band are given by Wilson and Yoffe, 1969 as 0.3 and 0.6 eV respectively for $MoTe_2$ and WTe_2.

Chapter 5. Introduction to the group IV transition metal trichalcogenides.

5.1 Introduction.

Interest in the group IV transition metal trichalcogenides (MX_3) follows from the vast amount of research devoted to the closely related transition metal dichalcogenides (MX_2: M= Group IVa,Va,VIa; X=S,Se,Te). These two groups of compounds share many features since, in a first approximation, one of the chalcogen atoms of the MX_2 unit formula is replaced by a covalently bonded pair of chalcogen atoms to give MX_3. Due to the limited amount of theoretical data experimental electronic structure studies of MX_3 compounds have utilized this interpretation - allowing a close comparison of the 2 groups.

Both the MX_2 and MX_3 compounds belong to a wider group of layered transition metal chalcogenides and halides which show 2- and even 1-dimensional behaviour. These layer compounds (which are of increasing interest - especially since the discovery of charge density waves) provide a useful starting point for the description of MX_3's. In the most extreme cases 1-D behaviour is found and thus provides a useful source of data for an interesting and relatively new field of physics. The MX_3

compounds may be described as 2-D quasi-1-D crystals since they are certainly layered structures but they also show some one dimensional character.

Interest in the layered chalcogenides was renewed with the study of intercalated systems- where electron donors are taken up in the van der Waals gap. One important application is the use of a dichalcogenide cathode in a high energy density reversible battery with a lithium anode (Whittingham, 1976). The MX_3 compounds show a reduced degree of reversibility compared with the MX_2 compounds as described in chapter three.

The group IV transition metal trichalcogenides exist as two structural variants, one being almost the mirror image of the other. This allows an interesting comparison of the electronic structure for the two closely related forms. The MX_3 crystal structures are detailed in section 5.2.

A simple bonding model to account for the observed electronic structure of the MX_3's is given in section 5.3. This based on a molecular orbital scheme with the covalently bound pair X_2^{2-}.

Excitations are an important area of study of these layered compounds. Excitons in particular play a crucial

role here since they dominate in the measurement of semiconducting gap values - a useful parameter for the comparison of experimental and theoretical electronic studies. A short description of the role of excitations in these materials is given in section 5.4.

The conduction and valence bands for all the MX_3 compounds studied here show (expected) similarity because they all crystallize with the same space group and all atoms belong to the same groups of the periodic table group (IVA for the metals and VII for non-metals). The major electronic structure studies, to date, are briefly reviewed in sections 5.5 and 5.6. Also mentioned here is the dichroism which has been found in these monoclinic crystals- after overcoming the difficulties of growing sufficiently large crystals plus problems of polycrystallinity,twinning and non-stoichiometry which are common in these crystals.

The final section of this chapter is given over to $ZrTe_3$ which, in contrast to the other MX_3's, appears to show semi-metallic behaviour.

In summary, the reasons for interest in the group IVA trichalcogenides are briefly given here :-

1) these layered crystals show anisotropic behaviour of

both 1- and 2-D character

2) they exist as two closely related variants

3) they show reversible intercalation of electron donors

4) they provide a useful study for the effect on electronic structure of the consequences of moving within a group of the periodic table

5) to help resolve the debate- "Is ZrTe3 an intrinsic or extrinsic semi-metal?".

5.2 Structure

This group of compounds consists of TiS_3, ZrS_3, $ZrSe_3$, $ZrTe_3$, HfS_3, and $HfSe_3$- collectively MX_3's. They form a homomorphic set of space group $P2_1/m$ with atoms at 2(e), and are usually represented by $ZrSe_3$. The synthesis and identification of these crystals was originally carried out by McTaggart (1968), McTaggart and Wadsley (1958), Bear and McTaggart (1958), and Kronert and Plieth (1965). To date, all three chalcogenides of Zr and Hf exist but only one (the sulphide) for Ti; although $HfTe_3$ has not yet been grown as a good enough crystal for detailed structure refinement determinations.

These monoclinic crystals contain 2 formula units per unit cell, with "chains" running through the crystal in the crystallographic 'b' direction; the two chains in a unit cell are displaced by half the unit cell parameter in the 'b' direction. The metal atoms within the chain are coordinated to 6 chalcogens in a trigonal prismatic arrangement, as shown in fig. 5.1. The large interatomic spacings between units cells in the 'c' direction gives a van der Waals gap, and the 1-D character is to some extent suggested by the spacing along the 'a' direction. The gap in the 'c' direction is clearly large enough to justify the description of these crystals as layered (ie. 2-D), but the 'a' gap and resultant chains also prompts the use of the term quasi-1-D, which is shown to be a useful description by experimental results of transport properties.

Two of the chalcogen atoms (X_{ii} and X_{iii}) have a bond length small enough to be considered as a single ligand to the metal, and this transpires to be a very useful aid to analysis of physical properties, as outlined below. Some workers (eg. Jellinek 1974; Schairer and Schafer 1973) have reported nonstoichiometric crystals in which this ligand pair is replaced by a single chalcogen atom- although others (McTaggart and Wadsley, 1958; Furuseth et al., 1975) find crystals with the stoichiometric ratio 1:3 accurate to within experimental

Fig. 5.1 MX_3 Type A

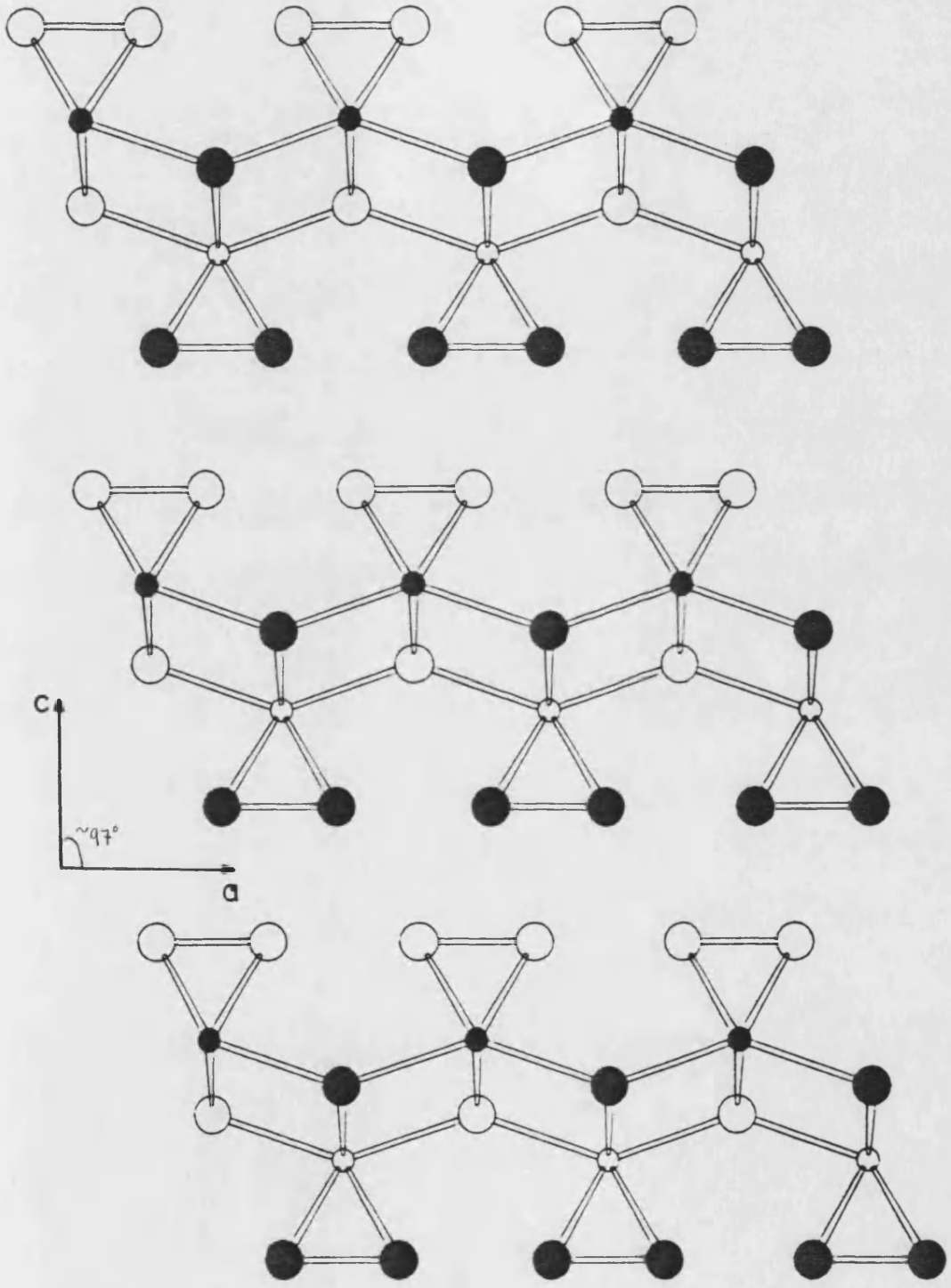

Small Circles metal , Large Circles chalcogen

Filled b=1/2, Empty b=0

limits. Thus it would appear possible to grow these crystals chalcogen deficient- but there is no necessity to do so.

Furuseth et al. (1975), analysing X-ray data, were surprised to discover two closely related variants of the $ZrSe_3$ structure. Initially type A was identified with $ZrSe_3$ and type B with TiS_3, but closer examination revealed that crystals may appear as both variants or even twinned with one crystal(lite) showing both types. The occurrence of both variants for a given material suggest a small free energy difference between the two variants- this idea is further reinforced since the average bond lengths are almost identical. Tables 5.1 and 5.2 show the unit cell vectors and atom positions for the 6 MX_3's studied here. It can be seen from these that there exists a simple relationship between variants A and B- to a good approximation the x lattice parameter becomes 1-x for the other variant. Because of the monoclinic angle (97-98^0) perfect left/right hand symmetry is not preserved by this operation. This introduces some interesting and fundamental differences between the two variants. The variations in atomic spacings for the two variants are shown in table 5.3, taken from Furuseth et al., 1975. Here it can be seen that the two chalcogens X_{ii} and X_{iii} are no longer equidistant from the metal atom in the B variant in

Table 5.1 MX_3 lattice parameters

$ZrSe_3$ structure, monoclinic, C_{2h}^2—P $2_1/m$ (No. 11), $Z = 2$.
All atoms in 2(e): $\pm(x, \frac{1}{4}, z)$

Compound	a(Å)	b(Å)	c(Å)	β(°)
TiS_3	4.973	3.433	8.714	97.74
	4.958	3.400 6	8.778	97.32
ZrS_3	5.123	3.627	8.986	97.15
	5.124 3	3.624 4	8.980	97.28
$ZrSe_3$	5.410 9	3.748 8	9.444	97.48
$ZrTe_3$	5.893 9	3.925 9	10.100	97.82
HfS_3	5.100	3.594	8.992	98.16
	5.092 3	3.595 2	8.967	97.38
$HfSe_3$	5.388	3.721 6	9.428	97.78
$HfTe_3$	5.879	3.902 2	10.056	97.98

Table 5.2 MX_3 structure refinement parameters

Compound	x(M)	z(M)	$x(X_I)$	$z(X_I)$	$x(X_{II})$	$z(X_{II})$	$x(X_{III})$	$z(X_{III})$
Type A								
ZrS_3	0.716 3	0.344 7	0.236 9	0.445 7	0.527 5	0.828 4	0.120 1	0.830 1
$ZrSe_3$	0.715	0.343	0.236	0.447	0.545	0.825	0.112	0.831
HfS_3	0.716 1	0.345 2	0.238 9	0.445 4	0.535 8	0.829 8	0.123 2	0.830 3
Type B								
TiS_3	0.284 8	0.347 2	0.760 8	0.449 5	0.468 0	0.823 8	0.879 5	0.826 3
$HfSe_3$	0.285 5	0.343 7	0.763 0	0.446 7	0.454 5	0.826 7	0.888 7	0.832 7
$ZrTe_3$	0.293 1	0.334 0	0.760 9	0.443 9	0.433 9	0.832 4	0.903 7	0.838 4

$x_B = -x_A$, $y_B = y_A$, $z_B = z_A$.

Table 5.3 Interatomic distances (au).

	TiS_3		ZrS_3		$ZrSe_3$		$ZrTe_3$		HfS_3		$HfSe_3$	
Variant	A	B	A	B	A	B	A	B	A	B	A	B
M-X_I[a]	4.65	4.73	4.91	4.99	5.02	5.11	5.60	5.73	4.90	4.98	5.10	5.19
M-X_I[b]	4.97	4.56	5.14	4.74	5.51	5.03	5.88	5.35	5.11	4.68	5.43	4.96
M-X_I[c]	4.98	5.39	5.12	5.53	5.46	5.95	6.01	6.55	5.10	5.53	5.38	5.58
M-X_{II}	4.70	5.04	4.92	5.26	5.18	5.57	5.52	5.97	4.93	5.31	5.15	5.56
M-X_{III}	4.70	4.45	4.93	4.68	5.20	4.91	5.60	5.24	4.90	4.64	5.19	4.89
X_{II}-X_{III}	3.86	3.86	3.95	3.95	4.43	4.42	5.25	5.22	3.98	3.98	4.44	4.42
X_{II}-X_{II}[d]	6.76	6.62	6.85	6.73	7.32	7.12	7.72	7.38	6.81	6.65	7.27	7.05

Key

[a] same chain

[b] same unit cell

[c] adjacent unit cell

[d] across van der Waals gap.

contrast with the A variant. Fig. 5.2 shows the atom positions within the unit cell for the B variant, and thus the reason for this change in interatomic spacings. The line connecting the metal atom and chalcogen X_i, within a trigonal prism, is almost perpendicular to the X_{ii}-X_{iii} line (which, in turn is parallel to the 'a' lattice vector) for the A variant. In the B variant the effect of x becoming 1-x results in a unit cell of much lower symmetry, and the metal-Xii and metal Xiii are dissimilar since the quasi-mirror plane (transforming x to 1-x) and the perpendicular to the X_{ii}-X_{iii} line no longer coincide. The transition from A to B type is accompanied by a decrease in dimensionality as the quasi-1-D character is emphasised by the decreased interaction along the 'a' lattice direction.

All the MX_3 crystals show a high incidence of twinning (Furuseth et al. 1975; Kronert et al. 1965; Mc Taggart et. al. 1958; Hahn et. al. 1959; Jellinek 1963). Kronert and Plieth (1965) have suggested that this may be caused by mechanical vibrations, but Furuseth et al. (1965), even with precautions to minimise disturbance, report twinning in about 10% of crystals examined.

Fig. 5.2 MX_3 Type B

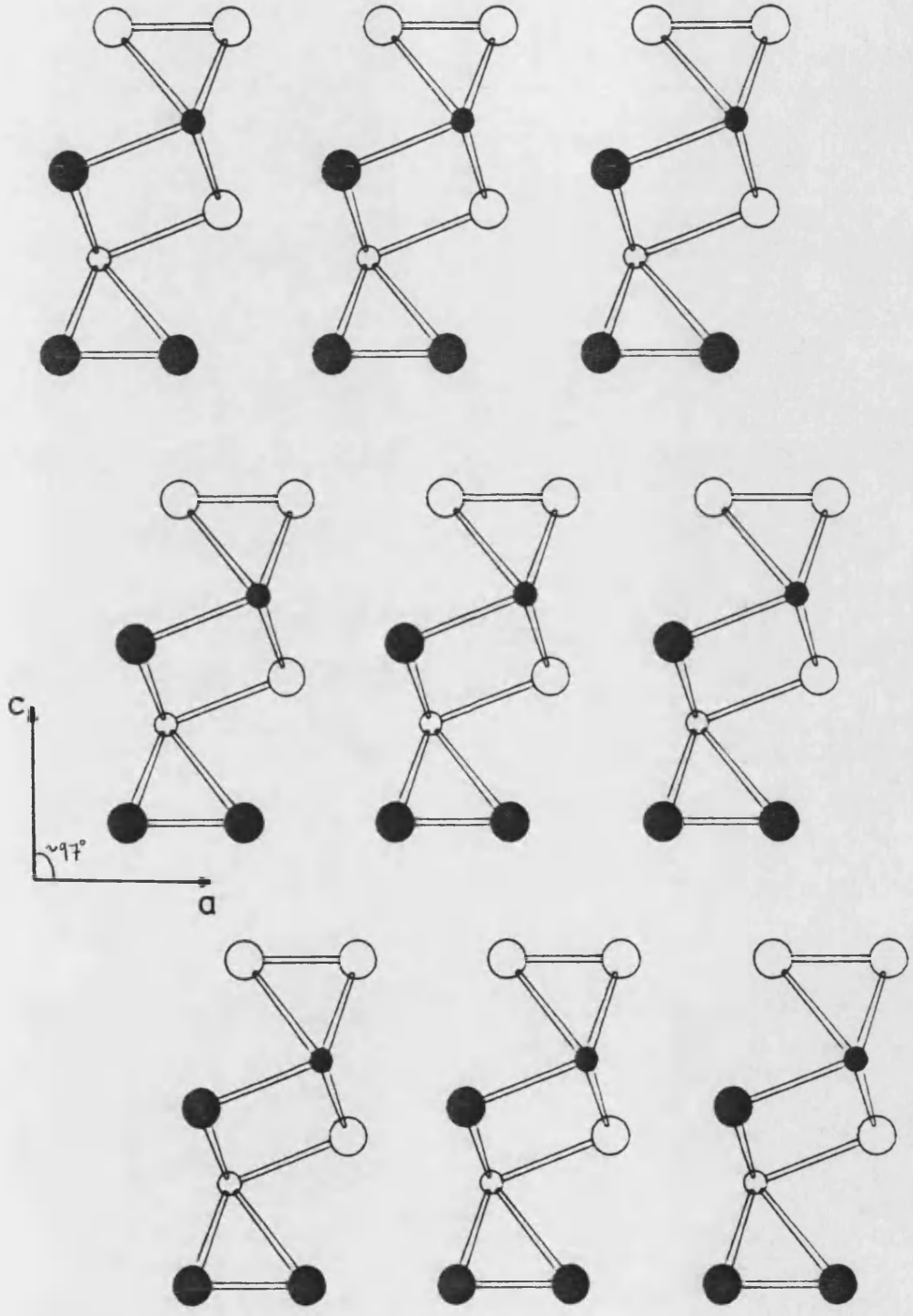

Small Circles metal , Large Circles chalcogen

Filled b=1/2, Empty b=0

The naturally occurring variants are (Levy, 1976) :-

Type A	Type B
ZrS_3	TiS_3
$ZrSe_3$	$HfSe_3$
HfS_3	$ZrTe_3$

5.3 Simple bonding model.

Comparisons of the photoelectron spectra of the di- and tri-chalcogenides have reinforced the Jellinek (1974) X_{ii}-X_{iii} ligand interpretation of the MX_3 electronic structure. They proposed a correlation diagram based on a simple molecular orbital (m.o.) picture to account for the spectra due to the X_{ii}-X_{iii} pairs. The spectra show slightly higher binding energies for the ligand bond pair than for the isolated chalcogen (X_i), suggesting that this pair may be covalently bound- while the X_i electron's binding energy closely approximate the value found for the related MX_2's.

Figure 5.3 is a schematic for the m.o. of the bonded pair of chalcogens in which the s bonding and antibonding orbitals ($\sigma_g(s)$, $\sigma_u^*(s)$) are fully occupied. The $s\sigma_g$ orbital will overlap with the metal s,p and d orbitals to form a broad band while the $\sigma_u^*(s)$ has 'edge-on' coordination with the metal atoms and thus orbitals of Π symmetry and can therefore combine only

Fig. 5.3 Schematic molecular orbital

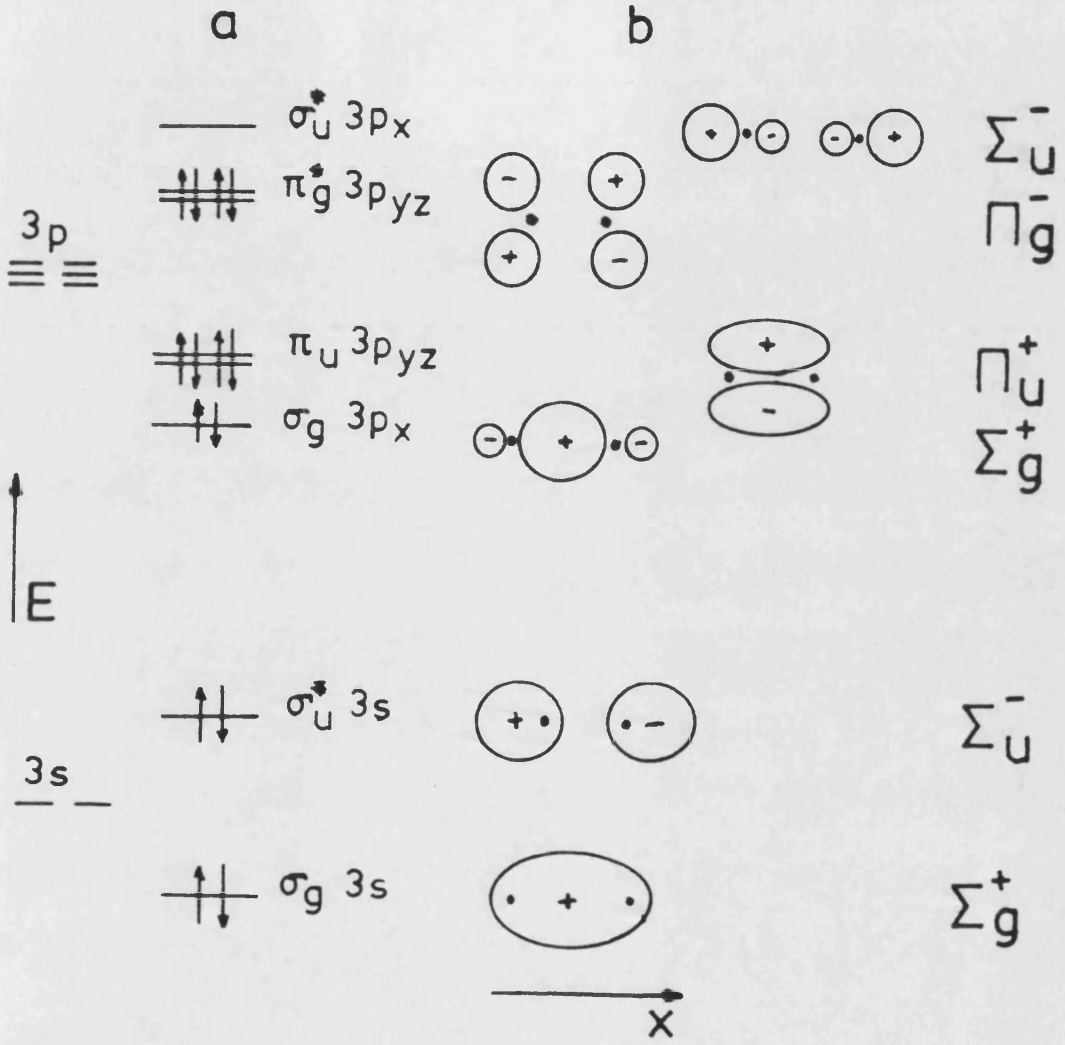

Molecular orbitals for a S_2^{2-} ion.

Ion axis is along x direction.

a) energy levels and occupation

b) symmetry of the molecular orbitals.

with p and d orbitals- producing a narrower band. Moving to higher energies, the chalcogen p orbitals mix with the metal orbitals to result in the band forming the top of the valence band- with the 'molecule' parallel to the x axis the anti-bonding p orbital (σ_u^* p_x-p_x) is proposed to lie above the fermi level. The molecular Π bonding orbitals are less displaced from their free atomic values and are thus filled (ie. below E_f). Again 'edge-on' coordination determines the chalcogen-metal bonding symmetry. The σ_g (p_x) and Π_u (p_{xy}) combine with σ symmetry with respect to the metal atom s,p and d orbitals and, as a result, give broad bands at the top of the valence band. The Π_g^* (p_{xy}) forms narrower bands since it is more restricted in its bonding possibilities- orbitals of Π symmetry only (ie. with metal p and d). This picture of a covalent semiconductor for the MX_3's is supported by Haraldsen et al (1963) backed by evidence of crystal growth from the vapour phase (eg. McTaggart and Wadsley, 1958) and from conductivity measurements (eg. Grimmeiss et al., 1961). Many workers have adopted this simple m.o. diagram to account for experimental results (Khumalo and Hughes (1980), Zhao et al. (1982)).

5.4 Dichroism and excitons

Some investigations seeking dichroism in the MX_3 compounds failed to reveal any difference between light polarised parallel to the b axis (E//b) and perpendicular (E⊥b) to it (Adachi et al., 1980). Dichroism is expected to be clear in these monoclinic layered crystals (Khumalo and Hughes, 1980). The absence of dichroism may be attributed to the polycrystalline nature of the samples, especially at higher photon energies where the bulk structure is being probed. Twinning in the [100] direction (Kronert and Plieth, 1965) will also act to 'dilute' any dichroism. However Schairer and Schafer (1973) have reported the existence of dichroism in $ZrSe_3$ and $HfSe_3$ (which distinguishes them from the dichalcogenides).

Two factors have led spectroscopists to believe in an excitonic spectrum for the MX_3 compounds:-

i) the failure of the absorption edge to be fitted by power laws for band to band transitions (Knox, 1967)

ii) an obvious peak at the end of the absorption edge.

This excitonic edge makes it difficult for spectroscopists to estimate the band gaps in these

materials but, for ZrS_3 and HfS_3, Schairer and Schafer (1973) predict semiconductors with direct, allowed optical band gaps. In contrast Kurita et al. (1981) conclude that ZrS_3 and $ZrSe_3$ have indirect semiconducting gaps- eg. ZrS_3 has an indirect exciton gap of 2.085 eV for $E \perp b$ and 2.055 eV for E//b, compared with a direct gap of 2.56 eV. Unfortunately in analysing their data they refer to Myron et al. (1981) who have published an electronic band structure for $ZrSe_3$ which is erroneous since the $\underline{k}$ space vectors are incorrectly defined. In $ZrSe_3$ Kurita et al. (1981) found a direct transition allowed for E//$\underline{b}$ only, at 1.81 eV. The exciton indirect band gap value of 1.535 eV has a negligible polarization dependence. Khumalo et al. (1981) found exciton-like peaks at 1.78 eV and 2.1 eV for E//$\underline{b}$ and 1.80 eV for $E \perp \underline{b}$ for $ZrSe_3$, attributed to optical excitation in the X_{ii}-X_{iii} pairs. Predating the above results is Jellinek (1974) who, for $ZrSe_3$, found exciton peaks at 1.78 eV and 1.95 eV (E//$\underline{b}$) and 1.92 eV ($E \perp \underline{b}$) from optical absorption spectroscopy. The nature of the excitations given can be seen in fig. 5.4. This shows the effect of spin-orbit coupling on the X_{ii}-X_{iii} pairs. and the allowed transitions for light polarised with respect to the $\underline{b}$ axis. Spin-orbit coupling splits the $^3\Pi_u$ state into three non-degenerate states. The two types of transition are shown:-

Fig. 5.4 Spin-orbit coupling

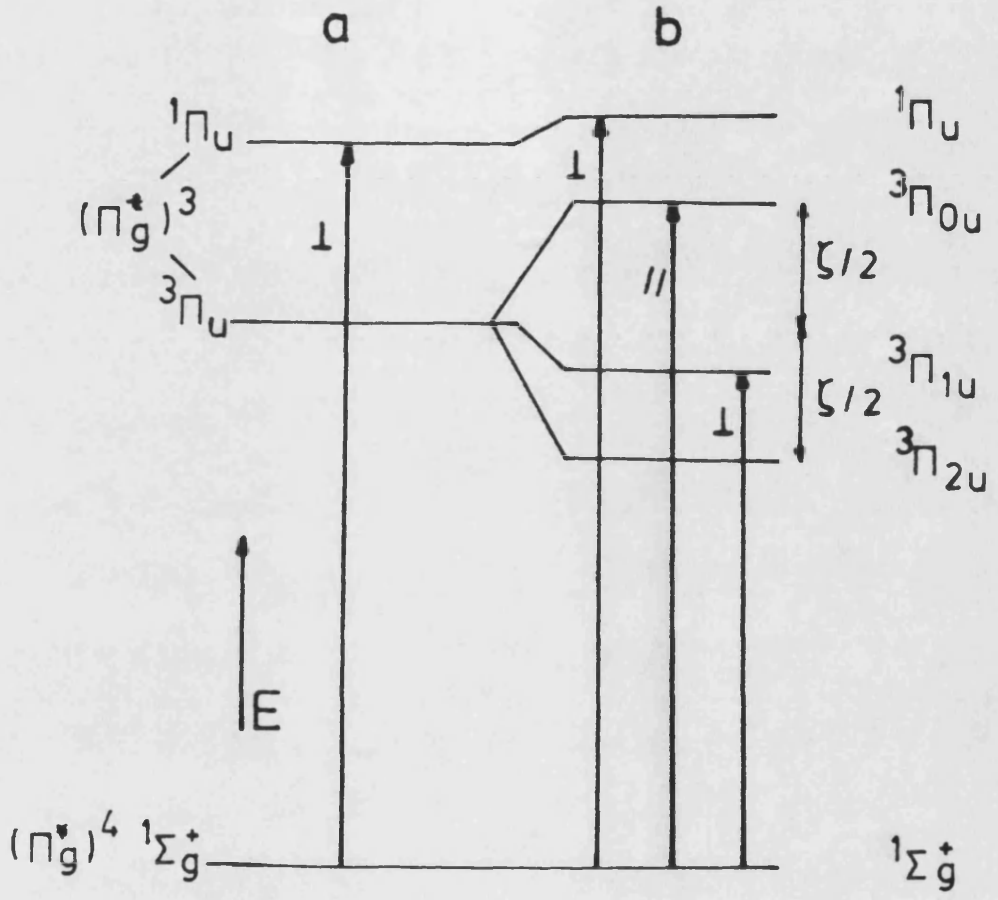

Energy levels resulting from spin-orbit coupling in a Se_2^{2-} ion.

Polarization is with respect to the ion axis.

a) without spin-orbit coupling

b) with spin-orbit coupling.

i) the spin-forbidden transition $^3\Pi_{0u} \leftarrow {}^1\Sigma_g^+$ for photons polarised // to the bond axis

ii) the spin-forbidden transition $^3\Pi_{1u} \leftarrow {}^1\Sigma_g^+$ and the spin-allowed transition $^1\Pi_u \leftarrow {}^1\Sigma_g^+$ for photons polarised $\perp$ to the bond axis.
(Note that the bond axis is along a).

Further support for the m.o. model comes from the work of Myron et al. (1981) who found the band gap extremely sensitive to the Se-Se bond length in $ZrSe_3$. Increasing the Se-Se distance by just 5% caused the σ^*_u (p_x-p_x) conduction bands to fall- reducing the band gap from 1.3 Ev to 0.8 eV.

5.5 The valence bands

Table 5.4 shows the main features of the upper valence band of the electronic structure of $ZrSe_3$, ZrS_3, $ZrTe_3$ and $HfSe_3$ from various sources. Similar results are shown for the relevant MX_2's- this is in the belief that the 'lone' X_i atom in MX_3 will closely resemble that in MX_2- thus providing a useful tool to analysis of the features listed. $ZrTe_3$ can be seen to deviate from the general trend in that it has only 3, rather than 5, features in this region and is thus dealt with in a separate section below. Using the ordering of energies

Table 5.4 MX_3 valence band features.

Electron distribution curve (EDC) peaks and upper valence band width (W).

EDC peak (eV)	A	B	C	D	E	W(eV)	reference
$ZrSe_3$ (UPS)	-1.2	-1.9	-3.1	-4.2	-5.1	5.8	Zhoa et al., 1982
$ZrSe_3$ (XPS)	-1.5		-3.4		-5.0	6.5	Jellinek,1974
$ZrSe_3$ (theory)	-1.2	-2.3	-3.2	-3.8	-5.1	5.8	Myron et al., 1981
$ZrSe_3$ (theory)	-1.2	-2.1	-3.0	-3.8	-5.0	6.0	Bullett, 1979
$ZrSe_2$ (UPS)	-1.6	-2.9		-4.1	-4.8	5.5	Shepherd et al., 1974
$ZrSe_2$ (XPS)		-2.0	-3.0	-4.0		5.8	Jellinek, 1974
ZrS_3 (UPS)	-1.0	-1.9	-3.0	-4.1	-5.2	6.1	Zhao et al., 1982
ZrS_3 (XPS)	-1.4			-4.4	-5.4	6.5	Jellinek, 1974
ZrS_2 (UPS)		-1.8	-3.1	-3.9,-4.5		5.5	Shephered et al., 1974
ZrS_2 (XPS)		-1.9	-3.0	-4.0		5.3	Jellinek, 1974
$ZrTe_3$ (UPS)	-1.5	-2.5			-4.7	5.9	Zhao et al., 1982
$HfSe_3$ (UPS)	-1.2	-2.5	-3.0	-4.4	-5.2	6.0	Zhao et al., 1982
HfS_3 (UPS)	-0.6	-1.5	-3.4	-4.6	-5.2,-5.6	6.2	Zhao et al., 1982
HfS_2 (XPS)		-1.8	-3.1	-4.0		5.7	Wertheim et al., 1973

Positions from top of valence bands, error $\pm$0.1 eV. Width error $\pm$0.15 eV.

given in the m.o. diagram earlier and comparing with the MX_2 results the main features can be identified (see Zhao et al., 1982):-

i) $ZrSe_3$ 3 peaks are assigned to the Se-Se pair thus- E σ_g, C Π_u, A Π_g^*.

ii) ZrS_3 has E σ_g, D Π_u, A Π_g^*.

iii) For the Hf compounds the picture is not so clear but it would appear that peaks A and E may be attributed to the ligand pair.

5.6 The conduction bands

A good overall picture of the conduction band features in the MX_3 compounds is given by Ohno et al. (1984). This is again in terms of the ligand pair and lone chalcogen. They place the ligand pair (X_{ii}-X_{iii}) antibonding p orbital (σ_u^*) at the bottom of the conduction band, with some hybridization of the metal orbitals. Khumalo and Hughes (1980) originally placed the highest ligand pair antibonding orbitals at the top of the valence band and well up in conduction band respectively; however in a later publication (Khumalo et al., 1981) they revise the position of the highest orbital (p σ_u^*) and place it at the bottom of the

conduction band, thus the semiconducting gap is defined by the ligand antibonding orbitals. This was in order to account for basal plane normal incidence reflectivity spectra using polarised light.

The two main effects governing differences between the relative energies of the σ_u^* chalcogen antibonding band and the metal d orbital based band are the symmetry permitted bonding possibilities and the relative energies of these orbitals. The symmetry of these crystals is obviously preserved for substitutions of the chalcogen or metal atoms (within variant A or B) but the degree of splitting of the bonding and antibonding σ orbitals decreases as a function of increasing atomic number. (eg. of X for a given M). The metal d free atom orbital energy moves up as the core size increases- ie. the outer electrons are less tightly bound. Thus, in comparing the sulphides for example, the S-S ligand pair distance is less and the metal d levels are lower in TiS_3 than in ZrS_3 and HfS_3. Thus the σ_g-σ_u^* gap is reduced in ZrS_3 and HfS_3 and the metal d based bands are higher: therefore the antibonding chalcogen bands are low compared to the metal d bands in these compounds. The effect of the two variants A and B also plays a role in the band structure of these compounds and is further discussed in the next chapter.

The sulphur K absorption spectra giving information of the chalcogen ligand pair 'molecular' orbitals can give no information of the metal d_{z^2} orbitals (which lie near the bottom of the conduction band) due to selection rules- and cannot show the degree of overlap with the ligand pair antibonding bands. The metal L_{III} absorption (Ohno et al., 1984) however appears to confirm a large degree of overlap between the σ_u^* and metal d_{z^2} orbitals for the Zr compounds.

A general picture of the conduction bands emerges with the antibonding chalcogen s(σ_u^*) bands at the bottom of the metal d bands- with a total width of 4-5 eV. The higher conduction bands of metal s character show increasing overlap with the metal d as the chalcogen atomic weight increases and metal p bands are higher still with a width of about 7 eV. The degree of metal s and d mixing is increased when moving down the periodic table, as noted previously, since the orbital energies are closer.

Khumalo et al. (1981) point out that the metal d bands are futher split (in addition to the non-bonding d_{z^2} orbital) into 2 pairs of d_{xy} and $d_{x^2-y^2}$ like bands and d_{xz} and d_{yz} like bands. This is due to the crystal field and is shown by a dip in the spectra of ZrS_3, $ZrSe_3$ and $HfSe_3$- with ZrS_3 showing a more pronounced division

between the two pairs. Khumalo et al. (1981) obtained near-normal-incidence reflectivity spectra for these MX_3 compounds from the basal faces of freshly cleaved single crystals using photons of energies in the range 3.7-30.0 eV. The analysis of these results, however, was based on a model which put the antibonding chalcogen orbital based bands at the top of the metal d orbitals. Their revised band structure (Khumalo et al., 1981) is shown in fig. 5.5 with the chalcogen p antibonding σ_u^* moved to the bottom of the conduction bands and showing little overlap with the metal d_{z^2} non-bonding band.

5.7 MX_3's and the periodic table.

A study of the MX_3 compounds can provide a useful demonstration of the consequences of moving down a column of the periodic table. Listed below are some of the predicted effects of this and how they affect the compounds studied here.

1) The first element in a column is usually atypical of a group since there is no screening from the nuclear core by a filled orbital of the same angular momentum. This effect is shown by TiS_3 compared with ZrS_3 or HfS_3.

2) The electronegativity of elements decreases moving down the columns. This acts to decrease the charge

Fig. 5.5 $ZrSe_3$-Schematic band structure

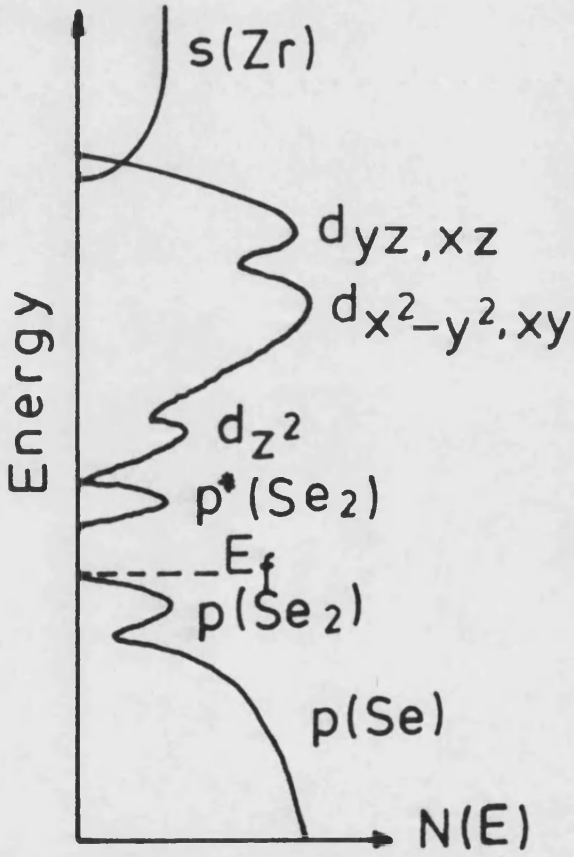

transfer to the chalcogen atoms from the metal- thereby decreasing the ligand field effect of the chalcogen pair. The smaller outer orbital radius of Ti (1.36A), compared with Zr and Hf (both at 1.51A), also acts to reduce the ligand field effect for the Ti compounds.

3) The isolated atomic orbital (n-1)d and ns energy difference decreases moving down the table. This increases the hybridization of the s and d orbitals and thus a greater s-d overlap.

4) Hf shows a lanthanide contraction of 0.21A (Pauling, 1960) as a consequence of its filled f orbital. This reduces the atomic radius of Hf to close to the value for Zr, even though their atomic numbers are 40 and 72 respectively. This accounts for much of the similarity of the Zr and Hf compounds.

Table 5.1 shows the variation in the b lattice parameter for the sulphides. It can be seen that Ti would be expected to show a larger degree of metal-metal overlap since this parameter is a measure of the metal-metal distance. However this is reversed by the increased size of the Zr and Hf atoms. Hf and Zr show greater metal-metal orbital overlaps- thus broadening the metal d/chalcogen $p\sigma_u^*$ band and metal s band in the conduction band region. This can act to reduce the semiconducting

gap if the metal non-bonding d_{z^2} band falls below the chalcogen σ_u^* band and also promotes metal d/s overlap. The increased ligand/crystal field effect for Zr and Hf will also increase the band width of the metal d manifold. It should be noted that oxygen and not sulphur is the first element in the chalcogen column- thus S does not show the 'normal anomalous' behaviour that Ti does. Te does not contain a filled f orbital and is thus a large ion. This tends to reduce the Π bonding whilst increasing the σ bonding (Coles and Caplin, 1976)- again reducing the ligand field. However the increasing atomic size of the chalcogens broadens the bands and this reduces the energy gap and increases the metal s/d overlap. This effect is demonstrated by Khumalo and Hughes, 1980) who note a shift in energies for reflectivity spectra with increasing atomic number (S-Se, 0.6 eV; Se-Te, 0.9 eV): these features are also broadened.

5.8 $ZrTe_3$

$ZrTe_3$ is an anomaly in the MX_3 group in that it appears to exhibit metallic behaviour. It normally exists as the B-type, so that the interchain interaction is reduced compared with the A type. The electronegativity difference for Zr and Te is small (1.4-2.01) compared with S (2.58) and Se (2.55) giving the metal-chalcogen

bond more covalent character- thus delocalizing the electrons which are more readily available for metallic conduction. Hall effect measurements (Takahashi et al., 1983) on $ZrTe_3$ show a negative Hall coefficient of -1.8x 10^{-3} cm^3 C^{-1} at 300K which remains fairly constant until rising sharply at about 100K. Therefore the room temperature single carrier density (electrons) of 3.5x 10^{27} m^{-3} can be compared to Cu with 7x 10^{28} m^{-3}. Weiting et al. (1981) also deduce a semi-metallic behaviour from optical excitations. McTaggart and Wadsley (1958) and Takahashi et al. (1983) quote room temperature resistivities of 2.0x 10^{-4} and 2.5x 10^{-4} Ω cm^{-1} respectively. Takahashi et al. also show the anisotropic nature of these crystals since the ratio of the conductivities along the major axes show favourable conduction mechanisms along the c^* axis at a ratio of 10:1 compared with the a and b axes. The resistance also shows a strong anomalous feature in the a-c^* plane at about 70 K- suggestive of a charge density wave (CDW) transition. Further evidence for a CDW comes from electron diffraction work (Eaglesham, 1984) where two extra spots appear at 63K; there is also a contraction in the chain direction (Herrenden-Harker, 1984). $ZrTe_3$ also shows a strong excitonic feature (Bayliss and Liang, 1981) suggesting an electron-hole coupling approach as in $TiSe_2$ (Wilson and Mahajan, 1977). One possible cause for the metallic properties of $ZrTe_3$ is

defects in the form of Te vacancies- common in tellurium compounds. This being an extrinsic mechanism permits a postulated semiconducting gap in the perfect crystal of about 1.0 eV by comparing it with the other members of the MX_3's, and taking into account the effect on the bands of the B variant (Wilson, 1985).

Chapter 6 The transition metal trichalcogenides- calculations and discussion.

6.1 Method.

Collected in this chapter are the results of the calculations for the MX_3 compounds followed by a discussion and comparison with the experimental data as given in chapter five. The densities of states (dos), projected densities of states and band structures (E v. $\underline{k}$) were found using the ab-initio method as described in chapter 2. The Herman and Skillman program produced atomic orbitals utilising the Hartree-Fock-Slater scheme with $\alpha = 0.7$ (Slater, 1974) throughout. These were then taken as solutions to the localized orbital pseudopotential equations. Three centre terms were considered negligible and thus disregarded as explained earlier, while two centre terms are taken up to an interatomic separation of 8 au. The basis set comprised chalcogen s and p and metal s, p and d valence orbitals. Thus a matrix of 42x42 was diagonalized since these crystals have 2 formula units per unit cell. Due to the limited basis set used in this method the band structure above the Fermi level must be treated with some caution, however this method has been shown to reproduce the semiconducting gaps in a variety of other transition metal compounds (eg. Bullett, 1979). The metal p orbital

was assigned an occupation of 0.2 electrons as in the elemental solid metal. The metal d orbital (which shows a strong dependence of energy to charge since this orbital is tightly bound) was calculated by achieving input and output charge consistency iteratively. Table 6.1 shows the converged input atomic orbital energies used in these calculations.

6.2 Results

The band structure (E v. $\underline{k}$) and dos are calculated within the irreducible part of the Brillouin zone shown in fig. 6.1. The data for the dos graphs (figs. 6.2-6.13 inclusive) were held in the form of a histogram of width 0.01 eV and smoothed by gaussian convolution of half width 0.09 eV. A total of 3000 points in the irreducible part of the Brillouin zone were used for each graph. The total dos is presented at the bottom of each figure, with these projections:-

i) the total metal with metal d superimposed
ii) the chalcogen X_I
iii) the chalcogen X_{II}
iv) the chalcogen X_{III}.

The main regions of interest on the graphs are labelled A-M on figure 6.2 (TiS_3), and apply to the other dos graphs.

Fig. 6.1 Monoclinic Brillouin zone.

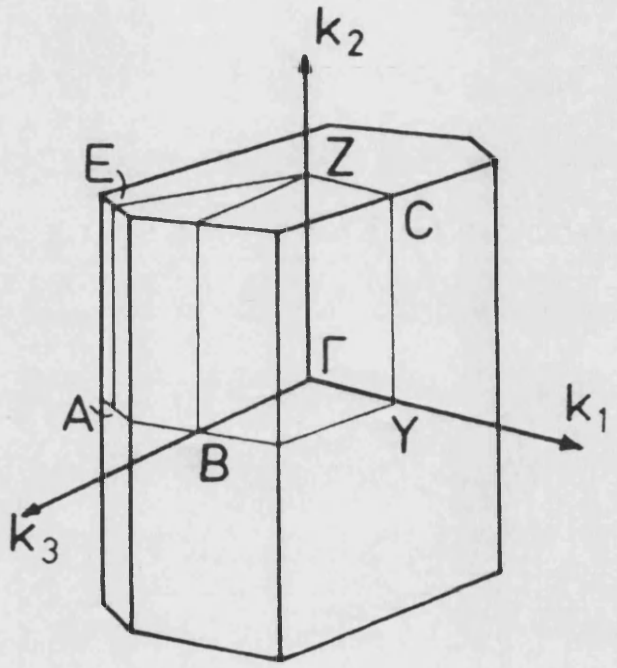

Co-ordinates of symmetry points.

	k_1	k_2	k_3
A	1/2	-1/2	0
B	1/2	0	0
C	0	1/2	1/2
D	1/2	0	1/2
E	1/2	-1/2	1/2
Y	0	1/2	0
Z	0	0	1/2

Fig. 6.2

TiS3 (Type A)

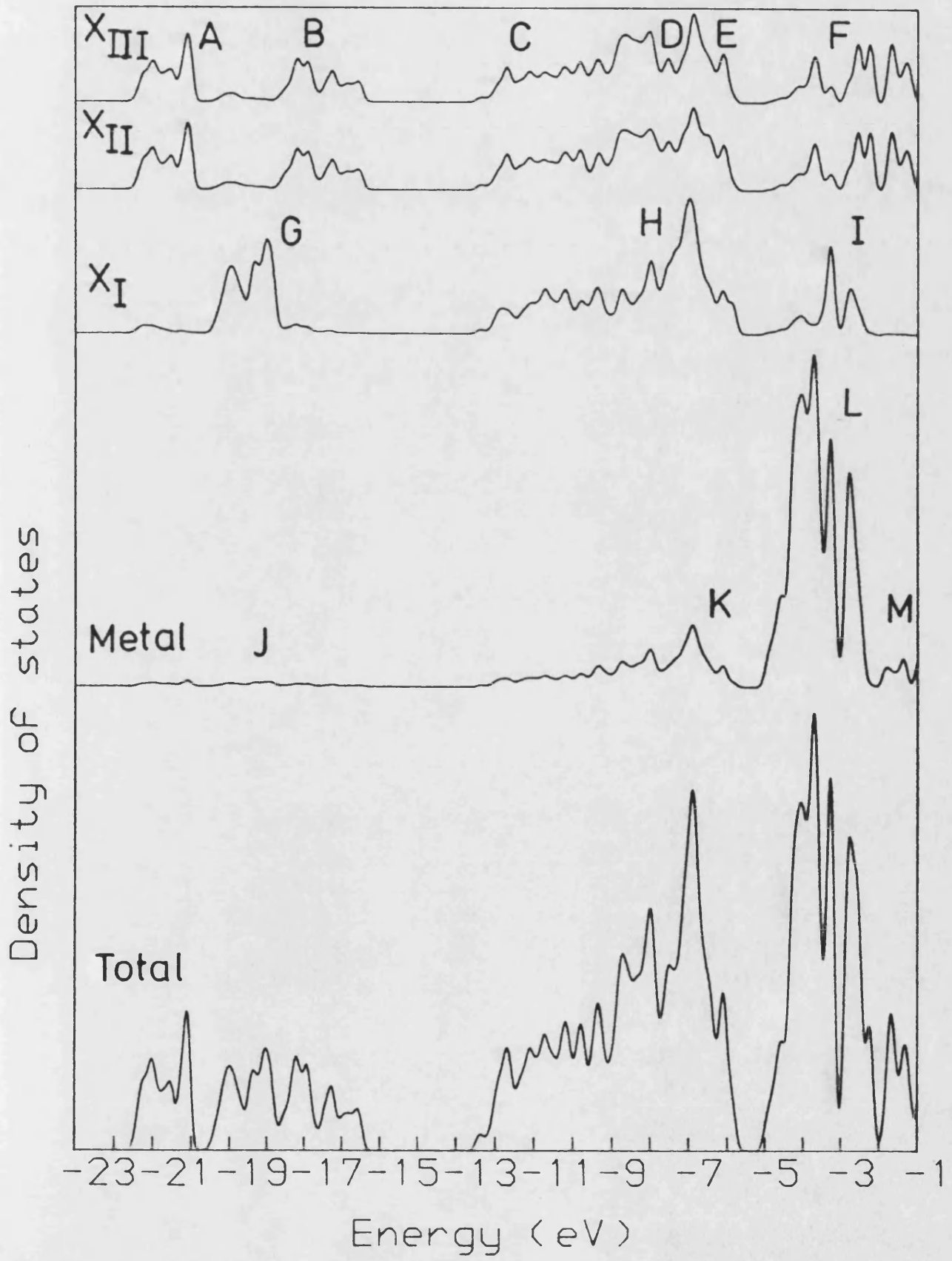

Fig. 6.3

Tis3 (Type B)

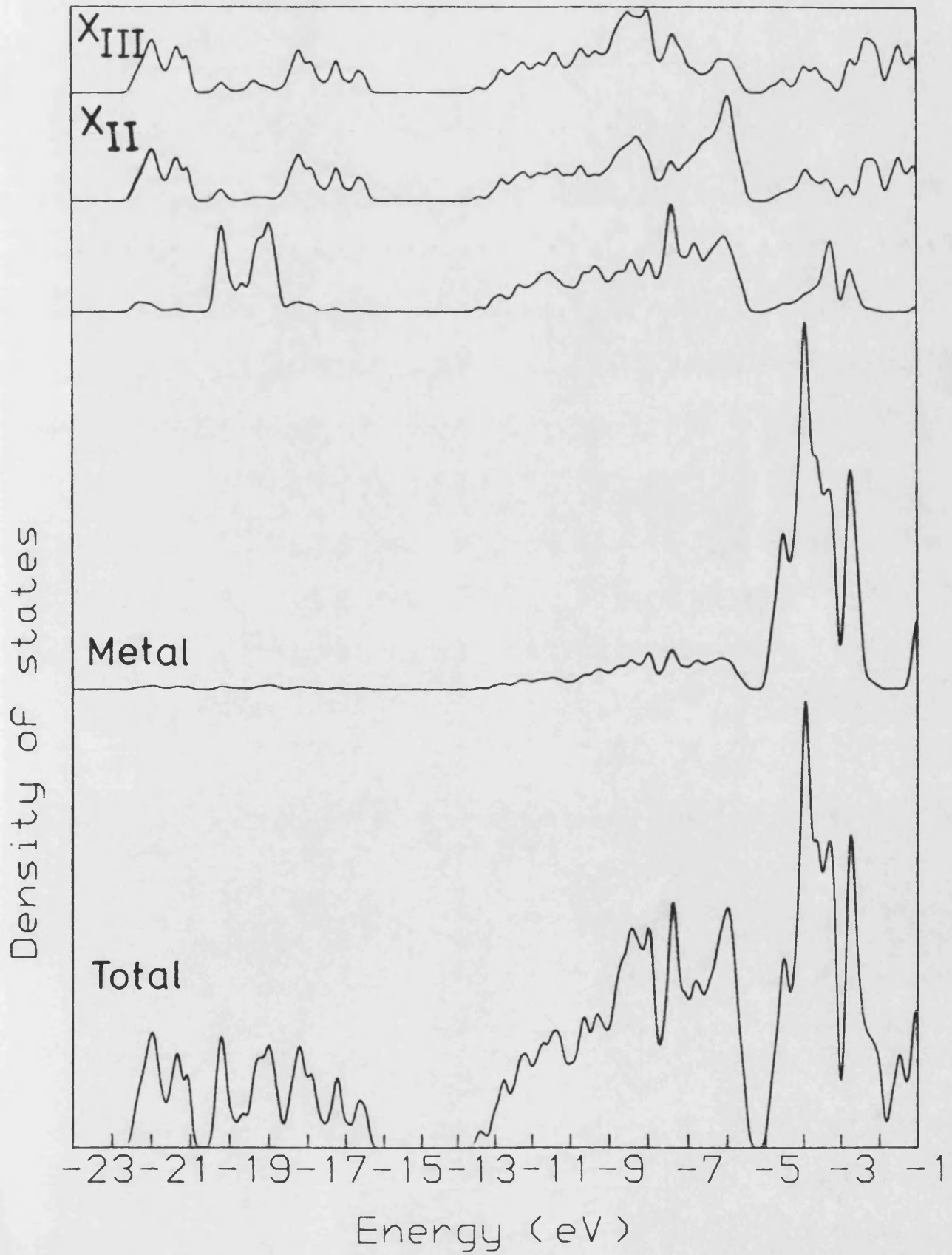

Fig. 6.4

ZrS3 (Type A)

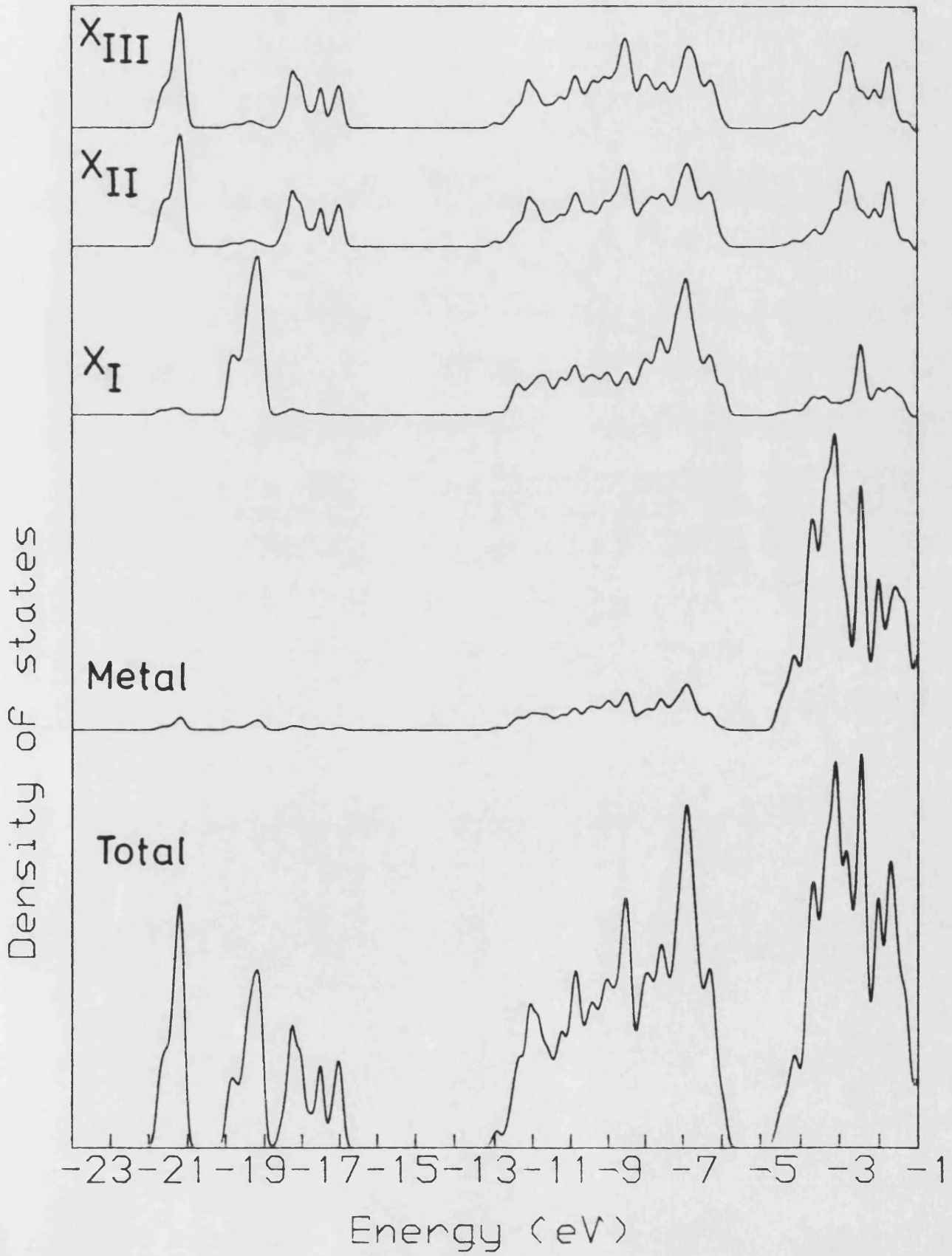

Fig. 6.5

ZrS3 (Type B)

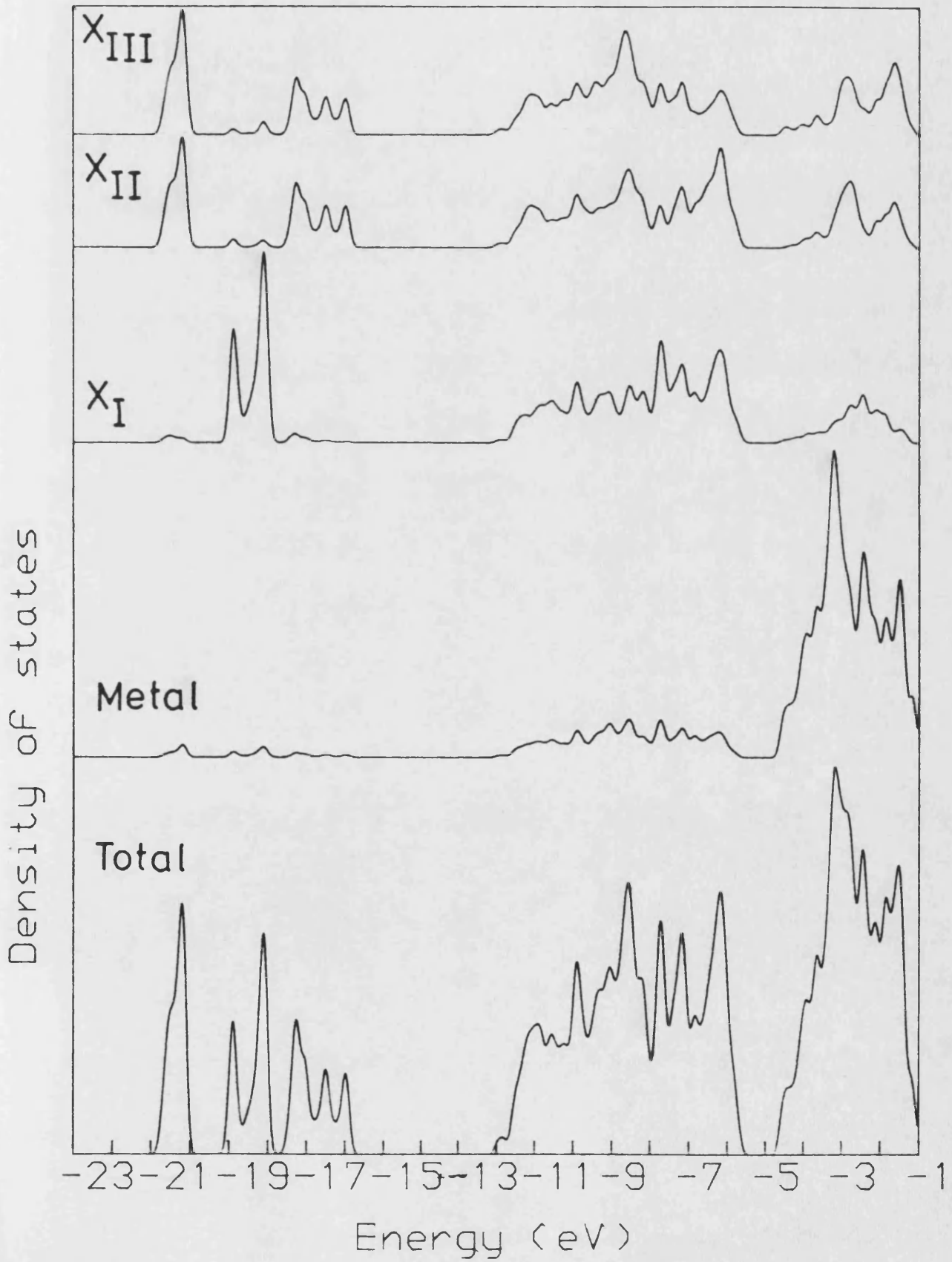

Fig. 6.6

ZrSe3 (Type A)

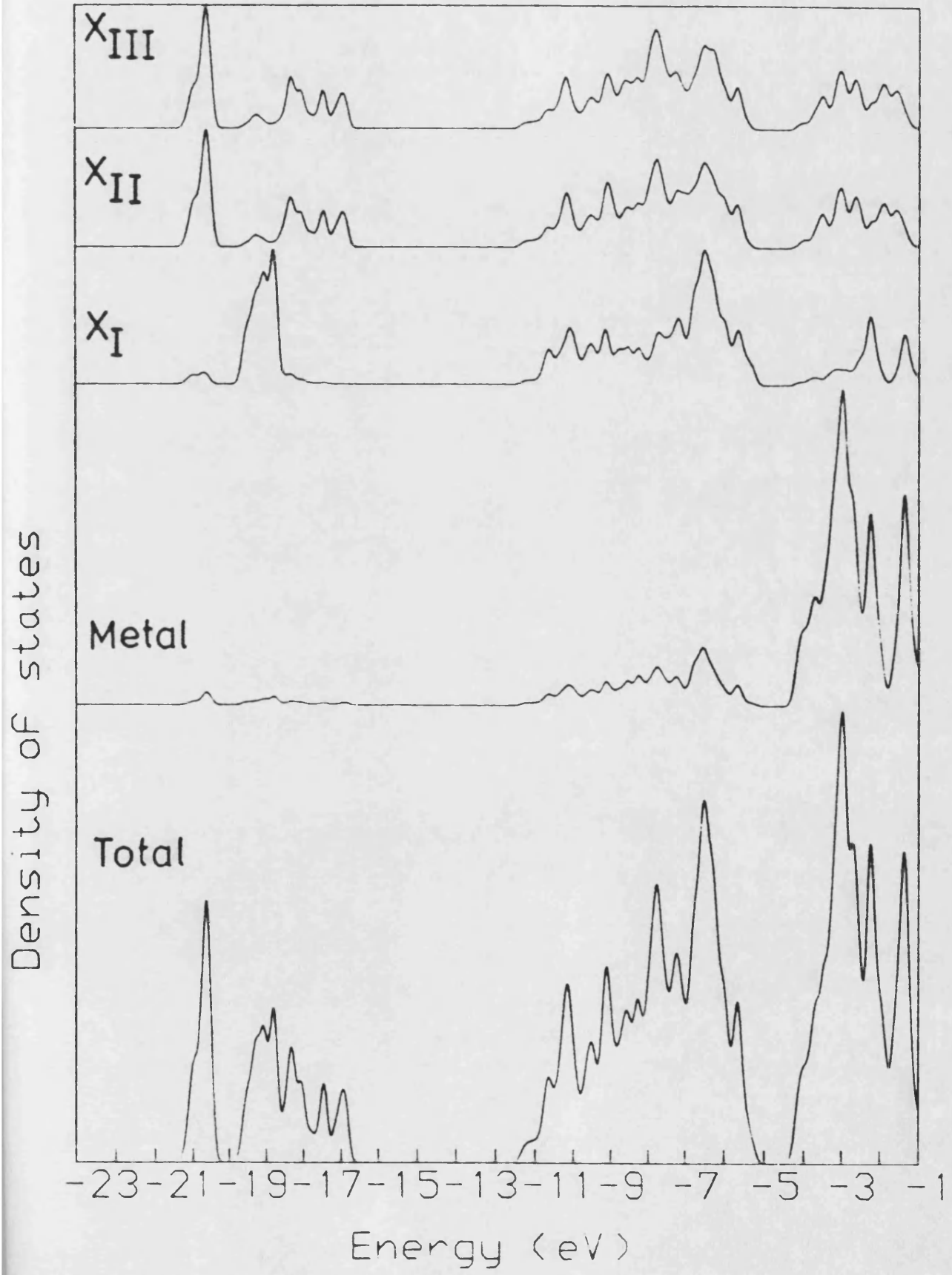

Fig. 6.7

ZrSe3 (B Type)

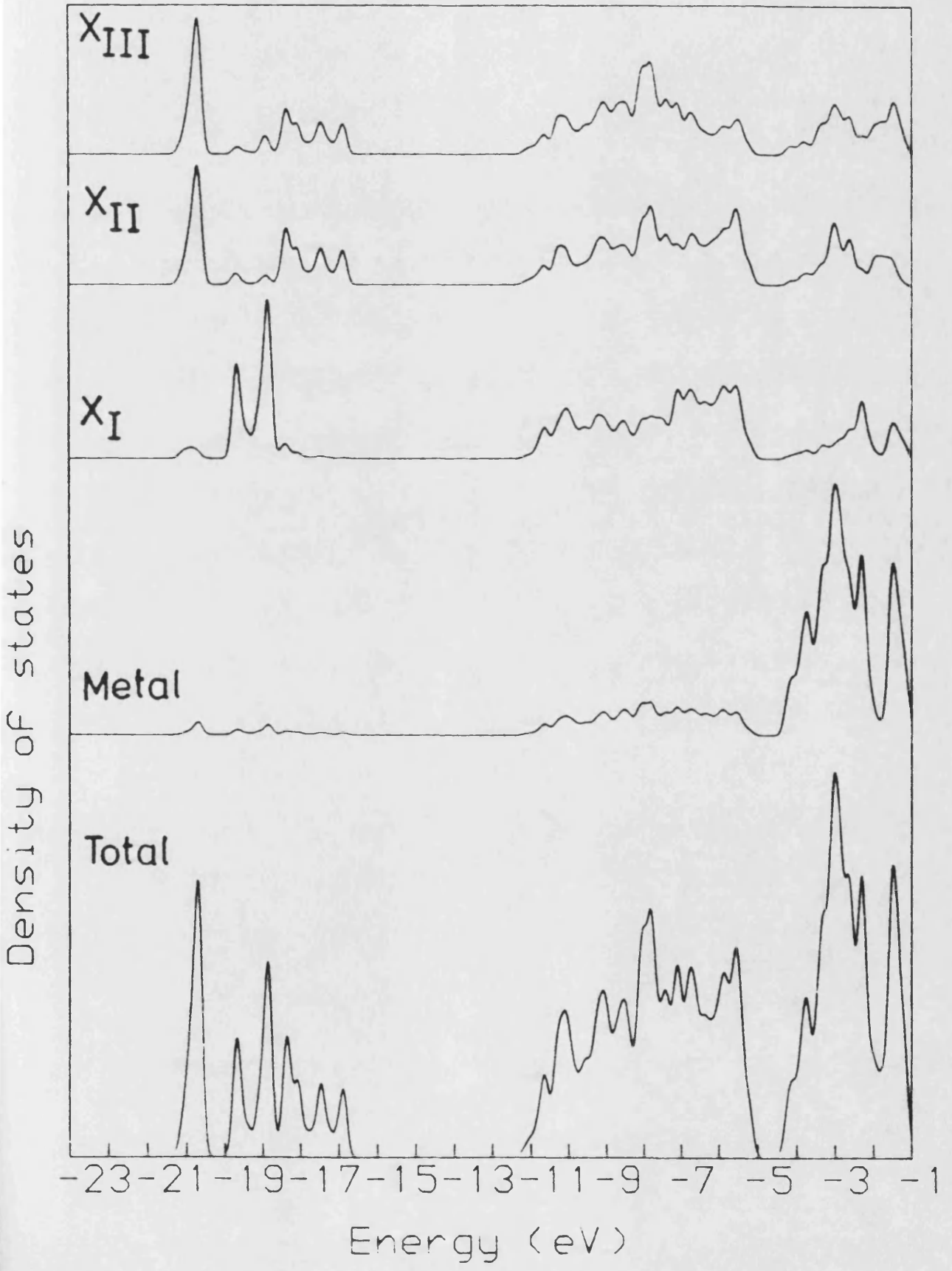

Fig. 6.8

ZrTe3 (Type A)

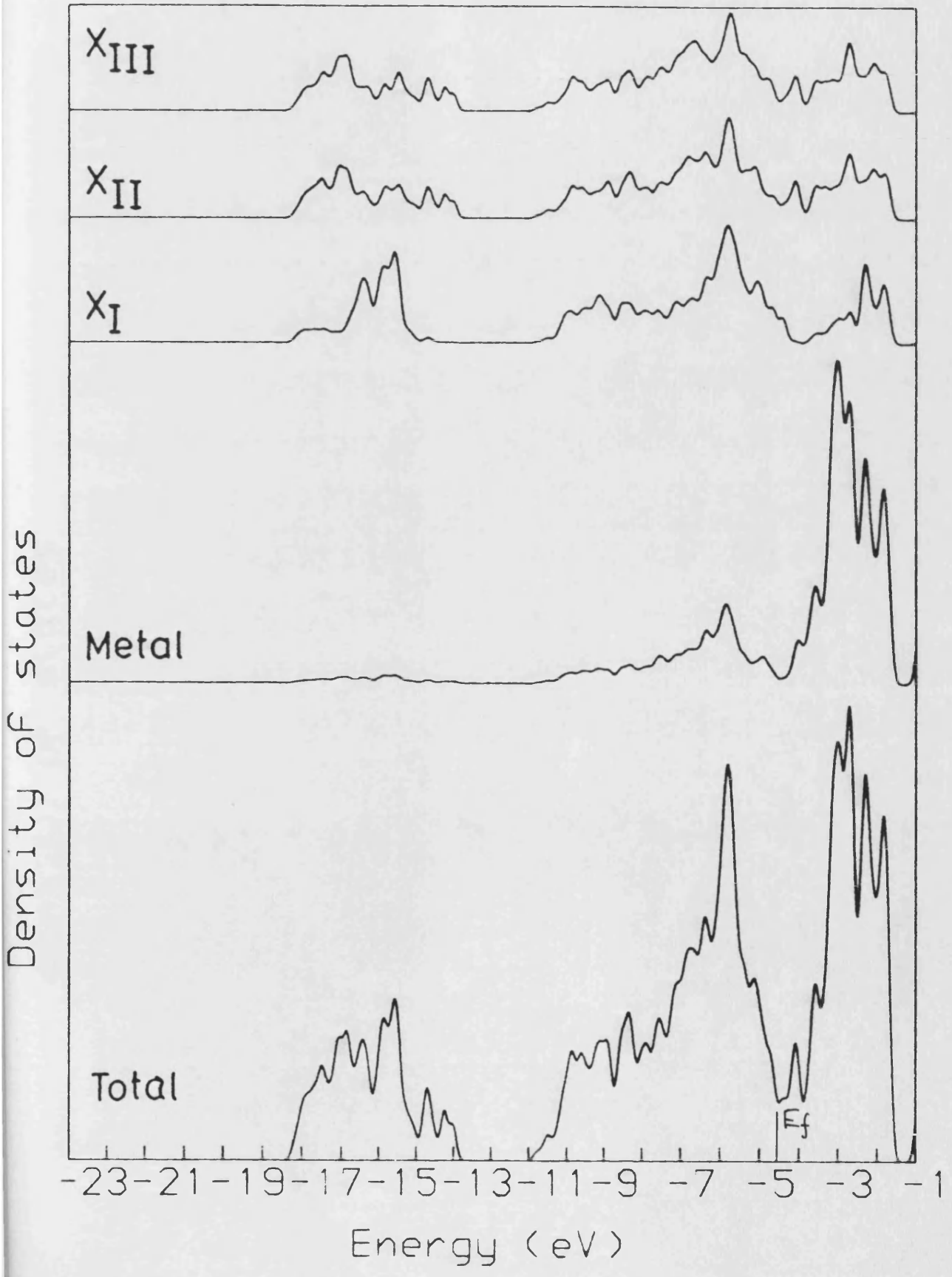

Fig. 6.9

ZrTe3 (Type B)

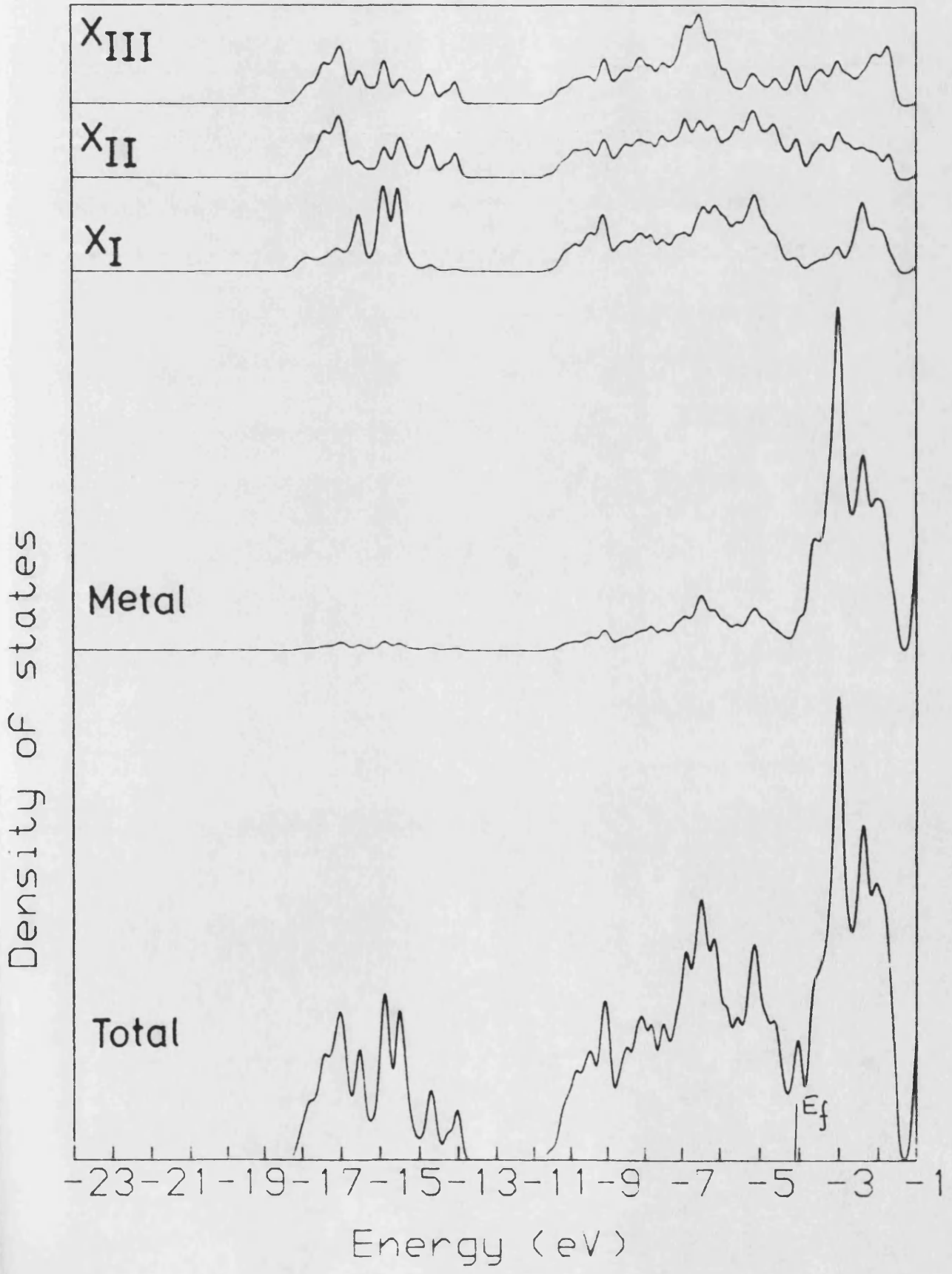

Fig. 6.10

HFS3 (Type A)

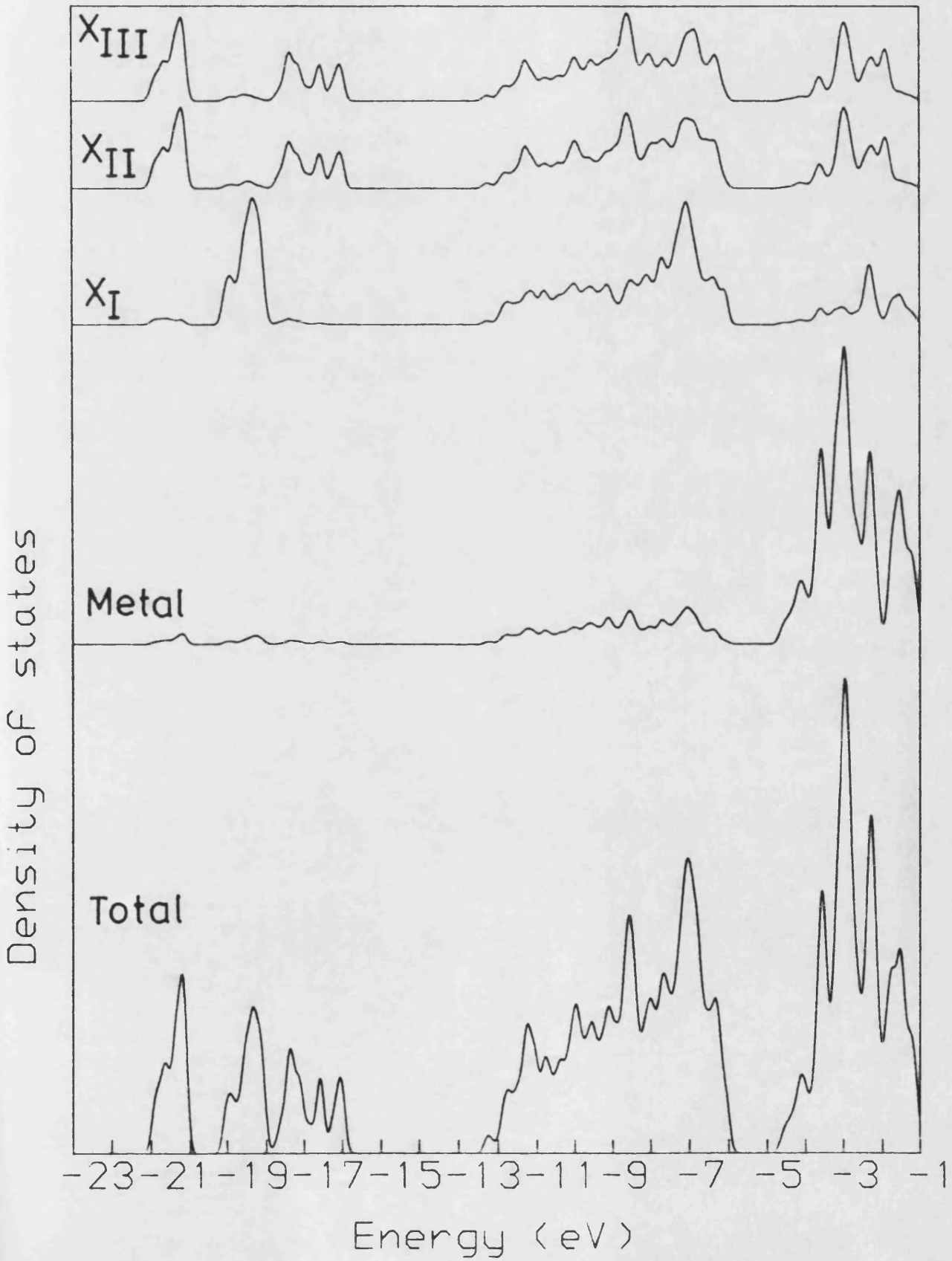

Fig. 6.11

HFS3 (Type B)

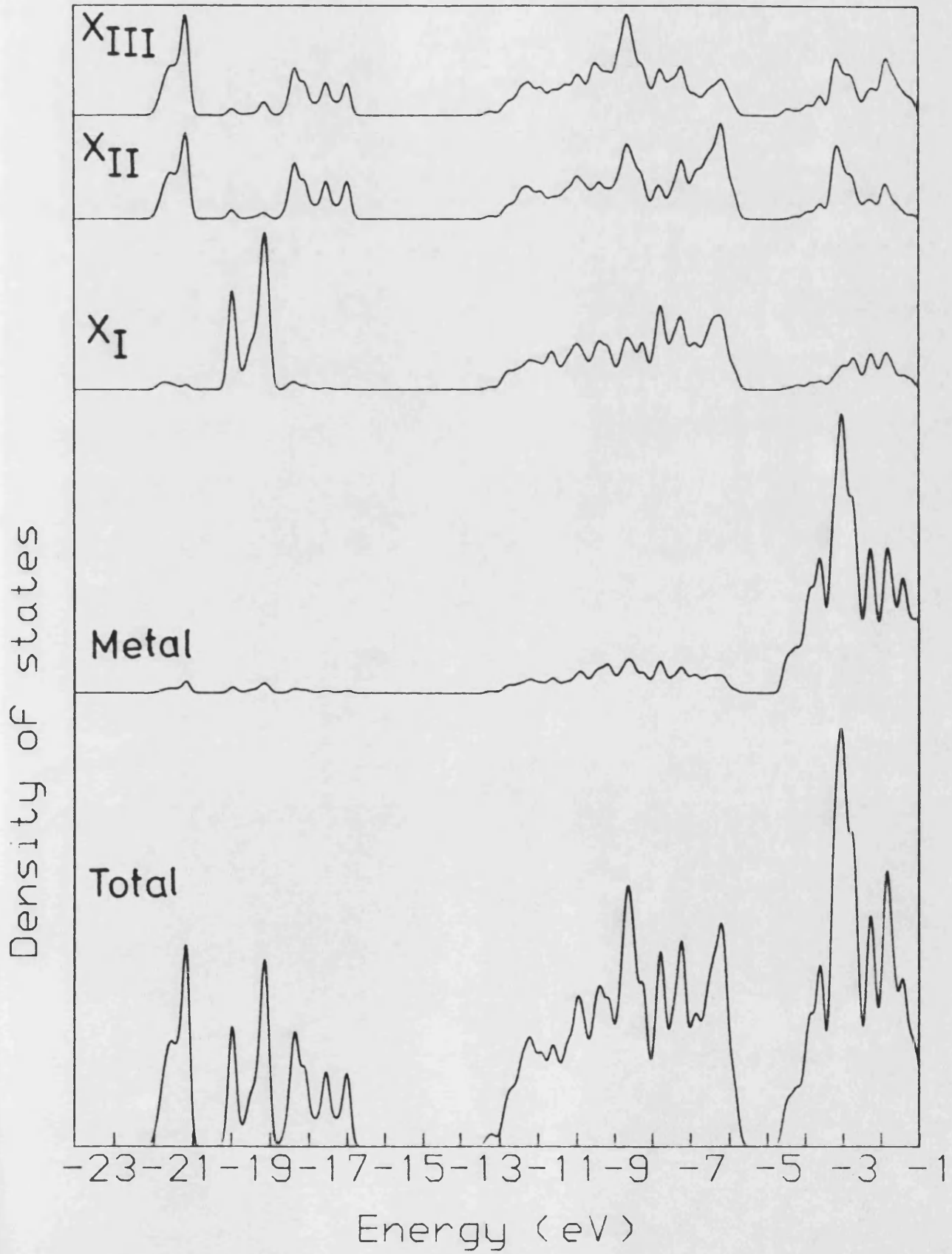

Fig. 6.12

HFSe3 (Type A)

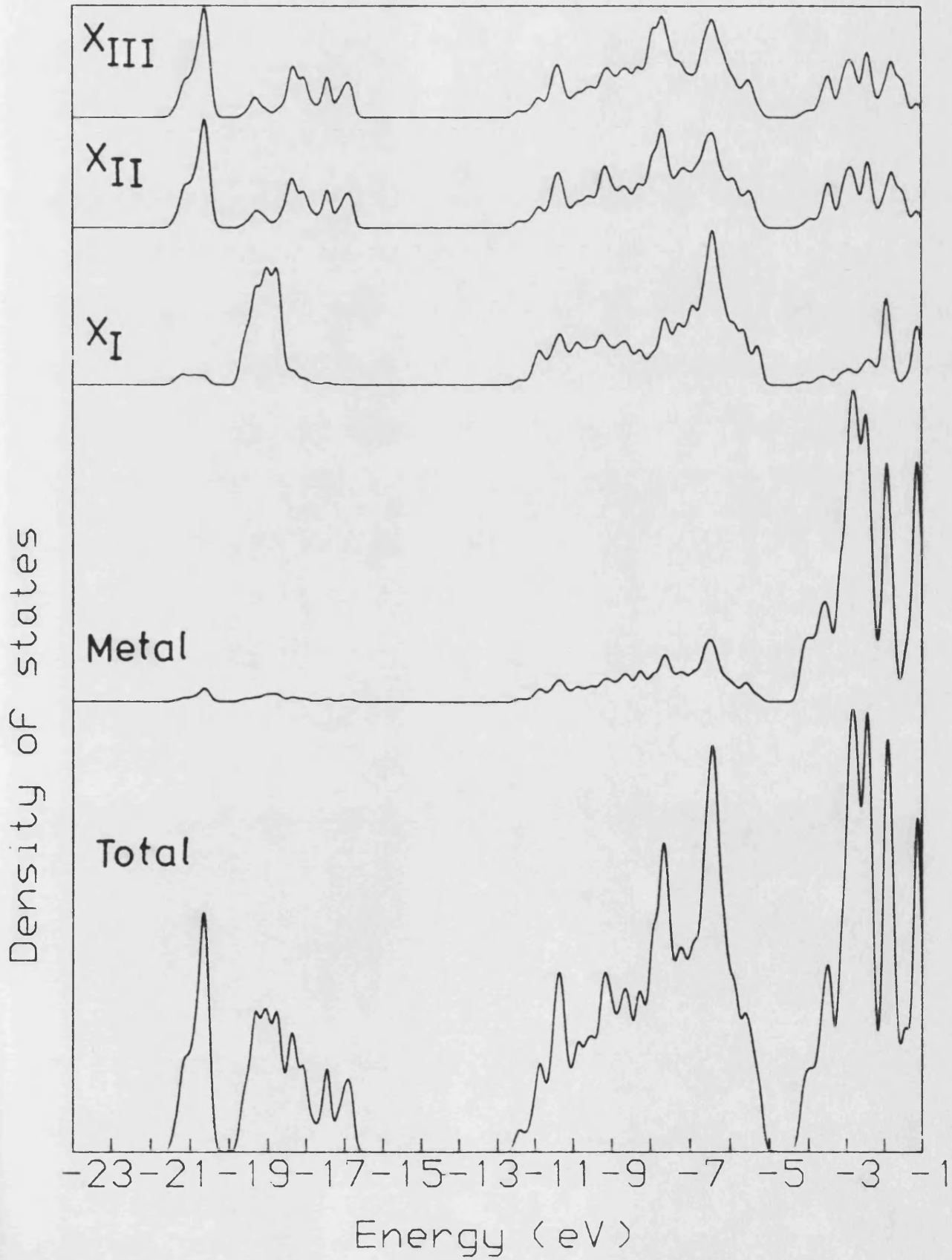

Fig. 6.13

HfSe3 (Type B)

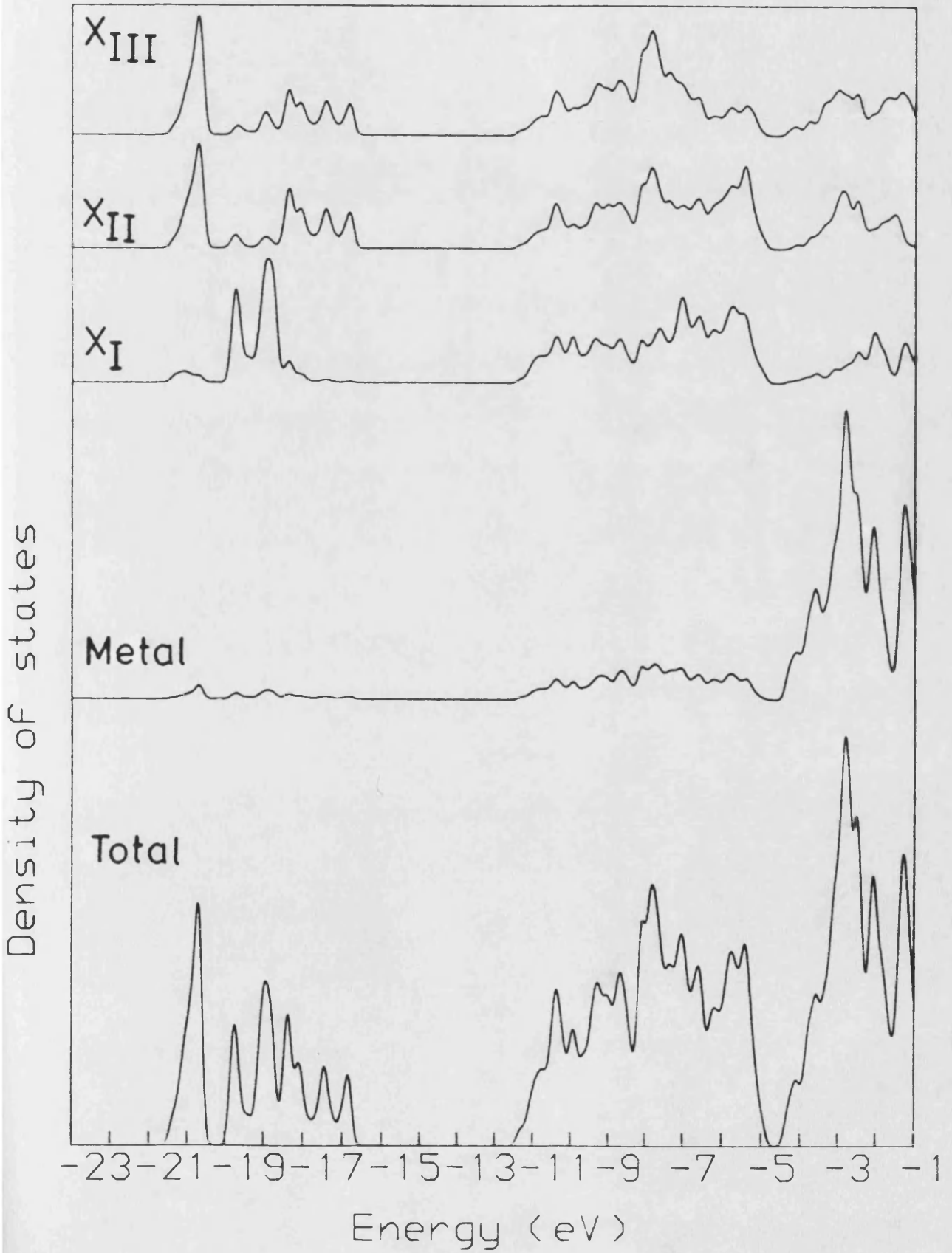

The E v. $\underline{k}$ plots (figs. 6.14-6.25 inclusive) show the bands along the high-symmetry lines of the irreducible Brillouin zone. 50 $\underline{k}$ points were used between each symmetry point (ie. a total of about 19,000 points per graph). This was in order to reduce the possibility of erroneous band crossing by increasing the resolution.

Table 5.1 from Holliger (1976) shows the unit cell and structure refinement parameters used for this work. Table 5.2 shows the interatomic distances calculated from the above parameters up to a cut-off distance of 8 au. beyond which all matrix elements are considered negligible. Table 6.2 shows the following collected data:-

i) the metal d occupation after achieving consistent input and output configurations

ii) the fermi level (highest energy occupied band) for each material.

iii) the width of the upper valence band region

iv) the difference in electronegativity of the constituent atoms

Fig. 6.14

TiS3 (Type A)

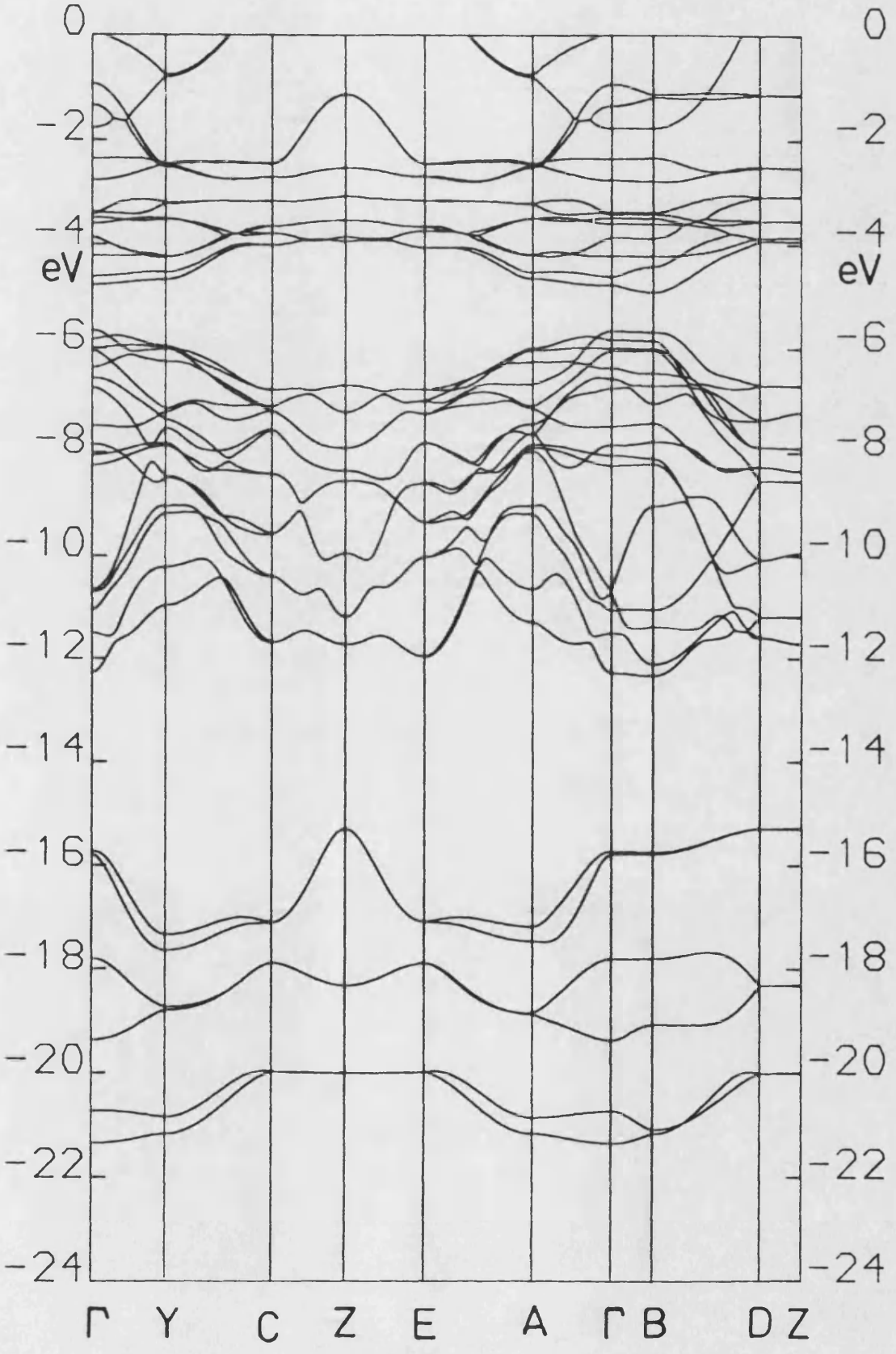

Fig. 6.15

Tis3 (Type B)

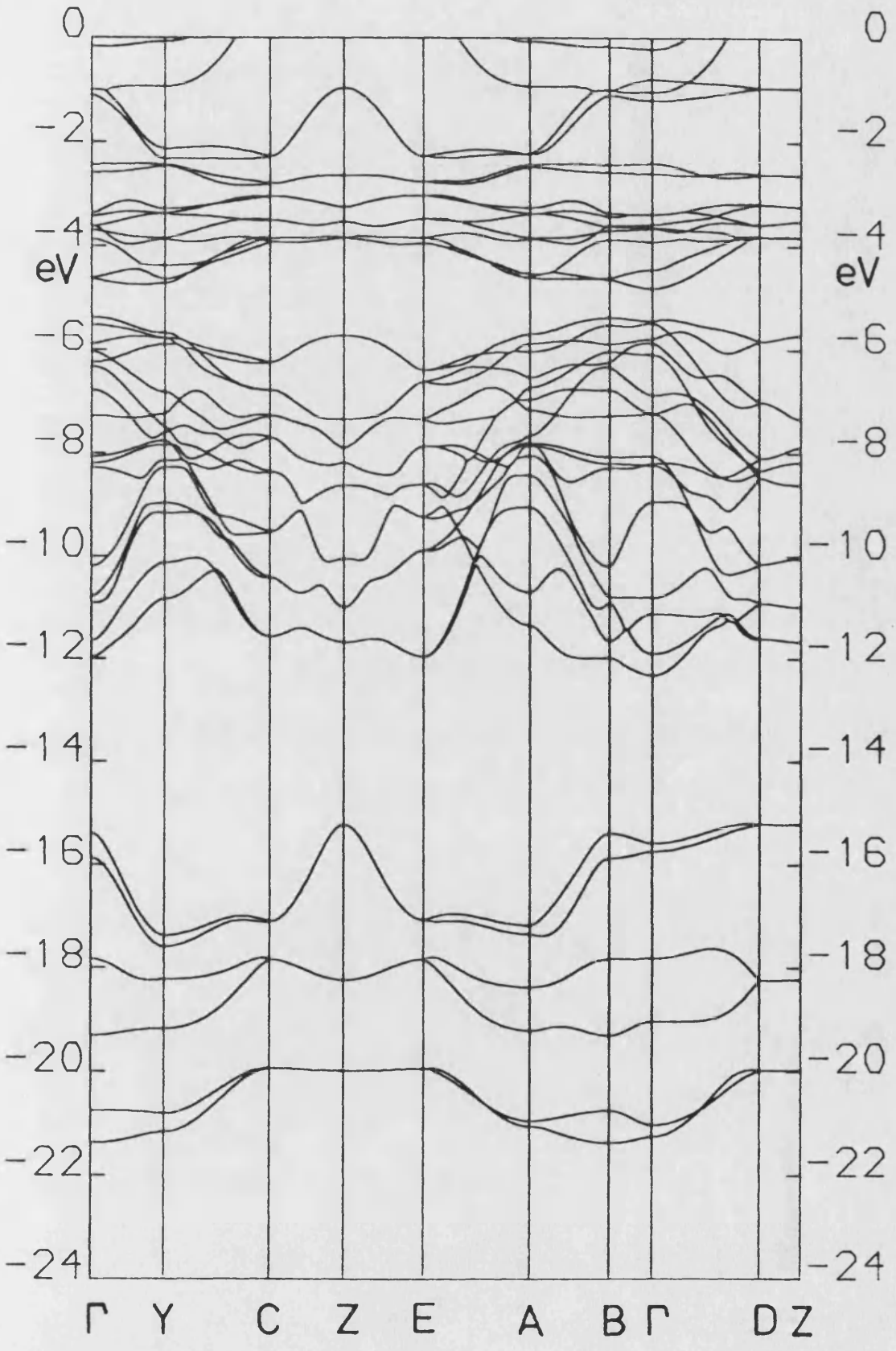

Fig. 6.16

ZrS3 (Type A)

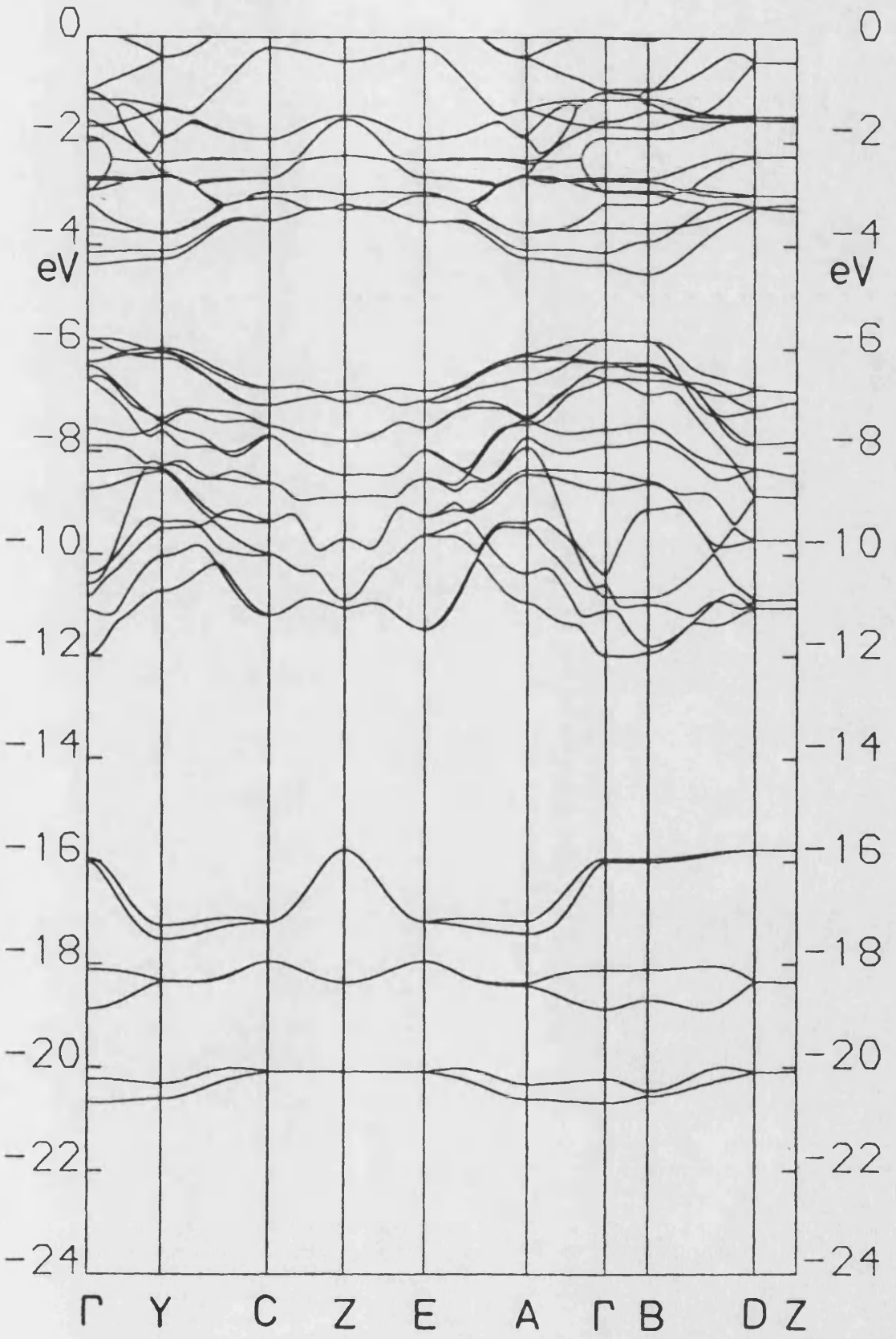

Fig. 6.17

ZrS3 (Type B)

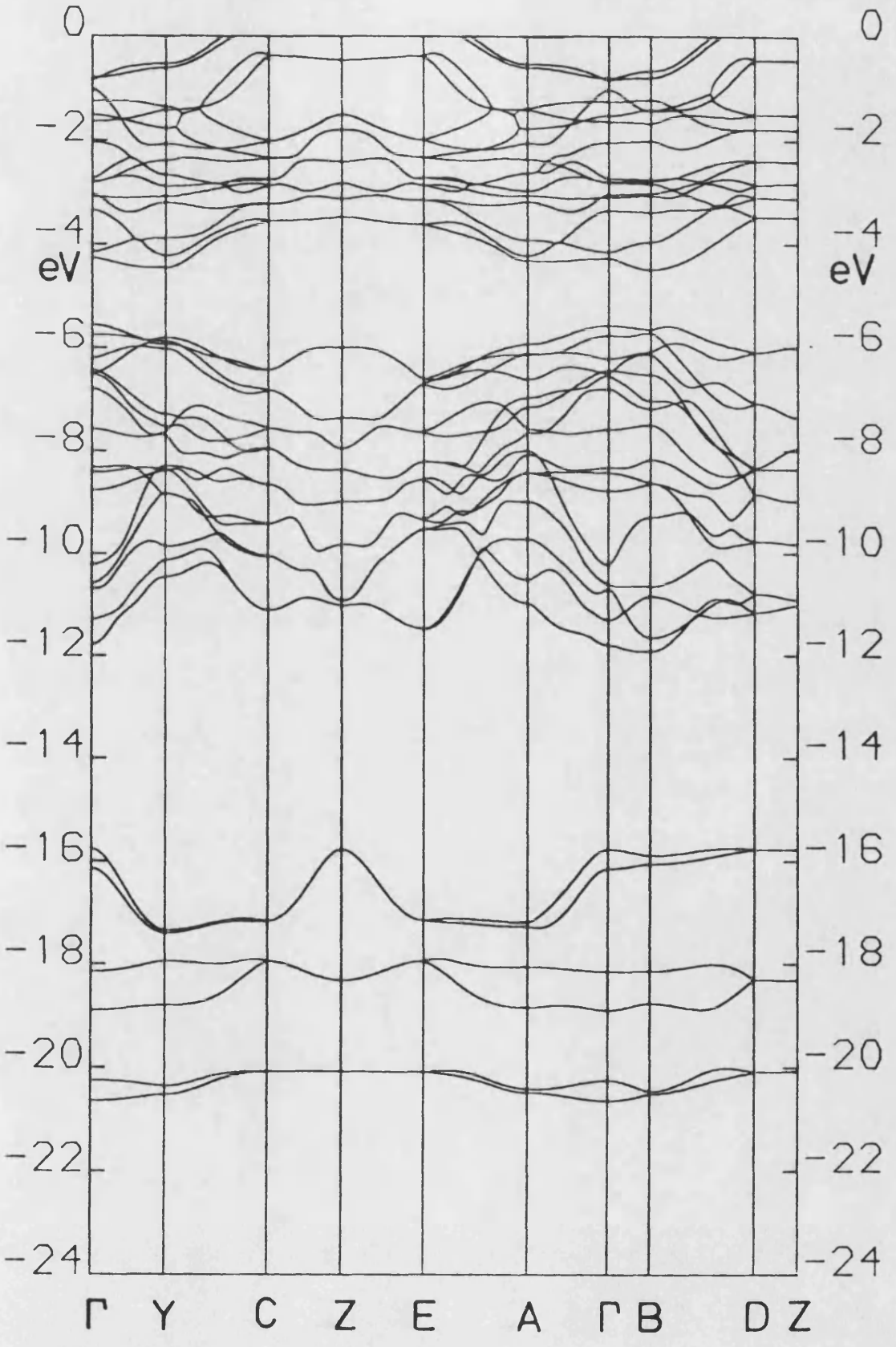

Fig. 6.18

ZrSe3 (Type A)

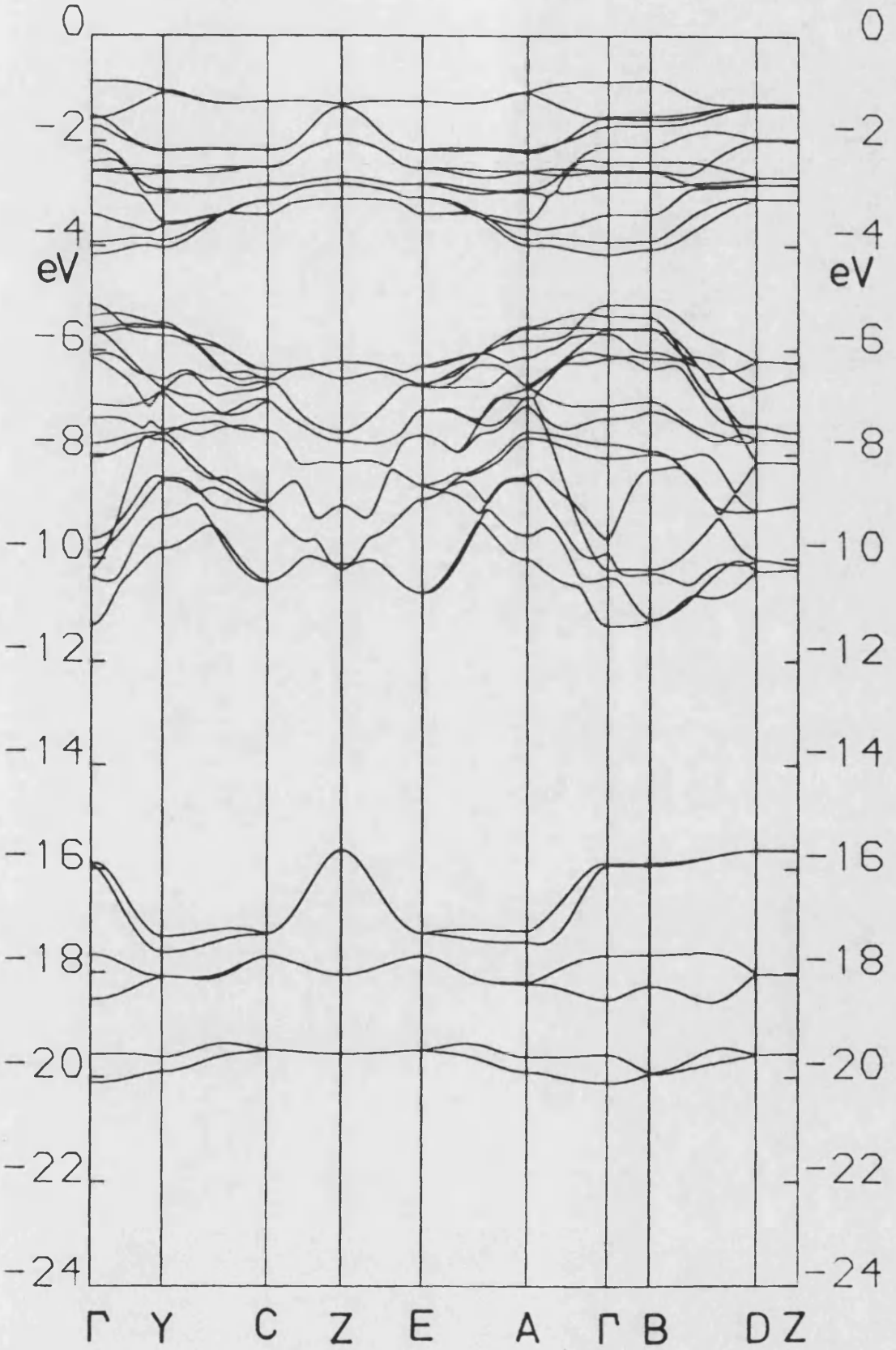

Fig. 6.19

ZrSe3 (B Type)

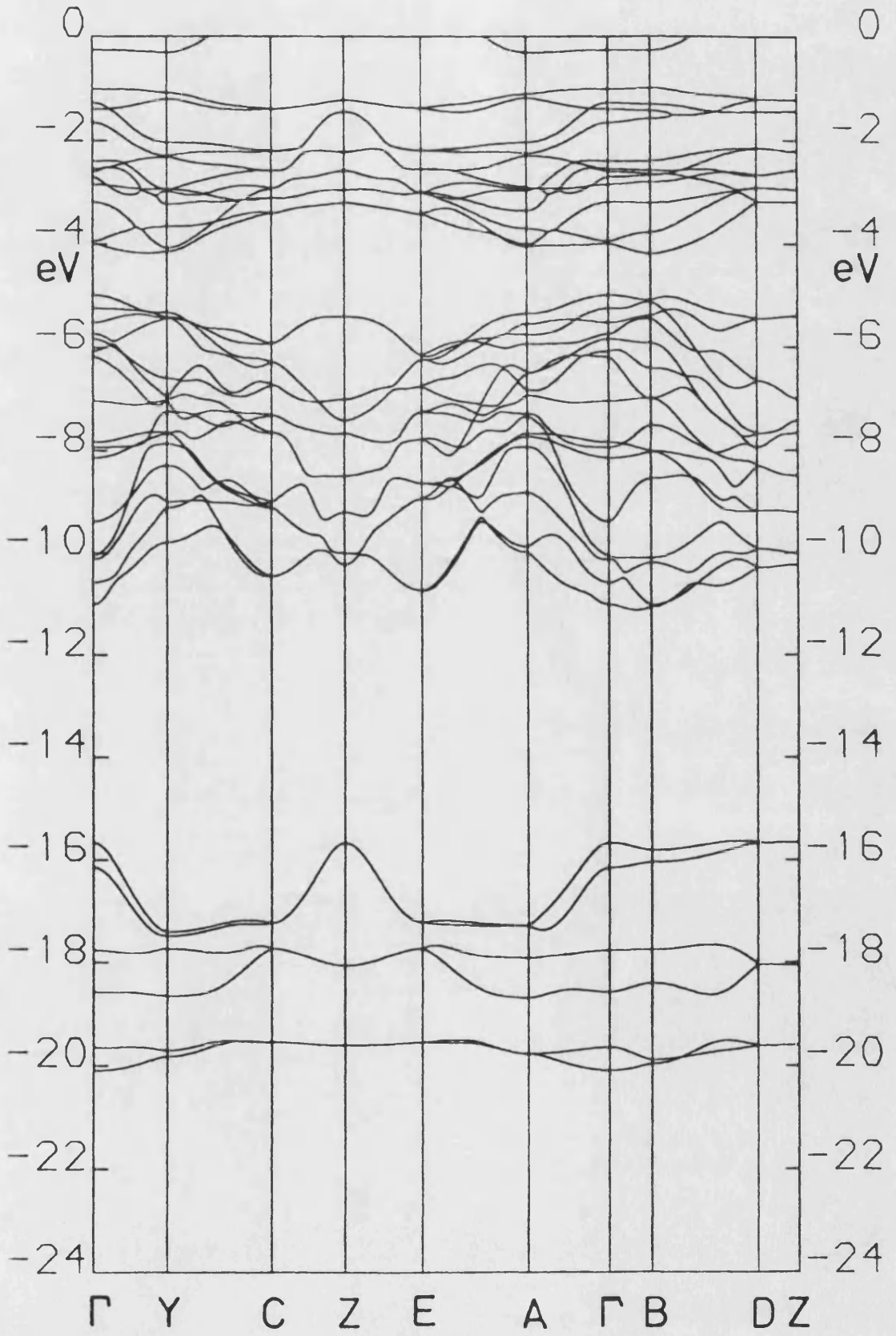

Fig. 6.20

ZrTe3 (Type A)

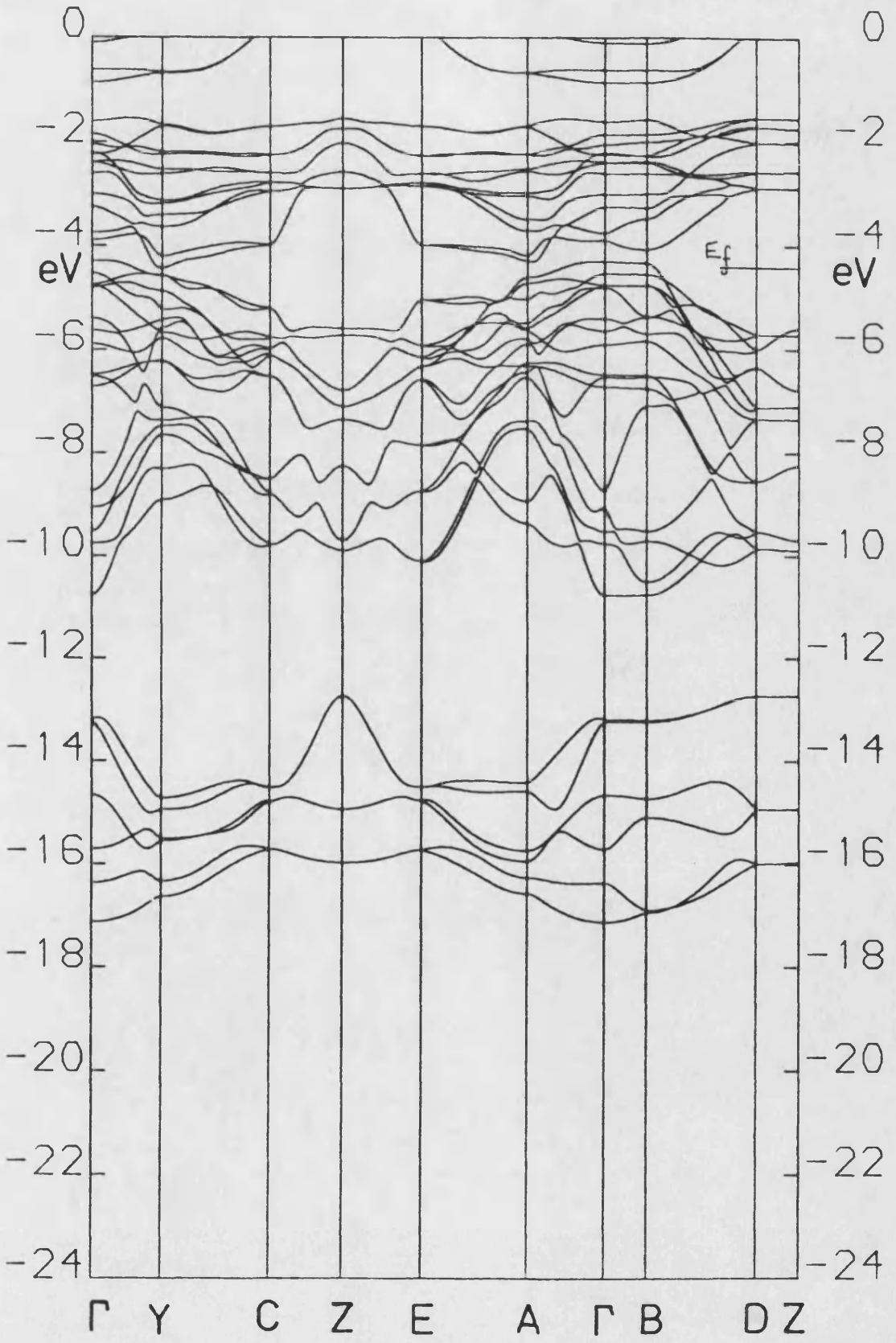

Fig. 6.21

ZrTe3 (Type B)

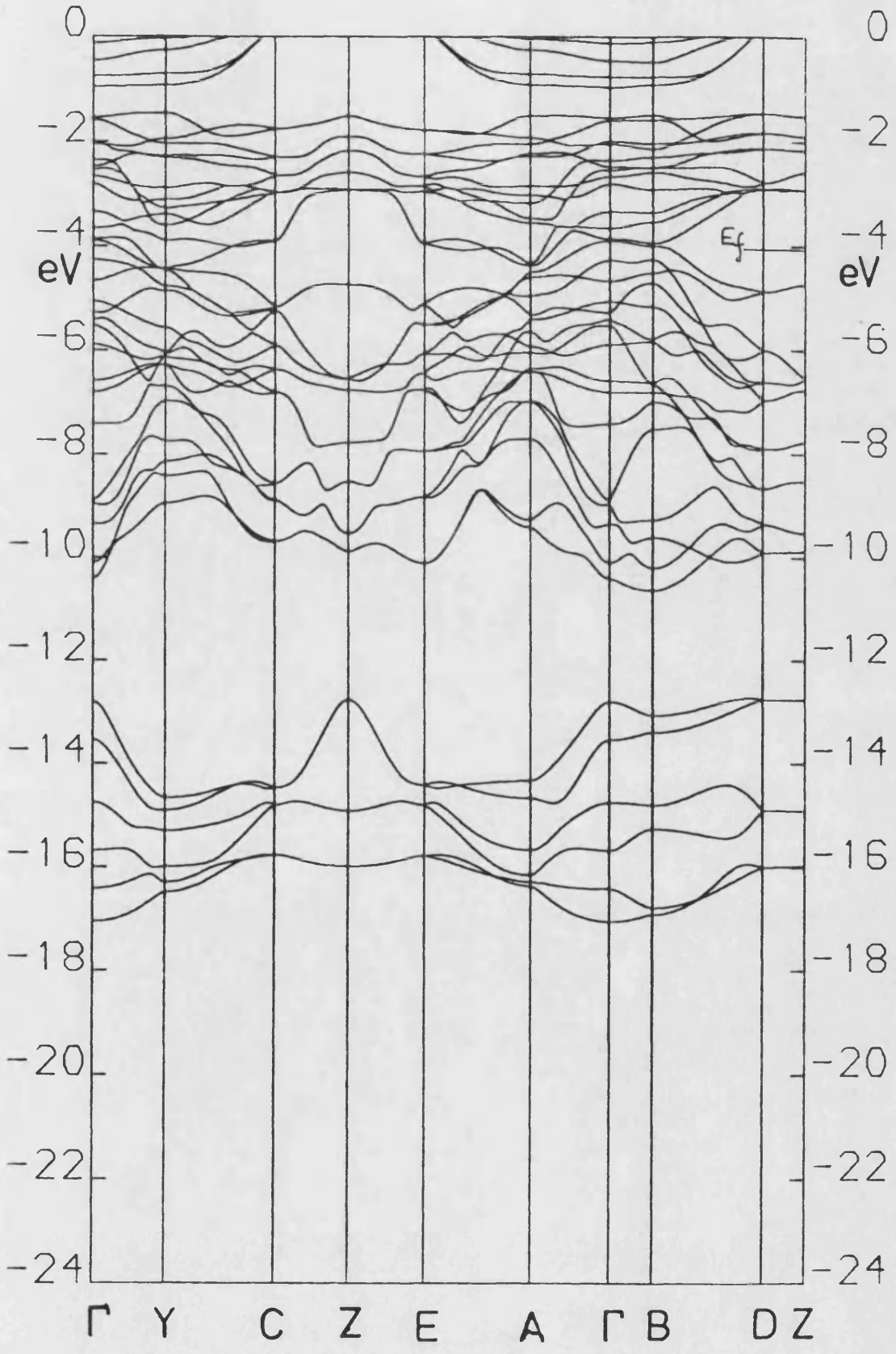

Fig. 6.22

HFS3 (Type A)

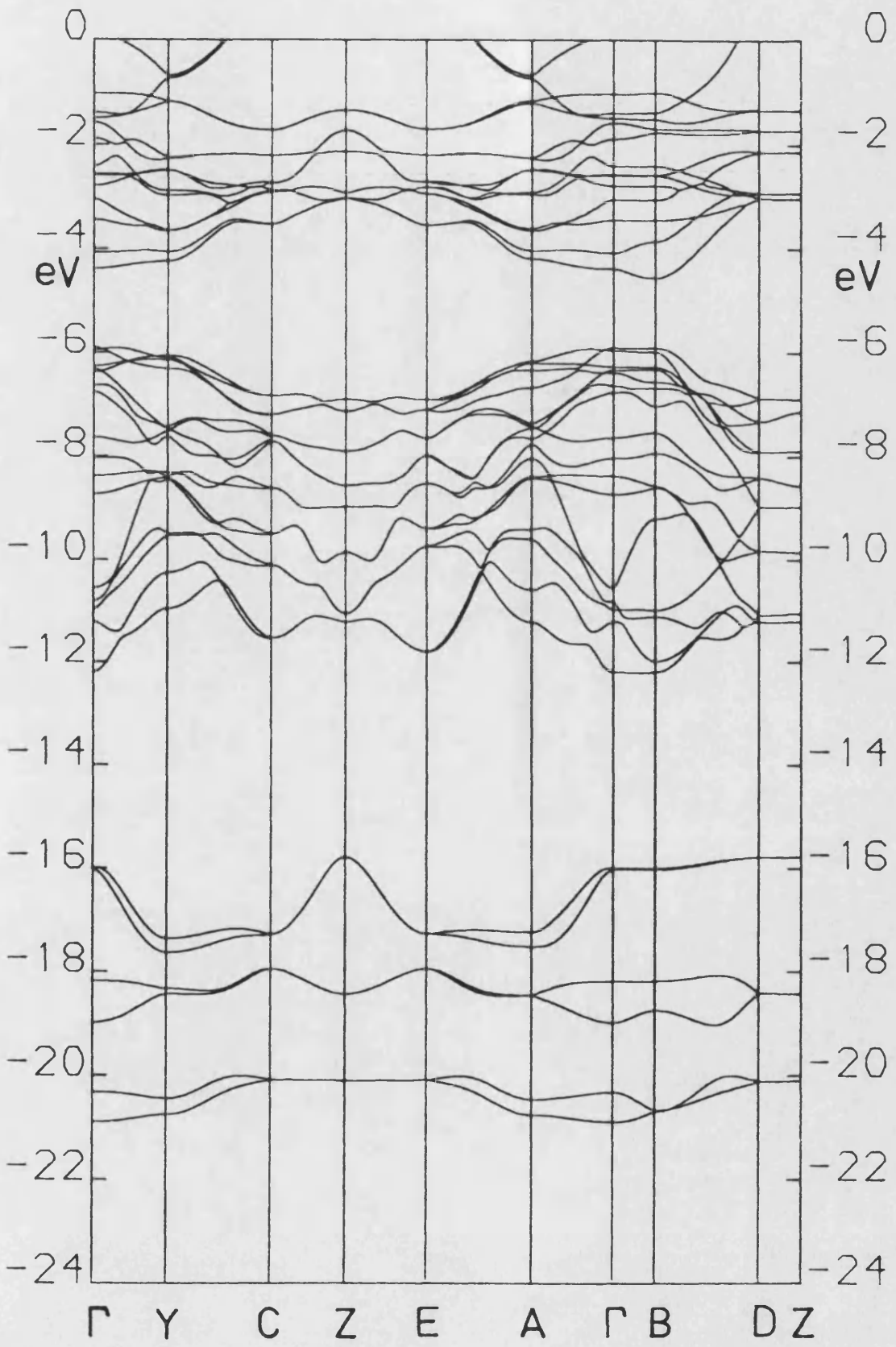

Fig. 6.23

HfS3 (Type B)

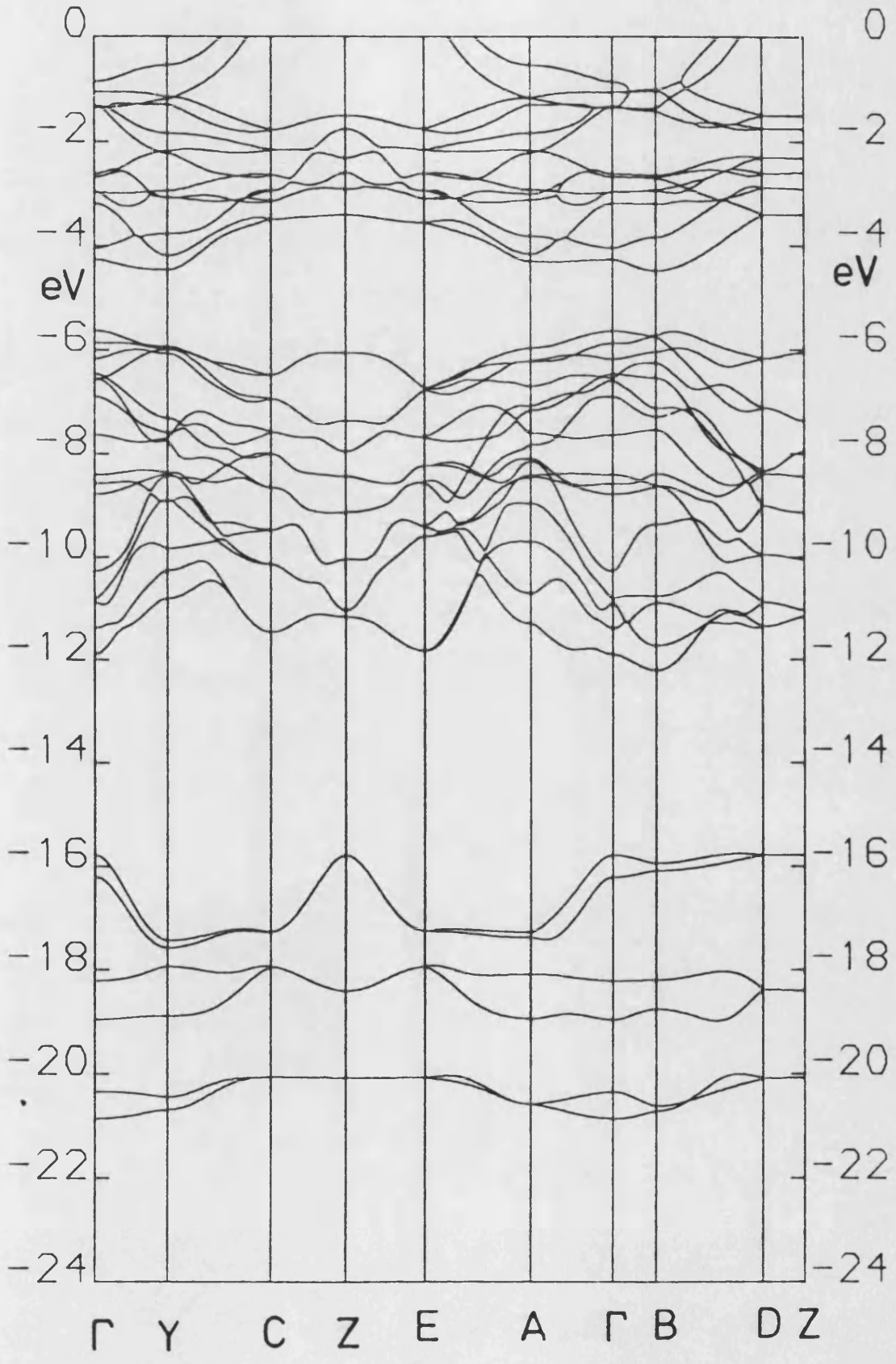

Fig. 6.24

HfSe3 (Type A)

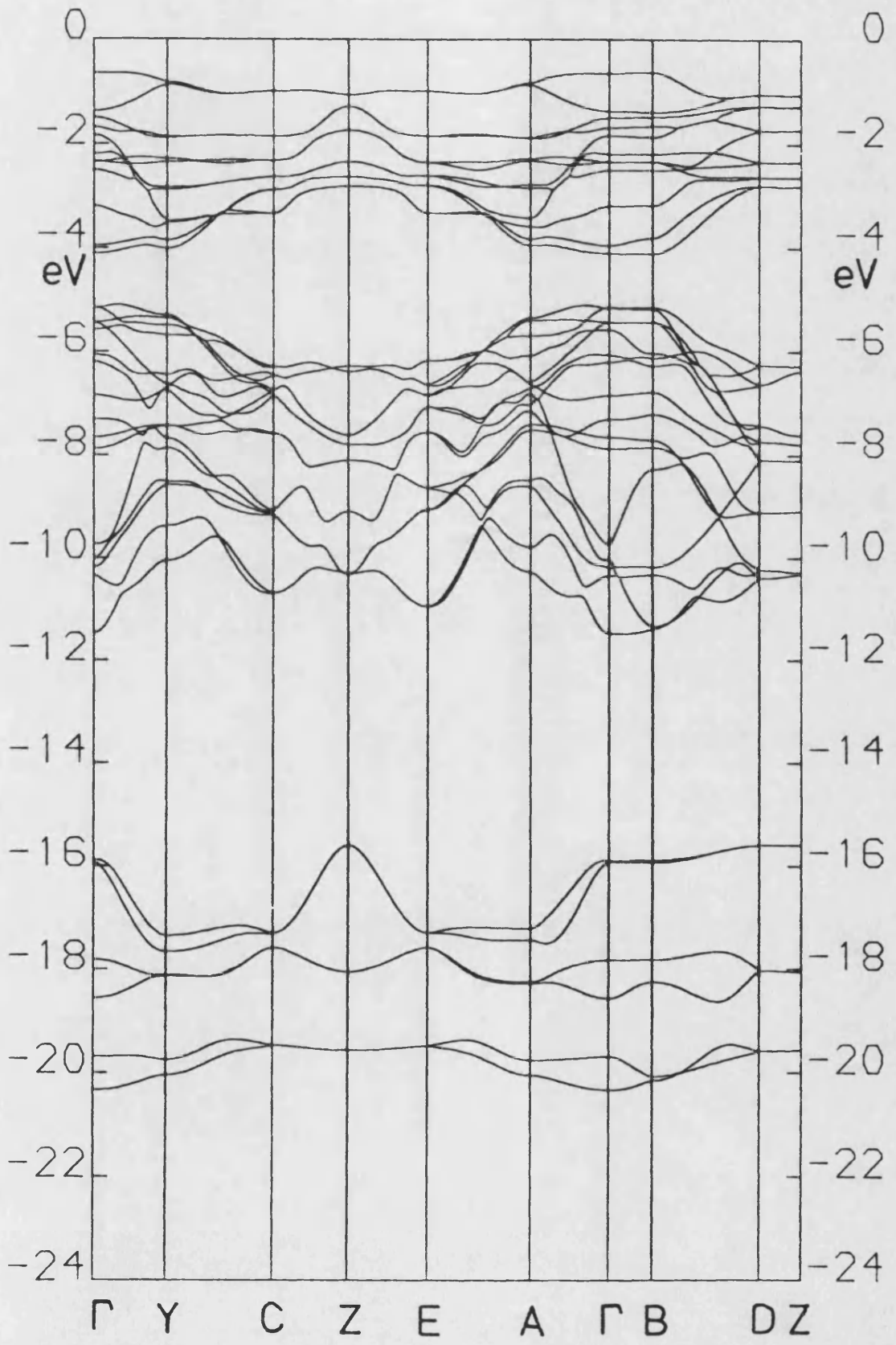

Fig. 6.25

HfSe3 (Type B)

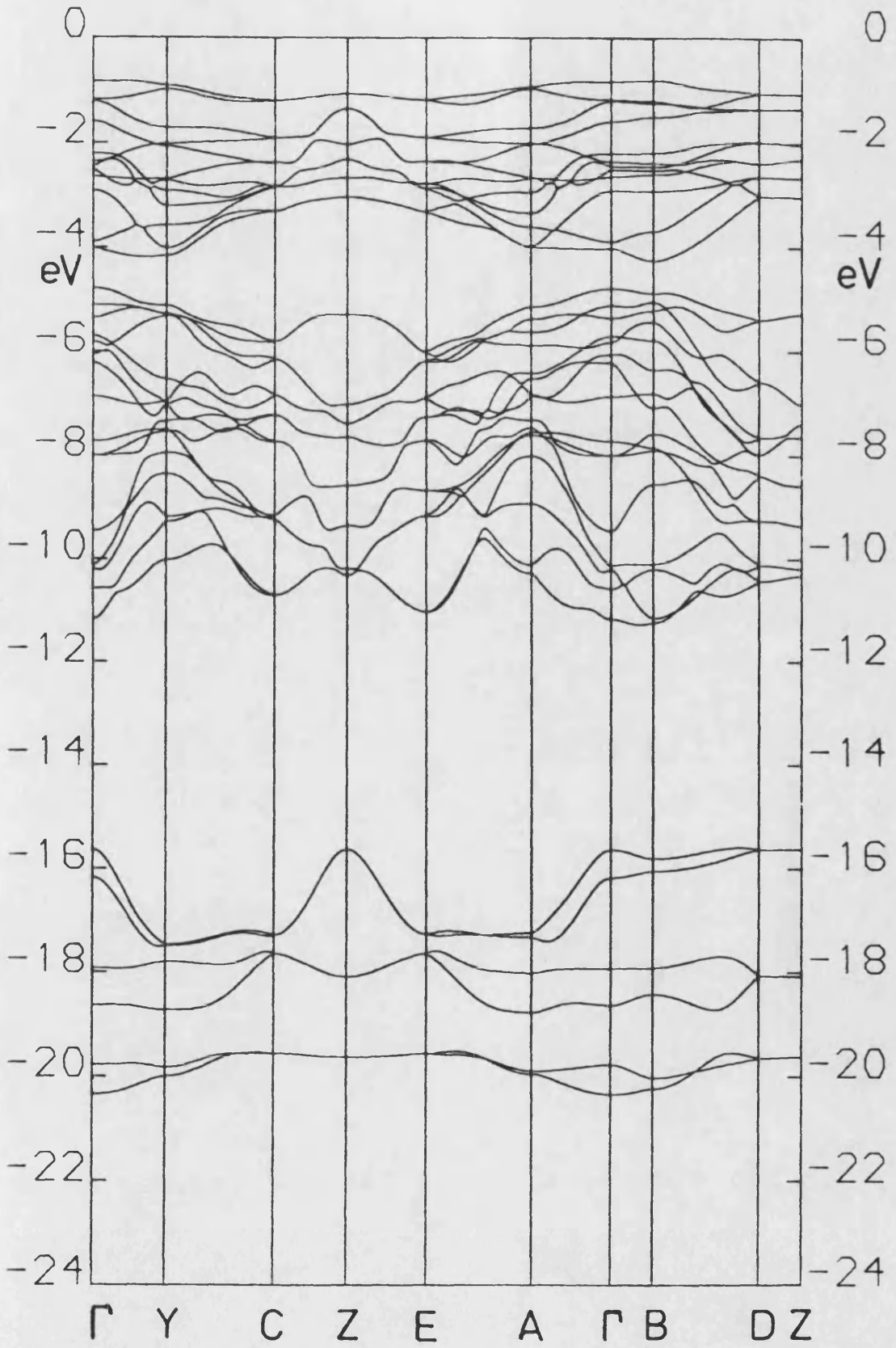

Table 6.1 Isolated atomic orbital energies (eV)

	chalcogen		metal		
	s	p	s	p	d
TiS_3	-17.8	-8.0	-5.4	-3.0	-4.6
ZrS_3	-17.8	-8.0	-5.2	-2.9	-4.2
$ZrSe_3$	-17.5	-7.4	-5.0	-2.9	-4.1
$ZrTe_3$	-14.6	-6.7	-4.9	-2.8	-3.7
HfS_3	-17.8	-8.0	-5.2	-2.9	-4.2
$HfSe_3$	-17.5	-7.4	-5.1	-2.9	-4.0

Table 6.2 Collected results

Variant		metal d charge. electrons	upper valence band width. eV	E_F	ΔE_{neg}	E_{gap}
TiS_3	A	2.19	6.8	-5.9	1.38	0.9
	B	2.24	7.1	-5.4		0.6
ZrS_3	A	2.24	6.3	-6.0	1.38	1.4
	B	2.24	6.5	-5.6		1.0
$ZrSe_3$	A	2.37	6.2	-5.4	1.35	1.2
	B	2.34	6.2	-5.0		0.7
$ZrTe_3$	A	2.73		-4.6	0.81	
	B	2.74		-4.13		
HfS_3	A	2.17	6.3	-6.18	1.38	1.4
	B	2.18	6.7	-5.7		1.1
$HfSe_3$	A	2.37	6.4	-5.4	1.35	1.1
	B	2.34	6.5	-4.9		0.6

v) the calculated semiconducting gaps.

All the materials are calculated here for both the A and B variants. As can be seen in figures 6.20 and 6.21, $ZrTe_3$ shows valence and conduction band overlap and thus no values are given for the semiconducting gap and upper valence band width, however the overlap for the naturally occuring B type is estimated at 0.6 eV.

The semiconducting gaps of table 6.2 are consistently much smaller than experimentally reported values (Brattas and Kjekshus, 1971; Grimmeiss et al., 1961; Schairer and Schafer, 1973) with the exception of $ZrSe_3$ which agrees to within 0.1 eV for the naturally occuring A variant. The position of the smallest direct gap is at B for all compounds again with $ZrSe_3$ (A variant) being the exception with a gap at gamma, however the gap values at B and Γ are very close in all cases.

6.3 Discussion

The main features of the densities of states with projections are shown labelled only for the first member of the series (TiS_3) since these feature are recognizable in all the dos figures shown; although in each case it can be seen that the B variant shows a smoothing of the densities of states, ie. the peaks are now not so

distinct.

The projected densities of states show a large degree of hybridization of the metal with the chalcogen ligand (X_{II}-X_{III}) p antibonding molecular orbital ($p\sigma^*_u$) and also with the top of the valence band p bonding orbitals. Chalcogens X_{II} and X_{III} show very similar features differing slightly for the B variant where the two atoms have dissimilar environments. The broad character of the labelled features are identified here :-

1) the chalcogen ligand pair

A- the chalcogen bonding s orbital

B- the chalcogen antibonding s orbital

C,D,E- contain the bonding p orbitals σ and Π (with σ the lowest energy) which are hybridized with the metal d orbitals and the X_I p orbitals.

F- chalcogen anti-bonding σ^*_u - again hybridised with the metal d orbitals.

2) the lone chalcogen

G- the X_I s orbitals which appear to show little hybrization. A small amount of mixing can be seen just below G, possibly with the metal d.

H- the X_I p orbitals with heaviest weighting at the non-bonding energy but showing also considerable mixing with the metal/ligand pair p orbitals.

3) the metal

J- the metal d orbitals mixed with the chalcogen s but, of course this is heavily weighted on the chalcogen orbitals.

K- metal d hybridised with the chalcogen p orbitals.

L- mainly metal d orbitals

M- the metal p orbitals with metal s which are pushed up from their free energy values by strong mixing with the chalcogens.

Comparing the size and shape of feature K it can be seen that the metal d orbitals are mixed less well with the more asymmetric B variant 'ligand pair' than in the A

variant. This is because in the A type the chalcogen II and III atom are equidistant from the metal and strong hybridization of this ligand molecular orbitals with the metal can occur. For the B type this is no longer true since the chalcogen X_{II} is closer to the metal and this asymmetry means that the molecular orbital cannot mix so strongly with the metal orbitals. Tables 6.3 to 6.14 show the trends in terms of projections of the basis orbitals for a given angular momentum (l=0,1,2) at the Brillouin zone centre for all materials studied in this chapter. The low valence band region, which contains the ligand pair is essentially unaltered for the A and B types since the distance between the two atoms X_{II} and X_{III} is conserved in the transition from A to B type. It is not straightforward to draw out the actual orbital combinations which produce the eigenvalues shown in tables 6.3 to 6.14, but an example of their use is demonstrated by the double eigenvalue degeneracy of orbitals in the A variant when the 'linking' atom X_I is forbidden by symmetry from bonding. This occurs in TiS_3 for example at -15.7, -6.0 and -3.6 eV; similarly, in $HfSe_3$ at -15.9, -5.4 and -2.3. This double degeneracy is lost when the atoms of the unit cell are in the B variant as can be seen by comparing alternate tables of eigenvectors. In the B type the X_I atom also approaches the metal atom in the other chain of the unit cell more closely than in the A type as shown in table 5.2 of the

Table 6.3 TiS_3 (A). Eigenvectors at Gamma.

Energy (eV)	Percentage character									
	Metal			X(I)		X(II)		X(III)	
	s	p	d	s	p	s	p	s	p
-21.3	4			18		38	2	36	2
-20.7	2				2	43	4	46	2
-19.4	2	2		74		10	2	8	2
-17.8			6	90			2		2
-15.8			2			43	2	50	4
-15.7			2			49	4	43	2
-12.3			8		12	4	36		39
-11.5			2	6	14		34	2	42
-11.0			14		80		5		
-10.7	2		13		21	4	31	4	26
-10.6			7	4	5		45		40
- 8.2			20		10		35		35
- 8.0			15		4		40		41
- 7.8			18		62		10		12
- 7.5			6		72		12		10
- 6.8			3		28		11		58
- 6.6			14		1		41		43
- 6.5					52		46		3
- 6.0			29				35		37
- 6.0			26				35		38
- 5.8			4		86		7		4
- 5.7			16		70		10		6
- 4.8			86		4		6		4
- 4.6			89		2		4		4
- 4.2			92	4			2		2
- 3.9			80		8		6		6
- 3.6			71				14		14
- 3.5			73				14		13
- 3.4	8		72	2	18		2		
- 3.4	2		69		16		6		6
- 2.8			80		10		4		4
- 2.4			74		18		4		4
- 1.8	70	14	6	2	4		2		
- 1.3						2	49	2	49

Table 6.4 TiS_3 (B). Eigenvectors at Gamma.

Energy (eV)	Percentage character								
	Metal			X(I)		X(II)		X(III)	
	s	p	d	s	p	s	p	s	p
-21.4	4			20		38	2	34	2
-20.8	2				2	42	4	46	2
-19.3	2			72		10	2	12	2
-17.8			6	86	2	2	2	4	
-15.9			2			46	2	46	4
-15.4			2	4		48	2	42	4
-12.0			8		16	2	32	2	40
-11.6			4	4	12		36		42
-10.9			12		50		24		12
-10.8	2		14		22	4	26	4	28
-10.2			10	2	28		22		38
- 8.3			16		42	2	22		16
- 8.2			20		4		24		52
- 8.1			16		4		30		50
- 7.3			8		76		12		4
- 6.7			16		42				40
- 6.3			12		22		40		26
- 6.2			10	2	56		26		6
- 6.0			22		36		18		12
- 5.9			26		4		50		22
- 5.5			16		36		48		2
- 5.4			10		48		42		2
- 4.6			90		2		2		8
- 4.6			78		4				18
- 3.9			78		6		6		8
- 3.7			74		2		7		10
- 3.6			76		4		12		6
- 3.6			74	2	20		4		
- 3.4			74		16		4		8
- 3.4	4	2	74	2	18		4		
- 2.6			76		8				16
- 2.4			72		14				12
- 1.1			2			4	50	4	52

Table 6.5 ZrS_3 (A). Eigenvectors at Gamma.

Energy (eV)	Percentage character									
	Metal			X(I)		X(II)		X(III)	
	s	p	d	s	p	s	p	s	p
-20.7	4			12		42	2	40	2
-20.2	2		2			44	4	46	2
-18.9	2			81		6	2	6	2
-18.1			8	88					
-16.0			2			43	2	50	4
-16.0			2			50	4	44	2
-12.0			12		12	4	34	2	36
-11.1			4	4	12		34	2	42
-10.8		2	20		76		2		
-10.6	2		18		18	4	30	4	26
-10.4			10	2	2		48		38
- 8.7			22		16		32		32
- 8.4			16		6		38		40
- 7.9			14		60		10		14
- 7.6			4		69		14		14
- 6.6			3		25		14		58
- 6.6			10		1		43		45
- 6.3			23				38		40
- 6.3					58		41		4
- 6.3			21				40		40
- 5.8			2		89		6		6
- 5.8			14		72		1		4
- 4.4			79		7		8		6
- 4.1			86		2		2		6
- 3.7	2	2	86	6			2		2
- 3.2			84		8	2	4	2	4
- 3.0	56	12	12	4	4				
- 2.9			77				12		12
- 2.7			79				10		10
- 2.7			68		22		4		4
- 1.9	20	8	52		19		2		2
- 1.7			81		8		6		4
- 1.6						2	50	2	50
- 1.2			72		16		6		6
- 1.0		50				2	24	2	24
- 1.0		50				2	24	2	24

Table 6.6 ZrS_3 (B). Eigenvectors at Gamma.

Energy (eV)	Percentage character								
	Metal			X(I)		X(II)		X(III)	
	s	p	d	s	p	s	p	s	p
-20.6	4			12		42	2	40	2
-20.3	2		2			42	4	48	2
-18.9	2			82		4	2	8	2
-18.4			8	86	2	4	2		
-16.1			2			46	2	46	2
-15.7			2	4		46	2	44	2
-11.8			12		10	2	30	2	42
-11.3			4	4	12		36	2	42
-10.7			16		66		12		4
-10.6	2		18		18	4	26	4	28
-10.2			10	2	16		32		38
- 8.8			22		13		20		44
- 8.4			16		4		32		48
- 8.3			14		42		28		14
- 7.6			4		66		24		6
- 6.8			14		44				41
- 6.5			7	2	63		26		2
- 6.5			9		21		38		32
- 6.4			20		30		20		30
- 6.2			18		7		45		30
- 5.8			16		30		52		4
- 5.6			4		56		40		3
- 4.3			72		6				20
- 4.1			88				2		10
- 3.3			82		8		2		6
- 3.1			82				10		8
- 3.0			66	4	20		10		
- 2.8			80		8		8		4
- 2.8			79		21		2		8
- 2.7	18	4	54	2	14		6		
- 2.0	60	24	12	2	6				
- 1.6		2	79		4				14

Table 6.7 $ZrSe_3$ (A). Eigenvectors at Gamma.

Energy (eV)	Percentage character								
	Metal			X(I)		X(II)		X(III)	
	s	p	d	s	p	s	p	s	p
-20.1	2			18		40		38	
-19.6	2		2		2	44	2	48	2
-18.5	2	2		76		10	2	8	2
-17.7			8	90			2		
-15.9			2			45		51	2
-15.9			2			49	2	45	
-11.3			14		14	2	34		36
-10.4			4	4	12		37		44
-10.2			18		80		4		
- 9.9	2		16		26	2	28	2	23
- 9.6			12	2	2		45		39
- 8.1			20		16		33		32
- 7.8			15		5		40		40
- 7.3			18		55		10		16
- 7.0			4		66		14		14
- 6.1			6		9		26		59
- 6.1			9		2		44		44
- 5.7					51		40		9
- 5.6			29				35		37
- 5.6			29				37		36
- 5.3			6		85		4		6
- 5.1			16		82		2		
- 4.2			87		2		6		6
- 3.9	2		80		4		6		6
- 3.4			76		12		6		6
- 2.9	2		89	6	2		2		2
- 2.6			72				14		14
- 2.6			72				14		14
- 2.4	4		67		27				
- 2.1			70		18		5		6
- 1.7						2	49	2	49
- 1.6		2	79		10		4		4
- 1.5						2	49	2	49

Table 6.8 $ZrSe_3$ (B). Eigenvectors at Gamma.

Energy (eV)	Percentage character								
	Metal			X(I)		X(II)		X(III)	
	s	p	d	s	p	s	p	s	p
-20.1	4			20		38		38	
-19.6	2		2		2	46	2	48	2
-18.6	2	2		74		8	2	12	2
-17.8			8	86		4	2		
-16.2			2			50	2	44	2
-15.7			2	4		46		46	2
-11.0			12	12		32		2	41
-10.6			6	4	14		36		42
-10.1			18		76		6		1
-10.0	2		16		20	2	28	2	28
- 9.4			12	2	4		34		48
- 8.1			22		12		21		44
- 7.9			14		34		38		14
- 7.8			14		4		34		49
- 7.0			6		66		22		8
- 6.2			14		43				41
- 6.1			11		27		32		30
- 5.8			25		41		12		24
- 5.7			8	2	50		38		2
- 5.5			24		5		43		27
- 5.2			22		37		38		2
- 5.0			8		41		45		6
- 4.0			71		7		1		20
- 3.9			86		1		4		9
- 3.2	2		79		7		4		8
- 2.8			75				13		11
- 2.7			62	3	21		10		2
- 2.6	2		63		21		6		8
- 2.5			73		9		9		8
- 2.4	2	2	66		19	2	6		1
- 1.7			10				40		52
- 1.4		2	77		6				14
- 1.3			10		2		39	2	49
- 1.0			74		16				10

Table 6.9 $ZrTe_3$ (A). Eigenvectors at Gamma.

Energy (eV)	Percentage character									
	Metal			X(I)		X(II)		X(III)	
	s	p	d	s	p	s	p	s	p
-17.1	4			28		36		34	
-16.4	2			4	4	44	2	44	2
-15.7		2		64		14	4	14	2
-14.7			8	82			4	4	4
-13.2			2			46		50	2
-13.2			4			50	2	23	
-10.8	2		10		12	2	36		38
- 9.7			2	8	2		42	2	44
- 9.5		2	16		80		4		
- 9.1			12	4	4		40		40
- 8.7	4		14	2	36	4	20	4	18
- 6.7			20		6		38		38
- 6.5			22		50		14		14
- 6.5			18		4		40		38
- 5.9			10		74		8		6
- 5.6			4		16		30		50
- 5.4			12		4		40		42
- 4.8			12		54		22		10
- 4.7			38				28		32
- 4.7			38				26		34
- 4.5			30		62		4		2
- 4.3			4		88		6		4
- 3.9			86		2		6		6
- 3.7	2		70				14		14
- 3.2			62		22	2	10		6
- 3.0			90	4			2		2
- 2.6	2		70		26				
- 2.4			64				12		24
- 2.4			62				20		20
- 2.2		2		76		8		14	
- 2.2			64		18		8		12
- 2.0			2				50		50
- 1.9			6			2	50	2	48
- 1.6			72		20		6		4

Table 6.10 $ZrTe_3$ (B). Eigenvectors at Gamma.

Energy (eV)	Percentage character									
	Metal			X(I)		X(II)			X(III)	
	s	p	d	s	p	s	p		s	p
-17.1	4			32		34			30	
-16.4	2			6	4	48	2		40	
-15.7		2		60		14	2		18	2
-14.8			8	74	2		4	12	2	
-13.5			2		2	48			46	
-12.8			4	6		46			42	2
-10.4	2		10		12		34			42
-10.1			2	6	4		44			44
- 9.3		2	14		76		10			
- 8.9			12	4	10		34			40
- 8.9	4		14		32	4	20		2	24
- 7.4			16		26		28			30
- 6.8			22		6		26			28
- 6.6			18		4		34			46
- 5.9			10		70		18			2
- 5.5			24		42	2	2			28
- 5.4			18		26		34			18
- 5.3			10	4	50		26			8
- 5.1			34		32		16			18
- 4.7			32		8		38			24
- 4.3			18		30		48			2
- 3.9			10		50		40			2
- 3.9			86				4			10
- 3.7	2		78		2					18
- 3.3		2	64		6		8			18
- 2.8	4		60	2	22		6			6
- 2.7			70		2		20			8
- 2.5	2		40	2	22		18			7
- 2.5			74		18		8			
- 2.4			72		20	2	4			2
- 2.0		2	66				2			32
- 2.0			28	2	6		26			46
- 1.6			12		2		40			50
- 1.5			70		16					18

Table 6.11 HfS_3 (A). Eigenvectors at Gamma.

Energy (eV)	Percentage character									
	Metal			X(I)		X(II)		X(III)	
	s	p	d	s	p	s	p	s	p
-20.9	4			16		40	2	36	2
-20.3	2		2		2	42	4	46	2
-18.9	2	2		76		10	2	8	2
-18.2			8	88			2	2	
-16.0			2			42	2	50	4
-16.0			2			49	4	44	2
-12.2	2		12		14	4	33	2	36
-11.2			6	4	16		32		42
-11.0			20		78				
-10.8	4		16		16	4	30	4	26
-10.6			9	2	2		48		38
- 8.7			21		18		31		31
- 8.4			14		6		38		41
- 8.0			14		60		12		14
- 7.6			4		68		16		14
- 6.8			2		28		12		57
- 6.6			10				44		45
- 6.4					52		46		2
- 6.3			21				39		40
- 6.3			19				43		39
- 6.0			2		88		4		4
- 5.9			12		74		10		6
- 4.4			80		6		8		6
- 4.1			86		2		4		6
- 3.4		2	86	6			2		2
- 3.1			86		8		4	2	4
- 2.8			79				10		10
- 2.6			81				10		9
- 2.6			68		22		4		6
- 2.4	28	4	54	4	10				
- 1.9						2	49	2	49
- 1.6						2	49	2	49
- 1.5			83		6		4		6
- 1.4	50	10	22	2	10		2		2
- 1.0			77		16		4		6

Table 6.12 HfS_3 (B). Eigenvectors at Gamma.

Energy (eV)	Percentage character								
	Metal			X(I)		X(II)		X(III)	
	s	p	d	s	p	s	p	s	p
-20.9	4			18		38	2	38	2
-20.3	2		2		2	42	2	48	2
-19.0	2			76		8	2	10	2
-18.2			8	84	2	2	2		
-16.2			4			48	2	44	2
-15.8			2	4		48	2	41	2
-11.9	2		12		12		30	4	42
-11.4			4	4	12		36		42
-10.9	4		16		20	4	25	4	28
-10.8			16		58		16		10
-10.3			12	2	24		28		34
- 8.8			22		14		18		45
- 8.6			14		44	2	26		14
- 8.4			15		5		30		49
- 7.6			4		65		24		8
- 6.9			15		46				38
- 6.6			7		10		41		31
- 6.5			9	4	62		22		5
- 6.5			18		38		18		28
- 6.2			15		8		48		30
- 5.9			12		28		57		2
- 5.6			4		48		45		4
- 4.3			74		4				22
- 4.0			86				2		10
- 3.2	2		84		8		2		6
- 3.0			84				8		6
- 3.0		2	57	4	16	2	18		4
- 2.7			70		22		4		10
- 2.7			82		8		6		4
- 2.6	12	2	55	2	12	2	13	2	
- 1.3		2	80		2				16

Table 6.13 $HfSe_3$ (A). Eigenvectors at Gamma.

Energy (eV)	Percentage character									
	Metal			X(I)		X(II)		X(III)	
	s	p	d	s	p	s	p	s	p
-20.3	4			22		38		34	
-19.7	2				2	44	2	46	2
-18.6	2	2		72		12	2	10	2
-17.8			8	88			2		2
-15.9			2			44		50	2
-15.9			2			48	2	46	
-11.5	2		14		14	2	34		36
-10.3			2	6	8		40		47
-10.2		1	18		78		4		
-10.0	6		18		28	2	26	4	20
- 9.7			12	2	4		42		38
- 7.8			18		10		36		35
- 7.6			14		5		41		41
- 7.3			18		54		12		16
- 6.8			6	73		10		10	
- 6.2			4		12		28		55
- 6.1			10		2		43		44
- 5.6			2		56		32		12
- 5.4			27				36		38
- 5.4			27				37		36
- 5.2			4		88		4		6
- 5.1			18		78		4		2
- 4.1			86		2		6		6
- 4.0	2		81		2		8		6
- 3.2			76		12	2	6		6
- 2.5			88	6	2		2		2
- 2.3			74				14		14
- 2.3			73				14		13
- 2.2	4		70		24				
- 1.8			70		18		6		6
- 1.5						2	49	2	49
- 1.4		2	81		8		4		4

Table 6.14 $HfSe_3$ (B). Eigenvectors at Gamma.

Energy (eV)	Percentage character									
	Metal			X(I)		X(II)		X(III)	
	s	p	d	s	p	s	p	s	p
-20.34	4			24		36		34	
-19.8	2				2	46	2	46	2
-18.6	2	2		68		10	2	16	2
-17.9			8	84	2	2	2	2	
-16.2			2			50	2	44	2
-15.6			4	4		46		44	2
-11.2	2		12		12		31	2	40
-10.6			4	4	12		38		43
-10.2	4		16		20	4	27	2	26
-10.1			16		70		8		2
- 9.5			12	2	10		30		46
- 8.0			20		8		23		48
- 8.0			14		32		36		16
- 7.7			14		4		34		49
- 6.9			6		69		20		4
- 6.2			16		42	1		40	
- 6.1			10		28		34		27
- 5.8			7	2	58		29		4
- 5.7			24		40		14		24
- 5.4			22		8		44		28
- 5.1			20		32		48		2
- 4.8			6		44		43		6
- 4.0			69		6		2		22
- 3.9			86		2		4		8
- 2.9	2		79		8		4		8
- 2.6			78				1		10
- 2.5			58	4	19	2	15		4
- 2.4	2	2	60		20		8		8
- 2.3			76		8		9		6
- 2.2	2	2	67		18	2	8		2
- 1.6			17	2	2		34		50
- 1.2			11		4		36	2	46
- 1.2		2	80		4				14

previous chapter. The effect of this is to pair up chains within a unit cell but the increased M-X_I distance across unit cells for the B type enhances the 1-D character of these crystals. The character of the two bands at gamma at the fermi level in the A type may be descibed (in terms of a simple molecular orbitals model) as the combination of the X_{II}-X_{III} pair hybridizing with the metal d orbitals which in turn mixes with the X_I p orbital. This simple picture is lost when the X_{II} and X_{III} pair are no longer equidistant for the type B crystals- the close aproach of the X_{II} atoms to the metal gives equal weighting on the X_I and X_{II} atom at the fermi level at gamma. This is true for all the compounds studied in this chapter, including $ZrTe_3$.

Table 6.2 shows the upward movement of the upper valence band maximum (E_F) for the B type compared with the A type for each material. The consistent gap reduction for the B type as compared with the A type can be seen to be mainly attributable to this movement of the upper valence band edge, this difference is most clearly demonstrated at the Z point in the E($\underline{k}$) figures (6.14-25).

The predicted similarity between the Zr and Hf sulphides and selenides for both A and B types, as described earlier, is confirmed by:-

i) the semiconducting gap which are within 0.1 eV for both sulphides and selenides

ii) the upper valence band widths (within 0.3 eV)

iii) the position of the top of the valence band (within 0.1 eV)

iv) the crystal metal d charge (within 0.1 electron)

The metal d charge in the crystals reflects the electronegativity differences given in table 6.2. There is little change in the metal d charge induced by the asymmetry in going from the A to B type- as shown in table 6.2.

Comparison of tables 6.2 and 5.4 show good agreement for the upper valence band widths. Unfortunately the widest bands, those for TiS_3, are not given in table 5.4 but, since the X_{II}-X_{III} distance is smallest here, it would be expected that this compound would have a large upper valence band width because this manifold is of mainly chalcogen p character- the small metal-chalcogen distance will also act to broaden this manifold.

The natural occurrence of a crystal in the A variant or

B variant can be roughly predicted from the simple ionic ratio (see table 6.2). A large anion:cation ratio is indicative of type B, ie. TiS_3 and $ZrTe_3$. The same ratio of 2.51 is found for both $ZrSe_3$ (type A) and $HfSe_3$ (type B) but Furuseth et al. (1975) examined 15 crystals of $HfSe_3$ and found ten type B but three type A with the rest twinned. Thus there appears to be only a small energy difference between the two types at this ionic ratio.

6.4 $ZrTe_3$

$ZrTe_3$, which occurs naturally as the B variant, is shown to be a semimetal by these calculations, with a band overlap of approximately 0.6 eV. The calculated intrinsic nature of the conduction in this compound makes the possibility of a CDW transition to a semiconducting state feasible with consequent total energy reduction. The local density approximation, which inevitably underestimates semiconducting gap values, may well reduce this overlap but the comparison of values of the gap for the other materials with experimental values suggests that $ZrTe_3$ will remain semimetallic even with a correction for the reduced calculated gap. $ZrTe_3$ has the largest lattice parameter of all of the MX_3 compounds studied here, however Te is a large ion and, as a result, the upper valence band due to the chalcogen p

orbitals is very broad. The metal d orbitals, in contrast, are quite narrow- this may be due to the reduced crystal field splitting from the small electronegativity difference between the Zr and Te. $HfTe_3$ has not yet been grown as a sufficiently good crystal to measure the structure refinement parameters, but the unit cell parameters are published (Furuseth et al., 1975). The electronic structure of $HfTe_3$ would be expected to be very similar to $ZrTe_3$, especially considering the similarities between their sulphides and selenides, apart from spin-orbit coupling effects.

6.5 Conclusion

This chapter has shown the application of the ab initio tight-binding method to a series of closely related layered compounds. The electronic structure calculations undertaken here have shown the trends in moving down the periodic table in the group IVB transition metals and chalcogens (group VIA). The major features of these calculations compare favourably with the experimental results published to date. The semiconducting gaps found for all materials (except of course the semi-metallic $ZrTe_3$) are slightly smaller than quoted experimental values- this is a consequence of calculations within the local-density approximation which inevitably underestimate gap values.

The narrowing of the gap for the B type materials compared to A type is shown to be due to the slight broadening and raising of the mainly chacogen based upper valence band manifold, as the metal environment becomes more asymmetric.

In view of the calculated band overlap in the low dimensional compound $ZrTe_3$, the predicted CDW/superlattice transition appears likely to be a Peierls transition opening a gap over the whole Fermi surface.

A simple model using the anion:cation ratio can predict whether a compound will occur naturally in the A or B type.

Chapter 7. Applications to superconducting ceramics.

7.1 Introduction

Superconductivity was first discovered in Holland by Kamerlingh Onnes in 1911 in a wire of mercury with a transition temperature (T_c) of about 4.2K. Many other metallic elements have since been found to be superconducting (see for example Ashcroft and Mermin, 1981). Transition metal alloys were found to have superconducting transitions with the maximum temperature achieved by J. Gavaler in 1973 with a thin film of Nb_3Ge (T_c about 23.2K). Even in 1964 many thousands of alloys had been found to superconduct (eg. see Roberts, 1964). Many of these compounds have the A15 (beta-tungsten) structure and it was commonly felt that the maximum Tc had now been achieved with this class of compounds. Thus the search was on for new types of compound which could superconduct at temperatures that are technologically useful. A number of candidate materials were considered such as the transition metal dichalcogenides- after the discovery of charge-density-waves (see Wilson and Yoffe, 1969) and their superconducting intercalates (Whittingham and Jacobson, 1982). Much interest was shown in the superconducting (T_c(max.) 13K) oxide compound $BaPb_{1-x}Bi_xO_3$ (eg. Thanh et al., 1980). Two novel features characterise this compound- namely a low

density of states at the Fermi level and a metal-semiconductor transition for x about 0.3- these features were used in a search for other mixed-valence, perovskite-type, oxide superconductors. The breakthrough eventually came with the now famous report by Bednorz and Muller, 1986 of possible superconductivity at 30K in a mixed phase sample of Ba-La-Cu-O for which they were subsequently awarded the Nobel prize. This announcement caused a frenzy of activity both among experimentalists (in order to isolate the high T_c phase and find even higher T_c compounds) and theoreticians (to find the mechanism of the superconductivity).

The next barrier needed to be broken was a T_c above 77K- the boiling point of liquid nitrogen. This was achieved by Wu et al. (1987) with a T_c of about 90K in a Ba-Y-Cu-O system. The report in the New York Times of 16/2/87 and subsequent media reports of superconductivity above liquid nitrogen temperatures fired the imagination of the general public around the world. The great excitement caused by these new high T_c compounds resulted in the packed March meeting of the American Physical Society being dubbed "The Woodstock of physics" by M. Schluter of AT and T Bell Labs.. Laboratories around the world dropped all other work and concentrated on a search for even higher T_c compounds and analysing their crystal structures. Reports have

been made of compounds with T_c above room temperature but, so far, these have not been reproducible (see, for example, Jayaraman, 1987).

The potential applications for compounds with T_c above 77K are due to the relative cheapness and ease of use of liquid nitrogen compared with liquid helium. Possible uses include efficient electrical power transmission; powerful and low-loss magnets for use in, for example, medical NMR; levitation of trains; and super-fast computers. Problems must first be solved in making wires with these brittle ceramic compounds and increasing the current carrying capacity.

In this chapter we concentrate on the electronic structure of two types of compound- La_2CuO_4 in two phases and Ba-Y-Cu-O with two different oxygen ratios. A wide spectrum of stoichiometries are produced by the range of growth possibilities in these compounds, the O ratio is especially sensitive to crystal growth conditions. Many samples to date have been multiphased. La_2CuO_4 shows a metal-semiconductor transition on cooling, the mechanism of which is not yet properly understood- it has been attributed to a Peierls transition (commensurate ($\sqrt{2}, \sqrt{2}, 0$) PLD, Mattheiss, 1987 and Yu et al., 1987). This is further discussed below. The non-superconducting La_2CuO_4 has been shown to

become superconducting by the substitution of La with divalent group II compounds, such as Ba or Sr.

$Ba_2YCu_3O_7$ ceases to superconduct when the O ratio falls below 6.5, the O_7 and O_6 compounds are investigated here.

7.2 Structure

1) $La_2CuO_4/La_{2-x}Ba_xCuO_4$

Longo and Raccah (1973) showed that La_2CuO_4 has a low-temperature face-centred orthorhombic structure but that, at above about 260C, a phase transition to tetragonal structure occurs. The tetragonal K_2NiF_4 structure is stabilised at lower temperature by the substitution of divalent atoms such as Ba for trivalent La- this allows the material to remain metallic, and superconducting below about 40K: although there is still evidence in many of the other high-temperature, superconducting samples near 150-200K for structural changes that may be associated with ordering of oxygen vacancies and buckling of the CuO_4 units. Jorgensen et al. (1987) have shown that the superconducting phase of Ba-La-Cu-O has the K_2NiF_4 type structure with the formula $La_{1.85}Ba_{0.15}Cu\ O_4$. The substition of La by Ba to form the superconducting $La_{2-x}Ba_xCuO_4$ does not contain oxygen vacancies to charge compensate for the

reduced number of valence electrons for the group II Ba (Jorgensen et al., 1987).The lattice and structure refinement parameters for both crystal structures are given in table 7.1: the data for the one-face-centred orthorhombic structure is for space group Abma taken from Grande et al. (1977) and the body centred tetragonal phase (I4/mmm) of Ba-La-Cu-O from Takagi et al. (1987).

The tetragonal phase is shown in fig. 7.1, with Cu atoms at cell corners and at (0.5,0.5,0.5) each surrounded by an octahedron of O atoms. The octahedra are distorted by an elongation along the z axis and joined at a single corner in the x-y plane. The Cu-O bond lengths are 2x2.40A in the z direction and 4x1.90A in the x-y plane, as given in table 7.2.

The tetragonal and orthorhombic phases are related by a simple doubling of the unit cell in the basal plane, with the bct lattice parameter 'a' becoming almost $\sqrt{2}a$ for the 'a' and 'b' orthorhombic lattice parameters. A small distortion results in a unit cell with orthorhombic symmetry- the Cu-O octahedra shown in fig 7.1 are tilted in the Cmca structure (by about 5^0 at 10K), with neighbouring octahedra 'out of phase'. This is an almost rigid tilting of the octahedra such that the Cu-O nearest neighbour distance is negligibly

Table 7.1. Lattice parameters and structure refinement parameters for La_2CuO_4 (bct and fco).

I4/mmm					Abma				
Atom		x	y	z	Atom		x	y	z
La	(4e)	0	0	0.362	La	(8f)	0.007	0	0.362
Cu	(2a)	0	0	0	Cu	(4a)	0	0	0
O(1)	(4e)	0	0	0.182	O(1)	(8e)	1/4	1/4	0.007
O(2)	(4c)	0	1/2	0	O(2)	(8f)	0.969	0	0.187

Lattice parameters

a	3.81A	a	5.406A
		b	5.370A
c	13.15A	c	13.15A

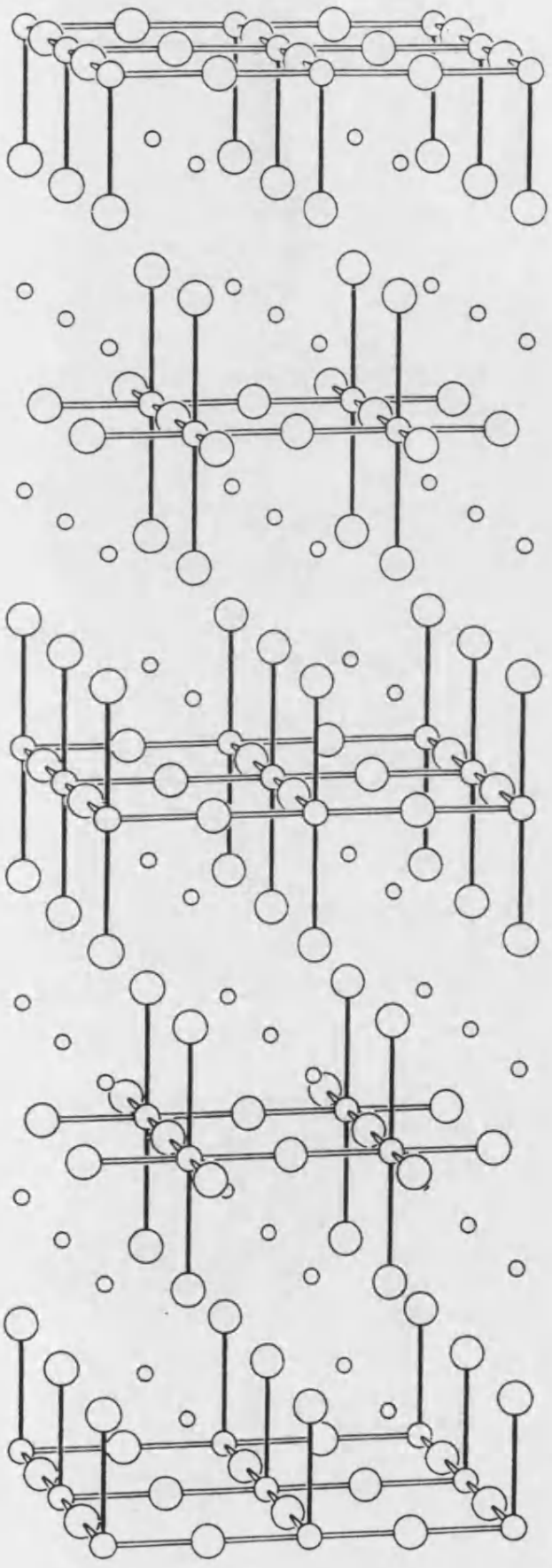

Figure 7.1

La_2CuO_4. I 4/mmm structure-showing 2x2x2 unit cells.

Key
- La
- Cu
- O

Table 7.2. Interatomic distances for La_2CuO_4- body centered tetragonal and base centered orthorhombic.

I 4/mmm		A bma	
Atoms	Distance(A)	Atoms	Distance(A)
Cu-O(1)x2	2.394	Cu-O(1)x2	2.465
Cu-O(2)x4	1.905	Cu-O(2)x4	1.908
Cu-Lax8	3.249	Cu-Lax2	3.226
		Cu-Lax4	3.241
		Cu-Lax2	3.289
La-O(1)x1	2.368	La-O(1)x1	2.311
La-O(2)x4	2.632	La-O(1)x1	2.581
La-O(1)x4	2.756	La-O(2)x2	2.589
		La-O(2)x2	2.677
		La-O(1)x2	2.764
		La-O(1)x1	2.981
O(1)-O(2)x4	3.060	O(1)-O(2)	3.117

altered- as shown in table 7.2. The small variation of interatomic distances between the two phases of La_2CuO_4 can be seen from table 7.2.

2)$Ba_2YCu_3O_7$

After the discovery of superconductivity at around 90K in Ba-Y-Cu-O the unit formula was rapidly determined by Grant et al. (1987) as $Ba_2YCu_3O_{7-x}$- many other structure determinations have been undertaken by neutron powder diffraction (Tarascon et al. (1987); Hazen et al. (1987); Siegrist et al., (1987); Cox et al. (1987); Capponi et al. (1987)) and X-ray diffraction of single crystals (Garbanskas et al. (1987), Hazen et al. (1987)). Many further studies have concentrated on the study of defects in the structure using electron microscopy since these are now believed to possibly play an important role in the mechanism of the superconductivity (Zandbergen et al., 1988 and refs. therein). The structure of $Ba_2YCu_3O_7$ used here is taken from the neutron powder diffraction data of Capponi et al (1987). An orthorhombic perovskite structure is given as the basic structure with Ba and Y ordered on the A site of the ABO_3 formula, tripling the c lattice parameter and with 2 oxygen vacancies in a unit cell.

The crystallographic space group is now Pmmm with the

ordered O(5) vacancies at 1b (1/2,0,0) in contrast to earlier work by Siegrist et al. (1987) which suggested the O vacancy split equally over the O(5) and O(4) (1e-(0,1/2,0)) sites- losing a mirror plane and resulting in the space group Pm2m. This was possibly due to twinning in the single crystal sample used. Two crystallographically inequivalent Cu atoms are now found- their environments are shown in fig 7.2 and table 7.4 shows the interatomic distances. Cu(1) has O atom vacancies along $\pm x$, but with close approaches of O along $\pm$ z (1.846A) and aong $\pm y$ (1.942A) compared with Cu(2) with O at $\pm$ x (1.929) and $\pm y$ (1.960A). Cu(2) is actually slightly displaced from the plane of a square of O atoms with one more O atom further away along z (2.26A). Cu(1) is at the centre of a slightly rhombically distorted square perpendicular to the xy plane. Referring to fig. 7.2 it can be seen that the Cu(2) and its co-ordinating O atoms form 2-dimensional layers in the xy plane. The Cu(1) atoms can be considered as forming 1-dimensional planes running along the y direction. The Cu(1) to O(1) distance of 2.298A is sufficient to isolate the layers from the chains. The Capponi et al. (1987) data shows no structural transition taking place between 5K and 300K but the crystals become superconducting at below about 90K.

$Ba_2YCu_3O_7$ loses oxygen reversibly at temperatures above

Figure 7.2

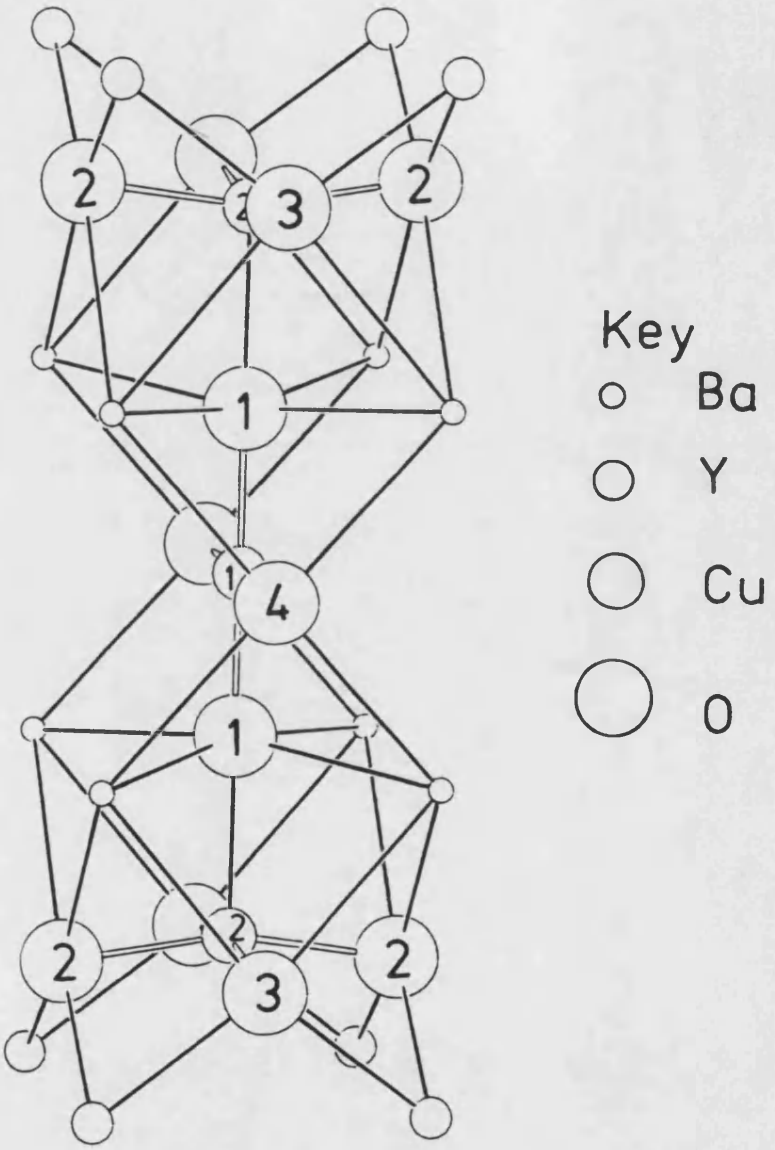

$Ba_2YCu_3O_7$ unit cell with ordered Oxygen vacancies. O(4) becomes a vacancy in $Ba_2YCu_3O_{6-}$ raising the crystal symmetry from orthorhombic to tetragonal.

about 500°C until, at around 900°C, the crystal composition has become $Ba_2YCu_3O_6$. However the precise composition of any sample is very sensitive to the method of preparation. This reduction of the oxygen ratio is accompanied by a (reversible) phase transition to tetragonal symmetry above about 600°C (Strobel et al., 1987). Crystals of $Ba_2YCu_3O_6$ have been grown (Bordet et al., 1987) and, in contrast to the O_7 compound, show no evidence of superconductivity right down to liquid helium temperatures. The tetragonal O_6 unit cell parameters vary little from the orthorhombic O_7 compound, as shown in table 7.3. The O_6 compound interatomic distances are compared with the O_7 compound in table 7.4. The oxygen vacancies are again found to be ordered (around the Cu(1) atom) with an absence of O(4) in addition to the O(5) vacancies found in the orthorhombic crystals. This reduces the Cu(1) coordination from square planar to simple linear and destroys the Cu-O chains which ran through the crystal in the orthorhomic form. The Cu(2)-O sheets remain in this structure. The O(4) vacancies cause the Cu(1)-O(1) bond length to be contracted to 1.80A, which is even shorter than that found for 2-fold coordinated Cu in Cu_2O . Consequently the Cu(2)-O(1) bond is weakened and lengthened to 2.43A from 2.30A found in the O_7 compound, that is extending the epical distortion of the oxygen octahedra. This accounts for the small increase in the c

Table 7.3. Lattice parameters and structure refinement parameters for $Ba_2YCu_3O_7$ and $Ba_2YCu_3O_6$.

$Ba_2YCu_3O_7$				$Ba_2YCu_3O_6$			
Atom	x	y	z	Atom	x	y	z
Y (1a)	0	0	0	Y (1d)	1/2	1/2	1/2
Ba (2q)	0	0	0.312	Ba (2h)	1/2	1/2	0.1921
Cu(1) (1h)	1/2	1/2	1/2	Cu(1) (1a)	0	0	0
Cu(2) (2t)	1/2	1/2	0.1444	Cu(2) (2g)	0	0	0.3605
O(1) (1d)	1/2	0	1/2	O(1) (2g)	0	0	0.154
O(2) (2t)	1/2	1/2	0.3438	O(2) (4l)	1/2	0	0.3794
O(3) (2r)	0	1/2	0.1233				
O(4) (2s)	1/2	0	0.1210				

Lattice parameters

a	3.8213A	a	3.8715A
b	3.8854A		
c	11.656A	c	11.738A

Table 7.4 Interatomic distances for $Ba_2YCu_3O_7$ and $Ba_2YCu_3O_6$.

$Ba_2YCu_3O_6$		$Ba_2YCu_3O_7$	
Atoms	Distance(A)	Atoms	Distance(A)
Ba-O(1)x4	2.775	Ba-O(1)x4	2.741
Ba-O(2)x4	2.929	Ba-O(2)x2	2.982
		Ba-O(3)x2	2.959
		Ba-O(4)x2	2.876
Y-O(2)x8	2.399	Y-O(2)x4	2.409
		Y-O(3)x4	2.385
Cu(1)-O(1)	1.804	Cu(1)-O(1)x2	1.846
		Cu(1)-O(4)x2	1.942
Cu(2)-O(1)	2.428	Cu(2)-O(1)	2.298
		Cu(2)-O(3)x2	1.960
Cu(2)-O(2)x4	1.948	Cu(2)-O(2)x2	1.929
Ba-Ba	3.871	Ba-Ba	3.885
Ba-Y	3.614	Ba-Y	3.688
Ba-Cu(1)	3.547	Ba-Cu(1)	3.470
Ba-Cu(2)	3.377	Ba-Cu(2)	3.376
Y-Cu(2)	3.190	Y-Cu(2)	3.208
Cu(1)-Cu(2)	4.232	Cu(1)-Cu(2)	4.144
Cu(2)-Cu(2)	3.274	Cu(2)-Cu(2)	3.388
O(1)-O(2)	3.281	O(1)-O(2)	3.199
O(2)-O(2)	2.738	O(1)-O(3)	3.217
		O(2)-O(3)	2.725

lattice parameter shown in table 7.3.

7.3 Calculations

The input atomic orbital energies are given in tables 7.5 and 7.6, along with the resultant calculated Mulliken populations, for the La_2CuO_4 and Ba-Y-Cu-O compounds respectively. The calculated densities of states (dos) with projections and E vs. $\underline{k}$ are shown for La_2CuO_4 (bct) (figs 7.3 and 7.4), La_2CuO_4 (fco) (figs 7.5 and 7.6), $Ba_2YCu_3O_7$ (figs 7.7 and 7.8) and Ba_2YCuO_6 (figs 7.9 and 7.10). The relevant Brillouin zones showing the irreducible wedge (which contains the volume sampled for the densities of states) and the high symmetry lines taken for the $E(\underline{k})$ are presented as fig. 7.11. The coordinates of the high symmetry k points shown are given in tables 7.7 and 7.8. Between 100 and 210 $\underline{k}$ points were used to calculate the dos and projected dos: the $E(\underline{k})$ graphs used from 15 to 20 intervals between each symmetry point. The deeper energy states of almost completely oxygen s character are not shown on the figures since they are well removed from the fermi level and thus play a minimal role in the physical properties of these compounds.

Table 7.5

La_2CuO_4- input atomic energy levels and charge occupations.

Atom	Energy	Occupation
La		
s	-4.99	-
p	-2.80	-
d	-4.57	0.98
Cu		
s	-7.00	0.09
p	-3.40	-
d	-10.00	9.28
O (average)		
s	-25.80	1.98
p	-11.40	5.46

Energy in eV, occupations in electrons.

Table 7.6

Converged energy and charges for $Ba_2YCu_3O_7$.

Atom	Energy	Occupatⁿ	Atom	Energy	Occupatⁿ
Ba			Cu(2)		
s	-3.86	-	s	-7.00	0.07
p	-2.48	-	p	-3.41	-
Y			d	-10.20	9.21
s	-4.99	-	O(1)		
p	-2.87	-	s	-25.76	2.0
d	-3.95	0.7	p	-11.43	5.82
Cu(1)			O(2,3)		
s	-7.00	0.12	s	-25.76	1.99
p	-3.41	-	p	-11.43	5.58
d	-10.33	9.19	O(4)		
			s	-25.76	2.00
			p	-11.43	5.71

Converged energy and charges for $Ba_2YCu_3O_6$.

Atom	Energy	Occupatⁿ	Atom	Energy	Occupatⁿ
Ba			Cu(2)		
s	-3.88	-	s	-7.04	0.1
p	-2.50	-	p	-3.37	-
Y			d	-9.39	9.36
s	-4.99	-	O(Average)		
p	-2.87	-	s	-25.76	2.0
d	-3.95	0.7	p	-11.43	5.75
Cu(1)					
s	-7.00	0.3			
p	-3.41	-			
d	-8.30	9.62			

Energy in eV, occuaptions in electrons.

Fig 7.3 La2CuO4 (bct)

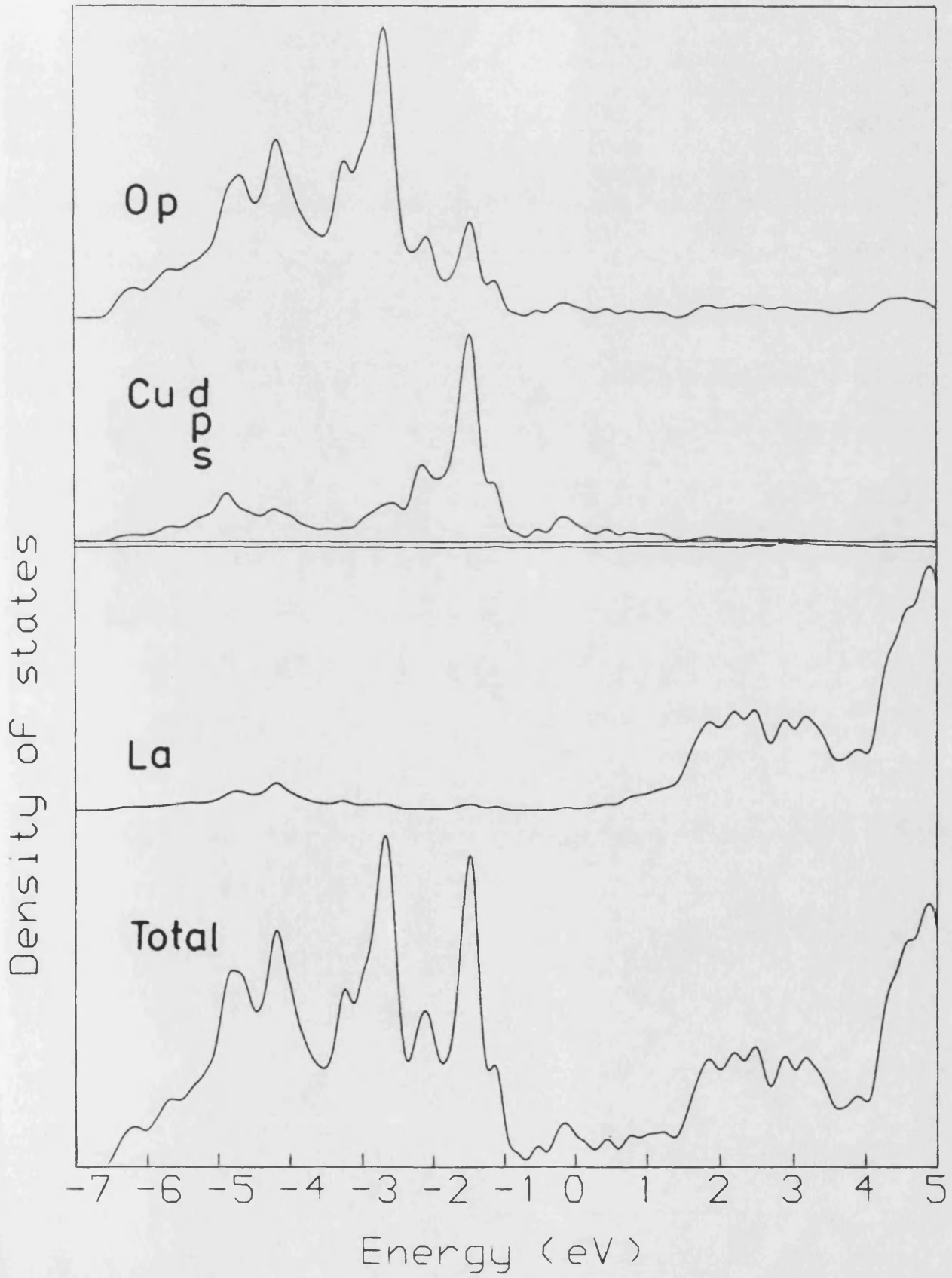

Fig 7.4 La2CuO4 (bct)

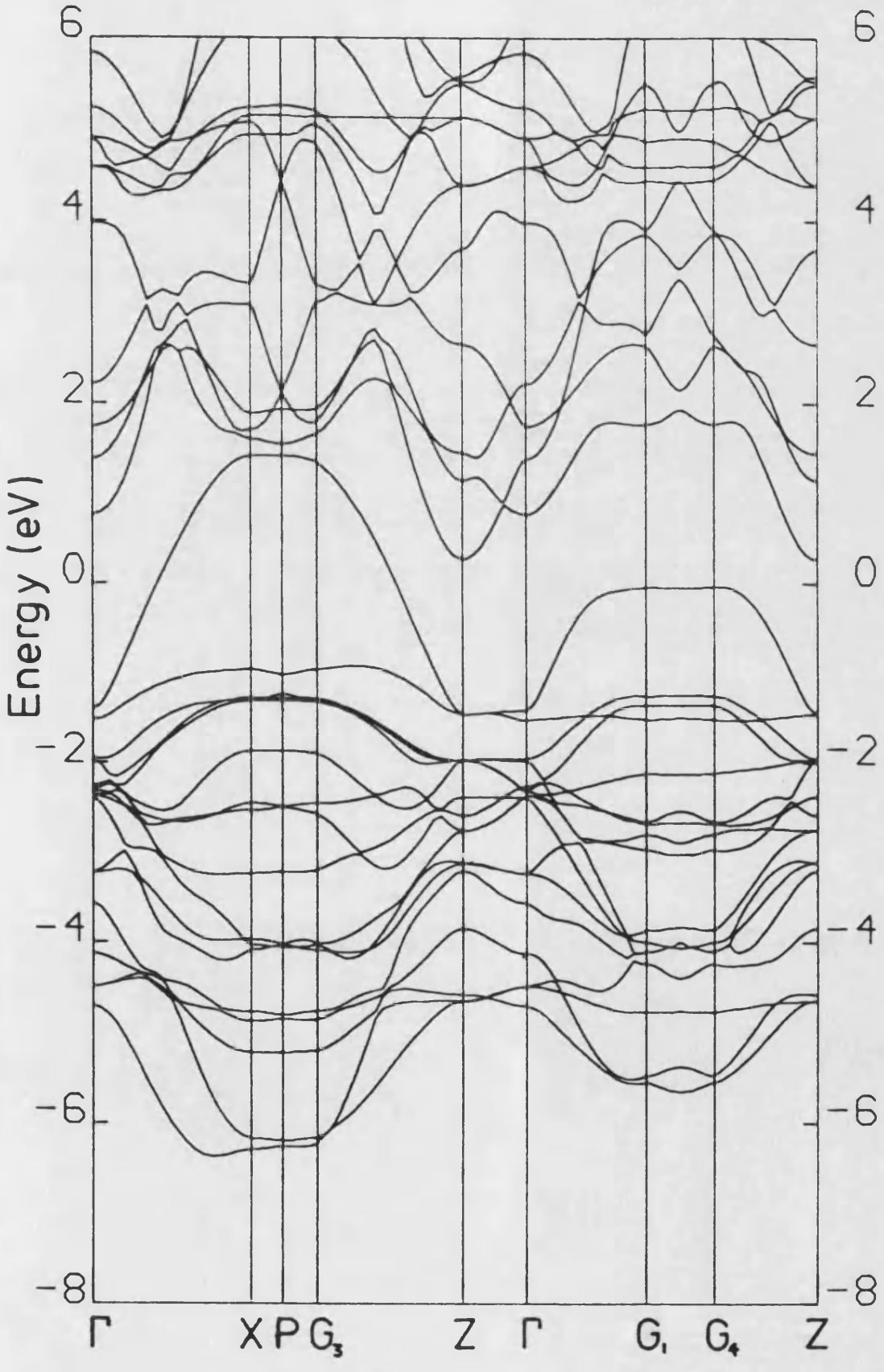

Fig 7.5 La2CuO4(Fco)

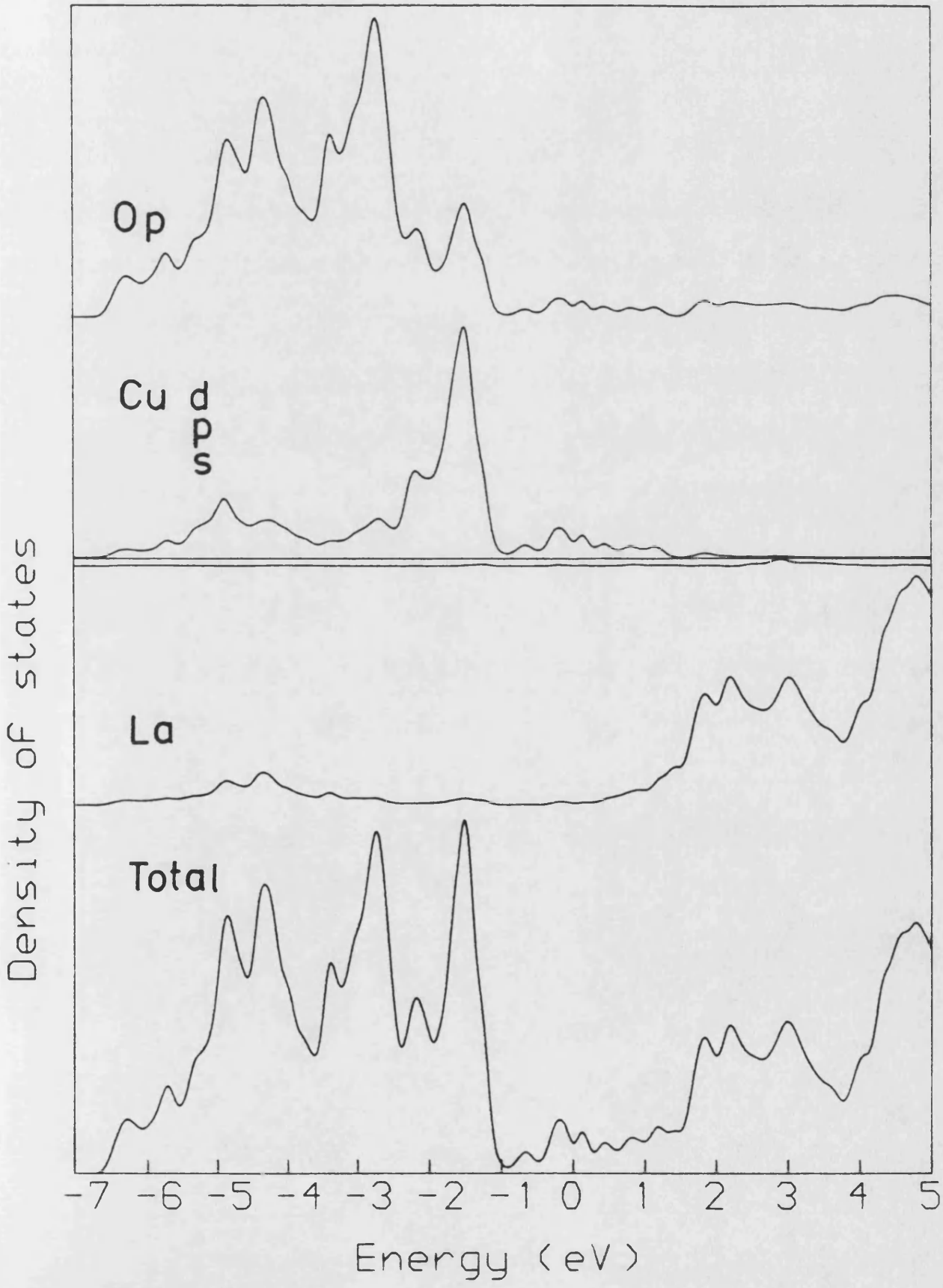

Fig 7.6 La2CuO4(fco)

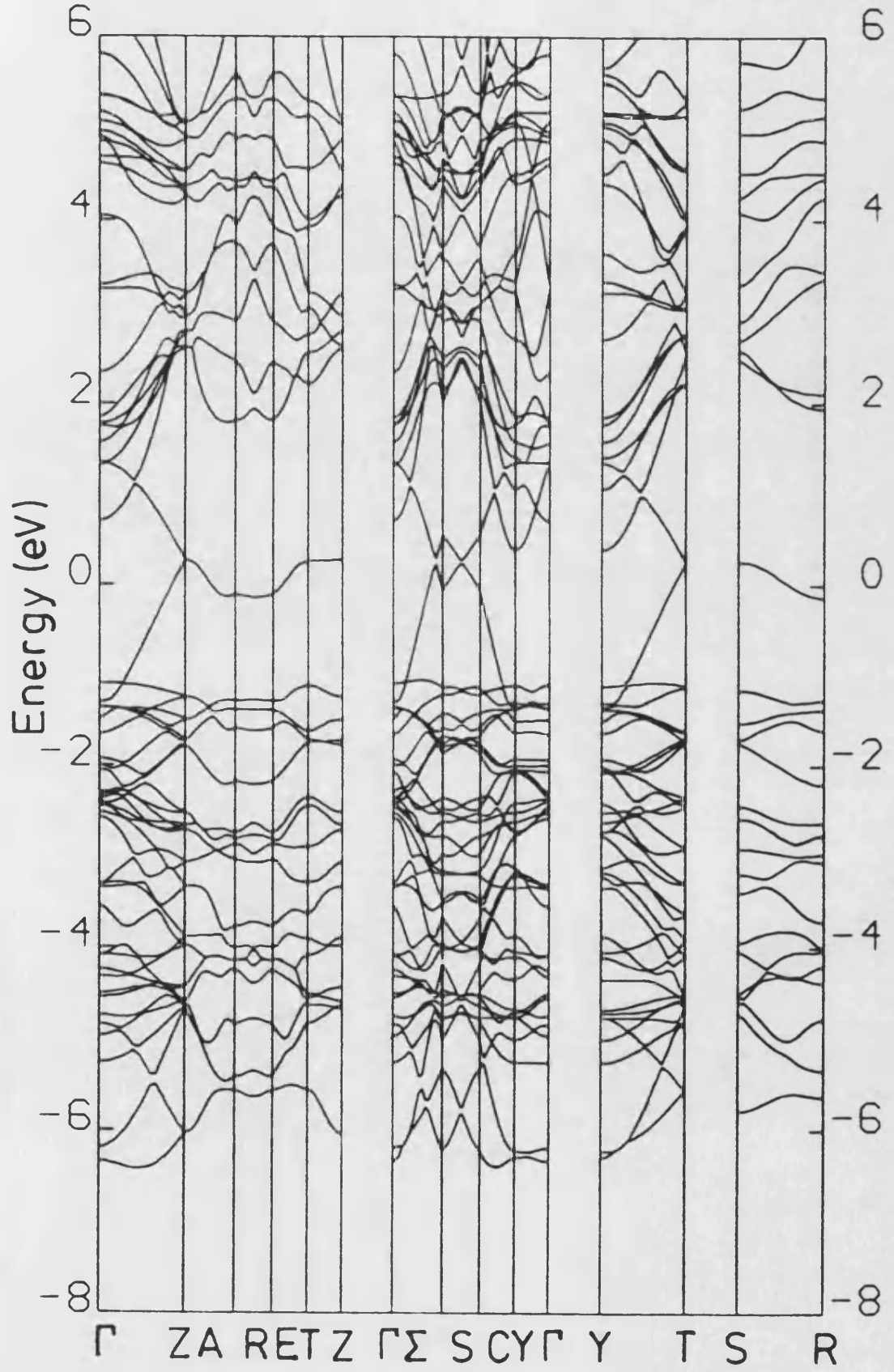

Fig 7.7 Ba2YCu3O7

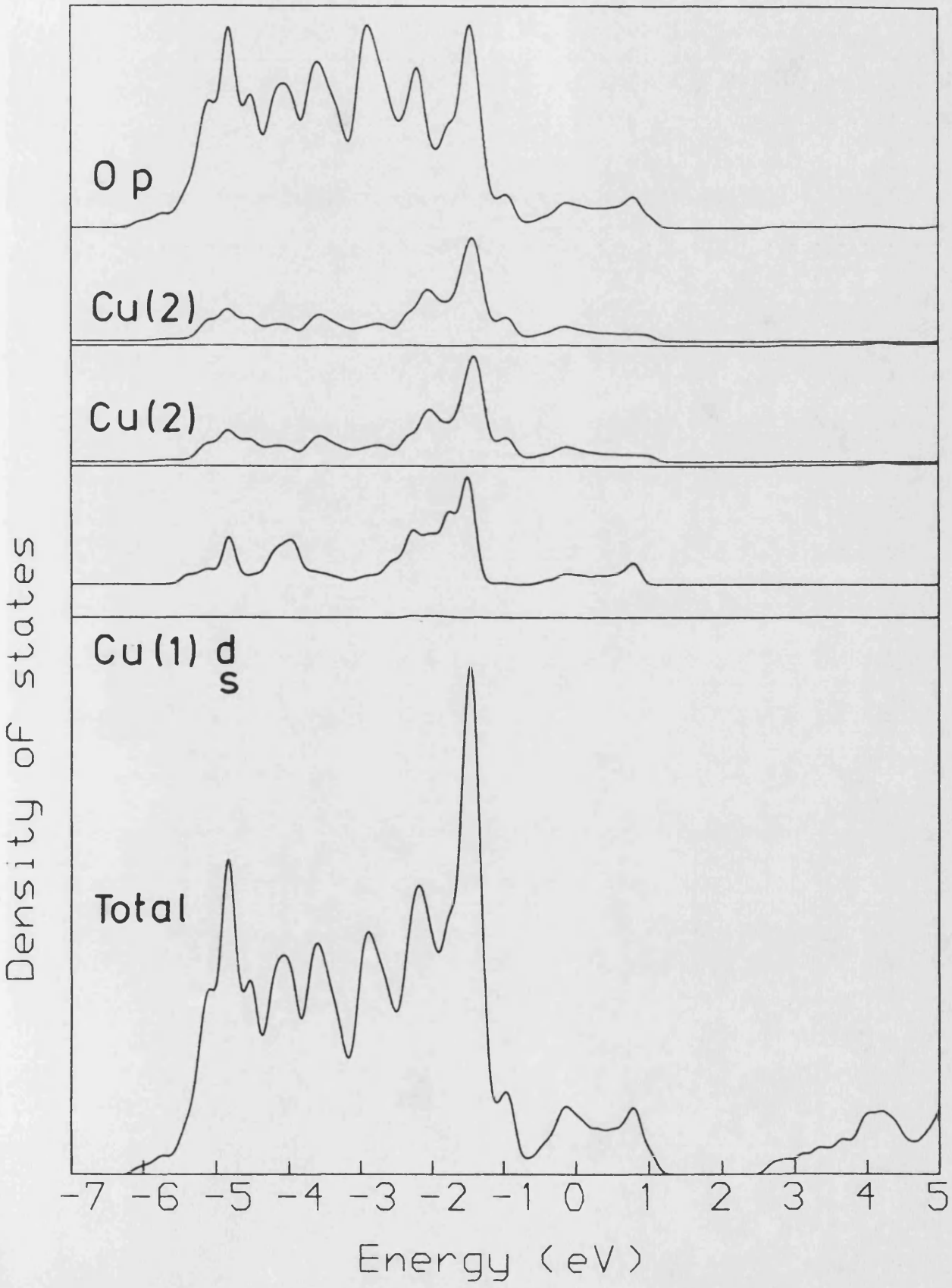

Fig 7.8 Ba2YCu3O7

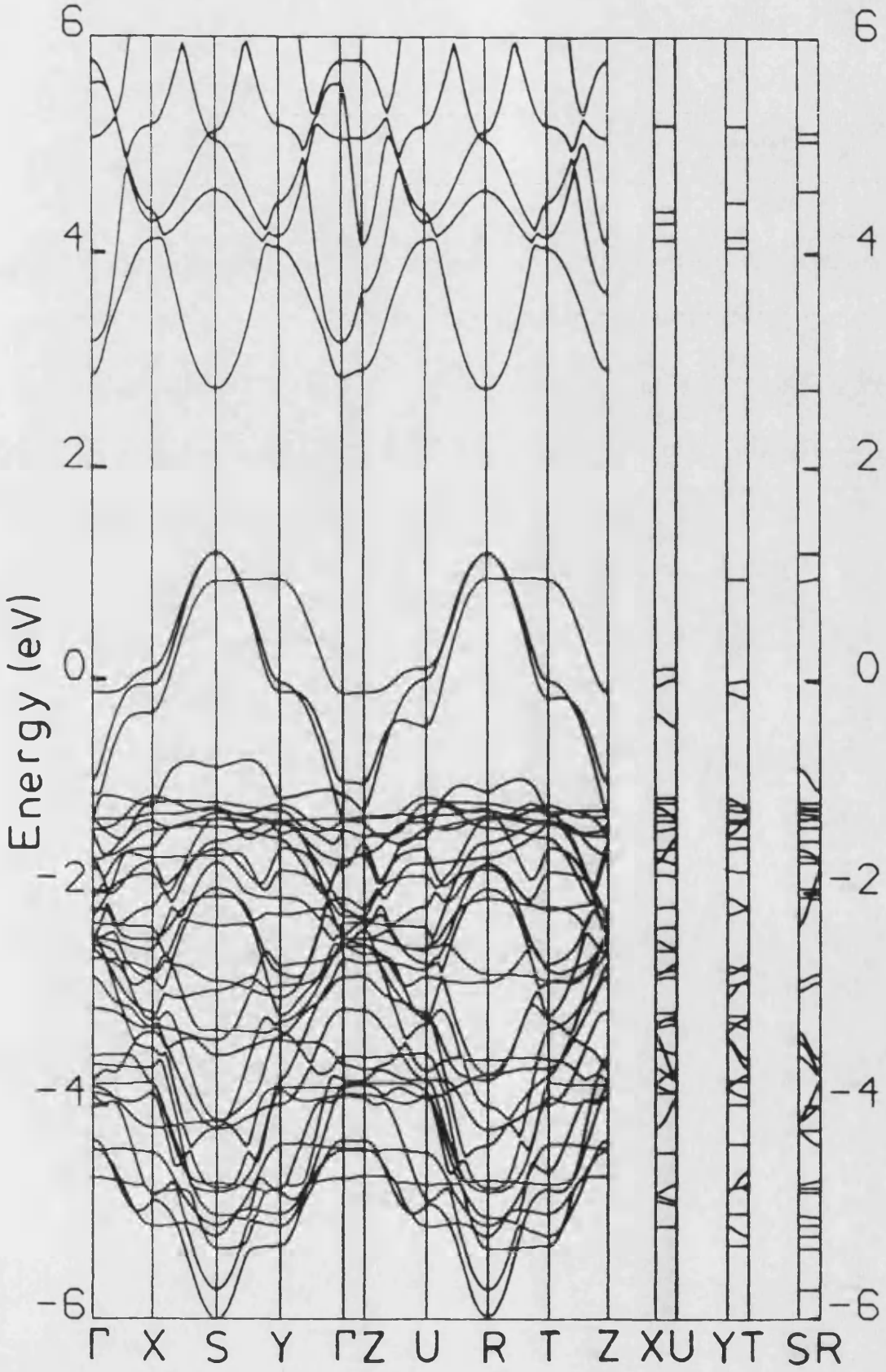

Fig 7.9 Ba2YCu3O6

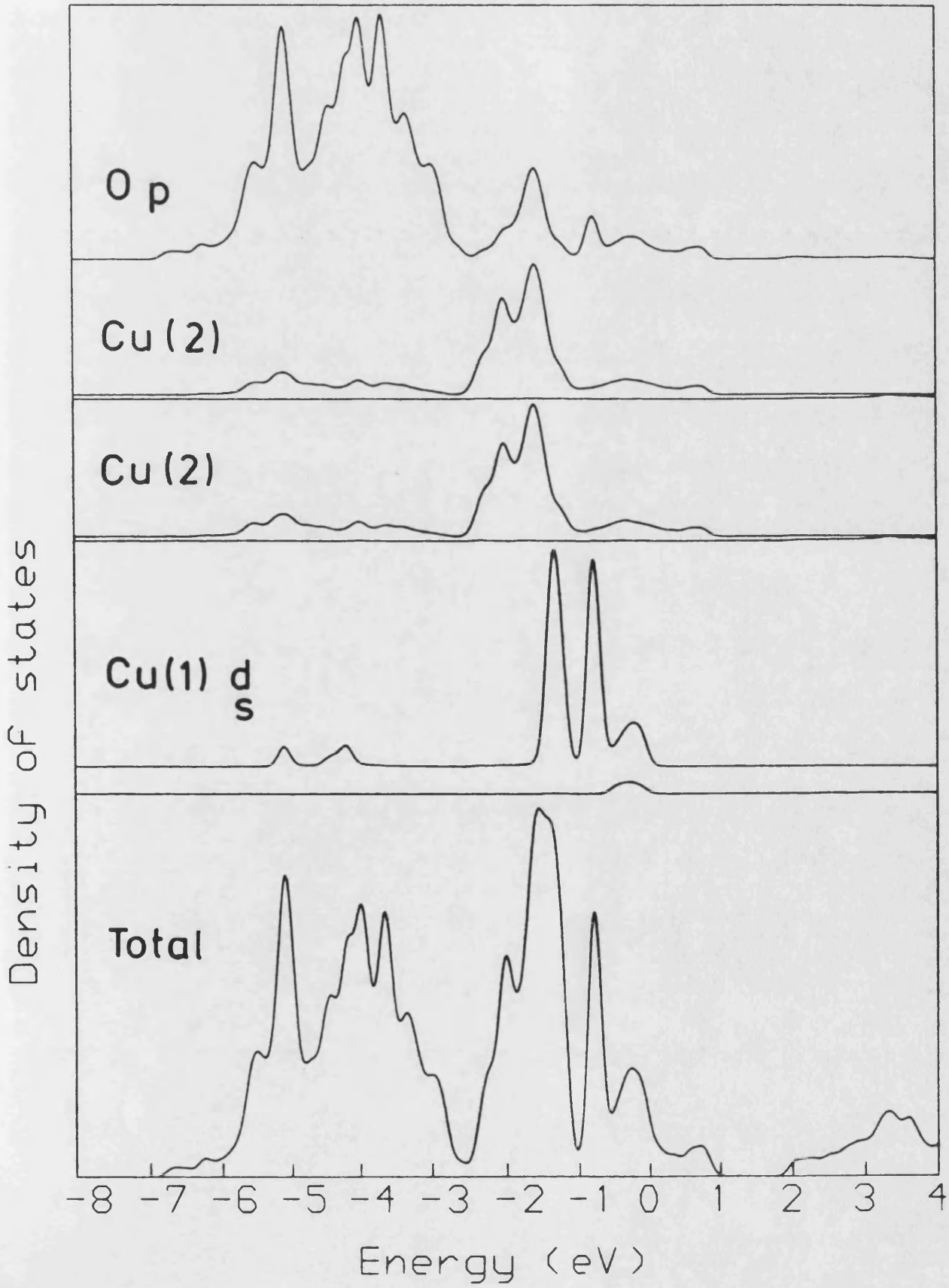

Fig 7.10 Ba2YCu3O6

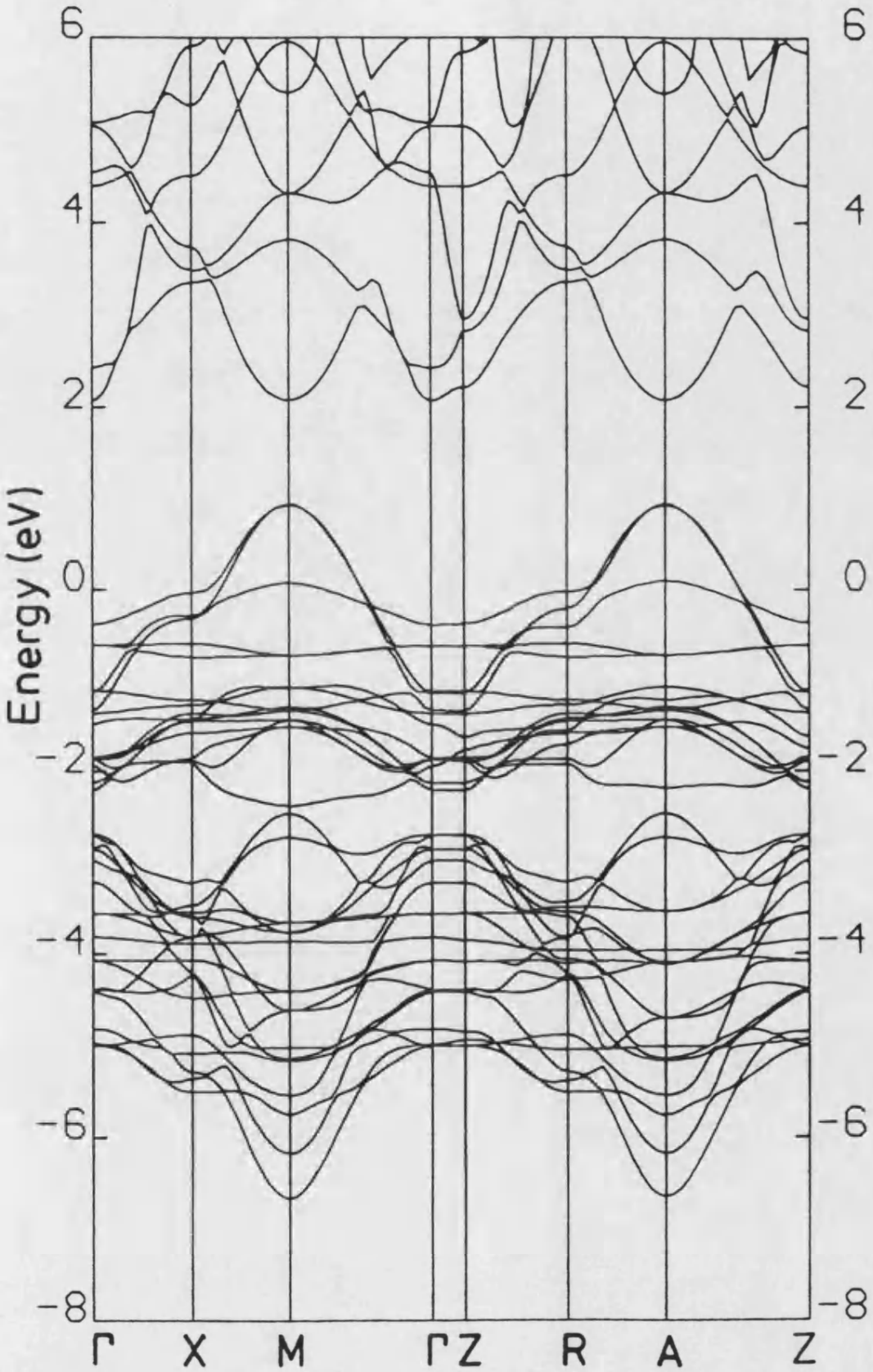

Table 7.7. La_2CuO_4- coordinates of symmetry points in Brillouin zones.

a) body centred tetragonal

	k_x	k_y	k_z
Γ	0.0	0.0	0.0
X	0.25	0.25	0.0
P	0.25	0.25	0.25
G_3	0.229	0.229	0.5
Z	0.0	0.0	0.5
Γ	0.0	0.0	0.0
G_1	0.271	0.0	0.0
G_4	0.229	0.0	0.5
Z	0.0	0.0	0.0

b) base centred orthorhombic

	k_x	k_y	k_z
Γ	0.0	0.0	0.0
Z	0.0	0.0	0.5
	0.2917	0.0	0.5
	0.2083	0.5	0.5
T	0.0	0.5	0.5
Z	0.0	0.0	0.5
Γ	0.0	0.0	0.0
	0.2917	0.0	0.0
	0.2083	0.5	0.0
Y	0.0	0.5	0.0
Γ	0.0	0.0	0.0
Y	0.0	0.5	0.0
T	0.0	0.5	0.5
S	0.25	0.25	0.0
R	0.25	0.25	0.5

Table 7.8. Ba-Y-Cu-O- coordinates

of high symmetry points in Brillouin zones.

$Ba_2YCu_3O_7$				$Ba_2YCu_3O_6$			
Orthorhombic				Tetragonal			
Γ	0.0	0.0	0.0	Γ	0.0	0.0	0.0
X	0.5	0.0	0.0	X	0.5	0.5	0.0
S	0.5	0.5	0.0	M	0.5	0.5	0.0
Y	0.0	0.5	0.0	Γ	0.0	0.0	0.0
Γ	0.0	0.0	0.0	Z	0.0	0.0	0.5
Z	0.0	0.0	0.5	R	0.5	0.0	0.5
U	0.5	0.0	0.5	A	0.5	0.5	0.5
R	0.5	0.5	0.5	Z	0.0	0.0	0.5
T	0.0	0.5	0.5				
Z	0.0.	0.0	0.5				
X	0.5	0.0	0.0				
U	0.5	0.0	0.5				
Y	0.0	0.5	0.0				
T	0.0	0.5	0.5				
S	0.5	0.5	0.0				
R	0.5	0.5	0.5				

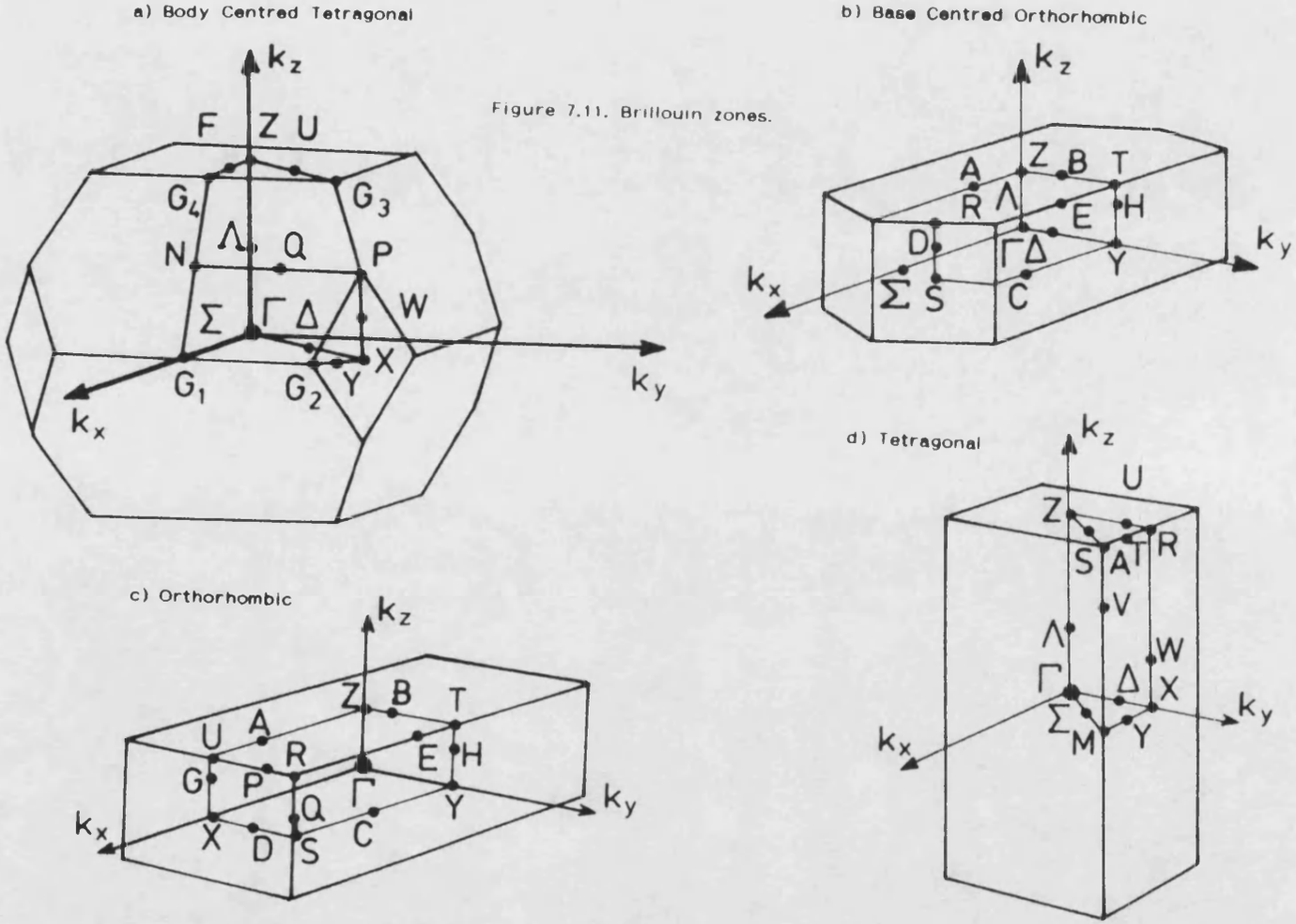

Figure 7.11. Brillouin zones.

a) La_2CuO_4

The similarity of the bct and fco structures is immediately apparent from figs. 7.4 and 7.6. In fact a folded version of the high temperature body centred tetragonal band structure is almost indistinguishable from the face centre orthorhombic low temperature structure. The doubling of the unit cell in the basal plane for the fco structure therefore has little effect on these one electron calculations. The experimentally observed semiconducting behaviour may therefore possibly be assumed to be attributable to electrron localization within the narrow upper d bands preventing normal itinerant banding effects (which are not easily predicted in these one electron calculations). The environment of each atom changes little as the oxygen octahedra tilt rigidly in the $\sqrt{2}x\ \sqrt{2}$ PLD (periodic lattice distortion). Also to be considered is the possibility of a spin-density-wave (SDW) which may act to split the doubly-spin-degenerate band passing through E_f and lower the total energy of the system (eg. see Chan and Heine, 1973). It has been proposed that spin-fluctuations may be responsible for high T_c superconductivity (eg. Anderson, 1987; Hirsh, 1987 and Emery, 1987). Hasegawa and Fukuyama (1987) proposed a ground state of a SDW in orthorhombic La-Cu-O; a low density of oxygen vacancies in La_2CuO_4 has been since

shown to exhibit antiferromagnetism (eg. Vaknin et al., 1987 and Freltoft et al., 1987). Recent band structure calculations (Guo et al., 1988) using a spin-polarised self-consistent LMTO-ASA method have investigated the possible antiferromagnetism in La-Cu-O in order to explain the observed semiconductivity. These results imply that La-Cu-O is on the verge of a SDW transition to an antiferromagnetic state since no reasonable total energy reduction is found for the SDW state but a small semiconducting gap can be induced. They also point out that the 'doping' of La-Cu-O with Ba substituting for La will leave the lower band of the semiconducting gap only partially filled and thus further reduce any total energy saving from the SDW state.

A large charge transfer from the La atoms is shown in table 7.6- this may be predicted from the input free atomic energy levels and remembering that the more tightly bound d electrons will not hybridise as strongly as the s orbitals. Approximately one d electron has therefore been assigned to the La d orbitals up to the Fermi level by the Mulliken population method.

The Cu atom in La-Cu-O sits in an essentially square planar crystal field- this coordination is well known for atoms containing 8 or 9 d electrons. The crystal field splitting induced by the oxygen atoms around the

Cu causes a characteristic lifting of the degeneracy of the five d orbitals and is shown in figure 7.11.1. The relative energy of the Cu d_{z2} orbital is sensitive to the particular environment of the Cu atom and fig. 7.11.1 shows a general case. The highly electronegative oxygen atoms will raise the energy of the Cu d_{x2-y2} orbital since the lobes of this orbital are directed toward the oxygen atoms. The similar energies of the Cu d and O p orbitals, which differ by less than 1.5 eV for the free atom input energy, also increases their interaction resulting in the highly dispersive anti-bonding band which cuts through E_f and the large total bandwidth of the upper valence band region (including the half-filled band). The total width of the Cu_d-O_p hybridised bands of about 8.0eV is in reasonble agreement with other band structure calculations giving 7.9eV, 9.0 eV, 9.0eV,and 9.5eV respectively from- Takegahara et al., 1987; Yu et al., 1987; Guo et al., 1988 and Mattheiss, 1987.

The lone band cutting through Ef in the bct form is half filled and is well nested in $\underline{k}$ space- suggestive of a doubling of the unit cell in a commensurate Peierls distortion. The observed bct to fco transition is indeed a $\sqrt{2}x\sqrt{2}$ transition but is not accompanied by the expected gap opening at Ef- it is restricted by symmetry requirements. However, the experimentally observed

Fig. 7.11.1

Crystal field splitting for square planar coordination.

Large dots represent negatively charged ligands.

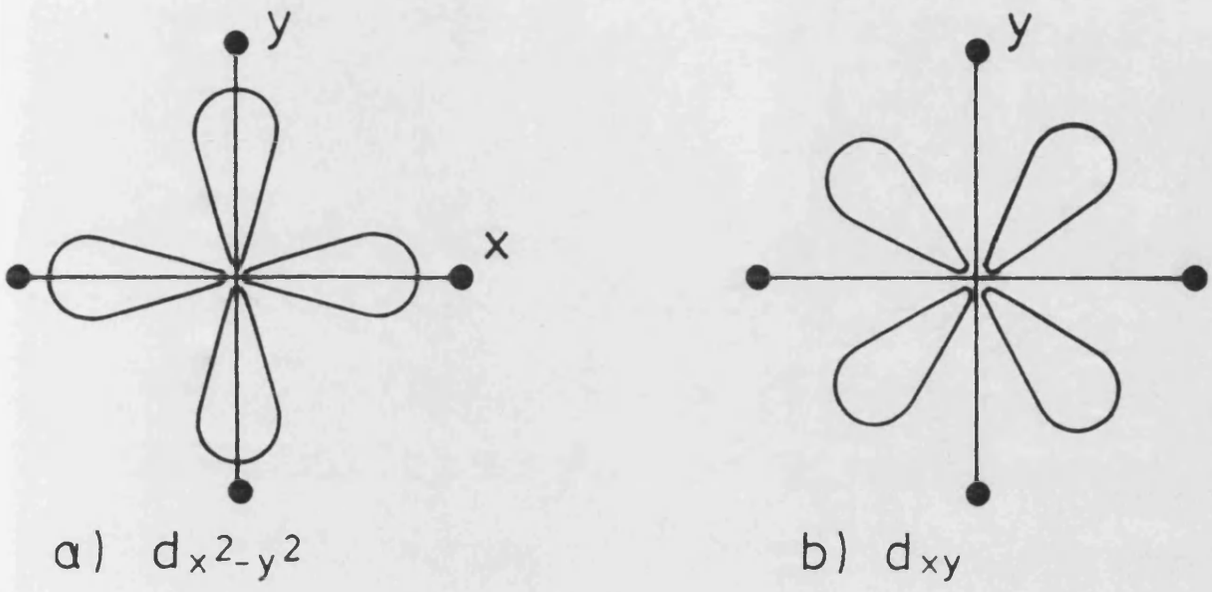

a) $d_{x^2-y^2}$ b) d_{xy}

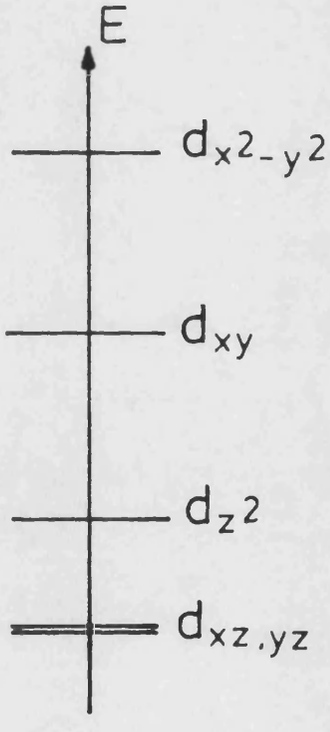

Relative energies of d orbitals.

semi-metallic/semiconductor transition which accompanies the tetragonal to orthorhombic phase change is shown in these calculations to lead to a reduction in the densities of states at the fermi level. The already low value of 1.6 states electron^{-1} Cu atom^{-1} for bct La_2CuO_4 falling to 1.1 states for fco La_2CuO_4- this is in reasonable agreement with the values for the tetragonal form of 1.39 states given by Temmerman et al., 1987a and 1.88 states given by Takegahara et al., 1987. Yu et al., 1987 calculate a lower value of 1.1 states per cell. There is an indirect overlap between the hybridised Cu d and O p bands and the higher bands beginning at about 0.5 above E_f in the bct structure.

The low dimensionality of these crystals shown in real space by the CuO_2 sheets is clearly demonstrated in $\underline{k}$ space by the minimal dispersion in the z* direction, for example along the gamma-Z symmetry line for the bct compound. The dos shows a wide band of states from about 6.5 eV below Ef upwards which is composed of metal d-/ oxygen p-states, this falls off rapidly from about 1.5 eV below Ef but with a small peak around Ef. This peak is caused by the dispersionless band between G_1 and G_4 (fig. 7.4) in the bct compound which is reduced in the fco case giving a pronounced dip at Ef (but see note below on stoichiometry- which may affect the dos at Ef). There is a large metal d contribution in this region

above about 2.5 eV below Ef.

b) $Ba_2YCu_3O_7$ and $Ba_2YCu_3O_6$.

The strong hybridisation of the Cu d and O p orbitals in $Ba_2YCu_3O_7$ can be seen from table 7.9 which shows the eigenvectors of the basis set near the Fermi energy for three points in the Brillouin zone.

The E(k) and densities of states for these two compounds show great similarities to the two La compounds. Here there are 3 Cu atoms per unit cell and these can be seen to produce the 3 bands crossing the Fermi level at the top of the valence band. There is now no overlap between the metal d-/ oxygen p-hybridisation broad band and the higher energy orbitals, thus there are no states from approximately 1eV to 3eV above Ef. The general shape of the density of states of fig. 7.7 has been confirmed by photo-emission spectroscopy of $Ba_2YCu_3O_{7-x}$ for which Brown et al., 1987, have observed an intense band about 4eV wide, beginning about 1.5eV below the Fermi level, with a small wing of states extending up to E_f, where the density of states is relatively low.

The square planar crystal field as (outlined above) also plays an important role in the Ba-Y-La-Cu compounds. Figure 7.12 shows schematically the anti-bonding

Table 7.9. Orbital decomposition of the three partially occupied bands in $Ba_2YCu_3O_7$ at three symmetry points in the Brillouin zone.

Eigenvalue	Percentage character of bands					
	Atom type					
eV	Cu(1)	Cu(2)	O(1)	O(2)	O(3)	O(4)
	$\underline{k}$=(0,0,0)					
-8.8	-	58	22	2	18	2
-8.7	-	66	4	25	5	
-7.9	54	6	36	1		1
	$\underline{k}$=(1/2,0,0)					
-8.0	44	28	18	6	2	1
-7.8		64	4	28	2	
-7.6	16	46	12	26		
	$\underline{k}$=(1/2,1/2,0)					
-6.8	53		22			24
-6.5		52		25	25	
-6.5		52		25	25	

Figure 7.12. Schematics showing the Cu d and O p antibonding orbital combinations which produce the d-band maxima.

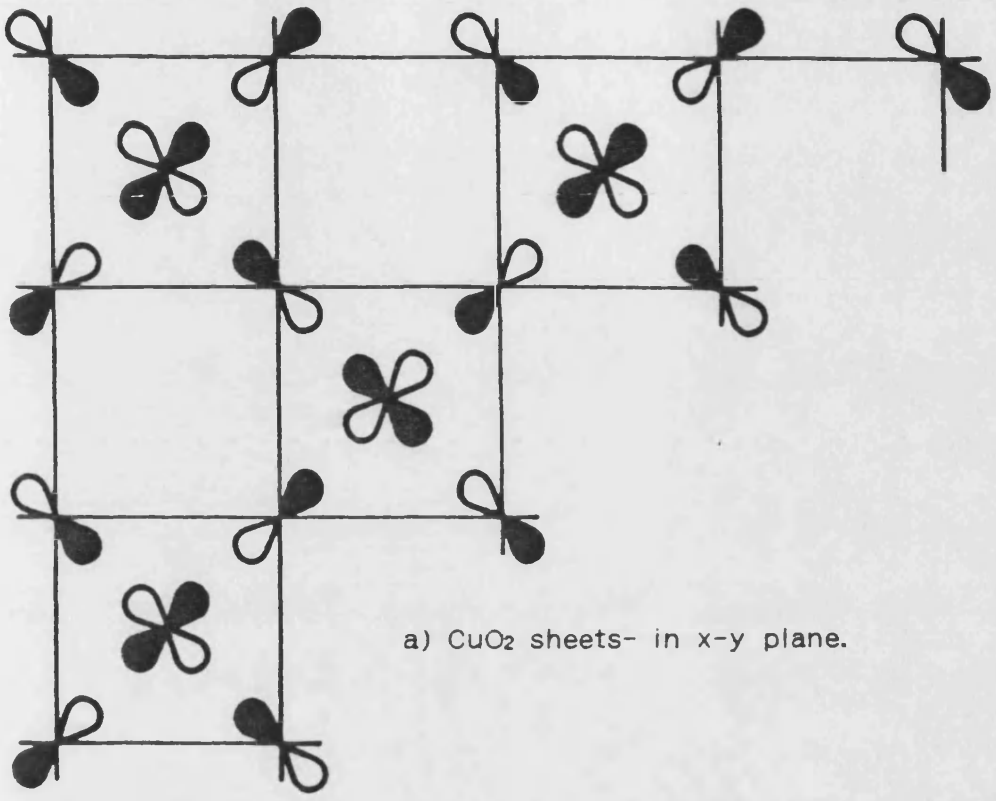

a) CuO_2 sheets- in x-y plane.

b) CuO_3 chains along y- in y-z plane.

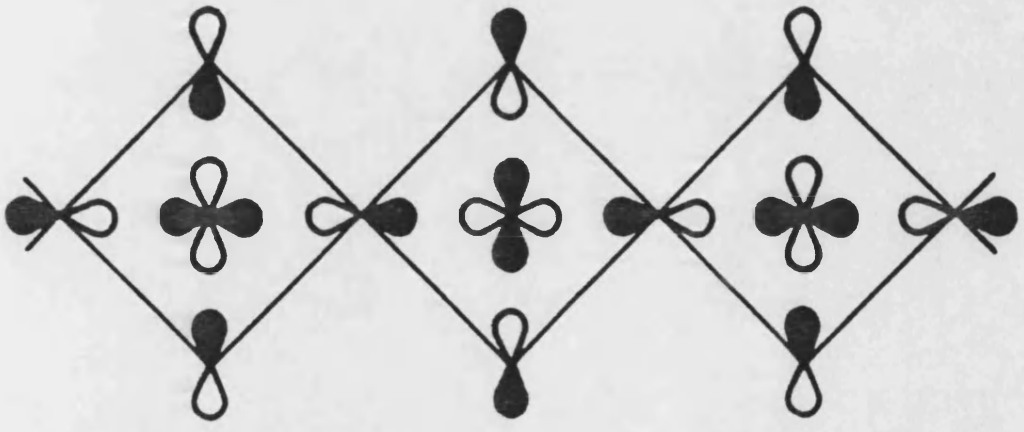

interaction of the Cu d and O p orbitals in this field. The axes are now rotated so that for the CuO_2 sheets the d_{xy} orbital has the highest energy and interaction with the O p orbitals and for the CuO_3 chain the d_{z2-x2} is the highest. This interaction results in the heavily $\underline{k}$ dependent bands cutting through E_f. The near double degeneracy thoughout the Brillouin zone of the Cu d bands for both these compounds is indicative of the small interaction between CuO_2 sheets. The reduced dispersion along z^* reinforces this view. The Cu(1) atoms in the O_7 compound which form the CuO_3 chains results in little dispersion of the bands with strong Cu(1) character in the x^* direction because of the O(5) vacancy along x; the Cu(1) in the O_6 compound gives bands showing small dispersion (ie. reduced $\underline{k}$ dependence) throughout the Brillouin zone and thus appears almost as a CuO_2 molecule trapped in the layers of $Cu(2)O_2$.

There is a further separation in the O_6 compound into predominantly O p based and Cu d based regions. This is a consequence of the increased Cu d charge when the O(4) vacancy appears- which lifts the Cu d atomic orbital level away from the O p level. A count of the bands of fig. 7.8 gives 15 bands in the upper valence region around Ef - the correct number to accomodate the 30 electron states from the 3 Cu atom's d orbitals. Below

these are the 18 bands attributable to the O p orbitals. Note that after the guassian convolution to smooth the densities of states (fig 7.7) a non-zero number of states is shown in the region where the p and d bands approach.

In E($\underline{k}$) figure for the O_6 compound (fig. 7.10) the two bands anti-bonding bands crossing E_f would be half-filled and therefore show metallic behaviour. The fact that, for oxygen ratio below 6.5, this material is semiconducting must be attributed to localisation effects.

The actual charge state of the copper is a matter of some interest since there may be some competition between the stable states of Cu^{1+} and Cu^{3+} (eg. see Wilson, 1987). In the case of Cu^{1+} the stabiltiy is provided by the Cu ion having a filled d shell which is then semi-core-like and localises the electrons to the copper. For Cu^{3+} the Cu ion has 8 d electrons and the square planar coordination around the ion is a favourable low energy state, as outlined above. The 3+ state for Cu in $Ba_2YCu_3O_7$ has not been observed experimentally and it appears that the Cu exists in the 1+ or 2+ states with the ratio of these being a function of temperature (Sarma and Rao, 1988). The exact atomic ratios of the particular sample analysed must be borne

in mind since, for example, the replacement of trivalent atoms by divalent atoms will act to decrease the charge on the copper ion. Table 7.5 shows 9.3 d electrons on the Cu atom in La-Cu-O, that is a charge state of +1.7 - this will increase as the La atom are substituted by group II atoms. For $Ba_2YCu_3O_7$ table 7.6 shows, suprisingly, Mulliken populations on both types of copper of 9.2 d electrons- it is more probable that the charge state of the atoms fluctuates around this value. While the formal charge on the O_6 compound is 1+ for Cu(1) and 2+ for Cu(2) table 7.6 shows Cu(1) having a population of 9.6 d electrons and Cu(2) with 9.4 electrons. The effects of localisation, however, are not considered in these calculations, as explained above, and therefore the copper d charges may well be underestimated.

Figure 7.13 shows the calculated fermi surface for $Ba_2YCu_3O_7$ which shows three bands passing through the fermi energy. Four sections are given here through the irreducible Brillioun zone along $\underline{z}^*$ at 0, 1/4, 1/2 and 1.0 of the zone. It is immediately apparent that there is little dispersion in this direction. The small region enclosing gamma is very sensitive to the electron count and is therefore heavily dependent on the stoichiometry of the sample. It is interesting to note the middle band in fig. 7.7 shows good nesting ($\sqrt{2}x\sqrt{2}$) in the $\underline{x}^*$-$\underline{y}^*$

Fig. 7.13 The Fermi surface of $Ba_2YCu_3O_7$.

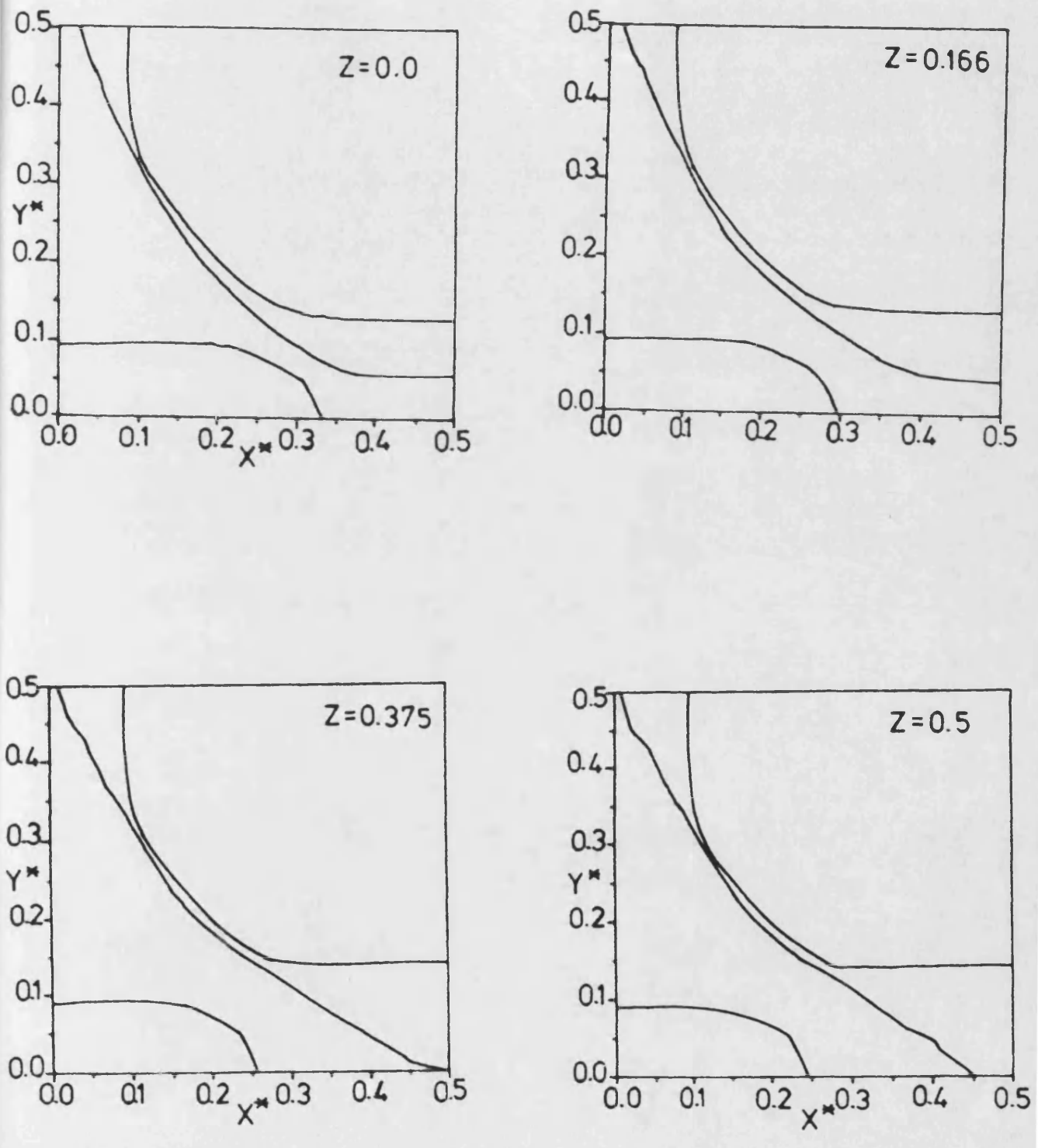

plane- reminiscent of the PLD in La_2CuO_4. As in the O_7 case the possible crossing of the third d band through Ef cannot be conclusively resolved.

7.4 Conclusion

These calculations reproduce the major features of similar calculations and spectroscopic analysis, with the added ease of using a basis of atomic orbitals. This allows a simple interpretation of the results without the need to resort to extrapolation schemes. The major findings of these calculations are listed below:-

1) The large oxygen p character of the bands around the Fermi level are clearly seen in the eigenvectors. This is an unusual and distinguishing feature of these ceramic compounds.

2) A low densities of states is found at the Fermi energy for all these compounds- with a reduction calculated for the semiconducting fco La_2CuO_4 and $Ba_2YCu_3O_6$ compounds.

3) Their 2-dimensional nature is clearly demonstrated in the E($\underline{k}$) calculations. The CuO_2 chains in the Ba-Y-Cu-O compounds become CuO_2 'molecules' trappped in the CuO_2 sheets with the creation of the O(4) vacancy- echoed in

the band structure as a reduced dispersion in all directions of k space.The 2-d Fermi surface is also shown here for $Ba_2YCu_3O_7$.

4) These calculations rule out a simple Peierls transition, doubling the unit cell and splitting the half filled band at Ef. The well nested band in La_2CuO_4 suggests this as a strong possibility. One of the three possible bands forming the Fermi surface in $Ba_2YCu_3O_7$ is also calculated to show good $\sqrt{2}$, $\sqrt{2}$ nesting. The breakdown of the one-electron-approximation is apparent in the failure to match the semiconducting behaviour of the low temperature La-Cu-O and $Ba_2YCu_3O_6$ compounds. The approximate exchange-correlation term of these calculations fails to account for the (probable) Mott localisation which produces the semiconducting gap.

Chapter 8 Conclusion

This thesis has shown the application of an ab initio LCAO method of calculating the electronic band structure of 3 systems of layered transition metal compounds. The results have been shown to be consistent with experimental results (where available), bearing in mind the one-electron approximation. The work of chapter four is particularly suited to this method since a large unit cell is encountered and a comparatively large number of $\underline{k}$ points were sampled for an accurate densities of states and relative Fermi level (highest occupied state) estimate since the basis set is small- thus reducing the size of the matrix to be diagonalised. The similarity of Mo and W ditelluride when having the same crystal structure implies the importance of spin-orbit coupling in determining the naturally occuring (lowest energy) crystal type. The role of the short metal-metal distances in Mo- and WTe_2 with a distorted octahedral coordination around the metal atoms was seen when the metal d bands resembled the trigonal prismatic crystal field splitting found in the sulphides and selenides of Mo and W- even though it does not appear energetically favourable to stack the large Te atoms above each other in a trigonal prismatic structure due to the large coulomb repulsion.

The group IVa transition metal trichalcogenides were thoroughly examined as both the A and B variants. Of great interest here was $ZrTe_3$ which appears to be semi-metallic- supporting the belief that this compound undergoes a Peierls type distortion at low temperature since it may be possible for it to assume a semiconducting state with a reduced total energy. Chemical trends from the periodic table were reflected in this series of calculations- the atomic orbital basis set proved extremely useful for this type of analysis.

The commonly applied one-electron approximation and the associated approximate treatment of the exchange-correlation potential showed that a Mott-type localisation process is important in the high T_c ceramic superconductors studied here. The fermi surface nesting driving the La_2CuO_4 semiconducting transition was clearly reflected in these calculations, with similarities shown in the Ba-Y-Cu-O system which (for the stoichiometric case at least) showed three sheets to the Fermi surface, one of which appeared $\sqrt{2} \times \sqrt{2}$ nested. The suggestion that this nesting was responsible for the Peierls transition opening up a semiconducting gap in the tetragonal/orthorhombic phase transition was shown to be ruled out by symmetry arguments. The role of a commensurate spin-density wave (antiferromagnetism) in breaking the double degeneracy at the Fermi level

causing a metal-semiconductor transition was discussed. The layered nature of these compounds was demonstrated clearly by the strongly 2D Fermi surface and also, for example, by the weak coupling of the CuO_2 planes in La_2CuO_4.

Two chapters of this thesis have recently been published- chapter 4, the tellurides of Mo and W (Dawson and Bullett, 1987) and chapter 7, the high T_c superconductors (Bullett and Dawson, 1987), see also Almond et al., 1987.

Two other low dimensional systems are currently being studied by this ab initio method- the group Va ditellurides Nb- and $TaTe_2$; and the family of ternary phosphides MPX_3 (M= Ni,Fe; X= S,Se).

Work has also been started on atoms and small molecules at transition metal surfaces (where the van der Waals gap is taken to infinity). Two systems have already been analysed: chemisorbed formate on [100] and [110] copper surfaces and the surface reconstructions driven by carbon on nickel [100] (Bullett and Dawson, 1988a,b).

References

Acrivos J.V., Liang W.Y., Wilson J.A., and Yoffe A.D.; J. Phys. C, 3, L18, 1971.

Adachi T., Goto T. and Nishina Y., J. Luminescence, 21, 169, 1980.

Adams W.H., Chem. Phys. Lett., 11, 71, 1971.

Almond D.P., Bullett D.W., Chapman B., Cooke R.G., Dawson W.G., Draper R.C.J., Ford P.J., Hampton R.N., Wang Hong, Lambson E.F., Saunders G.A., Sullivan R.A.L., Proceedings of European workshop on High T_c Superconductors and Potential Applications, Fiera Del Mare, Genoa, Italy, July, 1987.

Andersen O.K., Pawlowski Z., Jepsen O., Phys. Rev. B, 34, 8, 1986.

Anderson P.W., Phys. Rev. Lett., 21, 13, 1968.

Anderson P.W., Phys. Rev. B, 181, 25, 1969.

Anderson P.W., Science, 235, 1196, 1987.

Anedda A., Fortin E. and Raga F., Can. J. Phys., 57, 368, 1979.

Ashcroft N.W. and Mermin N.D., Solid State Physics, Holt-Sauders, Philadelphia, 1981.

Austin B.J., Heine V. and Sham L.J., Phys. Rev., 127, 276, 1962.

Azaroff L.V., and Brophy J.J.; Electronic Processes in Materials, Mc Graw Hill, New York, 1963.

Balachin A.A., in Levy F. (ed), Crystallography and Chemistry of materials with layered structure, D Reidel Publ. Co., Dordecht, Boston,1976.

Ballentine L.E. and Kolar M., J. Phys. C, 19, 981, 1986.

Barrow G.M., Physical Chemistry, Mc Graw Hill, 1979.

Bayliss S.C. and Liang W.G., J. Phys. C, 14, 803, 1981.

Bayliss S.C. and Liang W.Y., J. Phys. C, 15, 1283, 1982.

Beal A.R., and Liang W.Y.;Phil Mag, 33, 121, 1976.

Beal A.R. and Hughes H.P., J. Phys. C, 12, 881, 1979.

Bear J.A., and McTaggart F.K.; Aust. J. Chem., 11, 485, 1958.

Bednorz J.G. and Muller K.A., Z. Phys. B- Condensed Matter, 64, 1986.

Bird D.M., Eaglesham D.J., Withers R.L., Mc Kernan S. and Steeds J.W. (see also Wilson J.A.), in Lecture Notes in Physics, 217-Charge Density Waves in Solids, Springer-Verlag, Berlin, 1985.

Blitz W., Ehrlich P. and Miesel K., Z. Anorg. Chem., 288, 241, 1956.

Bongers P.F. et. al.; J. Phys. Chem. Solids., 29, 977, 1968.

Bordet P., Chaillout C., Capponi J., Chenavas J., Marezio M.; Nature, 327, 687, 1987.

Boys S.F., Proc. Roy. Soc., A309, 159, 1969.

Bransden B.H. and Joachain C.J., Physics of Atoms and Molecules, Longman, 1984.

Brattas L. and Kjekshus A., Acta Chem. Scand., 25, 2783,

1971.

Brixner L.H., J. Inorg. Chem., 24, 257, 1962.

Bromley R.A., Murray R.B. and Yoffe A.D., J. Phys. C, 5, 758, 1972.

Brown B.E. and Beerntsen D.J., Acta. Crystallog., 18, 31,1965.

Brown E.B., Acta Cryst., 20,268, 1966.

Brown F.C., Chiang T.C., Friedmann T.A., Ginsberg D.M., Kwawer G.N., Miller T and Mason M.G., unpublished, 1987.

Bullett D.W., J Phys C,11, 4501, 1978.

Bullett D.W., J. Phys. C, 12, 227, 1979.

Bullett D.W., in Solid State Physics: Advances in Research and Applications, 35, eds. Ehrenreich H., Seitz F., Turnbull D., Academic Press, New York, 1980.

Bullett D.W., in Theoretical Aspects of Band Structures and Electronic properties of Pseudo-One-Dimensional Solids (ed. Kamimura H.), Reidel, Dordrecht, 1985.

Bullett D.W. and Dawson W.G., J. Phys. C, 19, 5837, 1986a.

Bullett D.W. and Dawson W.G., Sol. St. Comm., 60, 767, 1986b.

Bullett D.W. and Dawson W.G., J. Phys. C, 20, L853, 1987.

Bullett D.W. and Dawson W.G., to be published in Prog. in Surf. Sci., 1988a.

Bullett D.W. and Dawson W.G., to be published in Vacuum (ISSC Proceedings), 1988b.

Capponi J.J., Chaillout C., Hewat A.W., Lejay P., Marezio M., Nguyen N., Raveau B., Soubeyroux J.L., Tholence J.L., Tournier R., submitted to Europhysics Letters, March 1987.

Chadi D.J. and Cohen M.L., Phys. Rev. B, 8, 5747, 1973.

Chan S.K., Heine V., J. Phys. F, 3, 795, 1973.

Clarke R., Marseglia E. and Hughes H.P., Phil Mag., 38, 121, 1978.

Cohen M.H. and Heine V., Phys. Rev., 122, 1821, 1961.

Coles B.R. and Caplin A.P., The Electronic Structures of Solids, Arnold, London, 1976.

Connell G.N., Wilson J.A. and Yoffe A.D., J. Phys. Chem. Solids, 30, 287, 1969.

Cox D.E., Moddenbaugh A.R., Hurst J.J. and Jones R.H., J. Phys. Chem. Solids (in press), 1987.

Dawson W.G. and Bullett D.W., J. Phys. C, 20, 6159, 1987.

DiSalvo F.J.,Schwall R.,Geballe T.H., Gamble F.R. and Oseiki J.H.; Phys. Rev. Letters,27, 310, 1971.

Eaglesham D., Bristol University, unpublished, 1984.

Eaglesham D.J., Bird D.M., Withers R.L., Steeds J.W., J. Phys. C,18, 1, 1985.

Eaglesham D.J., Withers R.L. and Bird D.M., J. Phys. C., 19, 359, 1986.

Emergy V.J., Phys. Rev. Lett., 58, 2794, 1987.

Engelsman F.M.R., van Laar B., Wiegers G.A., and Jellinek F., Acta Cryst. (Interact.), a25, 5247, 1969.

Freltoft T., Fisher J.P., Shirane G., Moncton D.E., Sinha S.K., Vaknin D., Remeika J.P., Cooper A.S., Harshman, Phys. Rev. B, 36, 826, 1987.

Friend R.A., Beal A.R. and Joffe A.D., Phil. Mag., 35, 1269, 1977.

Fung K.K., Mc Kernan S., Steeds J.W. and Wilson J.A., J. Phys. C, 14, 5417, 1981.

Furuseth S.,Brattas L., and Kjekshus A.; Acta. Chem. Scand., A29, 623, 1975.

Gamble F.R., Di Salvo F.J. Klemm R.A. and Geballe T.H., Science, 168, 568, 1970.

Gamble F.R. Osieki J.H., Cais M., Di Sharody R., DiSalvo F.J., Geballe T.H., Science, 174, 493, 1971.

Gamble F.R., J. Sol. St. Chem., 9, 358, 1974.

Garbanskas M.F., Arendt R.H., and Kasper J.S., Inorg. Chem., 26, 3191, 1987.

Gaspar R., Acta Phys. Acad. Sci. Hung., 3, 263, 1954.

Gavaler J.R., Appl. Phys. Lett., 58, 1987.

Gobrecht J., Gerisher H. and Tributsch H.; Ber. Bunsenges Phys. Chem., 82, 1331, 1978.

Goldberg A.M., Beal A.R., Levy F.A. and Davis E.A.; Phil. Mag., 32, 367, 1975.

Goodenough J.B., Mater. Res. Bull., 3, 409, 1968.

Grams G., Dissertation, Univ. of Tubingen, 1961.

Grande von B., MullerBuschbaum Hk. and Schweizer M., Z. anorg. allg. Chem., 428, 120, 1977.

Grant A.J., Wilson J.A., and Yoffe A.D., Phil. Mag., 25, 625, 1972.

Grant P.M. et al., Phys. Rev., B35, 7242, 1987.

Grimmeiss H.G., Rabenan A., Hahn H. and Ness P., Z. Electrochem,m 65, 776, 1961.

Guggenberger L.J. and Jacobson R.A., Inorg. Chem., 7, 2257, 1968.

Guo G.Y., Temmerman W.M. and Stocks G.M., J. Phys. (to be published), 1988.

Hamann S.D., Aust. J. Chem., 11,391, 1958.

Hahn H, and Harder B., Z. Anorg. Chem., 288, 241, 1956.

Hahn H., and Ness P.; Naturwissenshaften, 44, 534, 1957.

Hahn H., Harder B., Mutschke U. and Ness P; Z. Anorg. Allg. Chem., 292, 82, 1957.

Hahn H., and Ness P., Z. Anorg. Allg. Chem., 302, 37, 136, 1959.

Hambourger P.D. and Di Salvo F.J., Physica, 99B, 173, 1980.

Haraldsen, Acta Chem. Scand., 17, 1283, 1963.

Harrison W.A., Pseudopotentials in the theory of metals, Benjamin, New York, 1966.

Hasegawa Y. and Fukuyama, Jpn. J. Appl. Phys., 26, L322,

1987.

Hazen R.M., Finger L.W., Angel R.J., Prewitt C.T., Ross N.L., H.K. Mao, Hadidiacos C.G., Hor P.H., Meng R.L. and Chu C.W., Phys. Rev. B, 13, 7238, 1987.

Herman F. and Skillman S., Atomic Structure Calculations, Prentice-Hall, New Jersey, 1963.

Herrenden-Harker W.G. and Tothill N., Bristol University, unpublished, 1984.

Herring C., Phys. Rev., 57, 1169, 1940.

Hicks W.T., J. Electrochem. Soc., 111, 1058, 1964.

Hind S.P. and Lee P.M., J. Phys. C, 13, 349, 1980.

Hirch J.E., Phys. Rev. Lett., 59, 228, 1987.

Holliger F., Structural Chemistry of Layer Type Phases, Reidel, Holland, 1976.

Hughes H.P. and Friend R.H., J. Phys. C, 11, L103, 1978.

Huisman R., de Jonge R., Haas C. and Jellinek F., Nature, 192, 1065, 1961.

Huisman R., de Jonge R., Haas C. and Jellinek F., J. Sol. State Chem., 3, 56, 1971.

Isomaki H., von Boehm J. and Krusius P., J. Phys C, 12, 3239, 1979.

James P.B. and Lavik M.T., Acta Crystallogr., 16, 1183, 1963.

Jayaraman K.S., Nature, 327, 1987.

Jellinek F., Nature, 192, 1065, 1961.

Jellinek F., Ark. Kemi, 20, 447, 1963.

Jellinek F., Pollak R.A., and Schafer M.W., Mater. Res. Bull., 9, 845, 1971.

Jellinek F., Mat. Res. Bull., 9, 845, 1974.

Jorgensen J.D., Schuttler H.-B., Hinks D.G., Capone II D.W., Zhang K., Brodsky M.B., Scalapino D.J., Phys. Rev. Lett., 58, 1024, 1987.

Kawamura H., Shirotani I., and Tachikawa K.; Phys. Lett., A65, 335, 1978.

Kawamura H., Shirotani I., and Tachikawa K.; J. Sol. St. Chem., 27, 223, 1979.

Khumalo F. and Hughes H., Phy. Rev. B, 22, 2078, 1980.

Khumalo F., Olson C.G. and Lynch D.W., Physica B, 105, 163, 1981.

Knop O. and MacDonald B.D., Canad. J. Chem., 39, 897, 1961.

Knox R.S., Excitons, Academic Press, New York, 1963.

Kohn W and Sham L.J., Phys. Rev., 140, A1193, 1965.

Kronert W., and Plieth K.; Z. Anorg. Allg. Chem., 336, 207, 1965.

Krusius P., von Boehm J., Isomaki H., J. Phys. C, 8, 3788, 1975.

Kurita S., Staehli S.L., Guzzi M. and Levy F., Physica B, 105, 169, 1981.

Levy F., Structural Chemistry of layer-type phases, D.

Reidel, Dordrecht, 1976.

Levy F. (editor), Physics and Chemistry of materials with low-dimensional structures, Reidel, Dordrecht, 1977.

Longo J.M. and Raccah P.M., J. Sol. St. Chem., 6, 562, 1973.

Lowdin P. O-, Intern. J. Quantum Chem., 2, 867, 1968.

Lucovsky G., White R.M., Benda J.A., Revelli J.F.; Phys. Rev. B, 7, 3859, 1973.

McCanny J.V., J.Phys. C, 12, 3263, 1979.

Mc Govern I.T., Williams R.H. and Parke A.W., J. Phys. C, 12, 2689, 1979.

McTaggart F.K., and Wadsley A.D., Aust. J. Chem., 11, 445, 1958.

McTaggart F.K., Aust. J. Chem., 11, 471, 1968.

Manolikas C., van Landuyt J. and Amelinckx S., Phys. Status Solidi a, 53, 327, 1979.

Marinder B-O., Dorm E. and Seleberg M., Acta Chem. Scand., 16, 293, 1962.

Marinder B-O. and Magnelli A., Acta Chem. Scand., 11, 1635, 1957.

Matthiess L.F., Phys. Rev. B, 8, 3719, 1973.

Mattheiss L.F., Phys. Rev. Lett., 58, 1028, 1987.

Megaw H.D., Crystal Structures: a working approach, Saunders, 1973.

Minomura S. and Drickamen H., J. Appl. Phys., 34, 3043,

1963.

Mulliken R.S., J. Chem. Phys., 23, 1833, 1955.

Murray R.B., Bromley R.A., and Yoffe A.D.; J. Phys. C, 5, 746 and 759, 1972.

Myers G.E. and Montet G.L., J Appl. Phys., 41, 4642, 1970.

Myron H.W., Harmon B.N. and Khumalo F.S., J. Phys. Chem. Solids, 42, 261, 1981.

Ohno Y., Hirama K., Nakai S., Sugiura C. and Okada S., J. Phys. C, 16, 6695, 1983.

Ohno Y., Kaneda K. and Okada S., J. Sol. St. Chem., 54, 170, 1984.

Pauling L., The Nature of the Chemical Bond, Cornell U.P., New York, 1960.

Peierls R.E., Z. Phys., 80, 1763, 1933.

Peierls R.E., Quantum Theory of Solids, O.U.P., 1955.

Phillips J.C. and Kleinman L., Phys Rev., 116, 287 and 880, 1959.

Pick R. and Sarma G., Phys. Rev., 135, A1363, 1964.

Puotinen D. and Newham R.E., Acta Cryst., 14, 691, 1961.

Revolinsky E. and Beerntsen D.J., Phys. Chem. Sol., 27, 523, 1966.

Rimmington H.P.B., PhD Thesis, Brighton Poly., 1973.

Roberts B.W., Prog. Cryog., 4, 161, 1964.

Sarma D.D. and Rao C.N.R., Solid St. Comm., 65, 47, 1988.

Schairer W., and Shafer M.W.; Phys. Status Solidi; A17, 181, 1973.

Schutte W.J., De Boer J.L. and Jellinek F., J. Sol. St. Chem., 70, 207, 1987.

Shannon R.D., and Prewitt C.T., Acta Crystallog., B25, 925, 1969.

Sharma R.R., Phys. Rev. B, 19, 2813, 1979.

Shen T.H. and Liang W.Y., J Phys. C, 16, L83, 1983.

Shepherd F.R. and Williams P.M., J Phys. C, 7, 4416, 1974.

Siegrist T., Sunshine S., Murphy D.W., Cava R.J. and Zahurak S.M., Phys. Rev. B, 35, 7137, 1987.

Simon A., Angew. Chem. Int. Ed. Engl., 20, 1981.

Slater J.C., Phys. Rev., 81, 385, 1951.

Slater J.C., Quantum Theory of Molecules and Solids, volume 4, Mc Graw-Hill, 1974.

Slater J.C. and Koster G.F., Phys Rev., 94, 1498, 1954.

Smith N.V. Kevan S.D., DiSalvo F.J., J. Phys. C, 18, 3175, 1985.

Somoano R.B., Hadek V and Rembaum A., J. Chem. Phys., 58, 697, 1973.

Srivastava S.K. and Avasthi B.N., J. Mat. Sci., 20, 3801, 1985.

Strobel P., Capponi J.J., Chaillout C., Marezio M.,

Thoulence J.L.; Nature, 327, 306, 1987.

Takagi H., Uchida S., Kitazawa K. and Tanaka J., Jpn. J. Appl. Phys. Lett., to be published, 1987.

Takahashi S., Sambongi T. and Okada S., J. de Physique, 44, 1733, 1983.

Takegahara K., Harima H. and Yanase A., Jap. J. Appl. Phys., 26, L352, 1987.

Tarascon J.M., Greene L.H., McKinnon W.R. and Hull G.W., Phys. Rev. B, 35, 7115, 1987.

Temmerman W.M., Stocks G.M., Durham P.J. and Sterne P.A., J. Phys. F, 17, L135, 1987.

Thanh T.D., Koma A., Tanaka S., Appl. Phys., 22, 205, 1980.

Thomson A.H., Gamble F.R., and Revelli J.F.; Solid State Comm., 9, 981, 1971.

Upadhyayula L.C., Loferski J.J., Wold A., Grint W. and Kershaw R.; J. Appl. Phys., 39, 4736, 1968.

Vaknin D., Sinha S.K., Moncton D.E., Johnston D.C., Newsam J.M. Safinya C.R. and King H.E., Phys. Rev. Lett., 58, 2802, 1987.

Vellinga M., de Jonge R. and Haas C., J. Sol. St. Chem., 2, 299, 1970.

Verma A.R. and Krishna P.; in Polymorphism and Polytypism in Crystals, John Wiley and Sons Inc., New

York, 1966.

Weeks J.D., Anderson P.W. and Davidson A.G.H., J. Chem. Phys., 58, 1388, 1973.

Weiting T. and Verble, Phys. Rev. B, 3, 4286, 1971.

Weiting T.J., Grisel A. and Levy F., Physica B, 105, 366, 1981.

Wertheim G.K., DiSalvo F.J. and Buchanan D.N.E., Solid St. Comm., 13, 1225, 1973.

White R.M., and Lucovsky G.; Sol. State Comm., 11, 1369, 1972.

Whittingham MS,Science, 192, 1126, 1976.

Whittingham M.S. and Jacobson A. (eds.), Intercalation Chemistry, Academic Press, New York, 1982.

Williams P.M. and Shepherd F.R., J Phys. C, 6, 236, 1973.

Williams R.H. and Mc Evoy A.J., Phys. stat. solidi, 47b, 217, 1971.

Wilson J.A. and Yoffe A.D., Adv. Phys., 18, 193, 1969.

Wilson J.A., DiSalvo F.J., Mahajan S., Phys. Rev. Lett., 32, 882, 1974.

Wilson J.A., DiSalvo F.J. and Mahajan S., Adv. in Physics, 24, 117, 1975.

Wilson J.A. and Mahajan S., Comm. on Phys., 2, 23, 1977.

Wilson J.A., Phil. Trans. Roy. Soc., A314, 159, 1985.

Wilson J.A., J. Phys. C, 20, L911, 1987.

Withers R.L. and Wilson J.A., J. Phys. C, 19, 4809,

1986.

Wu M.K., Ashburn J.R., Torng C.J., Hor P.H., Meng R.L., Gao L., Huang Z.J., Wang Y.Q. and Chu C.W., Phys. Rev. Lett., 58, 908, 1987.

Wyckoff R.W.G., Crystal Structures, 1, 2nd edition, Interscience, 1963.

Yu J., Freeman A.J. and Xu J-H, Phys Rev. Lett., 58, 1035, 1987.

Zandbergen H.W., Gronsky R., Wang K. and Thomas G., Nature, 331, 596, 1988.

Zhao T-X., Katnani A.D., Perfetti P. and Margaritondo G., Il Nuovo Cimento, 1, 549, 1982.

Zunger A. and Freeman A.J., Phys. Rev. B, 16, 906, 1977.

Zunger A. and Freeman A.J., Phys. Rev. B, 19, 6001, 1979.